Peterhead CCS Project

Doc Title: Geomechanics Report

Doc No.	PCCS-05-PT-ZP-9025-00004
Date of issue:	12/09/2014
Revision:	K02
DECC Ref No:	11.115
Knowledge Cat:	KKD-Subsurface

KEYWORDS

Goldeneye, CCS, CO_2, Geomechanics, tensile failure, shear failure, fault reactivation, caprock integrity, temperature, wellbore.

Produced by Shell U.K. Limited
ECCN: EAR 99 Deminimus

IMPORTANT NOTICE

Information provided further to UK CCS Commercialisation Programme (the "**Competition**")

The information set out herein (the "**Information**") has been prepared by Shell U.K. Limited and its sub-contractors (the "**Consortium**") solely for the Department of Energy & Climate Change in connection with the Competition. The Information does not amount to advice on CCS technology or any CCS engineering, commercial, financial, regulatory, legal or other solutions on which any reliance should be placed. Accordingly, no member of the Consortium makes (and the UK Government does not make) any representation, warranty or undertaking, express or implied, as to the accuracy, adequacy or completeness of any of the Information and no reliance may be placed on the Information. Insofar as permitted by law, no member of the Consortium or any company in the same group as any member of the Consortium or their respective officers, employees or agents accepts (and the UK Government does not accept) any responsibility or liability of any kind, whether for negligence or any other reason, for any damage or loss arising from any use of or any reliance placed on the Information or any subsequent communication of the Information. Each person to whom the Information is made available must make their own independent assessment of the Information after making such investigation and taking professional technical, engineering, commercial, regulatory, financial, legal or other advice, as they deem necessary.

Table of Contents

2.1. Loss of containment: migration and leakage scenarios 7
2.1.1. The effect of CO_2/brine/rock interactions on hydrological and mechanical properties 8
2.1.2. Caprock seepage through diffusive processes and/or enhanced caprock permeability 9
2.1.3. Caprock leakage resulting from changes in effective stress state 10
2.1.4. Spill leakage resulting from induced fracturing 12
2.1.5. Potential for thermally-induced fracturing 13
2.1.6. Well bore leakage along legacy and injection wells 13
2.1.7. Fault leakage, movement and induced seismicity 13
2.2. Overview of geomechanical threats 14
3.1. Geology and structural model 15
3.2. In-situ stress state and pore pressures 19
3.2.1. Vertical stress 19
3.2.2. Horizontal stresses 19
3.2.3. Pore pressure in the over- and underburden formations 21
3.2.4. Pore pressure changes in the reservoir 21
3.3. Rock mechanical properties of the formations 23
3.3.1. Rock mechanical properties of the over- and underburden formations 23
3.3.2. Failure parameters of the Rødby shale caprock 26
3.3.3. Rock mechanical properties of the Captain Sandstone reservoir 27
4.1. Stress changes in the reservoir and definition of failure criteria 33
4.2. Initialisation of the simulation 35
4.3. Production phase 36
4.3.1. Stress changes during gas production 36
4.3.2. Production-related reservoir compaction and sea-floor subsidence 41
4.4. Injection phase 42
4.4.1. Stress changes during CO_2 injection 42
4.4.2. Injection-related inflation and sea-floor uplift 44
4.5. Stress changes in the caprock during production and injection 45
4.6. Tensile failure potential of the reservoir during production and injection 49
4.7. Summary of findings 51
5.1. Case B: Poisson's ratio + 0.05 54
5.2. Case C: Poisson's ratio - 0.05 55
5.3. Case D: Young's Modulus value divided by half for the over- and underburden formations 56
5.4. Case E: worst case scenario rock failure parameters for reservoir and caprock 57
5.4.1. Reservoir formation (Captain E&D) 58
5.4.2. Caprock (Rødby Shale) 61
5.5. Case F: worst case scenario failure parameters (case e) plus different stress path during the injection phase 63
5.6. Case G: pressure support from the aquifer, plus worst case scenario rock failure parameters for reservoir and caprock 65
5.7. Case H: injection pressure > hydrostatic pressure, plus worst case scenario rock failure parameters for reservoir and caprock 70
5.8. Case I: pressure at the end of depletion is assumed to be 13.8 MPa [2000 psia], plus worst case scenario rock failure parameters for reservoir and caprock 73
6.1. Introduction 75
6.2. Condition #1: effect of thermal changes on the state of stress 78
6.2.1. The near wellbore area 78

6.2.2. The farther field reservoir and base of the caprock *88*
6.3. Condition #2: continuous replenishing of cold CO_2 at the fracture tip 96
6.4. Condition #3: propagation of the fracture across an interface 98
6.5. Condition #4: sufficient permeability increase within the created fracture 101
6.6. Conclusions 102
6.6.1. Near wellbore, within the cemented region and within the open hole *102*
6.6.2. Farther field reservoir and at the base of the caprock *102*
7.1. Principle of fault stability 104
7.2. Fault interpretation for the Goldeneye field 105
7.3. Deterministic assessment: results and uncertainty 108
7.3.1. SVS case I: typical failure parameters for Rødby Shale *109*
7.3.2. SVS case II: typical failure parameters for Captain E&D reservoir *111*
7.3.3. SVS case III: worst case scenario failure parameters for Rødby Shale *112*
7.4. Uncertainty analysis: distribution of elastic fault properties 113
7.5. Conclusions 114
8.1. Geological barrier: geology of the field 116
8.2. Geological barrier: structural trapping 116
8.3. Operational barrier: bottom hole pressure 116
8.4. Operational barrier: tracking wellbore leakage 117
8.5. Geomechanical barrier: fracturing of the caprock by thermal effects 117
8.6. Geomechanical barrier: fracture propagation across interface 117
9.1. General conclusions from the geomechanical modelling efforts 118

Tables

Table 0-1—Assessment of geomechanical threats assessed for the Peterhead CCS project 2
Table 2-1—Overview of the geomechanical threats and risks discussed, with references to the Chapters in which they will be addressed. 14
Table 3-1—Data inventory for geomechanical model construction 15
Table 3-2—k-values for both depletion and injection modelling as used in the different formations. Total horizontal stress is taken the same in all directions. 21
Table 3-3—Dynamic elastic rock properties for five overburden and two underburden formations 24
Table 3-4—Key findings from literature for failure parameters of the caprock. 26
Table 3-5—Results from triaxial tests on Goldeneye reservoir core samples of the Captain D Sandstone. Sample 1 broke during the second cycle. 28
Table 3-6—Results from triaxial tests on Goldeneye reservoir core samples of the Captain D Sandstone, employing fluid flow with brine and subsequently with CO_2-saturated brine. 29
Table 3-7—Base case values for the mechanical properties of the Captain Sandstone. 31
Table 3-8—Results from literature and experiments of failure parameters of reservoir rock 32
Table 5-1—Cases that were modelled to investigate the effect of different rock properties and pressures in the integrity of the reservoir and caprock 53
Table 5-2—Base case results 54
Table 5-3—Key results for Case B 54
Table 5-4—Key results for Case C 55
Table 5-5—Key results for Case D 56
Table 5-6—Key results for Case E 57
Table 5-7—Key results for Case F 63
Table 5-8—Key results for Case G 67
Table 5-9—Key results for Case H 71
Table 5-10—Key results for Case I 73
Table 6-1—Thermal stresses due to 60°C cooling of the Goldeneye reservoir and caprock. 77
Table 6-2—Overview of the four key conditions for the different cooling area: 1) near wellbore area, within the cemented region of the caprock ; 2) near wellbore area, within the open hole section of the caprock; and 3) in the farther field of the reservoir and at the base of the caprock. References indicate the sections where each condition will be discussed. 78
Table 6-3—Undrained material parameters for the Rødby Shale used in the near wellbore stress analysis 82
Table 6-4—Drained material parameters for the Rødby Shale used in the near wellbore stress analysis. 83
Table 6-5—Base and low case parameters used in the PBore model 84
Table 6-6—Details of the model versions for the PWRI-Frac simulations. 91
Table 6-7—Results of the different model versions for the PWRI-Frac simulations. 91
Table 6-8—Notation and values for the calculation of the change of in-situ stress for an elliptical cooled zone. 94
Table 6-9—Input parameters for the calculation of the CCC (76) 99

Table 6-10—Overview of the four key conditions for the different cooling area: 1) near wellbore area, within the cemented region of the caprock ; 2) near wellbore area, within the open hole section of the caprock; and 3) in the farther field of the reservoir and at the base of the caprock. 102
Table 7-1—Parameter sensitivity study 109
Table 7-2—Normal distribution functions for Young's modulus and Poisson's ratio of the main formations, as well as fault cohesion and friction angle for the faults, specified by their P10, P50 and P90 values. 113
Table 11-1: Unit Conversion Table 123
Table 11-2: Well name abbreviations 123

Figures

Fig. 1-1—Schematic diagram illustrating a CO_2 injection site consisting of a depleted oil or gas reservoir, or aquifer 3
Fig. 1-2—Schematic diagram showing the subsurface processes that are perturbed by CO_2 injection, and the concomitant changes in temperature, pressure and pore fluid density. 4
Fig. 2-1—(a) Outward pointing DP vector in case for aquifer storage, and (b) inward pointing DP vector in case of depleted reservoir storage. 7
Fig. 2-2—Simple bow-tie diagram for the geomechanical threats and consequences during CO_2 containment 8
Fig. 2-3—Hypothetical in-situ stress response to changes in pore pressure during production and injection phase. 10
Fig. 3-1—Stratigraphic column of the formations in the Goldeneye area (left hand) and the formations modelled in GeoMec (right hand). 16
Fig. 3-2—Bird's-eye view from the south-west towards the northeast direction of the geomechanical model. 17
Fig. 3-3—Cross-sectional view showing key formations. 17
Fig. 3-4—Plan view of model showing nested mesh resolution. 18
Fig. 3-5—Thickness map of Captain E&D reservoir as in GeoMec. 18
Fig. 3-6—Thickness of Rødby Formation (caprock) as in GeoMec. 18
Fig. 3-7—Vertical stress profile of all the eight wells in the Goldeneye area. 19
Fig. 3-8—Total minimum principal stress gradient, i.e. leak off pressure test gradient, trend is represented as the lower bound of LOT data. 20
Fig. 3-9—Pore pressure as a function of time for a typical location in the reservoir 22
Fig. 3-10—Top view maps of upscaled pore pressures for Captain E&D reservoir formations at initial (a), end of production (b), and end of injection (c) phase. 23
Fig. 3-11—Log of Well 14_29a-3 with DTP, DTS, RHOB and derived E_d and $\boldsymbol{\nu}_d$. Depth is given as measured depth MD. 25
Fig. 3-12—Rock properties of the Captain E&D reservoir package during the production phase 30
Fig. 4-1—Schematic failure modes, showing tensile failure (top) and shear failure (bottom). 33
Fig. 4-2—Mohr-circle diagram relating the principal stress state and the Mohr-Coulomb failure condition 34
Fig. 4-3—Map view of the pore pressure change within the Captain E&D formations, from the initial phase to the end of the production phase. 35
Fig. 4-4—Initial in-situ stresses and pore pressure profile compared to GeoMec computed initial total maximum principal stress and initial total minimum principal stress. 36
Fig. 4-5—3D bird's-eye view of two cross sections through all the formations 37
Fig. 4-6—Map view of Captain E&D reservoir 38
Fig. 4-7—Mohr circles and Mohr-Coulomb failure line for the Captain E&D reservoir formation 39
Fig. 4-8—Map of the shear capacity distribution for the Captain E&D reservoir 40
Fig. 4-9—Bird's-eye view of the sea-floor with subsidence (max 4.6 cm [1.8 in]) after production. 41

Fig. 4-10—Cross section of overburden, reservoirs (indicated by white arrows), and underburden with vertical displacement (8.9 cm [3 in] at the top of the Captain E&D reservoir) after production. 41
Fig. 4-11—3D bird's-eye view of two cross sections through all the formations 43
Fig. 4-12—Map view of Captain E&D reservoir 44
Fig. 4-13—Bird's-eye view of seafloor subsidence (max 3.6 cm [3.4 in]) after injection. 45
Fig. 4-14—Cross section of overburden, reservoirs (indicated by white arrows), and underburden with vertical displacement (5.6 cm [2.2 in] at the top of the Captain E&D reservoir) after injection. 45
Fig. 4-15—3D zoomed-in bird's-eye view of two cross-sections (west-east and north-south, intersecting at black line) through parts of the reservoir, caprock, under- and overburden. 46
Fig. 4-16—Mohr circles and Mohr-Coulomb failure line for the Rødby Shale caprock formation, before production, after production, and after injection 47
Fig. 4-17—Map of the shear capacity distribution for the Rødby Shale caprock formation 48
Fig. 4-18—Minimum effective principal stress 50
Fig. 5-1—Case B: Map of the shear capacity distribution throughout the Captain E&D formation (a) at the end of production and (b) at the end of injection 55
Fig. 5-2—Case C: Map of the shear capacity distribution throughout the Captain E&D formation (a) at the end of production and (b) at the end of injection. 56
Fig. 5-3—Case D: Map of shear capacity distribution within the Captain E&D formation (a) at the end of production and (b) at the end of injection. 57
Fig. 5-4—Case D: Map of the shear capacity distribution within the caprock formation (Rødby Shale) (a) at the end of production and (b) at the end of injection. 57
Fig. 5-5—Case E: Mohr-Coulomb failure line for the Captain E&D formation 59
Fig. 5-6—Case E: Distribution map of the shear capacity values within the Captain E&D, assuming extreme worst case scenario failure parameters, i.e. a very weak, unconsolidated sandstone reservoir 60
Fig. 5-7—Case E: Mohr-Coulomb failure line for caprock, modelled using worst case scenario failure parameters. In addition, Mohr circles are shown for the initial state of stress, the state of stress after production, and the state of stress after injection. 61
Fig. 5-8—Case E: Map of the shear capacity distribution throughout the caprock formation, assuming extreme worst case scenario failure parameters for essentially unconsolidated shale. 62
Fig. 5-9—Case F: Mohr-Coulomb failure line for Captain E&D reservoir for a worst case scenario represented by rock failure parameters representing an unconsolidated sandstone reservoir. Mohr circles represent the different stress states prior to depletion, at the end of production and at the end of injection. 64
Fig. 5-10—Case F: Map of shear capacity values throughout the Captain E&D formation at the end of the injection phase, assuming extreme worst case scenario rock failure parameters for the reservoir rock. 65
Fig. 5-11—Case G: Top view map of pressure changes in the Captain E&D reservoir (marked area) and the surrounding aquifer due to gas production, accounting for aquifer support. 66

Fig. 5-12—Case G: Top view map of pressure changes in (a) solely the Captain E&D reservoir (marked area), assuming no aquifer support, and (b) the Captain E&D reservoir plus surrounding aquifer, accounting for aquifer support. 66
Fig. 5-13—Case G: Distribution map of the shear capacity values for Captain E&D formation (a) for the initial stress state, (b) for the stress state after production, and (c) for the stress state after injection. 68
Fig. 5-14—Case G: Map of shear capacity values throughout the caprock formation (a) prior to depletion, (b) at the end of production, and (c) at the end of the injection phase. 69
Fig. 5-15—Case H: Distribution map of the injection pressure in the Captain E&D reservoir in 2025. 70
Fig. 5-16—Case H: Map of the pressure difference between the final injection pressure in the Captain E&D reservoir in 2025 and the hydrostatic pressure. 71
Fig. 5-17—Case H: Map of shear capacity results for Captain E&D reservoir, using the worst case scenario failure parameters, after the injection pressure was increased by 2.2 MPa [319 psia]. 72
Fig. 5-18—Case H: Map of shear capacity distribution throughout the caprock formation after having injected the reservoir with a pressure that is 1.5 MPa [218 psia] higher than the hydrostatic pressure. 72
Fig. 5-19—Case I: Distribution map of shear capacity values for Captain E&D reservoir, assuming it consist of unconsolidated sandstone (worst case scenario failure parameters), at the end of the depletion stage, when the minimum pore pressure was 13.8 MPa [2000 psia]. 74
Fig. 5-20—Case I: Distribution map of shear capacity results for the Rødby Shale caprock, assuming worst case scenario failure parameters, after depletion has ended, resulting in a minimum pore pressure of 13.8 MPa [2000 psia] (b). 74
Fig. 6-1:--Reservoir simulation of cooling in the grid block adjacent to injection well. 75
Fig. 6-2—Prediction of cooling by diffusion, over a 10 year period, in the Rødby caprock adjacent to the Captain reservoir 76
Fig. 6-3—Schematic diagram illustrating the impact of the temperature change on the in-situ stresses and the range of predicted injection pressures 77
Fig. 6-4—Near wellbore temperature profiles as a function of time 79
Fig. 6-5—Pore pressure profiles as a function of radial distance from the wellbore and time for permeability in the range of 1 (left) to 10 (right) nanoDarcy. 81
Fig. 6-6—Effective stress state of the near wellbore environment after cooling under undrained conditions. 82
Fig. 6-7—Effective stress state of the near wellbore environment after cooling under drained conditions. 83
Fig. 6-8—(a) Temperature and (b) pore pressure distributions as a function of time for the base case PBore model assuming a 100 nD permeability. 86
Fig. 6-9—Comparison of the failed zone (red area) around well from the base case PBore simulation with (a) cooling of the formation for 4 years, and (b) no temperature change in the formation. 87
Fig. 6-10—Evolution of wellbore shear failure (red areas) from the low case PBore simulation as a function of time under cooling conditions. 88
Fig. 6-11—PWRI-Frac simulation for Goldeneye reservoir 89

Fig. 6-12—PWRI-Frac calculates the thermo-poro-elastic effects where fluid leak-off occurs in the permeable units. 89
Fig. 6-13—Schematic diagram to illustrate the problem with diffusive cooling of the caprock adjacent to a fracture and plume of CO_2 90
Fig. 6-14—lot of the predicted vertical fracture growth for the different model versions of the PWRI-Frac simulations. 92
Fig. 6-15—Plot of the predicted vertical height growth for model versions V9-V11, where the minimum principal stress in the Rødby was reduced by the high case thermo-elastic stress across the whole unit 93
Fig. 6-16—Illustration of the formation of secondary fractures due to the change in the ratio of the in-situ stresses in an elliptical cooled zone (65). 94
Fig. 6-17—2D in-situ stresses for an elliptical zone; (a) the long-axis is parallel to the major principal stress and (b) the short-axis is parallel to the minor principal stress. 94
Fig. 6-18—Calculated change in the major (S1) and minor (S2) principal stress for the elliptically cooled zone in the Rødby caprock. 96
Fig. 6-19—Example of 3 models used to calculate the morphology of hydraulic fractures in simulation software. From left to right: elliptical, PKN and GDK (68). 96
Fig. 6-20—Examples of hydraulic fracture morphology reported in the literature. 97
Fig. 6-21—Interface geometry and coordinate system to describe the 2D stresses near a fracture tip approaching a frictional interface (76). 98
Fig. 6-22—Plot of the crossing stress ratio criterion from Renshaw & Pollard (76) 99
Fig. 6-23—Calculation of the compressional crossing ratio for an interface such as between the Captain and Rødby Formations 100
Fig. 6-24—Calculation of the compressional crossing ratio for an interface such as between the Captain and Rødby Formation 101
Fig. 7-1—Schematic diagram showing the stresses acting on a fault 104
Fig. 7-2—3D top view of the Captain D with potential faults, gas water contact (blue line), wells and seismic sections. 106
Fig. 7-3—Top view of many potential faults (indicated by green lines) crossing the Captain D reservoir 107
Fig 7-4—3D bird's-eye view (south-west to north-east direction) of many potential faults through the reservoir formations 107
Fig. 7-5—3D bird's-eye view (south-east to north-west direction) of many potential faults through the reservoir formations 108
Fig. 7-6—3D bird's-eye view (south-west to north-east direction) of many potential faults 108
Fig. 7-7—SVS case I scenario after injection: 3D bird's-eye view 110
Fig. 7-8—SVS case I scenario: 3D bird's-eye view 111
Fig. 7-9—SVS case II scenario: 3D bird's-eye view 112
Fig. 7-10—3D bird's-eye view 112
Fig. 7-11—Tornado chart showing the impact of the uncertainties in Young's modulus and Poisson's ratio of the formations, and in fault cohesion and friction angle of the faults, on the maximum SCU of the most critical fault. 114

Executive Summary

In response to CO_2 injection, the temperature, pressure and chemical equilibrium of the reservoir-caprock system will be changed, resulting in a range of coupled processes affecting the geomechanical response and state of stress of the system. Therefore, the long-term integrity of the reservoir and overlying caprock need to be investigated, focussing on the potential for CO_2 migration from the store.

This report summarises the results obtained from experimental and modelling efforts to quantify the effect of CO_2 injection on the geomechanical behaviour of the Goldeneye field reservoir-caprock system. An investigation was performed of a range of relevant geomechanical threats, as identified in other CCS projects, such as Barendrecht and Barendrecht-Ziedewij (The Netherlands), Sleipner (Norway), and In Salah (Algeria). A summary of these geomechanical threats is given in Table 0-1.

This report has been updated from the Longannet CCS Project version to be restructured to better support the containment risk assessment.

It should be noted that the models in this study are based on the storage of 20 million tonnes of CO_2 injected over a period of 10 years. The conclusions presented here are therefore based on this analysis. Currently, the total planned injection has been reduced to 10 million tonnes of CO_2 in 10 years. This means that the final CO_2 pressure in the Goldeneye field will be less than presented here, despite the potential of aquifer driven re-pressurisation of the reservoir, and the resultant stress changes will also be lower.

Overall, the conclusions of our studies are that no loss of containment through failure of the reservoir and/or caprock can be expected for the injection of 20 million tonnes of CO_2 over 10 years as described in this report. Under these operating conditions, fault reactivation, and associated induced seismicity, will be unlikely. The work has not explored the case of injection of the additional volumes of CO_2 (above 20 million tonnes) or at rates higher than 2 million tonnes per year and no comment can be made with reference to operating outside these boundaries.

Table 0-1—Assessment of geomechanical threats assessed for the Peterhead CCS project

Threat	Significant Risk	Evidence	Uncertainty
Tensile failure of the reservoir (Captain E&D Sandstones)	No	The maximum CO_2 injection will not be raised above the initial virgin pressure (cf. Chapters 4 and 5).	Negligible as stress state is far away from failure envelope determined by worst case scenario rock properties.
Shear failure of the reservoir (Captain E&D Sandstones)	No		
Tensile failure of the entire caprock	No		
Shear failure of the entire caprock	No	For a maximum bottom hole injection pressure of 24.4 MPa [3539 psi] the shear capacity is 0.94. A slightly higher injection pressure leads to slightly higher stresses in the caprock, while the fluid pressure is not changing. This has a stabilising effect on the state of stress within the caprock (cf. Chapter 5).	Worst case scenario might be too pessimistic as cohesion of the Rødby Shale is probably higher than zero. Also the total caprock package is thicker than in the current modelling effort, which assessed only the Rødby caprock and did not consider the Hidra and Plenus Marl Formations as part of the caprock.
Leaking close to the wellbore due to thermal fracturing	No	Detailed study on the coupled effects of temperature and pore pressure in the shale close to the wellbore (cf. Section 6.2.1).	Results modelled for vertical wells only.
Thermal fracturing of the Rødby caprock	No	Analytical solutions, coupled with hydraulic fracture simulations indicate the injection pressures will not be high enough to cause tensile failure (cf. Section 6.2.2).	Paucity of thermal data on shales, which gives a wide range in possible outcomes. Require numerical study of fracture propagation and thermo-elastic response of caprock.
Fault slip	No	Stresses in the field were mapped onto 43 faults. Failure parameters were taken to represent the weakest possible caprock, i.e. equal to worst case scenario rock properties of Rødby Shale (cf. Chapter 7).	Negligible uncertainties regarding risk as results were not found to be close to failure. Residual stress perturbations near faults due to previous movement on the faults have not been considered.

1. Introduction

The main objective of the work presented in this report is to identify and assess any geomechanical risks that might result from the injection and storage of CO_2 in the Goldeneye reservoir. Geological storage of CO_2 in depleted oil and gas reservoirs, or in deep saline aquifers, occurs via two main ways of trapping (1; 2; 3): (1) in the pore space, dissolved in the pore fluid (hydrodynamic or solubility trapping) and/or as a supercritical phase within the pore space (residual and structural trapping), and (2) through the formation of stable carbonate minerals (mineral trapping) – see Fig. 1-1 (4). It should be noted though that most formations have low mineralisation potential (5; 6), and mineralisation reactions are very slow (7; 8; 9). It is therefore more likely that CO_2 injected into a subsurface system will mainly be present as a supercritical phase and/or dissolved in any (residual) formation fluid (6), and will be kept in place by a top seal formation (caprock) and/or sealing faults bounding the reservoir (large-scale structural trapping).

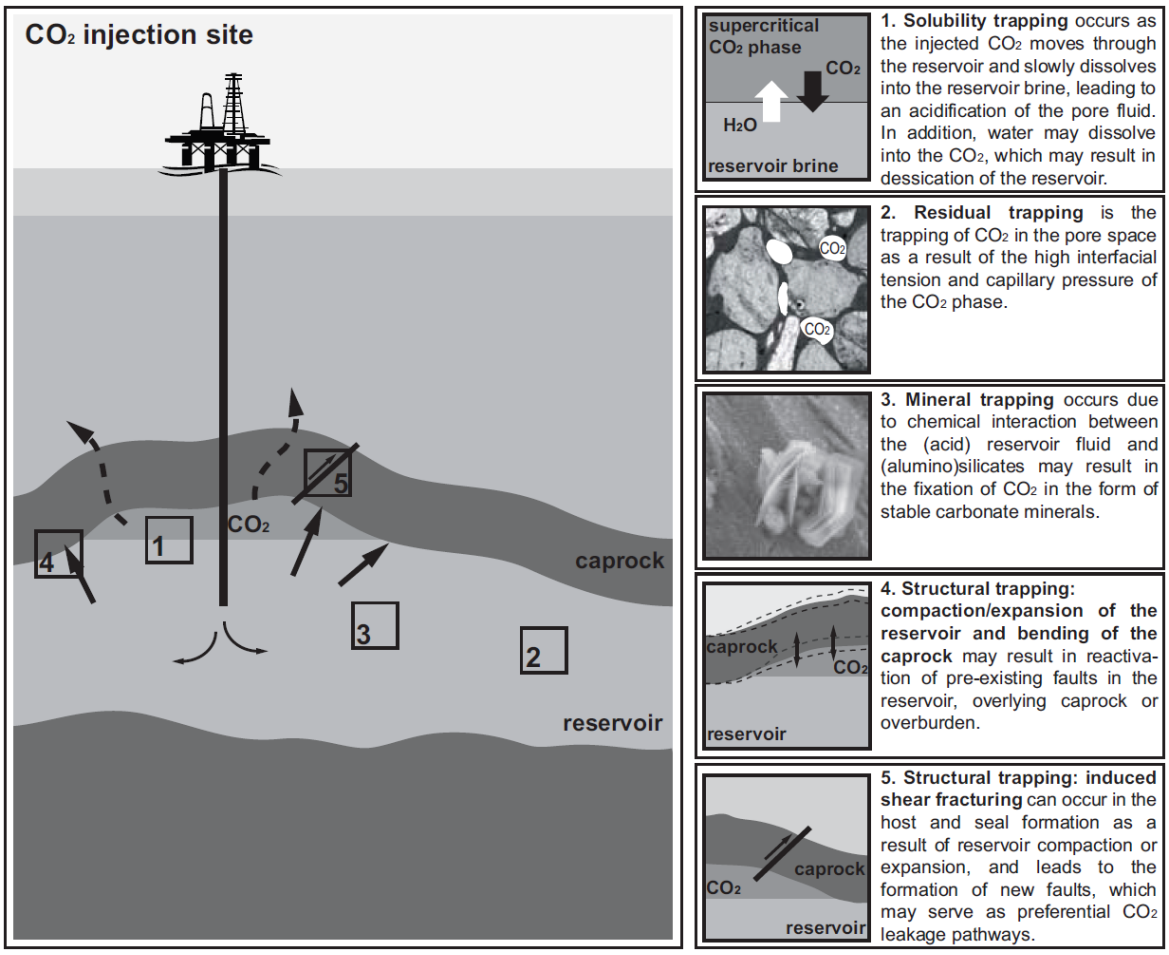

Fig. 1-1—Schematic diagram illustrating a CO_2 injection site consisting of a depleted oil or gas reservoir, or aquifer

Note: after injection, CO_2 spreads through the reservoir, displacing reservoir fluid and exerting forces on the overlying caprock. Some of the key storage (box 1-3) and release (4-5) mechanisms during structural trapping of CO_2 have been highlighted on the right (4).

Aspects influencing seal integrity include: mechanical damage and induced shear failure of unfaulted caprock, hydraulic fracturing of the reservoir and/or caprock near the point of injection, well bore

leakage, reactivation of faults within or bounding the reservoir, and/or reactivation of faults within the caprock or overburden (10).

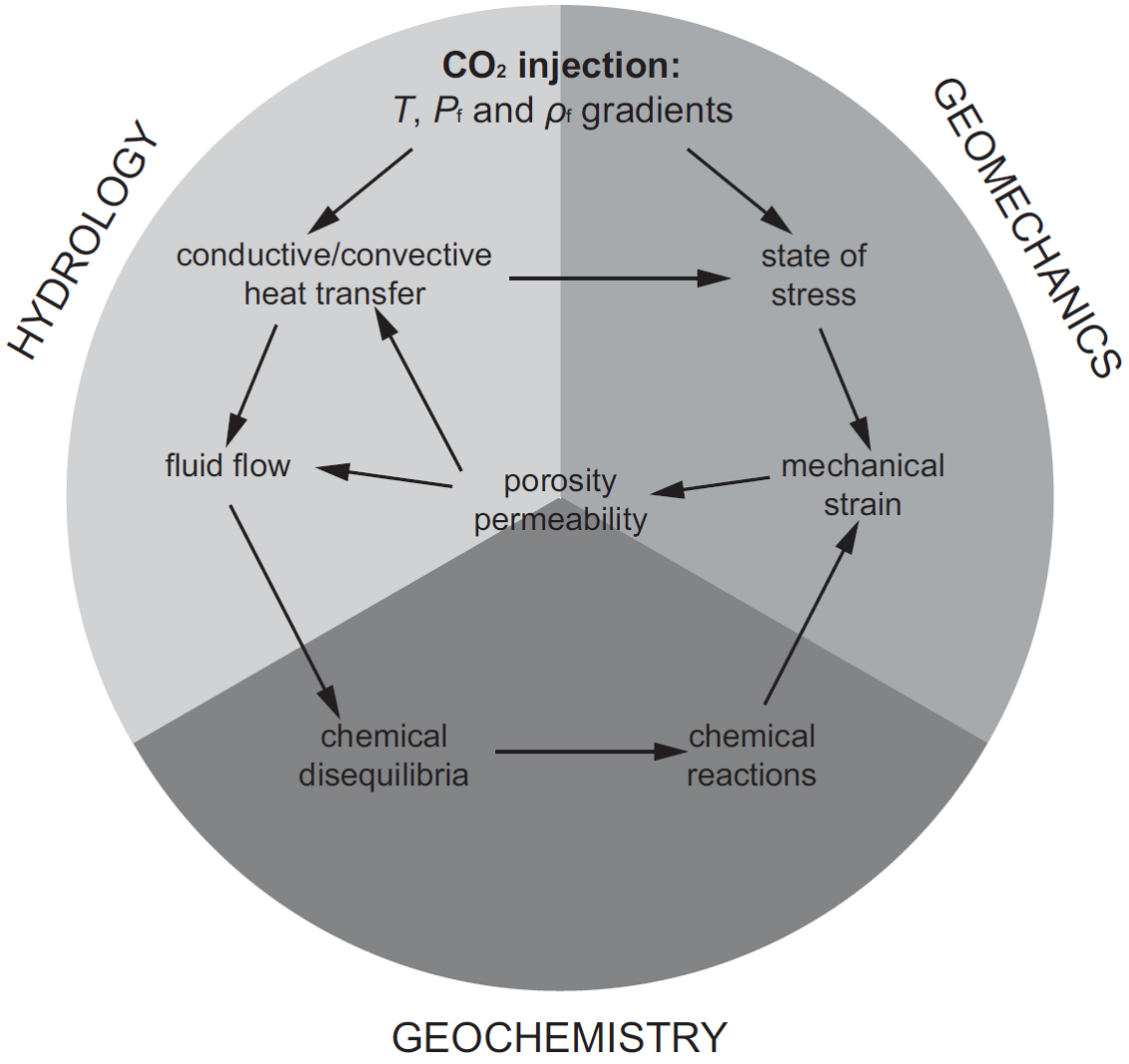

Fig. 1-2—Schematic diagram showing the subsurface processes that are perturbed by CO_2 injection, and the concomitant changes in temperature, pressure and pore fluid density.

Note: as can be seen, porosity and permeability are the key variables linking the hydrological, geochemical and geomechanical regimes (after **(11)**).

For any type project involved with the injection of fluids into the subsurface, the change in pore pressure of the formation will result in a change in the effective state of stress of this formation. Ultimately, it is the effective state of stress, i.e. principal stress minus the pore pressure, which controls mechanical rock deformation and rock failure (12). In the specific case of (supercritical or liquid) CO_2 injection, there is a range of additional hydrological, chemical and mechanical processes that are coupled to this direct effective stress effect, potentially affecting the mechanical behaviour of the storage complex, either on the short or on the long term, as seen in Fig. 1-2.

In general, the injection of CO_2 will not only result in a change in fluid pressure, but will also result in (local) disturbances in temperature. As the CO_2 plume propagates through the field, it will affect the state of stress of the field, as well as the fluid-rock chemical equilibria, due to dissolution of CO_2 into

the reservoir brine, resulting in an acidic pore fluid. As shown in Fig. 1-2, changes in stress state not only affect the geomechanical response of the reservoir caprock system to CO_2 injection, but indirectly also its transport properties. Furthermore, intimately coupled with geomechanical changes are geochemical fluid-rock interactions, which in the long-term may affect the rock mechanical behaviour of the reservoir and caprock (Fig. 1-2). The following is a list of potential geomechanical threats:

- The potential to induce CO_2-enhanced creep processes, which may cause reservoir compaction, while the poro-eleastic response of the reservoir to CO_2 injection may result in reservoir heave, as seen in Fig. 1-1, box 4 and 5. Such processes can potentially cause flexure of the top-seal, which may result in the reactivation of faults in the caprock or overburden (13; 14) and/or induce shear failure, leading to the formation of new faults (14). As these mechanisms are dependent on the magnitude of the changes in the state of stress, this puts constraints on the maximum CO_2 pressure that can be injected.
- Furthermore, hydraulic fracturing near the injection point, either in the formations or the well bore, as a result of high injection rates and cold injection fluids (local P and T changes) (10) may pose additional problems for maintaining seal integrity.
- In addition, the injection of CO_2 can reactivate existing faults, either in the reservoir or in the overlying caprock (13; 15). According to Hawkes et al. (10), there are several important mechanisms that can cause fault reactivation during fluid depletion or injection. These include pore pressure changes in fault planes and connected porosity throughout the reservoir rock, which may reactivate faults in the reservoir (15; 16).

Assessment of the effects of coupled processes affecting the mechanical behaviour of the system can be assisted by the combination of appropriate chemo-mechanical experiments with modelling efforts. This aids in the prediction of the long-term behaviour and performance of geological CO_2 storage systems. For the Goldeneye CCS field, chemo-mechanical experiments on the reservoir rock were performed, to study the effect of short-term chemical effects on mechanical properties. Furthermore, a geomechanical analysis of the entire field was performed by constructing a 3D-model of the Captain Sandstone reservoir and the under- and overlying formations. This model includes seismic, drilling and core data, as well as pressure data, and porosity and net to gross distributions.

The model is capable of simulating the deformation and stress changes due to pressure depletion by the original gas production phase, and the subsequent re-pressurisation of the field by injection of supercritical CO_2. Special care was taken to define the different (mechanical) behaviour and state of stress for the depletion and the injection phases, caused by hysteresis. The model was used to make stress path predictions and assess the mechanical stability of both the caprock formation and any faults within the reservoir caprock system. It should be noted that stress path predictions are sensitive to the input parameters, and therefore the modelling included a sensitivity analyses to quantify the effect on stress path predictions. The model was used to investigate the physical limits of CO_2 injection operations to minimise any risk to containment both during injection and after abandonment. Furthermore, the model predictions were used to aid in the process of the development of the monitoring program.

The results and analyses were informed by work done on other CCS projects. Chapter 2 provides an overview of relevant geomechanical threats as identified in other CCS studies, such as Barendrecht and Barendrecht-Ziedewij (The Netherlands), Sleipner (Norway) and In Salah (Algeria).

An extensive description of the Goldeneye field can be found in the static model (field) report (17). However, a short description of the geomechanical input parameters and pore pressures for the field, as well as the effect of chemo-mechanical changes on rock properties is given in Chapter 3. The effect of changes in pore pressure on the state of stress within the field is investigated in Chapter 4, including both the effect of gas depletion and of CO_2 injection on the stress field. The sensitivity of the model to small changes in the input parameters is shown in Chapter 5. Such changes include changes in mechanical properties of the formations, either due to uncertainty in the base case values or due to chemo-mechanical changes, changes in stress path, a higher CO_2 injection pressure and stronger aquifer support. Subsequently, the effect of thermal cooling on caprock integrity and wellbore stability (Chapter 6) is examined, as well as the potential of fault reactivation (Chapter 7). The modelling results are used as a guide to delineate a number of natural barriers, preventing CO_2 leakage from the storage complex (Chapter 8). A chapter recapping the main conclusions finalises this report (Chapter 9).

2. Other CCS studies and projects

At the time of writing, there are six key geological CO_2 Storage projects (18): the Sleipner and Snøhvit CO_2 injection projects in Norway, the In Salah CO_2 storage project in Algeria, Quest in Canada, the Gorgon CO_2injection project in Australia, and the Illinois Industrial Carbon Capture and Storage Project in the US. Of these projects the Sleipner, Snøhvit and In Salah projects have injected significant volumes, and none of them constitutes injection into a depleted hydrocarbon reservoir.

Considering these statistics, it is important to point out the fundamental difference in containment between aquifer and reservoir storage. The largest differentiator between these two storage options is the difference in pressure between the storage container and the over- and underburden. Aquifer storage implies that the reservoir pressure will become higher than the pore pressure in the over- and underburden, leading to an outward pointing differential pressure (DP), as visualised in **Fig. 2-1a**. In a depleted hydrocarbon reservoir the opposite is often the case. For much of the refill period the reservoir pressure will be below the pore pressure in the over- and underburden. This implies an inward pointing gradient vector, meaning that migration of water or natural gas into the reservoir is more likely than the migration of CO_2 into the overburden (see Fig. 2-1b).

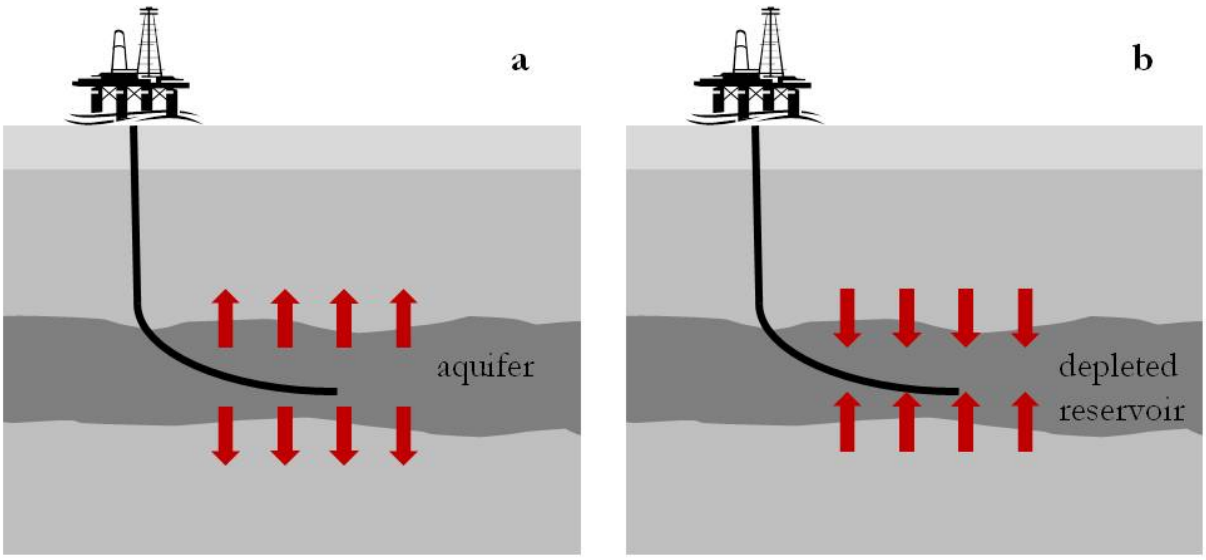

Fig. 2-1—(a) Outward pointing DP vector in case for aquifer storage, and (b) inward pointing DP vector in case of depleted reservoir storage.

In this chapter experience from the above projects is presented and discussed in the context of application to the Goldeneye field.

2.1. Loss of containment: migration and leakage scenarios

Before describing potential geomechanical threats it is useful and necessary to map them in possible risk scenarios. This can be visualised in a bow-tie diagram as it is used in the containment risk assessment (see Storage Development Plan (19)). A glossary of terms used in the presented risk assessment discussions is included at the end of this report to explain certain terms or abbreviations (see Chapter 10). The bow-tie consists of several elements that are described in the glossary and visualised in Fig. 2-2. The scenarios combine threats making cause–consequence relations that run from left to right through the bow-tie (consequence meaning the potential hazardous outcome arising

from the top event). A leakage scenario connects possible subsurface threats via the top event, i.e. leakage of CO_2 out of the container, to the possible consequences. In the context of the potential aspects affecting seal integrity, as described in Chapter 1, five main leakage scenarios were defined by NAM, Nederlandse Aardolie Maatschappij BV (Joint venture Shell/Exxon 50/50), in the development phase of the Barendrecht and Barendrecht-Ziedewij projects, some of which might also apply to the Goldeneye field:

- Caprock seepage as a result of caprock diffusion and/or enhanced caprock permeability. Enhanced caprock permeability can either occur as a result of chemical CO_2/brine/rock interactions within the caprock, or by changing stress conditions in the storage complex, due to CO_2 injection
- Caprock leakage as a result of changes in the state of effective stress due to reservoir depletion and subsequent CO_2 injection
- Spill leakage resulting from induced fracturing leading to lateral migration of the injected CO_2 beyond the boundaries of the storage complex
- Fault leakage and movement along pre-existing faults and fractures, potentially leading to induced seismicity, or the creation of new fractures resulting from temperature changes (Joule-Thomson effect)
- Well bore leakage along legacy wells and injection wells

Note that the difference between leakage and seepage is the difference in CO_2 flux and concentration during escape (see glossary – Chapter 10).

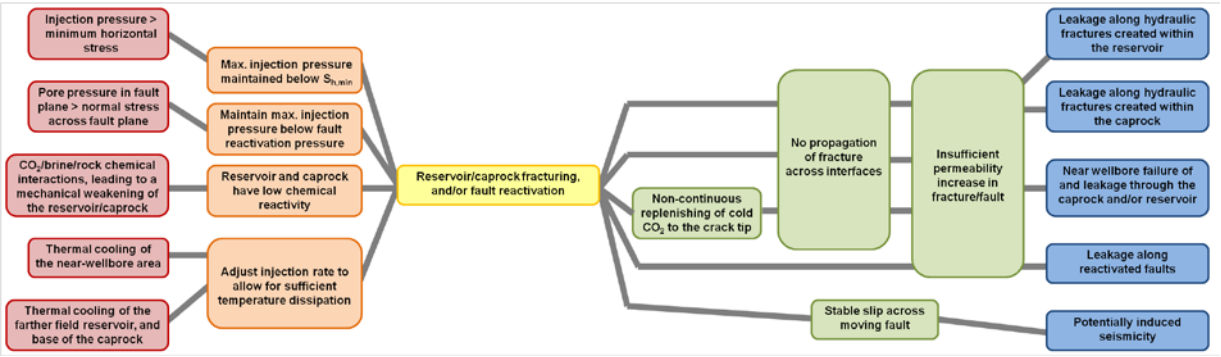

Fig. 2-2—Simple bow-tie diagram for the geomechanical threats and consequences during CO_2 containment

Note that this bow tie only covers the threats discussed in this report, and hence represents only a small portion of the bow tie in the Storage Development Plan **(19)**.

2.1.1. The effect of CO_2/brine/rock interactions on hydrological and mechanical properties

Given the reactivity of CO_2-saturated brine, CO_2/brine/rock chemical interactions may potentially lead to changes in porosity and permeability, as well as rock compressibility, via chemically-coupled hydrological and mechanical effects. Chemical reactions between host rock and fluids include relatively rapid dissolution of fast-reacting minerals such as carbonates, either present as framework grains or as intergranular cement, as well as slow, long-term CO_2 mineralisation through reaction with Ca-, Mg-, or Fe-rich framework minerals such as feldspars, clays, micas and Fe-oxides. Depending on their rates, CO_2-induced creep processes can have important effects on storage integrity, both during

the injection phase, as well as after abandonment. In response to these chemical reactions, rock porosity and permeability could increase or decrease. In addition, mechanical-related effects include creep due to dissolution reactions, CO_2-enhanced microcracking and diffusive mass transfer processes like pressure solution, leading to time-dependent reservoir deformation. Generally, creep can potentially cause reservoir compaction, leading to damage to wellbores, the overlying caprock and any fault/seal systems.

Generally, the amount of free water in a depleted oil or gas reservoir is limited. Hence, any pH reduction resulting from the dissolution of CO_2 will relatively quickly be buffered by mineral dissolution reactions. Modelling efforts, investigating static batch reaction of minerals and water, such as done for the Barendrecht and Barendrecht-Ziedewij reservoirs and seals (20), generally show a reduction in porosity and permeability for seals and reservoirs. It should be noted that chemical modelling predictions are sensitive to the geochemical modelling code used so these should be benchmarked (21) and validated by experimental observations. Many of these reactions are very slow, experiments require long reactions times. A seven year batch-reaction study for disintegrated caprock material from the Sleipner field showed no indication of major deleterious, geochemical reaction processes occurring with the caprock, besides some minor dissolution of carbonate minerals (22). This study is indicative of the low reactivity of many caprock-reservoir systems. Further evidence is obtained from naturally occurring CO_2 reservoirs, such as present in the Colorado Plateau (Utah) and the Otway Basin (Australia). Studies of these locations show that for relatively clean sandstones, such as those generally found in hydrocarbon reservoirs, little reactivity is seen (23; 24; 25). In contrast, in systems containing reactive particles, such as volcanic fragments and plagioclase feldspar, the extent of reaction is significantly larger, resulting in the precipitation of carbonate and clay minerals (26; 27).

Experiments were performed on Goldeneye core, aimed at studying the coupled chemo-mechanical effects by constantly flushing the reservoir material with CO_2-saturated brine, until all carbonate minerals were removed. From a geomechanical strength and failure point of view, this case was considered worst case scenario. It was shown that the dissolution of carbonate cement did not lead to changes in mechanical properties (Section 3.3.3). A coupled reactive transport study carried out for Goldeneye (28) showed no significant changes in mineralogy in the long term, which suggests that the elastic properties and failure strength of the reservoir rock will not change significantly over time.

2.1.2. Caprock seepage through diffusive processes and/or enhanced caprock permeability

Caprock seepage considers a low flux and low concentration flow out of the reservoir. Though significant integrity of the caprock is proven by the existence of low density hydrocarbons, seepage on a geological time scale (millions of years) can never be totally ruled out. Gas chimneys can reveal old or existing migration routes. Measurements of the diffusive properties of a range of different shale samples (29; 30; 31; 32), obtained from different locations around the world, suggested diffusion coefficient values of 10^{-10} to 10^{-12} m^2 s^{-1}. Given these values, diffusive seepage through the (intact) caprock of the Goldeneye field is expected to take tens of thousands of years.

However, production of hydrocarbons can also impact integrity, as production of a reservoir leads to a perturbation of the state of stress. Though this perturbation will have the highest impact in the reservoir itself, it can also lead to a change in volumetric strain impacting the porosity and permeability of the caprock. The change in stress around the reservoir can be assessed by finite element modelling, as was done for the Barendrecht-Ziedewij reservoir and other potential Dutch CCS sites (33). Such studies pointed out that both the changes in stress and volumetric strain in the caprock were very limited.

Therefore, it is likely that the risk for permeability increase at the base of the caprock as a result of a change in volumetric strain is negligible. The effect of pore pressure on the effective stress state of the Goldeneye field within both the reservoir and caprock will be discussed in Chapter 4.

2.1.3. Caprock leakage resulting from changes in effective stress state

Caprock leakage is defined as the migration and leakage of CO_2 out of the reservoir at a relatively high flux. In general, this scenario requires the existence of natural or induced fractures.

In the case of depleted field storage, gas occurrence has proven gas containment. Therefore, it can be assumed that the existence of natural, conductive fractures in the caprock is highly unlikely.

Despite the presence of natural gas in the Barendrecht location, deeming the presence of large conductive faults or fractures unlikely, caprock leakage attracted the most attention by both the public and external experts. Generally, it can be conceived that the 'very high pressure' would lead to rupturing of the subsurface and subsequent high flux leakage at the surface. Coupling between injection and fracturing is known from water disposal and cutting injection. This knowledge is, therefore, often used during technical discussions on containment.

Though the presence of conductive fractures is deemed unlikely, it is possible that pressure-induced stress changes during the depletion and subsequent injection phase could result in the creation of both tensile and shear fractures. It is therefore necessary to investigate the threat of fracturing in and outside the reservoir. Numerical modelling efforts for a number of depleted gas fields considered for CO_2 storage in The Netherlands have already shown that the extent of any stress changes is limited to less than 10 km away from the field (33). This is in contrast with predictions for deep saline aquifer storage sites, where perturbations persist for 10s to 100s of kilometres.

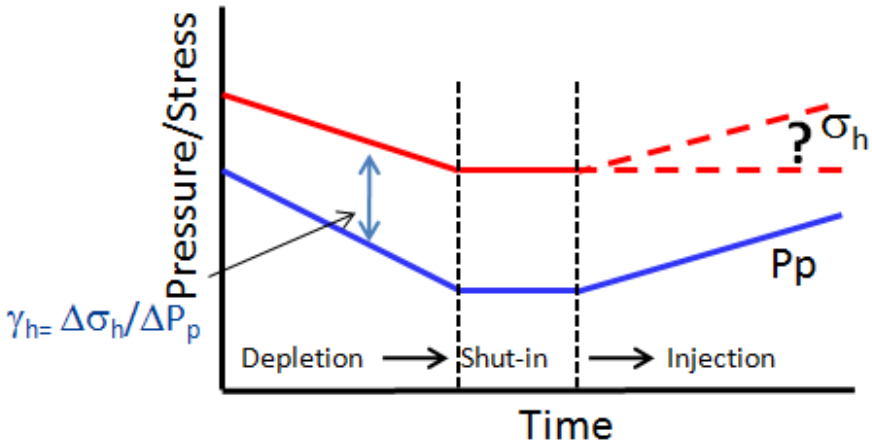

Fig. 2-3—Hypothetical in-situ stress response to changes in pore pressure during production and injection phase.

In order to be able to investigate the potential of damage caused by injection, it is needed to study the reversibility of the induced stress changes during these phases. In general, depletion leads to an effective stress increase (decrease in force from pressure opposing the applied stresses) in all directions and concomitantly to compaction of the reservoir. If the material behaves as an ideal elastic material, then the work that has been done on the system increases its potential energy, which

will be released again when pore pressure increases. This leads to the situation of perfect reversible compaction. However, rocks never behave ideally and compaction is the result of both instantaneous elastic and time-dependent plastic behaviour. Plastic behaviour caused by gliding, sliding and cracking of grains or small rock interfaces leads to dissipation of energy and irreversible behaviour during the phase of pore pressure increase. This is reflected in the possibility that the in-situ stress might not come back to their original values, even after re-pressurisation to the original pore pressure, as is shown in **Fig. 2-3**. Unequivocally, this means that after injection, the minimum horizontal stress could be lower than before depletion. This affects the conditions for tensile or shear fracturing to occur.

To quantify the effect of stress changes in relation to pressure changes, the reservoir depletion coefficient or γ is defined as the ratio of change in horizontal or vertical total stress ($\Delta\sigma$) and the change in pore pressure (ΔP_p). For horizontal stress changes, γ_h is defined as

$$\gamma_{\mathrm{h}} = \frac{\Delta\sigma_{\mathrm{h}}}{\Delta P_{\mathrm{p}}} \tag{1}$$

A similar definition holds for changes in the vertical stresses γ_v, as a result of depletion,

$$\gamma_{\mathrm{v}} = \frac{\Delta\sigma_{\mathrm{v}}}{\Delta P_{\mathrm{p}}} \tag{2}$$

For an elastic material, deforming under zero lateral strain, the reservoir stress path can be related to the Poisson's ratio of the rock, by using

$$\gamma_{\mathrm{h}} = \frac{\Delta\sigma_{\mathrm{h}}}{\Delta P_{\mathrm{p}}} = \frac{(1-2\nu)}{(1-\nu)} \tag{3}$$

However, the depletion coefficients that are calculated from measured values of Poisson's ratio or derived from sonic logs are not always in good agreement with field measurements. Explanations for this are:

- Rocks may not behave elastically upon loading (under normal in-situ stress conditions).
- Above the compacting reservoirs localised deformation could lead to stress arching, resulting in an increase (at the 'pillars', i.e. at the boundary of the field) or decrease (under the 'arch', i.e. in the central part of the field) of the vertical stresses, i.e. the loading condition is not uniaxial, as assumed in laboratory experiments.
- The structure of faults and overburden formations play a role.

Laboratory tests, consisting of depressurisation and repressurisation of core plugs, can reveal plastic behaviour. The basic idea behind this test is to mimic the process of production at reservoir conditions. Generally it is expected that plasticity can occur when depressurisation causes the effective stress to be higher than the maximum natural effective stress experienced by the reservoir. It is commonly observed for many rock types that there is a difference in stress-strain behaviour between a first and a second cycle of depletion-injection. However, though it is possible that this is partly a result from irreversible plastic behaviour of the sample, it can also be ascribed to core damage. Core damage leads to an additional component of inelastic deformation during the first-time loading of reservoir core in a laboratory experiment. In other words, this core-damage-induced inelastic strain may not occur in the in-situ reservoir. It should be noted that it is nearly impossible to distinguish the contribution of core damage from true plastic behaviour from laboratory experiments.

Field observations also do not give a conclusive view of the issue. Some indirect observations of compaction in north Netherlands support the hypothesis that most of the compressibility difference

between the first and second cycle can be explained by core damage: 1) it is observed in many fields in The Netherlands that the second cycle compressibility better matches the subsidence measurements, and 2) interferometric synthetic aperture radar (InSAR) measurements above the Norg underground gas storage (UGS) field support the theory that consolidated sandstone behaves in its majority as an elastic material. In this case, it was observed that at least 80% of the subsidence resulting from a depletion phase was restored during injection applying the same pressure difference for both phases.

In contrast, a paper by Santarelli et al. (34) used a direct measurement of the minimum in-situ total stress (XLOT) in an unconsolidated field in the North Sea operated by SAGA to support the idea of an irreversible stress path. Such partially irreversible stress paths are also commonly observed in soils, such as the overconsolidated soils in The Netherlands, resulting from ice-loading during the last ice age. Unfortunately, except for Santarelli's single data point, no other examples are known that describe this phenomenon for more competent (meaning stronger and stiffer, better cemented) rock types.

Geomechanical models should be able to predict depletion coefficients as observed in the field. Obviously, this requires rock properties that are representative for the field behaviour. In the case of the Barendrecht project, the concern of injection-induced damage was addressed by comparing, the predicted bottom hole pressure (BHP) with the evolution of the total minimum stress in- and outside the reservoir. The regional total minimum principal stress in the Barendrecht area could be reasonably constrained by the lower bound fit of many leak-off pressure (LOP) data and the fracture closure pressures observed during minifrac tests. However, the depletion constant, i.e. change in total minimum principal stress divided by the change in pore pressure, is unknown and results in uncertainty when trying to predict the effective stress evolution within the reservoir during depletion. Even more uncertain is the quantification of the inflation constant. Overall for the Barendrecht case, very conservative results were obtained, but they directly showed that the seal could not be fractured as the BHP was always lower than the total minimum principal stress in the caprock. However, given the total uncertainty in stress behaviour of the reservoir, some potential for fracture initiation could not be ruled out at the end of the injection phase at the Barendrecht site.

For the Goldeneye field, in order to populate the geomechanical model with realistic values to address the issue of repressurisation, laboratory experiments were performed on relevant core samples to determine the elastic properties of the reservoir, as is discussed in Section 3.3.3.1. Shear and tensile failure through the whole thickness of the caprock could lead to caprock leakage if the resultant fractures are conductive. The potential for failure can be assessed using stress-based evaluation criteria. The stress response due to gas depletion and subsequent CO_2 injection was predicted and used to evaluate the potential for shear and tensile failure, and these results are discussed in Chapter 4.

2.1.4. Spill leakage resulting from induced fracturing

The risk of spill leakage normally results from injection into high-permeable streaks within the reservoir. In case of very high injection pressures, it could be possible that the pore pressure in the streak at spill point exceeds the pore pressure in the adjacent aquifer leading to the flow of CO_2 into the aquifer. Fracturing could be an escalation factor that provides a fast route to the spill point (20). The surface area that arises from such a fracture would allow for a pressure reduction in a permeable reservoir. However, this fracturing scenario was considered to be unlikely, as the creation of a large fracture by the injection of a very low viscosity, supercritical fluid, like high-pressure CO_2, is

considered to be unlikely. For Goldeneye, fracturing of the reservoir and caprock formations is discussed in the injection fracturing report (35).

2.1.5. Potential for thermally-induced fracturing

Like in waterflooding, the CO_2 injected is generally at a lower temperature than the surrounding rock. The total minimum principal stress decreases with decreasing temperature where analytical expressions are provided for limit cases, e.g. Fjaer et al. (36). Recent modelling studies for the Barendrecht reservoir show that the cooled region will be limited to a close region around the well zone. The main cause for this is the limited heat capacity of the super critical CO_2. Fracturing as a result of temperature change can occur but is limited to a narrow zone around the well. For the Goldeneye field, these issues are addressed in Chapter 6.

2.1.6. Well bore leakage along legacy and injection wells

In all studied CO_2 storage opportunities, it is identified that the well leakage scenario is possible, though the impact is considered to be low. Leakage along the well bore can occur due to the creation of an annulus between the casing and the cement (37). The status of the cement can be examined using cement bond logs immediately after the cement job, but it is possible that stress and strain changes during the production could impact the coupling between the cement, casing and wall rock.

For the Barendrecht injection well fluxes were calculated for a worst-case scenario for leakage along a thin but continuous crack along the well bore annulus. These calculations showed that a fracture would result only in very low flow rates, comparable to the yearly CO_2 emission of a mid-sized car, due to the high friction between the fluid and the leakage pathway.

Another aspect to investigate is mechanical degradation; leading to the creation of micro-annuli or cement failure. This can be assessed by predicting the stress and strain evolution in the well bore and comparing these values with threshold values from the literature. They also predicted that, mechanical degradation as a result of depletion or injection is unlikely in the overburden cement section. Calculated strains were orders of magnitude lower than threshold strength values.

For the Goldeneye field, thermal cooling of the wellbore, and potentially induced fracturing, is addressed in Chapter 6.

2.1.7. Fault leakage, movement and induced seismicity

In a normal faulting tectonic regime, i.e. where the vertical stress is larger than the horizontal stresses, geomechanical models have shown that fault shear tractions in general decrease during injection. This depends highly on the assumed ranges of the model parameters and the pore pressure increase in the faults themselves. In geomechanical and dynamic reservoir models, faults are often described by simple planar surfaces having no thickness. According to what is concluded in the literature it is accepted that brittle crustal fault slip causes dilatant behaviour that results in an increase of the fault transmissivity parallel to the fault plane. It has been stated by Zoback (38) that faults that are mechanically alive are hydraulically alive and faults that are mechanically dead are hydraulically dead. The observation of earthquakes in the vicinity of main faults in a reservoir suggests that they are mechanically active and, therefore, are also hydraulically active. This means that structural blocks with different pore pressures can come in communication due to fault reactivation.

Therefore, it can be concluded that fluid injection should not take place in the vicinity of faults to avoid direct pore pressure increase in the faults themselves. Muntendam et al. (39) assessed a hazard zone with a radius of around 150m around the well. A distance larger than 150m should not lead to enhanced probability of fault reactivation. However, if high pressure fluid enters a fault plane, the probability of reactivation increases as the increased pore pressure lubricates the fault plane and reduces the effective normal stress to the fault plane. Muntendam et al. (39) describe in their Bergermeer UGS research two cases of observed induced seismicity during injection: in Grijpskerk and Norg two very small events were recorded during the repressurisation of the UGSs.

The significance of injection pressure on fracture-related leakage is clearly demonstrated during the In Salah CO_2 Storage project. This project entails the injection of CO_2, obtained from nearby gas production fields, into the water leg of the Krechba gas reservoir. On the basis of available field data, predictions of the flowing bottom hole pressure and fracturing pressure (P_{frac}) suggested that, on occasion, injection took place under fracturing conditions (40). Injection has resulted in surface uplift rates of +5 mm/year above each of the three injections wells (41), which for one of the wells is inferred to have been caused by the opening of a near-vertical fracture zone, extending 100 to 200 m into the 950 m-thick caprock. Associated with this uplift are thousands of microseismic events, related to formation fracturing (42). This clearly illustrates the importance of understanding, and respecting, the geomechanical limits of the storage complex. The potential for fracture development and fault reactivation within the Goldeneye field is discussed in chapters 6 and 7 of this report, respectively.

2.2. Overview of geomechanical threats

In general, the geomechanical threats, as described above, have a low to negligible impact on the risk for CO_2 migration. In fact, all studied (potential) CCS sites, show that CO_2 leakage to the surface is unlikely.

This report evaluates the geomechanical threats as discussed in this Chapter. A summary of these threats is given in Table 2-1, together with references to the Chapter that discuss them.

Table 2-1—Overview of the geomechanical threats and risks discussed, with references to the Chapters in which they will be addressed.

Geomechanical threat	Chapters				
	4	5	6	7	8
CO_2/brine/rock interactions	x				
Tensile failure of the reservoir		x			
Shear failure of the reservoir		x	x		
Tensile failure of the caprock		x			
Shear failure of the caprock		x	x		
Thermal fracturing near the wellbore				x	
Thermal fracturing of the caprock				x	
Fault slip					x

3. Geomechanical model: construction and parameters

This Chapter describes the geomechanical model developed for the Goldeneye field. The aim of the model is to evaluate the changes in stress state as a result of gas depletion and CO_2 injection (cf. Sections 2.1.2 and 2.1.3), as well as to assess the potential for shear and tensile failure (cf. Table 2-1). The geomechanics workflow used in this study makes use of the Shell proprietary pre- and post-processor called GeoMec that uses the commercially available finite element package DIANA to carry out the simulations. For the study described in this report, the choice was made to use a hexagonal mesh without explicit faults as this could be built relatively quickly. Fault slip is investigated via an alternative route (see Chapter 7).

The geomechanical model is composed of:

- The structural geometry of the reservoir, overburden and underburden formations,
- In-situ stress and pore pressure profile,
- Pressure changes in the reservoir due to depletion and injection at different times,
- Mechanical rock properties of all the formations.

Table 3-1 shows the data inventory and integrated approach to arrive at the geomechanical model for the Goldeneye field.

Table 3-1—Data inventory for geomechanical model construction

Geomechanical model construction	Data source
Structural geometry of reservoir, overburden and underburden	Petrel models SRM 3.1 (key reservoir formations) (43) and "Overburden model" (over- and under-burden formations) (44)
In-situ stress and pore pressure profile	Mainly from previous wellbore stability studies on the drilling of Goldeneye wells
Reservoir pressure change during production (of gas) and injection (of CO_2) cycles	Reservoir pressures from fluid flow simulation software. Upscaling method is based on 1D scale independent compaction (45)
Mechanical rock properties in overburden and underburden	Dynamic rock properties derived from six well logs using compressional and shear wave velocities, and densities
Mechanical rock properties in the reservoir section	Young's modulus and Poisson's ratio can be derived from the upscaled porosity and net to gross distributions from MoReS. So, variations in the geology have been taken into account. Also validated with nearby triaxial tests (of the FRAM field) and other empirical correlations.

3.1. Geology and structural model

The static reservoir model SRM3.1 (17) contains the key reservoir formations, as well as the overburden and underburden formations (44). A GeoMec model was constructed by combining the horizons from the two models. Several formations were grouped together for construction and run time efficiency, resulting in a total of five overburden formations, three reservoirs and two underburden formations (see Fig. 3-1).

- The overburden formations are: Nordland Group, Coals, Dornoch, Chalk Group (Ekofisk, Tor, Hod, Plenus, Hidra) and Rødby (Caprock).
- The three reservoir units are: Captain E and Captain D combined together, Captain C, and Captain A combined with Valhall and Scapa.
- The underburden formations are: Humber and Heron groups.

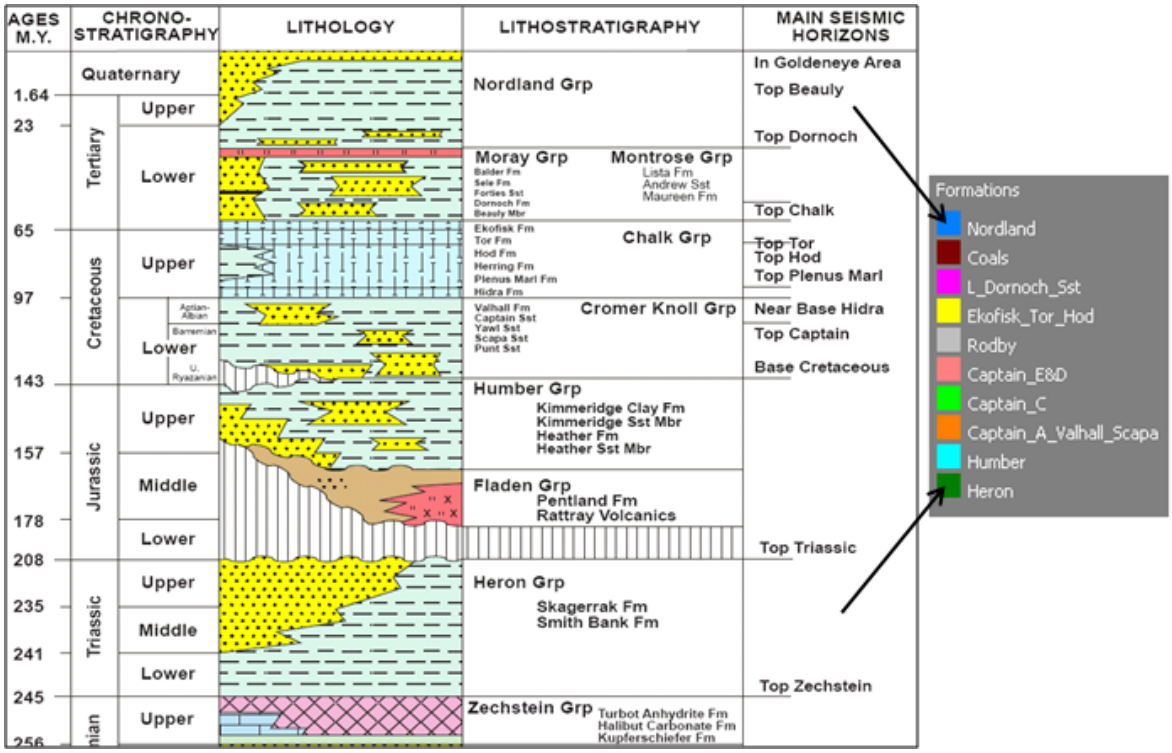

Fig. 3-1—Stratigraphic column of the formations in the Goldeneye area (left hand) and the formations modelled in GeoMec (right hand).

The GeoMec model with hexahedral elements has overall dimensions of 50 km east-west by 20 km north-south (see Fig. 3-2 and Fig. 3-3). The mesh resolution is 250 m in the area where production has taken place and injection is planned, surrounded by mesh elements that are 500 m in length (see Fig. 3-4). The model has a total of 364,736 elements. Unless otherwise stated all map views in the remainder of this report show an area of 20×50 km while the bird's-eye view shows a volume of 20 x 50 x 8 km. Therefore, cross sections are 20×8 km (north-south) and/or 50×8 km (west-east), with the actual reservoir area being smaller than that. Thickness maps of the Captain E&D units and the Rødby Formation (caprock) are displayed in Fig. 3-5 and Fig. 3-6 respectively. These thickness maps are discretised to hexahedral elements that go into the geomechanical model where a minimum thickness of 20 m is enforced to prevent numerical problems.

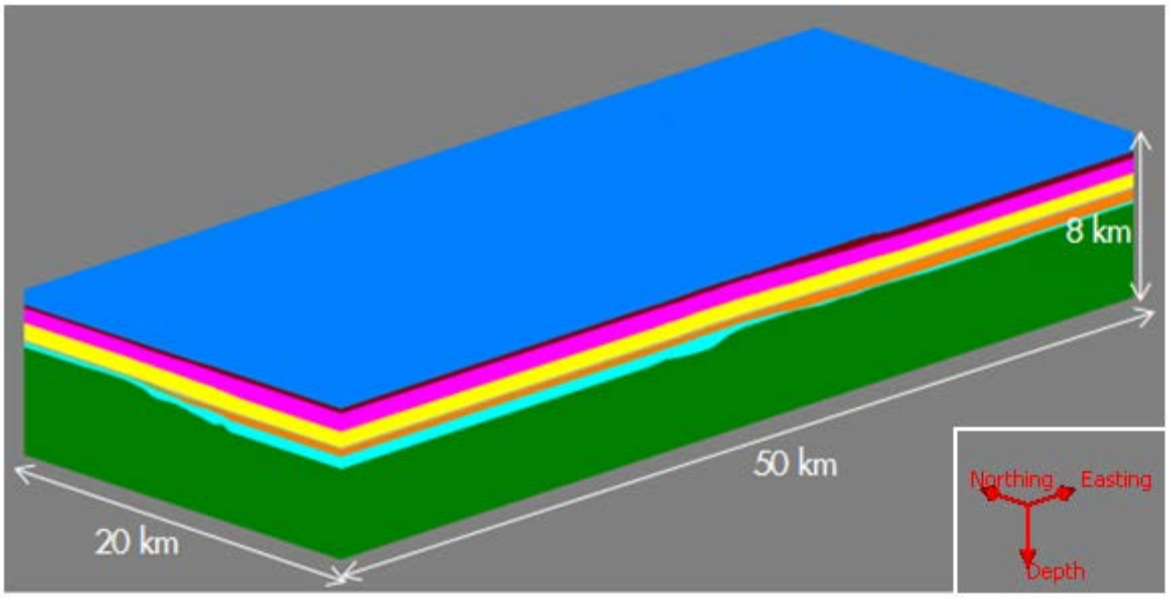

Fig. 3-2—Bird's-eye view from the south-west towards the northeast direction of the geomechanical model.

Note: colours represent different geological formations.

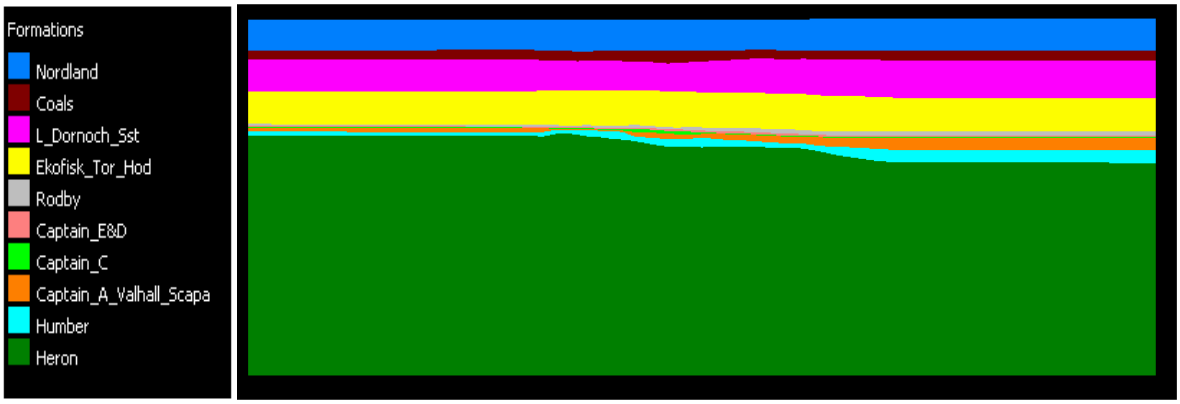

Fig. 3-3—Cross-sectional view showing key formations.

Note: slice was made in the middle of the model, north is to the left and south is to the right.

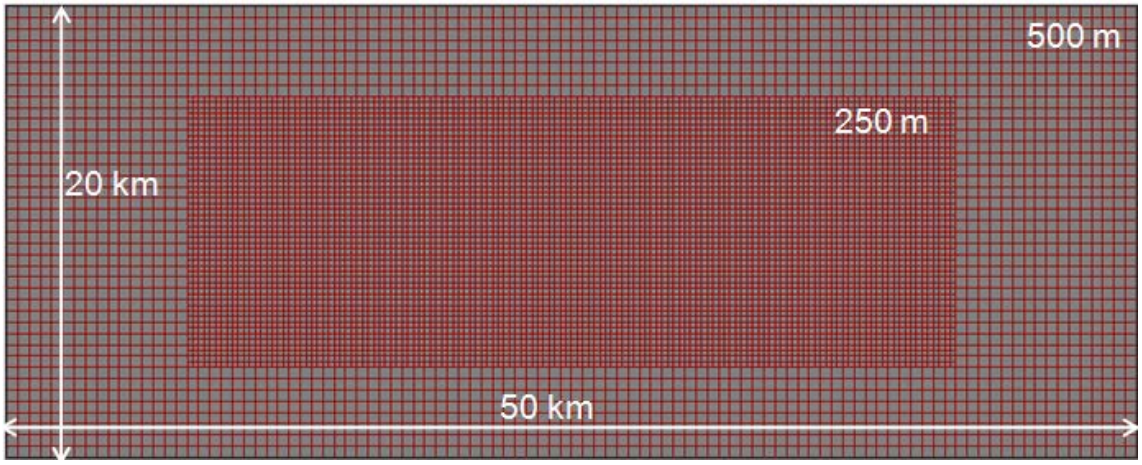

Fig. 3-4—Plan view of model showing nested mesh resolution.

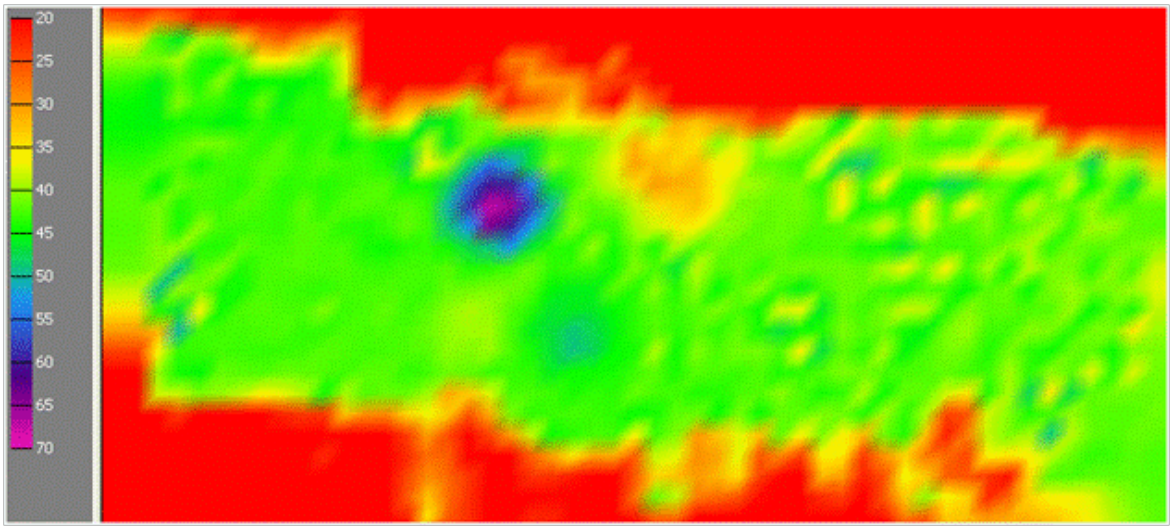

Fig. 3-5—Thickness map of Captain E&D reservoir as in GeoMec.

Note: colour scale runs from 65.6 to 229.7 ft [20 to 70 m]

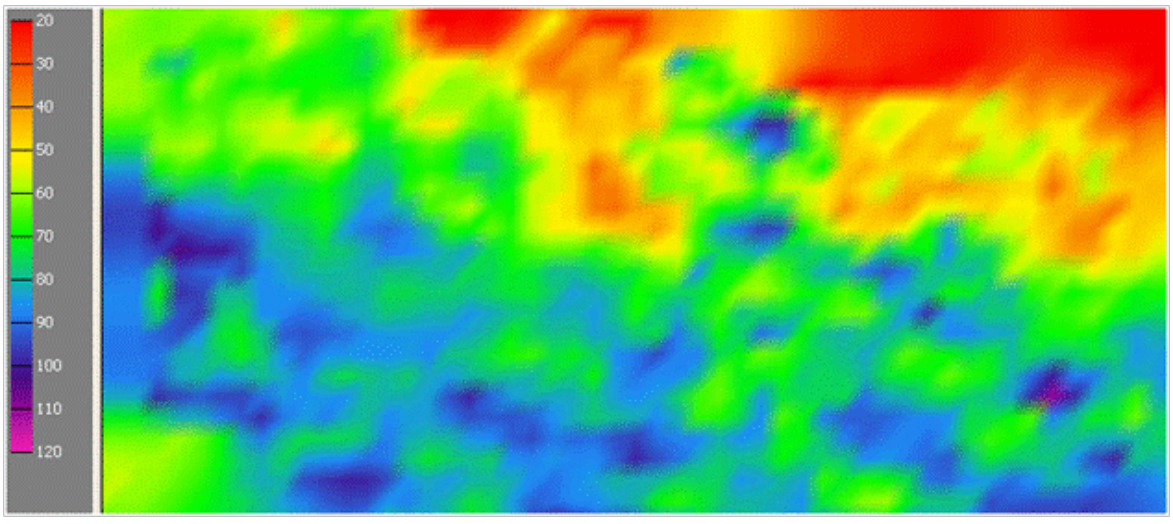

Fig. 3-6—Thickness of Rødby Formation (caprock) as in GeoMec.

Note: colour scale runs from 65.6 to 393.7 ft [20 to 120 m]

3.2. In-situ stress state and pore pressures

The in-situ stress and pore pressure profile for the Goldeneye area is constructed using pore pressure information, log data, leak-off test (LOT) and limit test (LT) data. There is a normal stress regime (vertical stress is larger than the horizontal stresses) in the Goldeneye area. The direction of maximum horizontal stress is NNW-SSE, as inferred from image log, calliper data and the World Stress map (46). The next sections describe in detail the data and methodology that was used to derive the stresses and pore pressures.

3.2.1. Vertical stress

Eight wells are available with density logs in the Goldeneye area. An estimate of the vertical stress is calculated by integrating the density logs of these wells. Vertical stress profiles generated from the well data are shown in Fig. 3-7. As the curves overlie each other there is sufficient consistency in the data to be conclusive in the vertical stress gradient, which is 23.3 kPa/m [1 psia/ft].

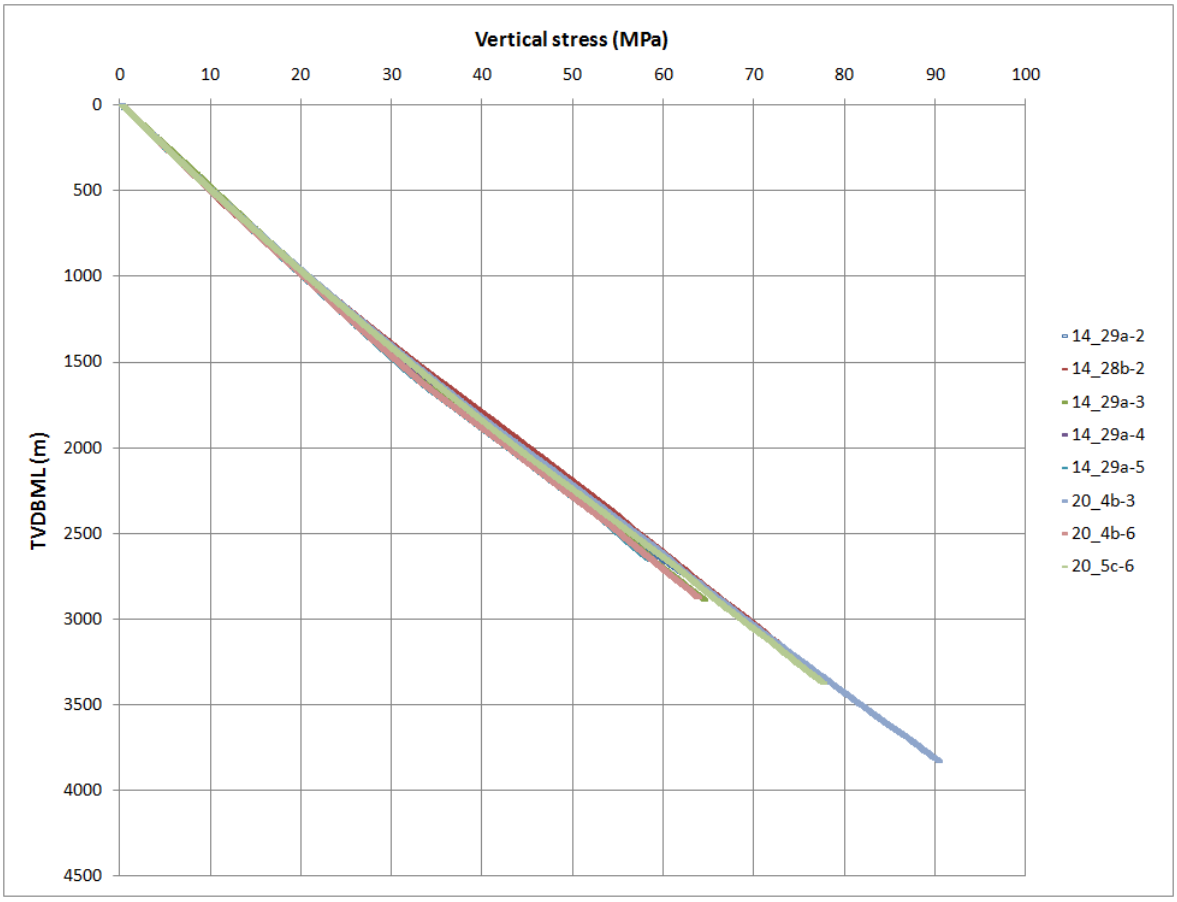

Fig. 3-7—Vertical stress profile of all the eight wells in the Goldeneye area.

3.2.2. Horizontal stresses

In the wider Goldeneye area, a normal-stress regime is seen so, the vertical stress is larger than the horizontal stresses. Borehole image logs show there is limited extent of borehole breakout and drilling induced tensile fracturing. Therefore, it is reasonable to assume that the horizontal stresses are not direction dependent, so maximum and minimum horizontal stresses are assumed to be equal. The small differences in the magnitudes of the horizontal stresses indicate the direction of the maximum horizontal stress is in the NNW-SSE direction. This is based on FMI/CBIL, UBI, caliper logs, and the World Stress Map (47).

LOT and LT data are available from 18 wells (Goldeneye field and offset wells less than 10 km away). This data is plotted in **Fig. 3-8**, taken from the recent pore pressure prediction study of Goldeneye. It can be seen that there is a clear change in the trend of the total minimum principal stress gradient that starts at the top of the Chalk Group at about 2000 m [6,562 ft]. Sand prone sediments above Chalk Group also give some variability to the LOT and have 7% lower LOT values, similar to other North Sea fields.

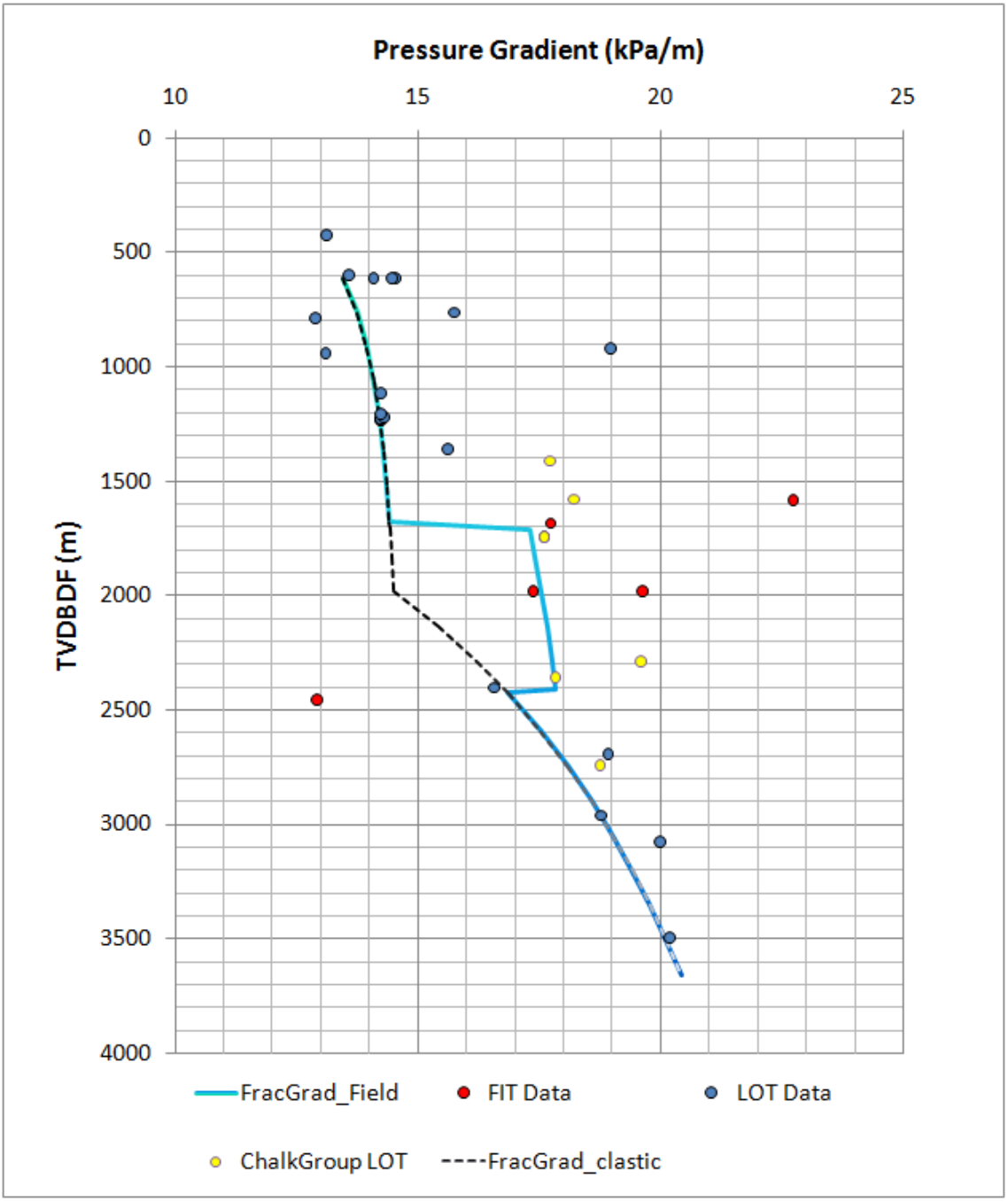

Fig. 3-8—Total minimum principal stress gradient, i.e. leak off pressure test gradient, trend is represented as the lower bound of LOT data.

Best results, i.e. those that give the fewest numerical errors for the Goldeneye structure, are calculated in GeoMec by implementing the minimal and maximum horizontal principal stresses as a constant

number per formation for modelling both the depletion and the injection phase. Note that the blue line in Fig. 3-8 has been sampled for each of the formations in Table 3-2. The total horizontal stress for each formation has been divided by the vertical stress (see Fig. 3-7) to calculate k-values, as shown in Table 3-2. The vertical stress was corrected for sea depth (400 ft [122 m]) and DFE (85 ft [26 m]).

Table 3-2—k-values for both depletion and injection modelling as used in the different formations. Total horizontal stress is taken the same in all directions.

Formation	k	Formation	k
Nordland	0.65	Captain E&D	0.84
Coals	0.66	Captain C	0.85
Dornoch	0.68	Captain A	0.86
Ekofisk	0.75	Humber	0.92
Rødby	0.82	Heron	0.92

3.2.3. Pore pressure in the over- and underburden formations

When the overburden formations, and a small part of the underburden, were drilled, pore pressures were found to be hydrostatic. So, a hydrostatic pore pressure gradient of 10 KPa/m [0.442 psia/ft] (see also the Dynamic Modelling Report (43)) is used outside the reservoir, which is assumed to be unaffected by pore pressure changes in the reservoir due to production or injection.

3.2.4. Pore pressure changes in the reservoir

The Goldeneye field started gas production in 2004 and is assumed to be close to cessation of production. This study pre-dated the Peterhead CCS Project and assumed that CO_2 injection would take place from 2014 until 2024 targeting two million tonnes of CO_2 per year. History-matched reservoir simulations (modelled by the Shell reservoir simulator MoReS) were available for the production phase. Forward reservoir simulations were done for the CO_2 injection phase.

The Peterhead CCS Project intends to start injection later: in 2019, but it will inject 10 million CO_2 at one million tonnes per year. The storage permit will still be applied for 20 million tonnes as studied here, however, at this point only 10 million tonnes of capacity is required.

Key pore pressure changes, shown in Fig. 3-9, are used in GeoMec to calculate stress changes during the production phase for the years 2005-2010 and the injection phase for the years 2014-2025. In between these periods, from 2010 until 2014, the aquifer causes the pressures in the reservoirs to rise.

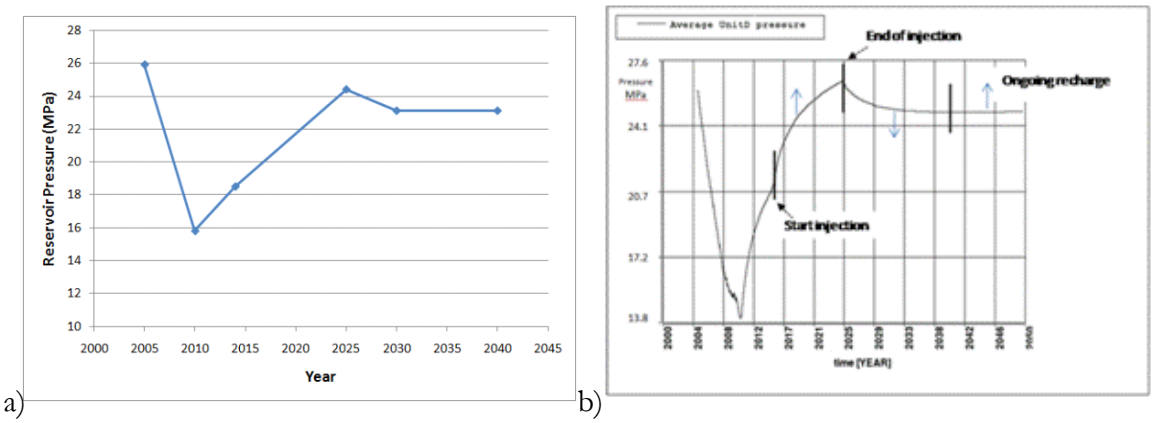

a) b)

Fig. 3-9—Pore pressure as a function of time for a typical location in the reservoir

Note: (a) schematic ranging from 10 to 28 MPa [1450 to 4061 psia], and (b) more precise (ranging from 13.8 to 27.6 MPa [2000 to 4000 psia]) with arrows indicating possible pressure changes due to uncertainty.

Reservoir pressures are not uniform in the reservoir but can have different values at different locations (laterally and vertically). The pressures that derived from the MoReS full field model need to be rescaled to the mesh used in GeoMec (meter scale to 250 m scale). An upscaling method is used whereby vertical compaction is analytically calculated (1D) for both scales and made equal (45). Maps of upscaled pressures are shown in **Fig. 3-10**. Furthermore, the MoReS Full Field Model (FFM) also takes pressure effects from the aquifer into account. These pressures were modelled analytically in the FFM and have been incorporated in pressure scenarios for geomechanical assessment.

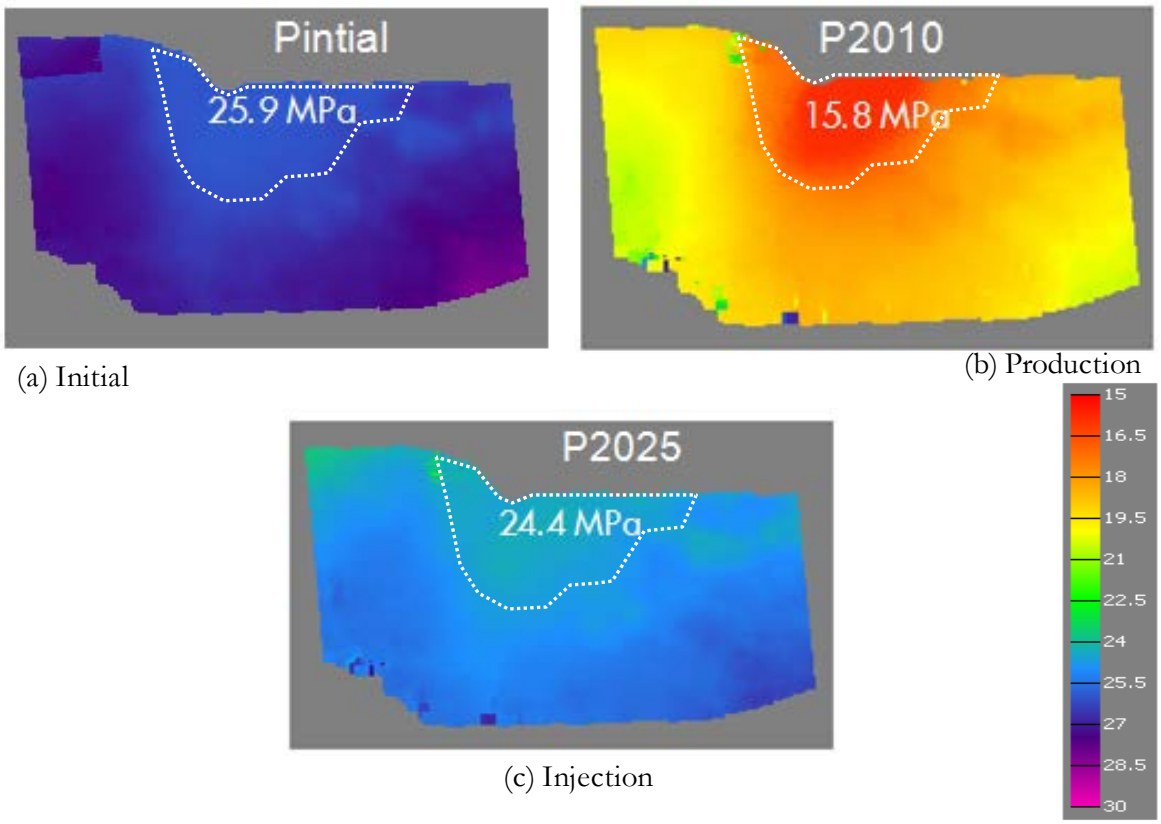

Fig. 3-10—Top view maps of upscaled pore pressures for Captain E&D reservoir formations at initial (a), end of production (b), and end of injection (c) phase.

Note: each plot has the average pore pressure indicated. Colour scale ranges between 15 and 30 MPa [2175 to 4351 psia]. The dotted lines show approximate field outlines.

3.3. Rock mechanical properties of the formations

3.3.1. Rock mechanical properties of the over- and underburden formations

Logs from six wells are available with compressional (DTP) and shear (DTS) wave travel times, and density (RHOB). From this data, the compressional or P-wave velocities, shear or S-wave velocities, dynamic Young's modulus and dynamic Poisson's ratio values can be derived using the standard theory for linear elastic wave propagation in isotropic, homogenous, and lossless solids, given as,

$$E_d = \rho v_s^2 \left(\frac{3v_p^2 - 4v_s^2}{v_p^2 - v_s^2} \right), \quad (4)$$

$$\nu_d = \frac{v_p^2 - 2v_s^2}{2(v_p^2 - v_s^2)}, \quad (5)$$

Where,

E_d is the dynamic Young's modulus (Pa),

ν_d is the dynamic Poisson's ratio,

ρ is the density (kg/m^3),

v_p is the compressional wave velocity (m/s), and

v_s is the shear wave velocity (m/s).

For deformation modelling, it is best to use the dynamic properties as they represent best the mechanical properties of the undrained rocks. Fig. 3-11 shows the log for Well 14_29a-3 with averaged/blocked dynamic elastic rock properties as computed from Equations (4) and (5). For all the over- and underburden formation material, behaviour is assumed to be linear elastic. The average dynamic elastic rock properties for these formations, as listed in Table 3-3, are used in the geomechanical modelling.

Table 3-3—Dynamic elastic rock properties for five overburden and two underburden formations

Stratigraphic unit	Dynamic Young's modulus [GPa]	Dynamic Poisson's ratio [-]	Density [kg/m^3]
Nordland	2	0.46	2200
Coals	2	0.46	2100
Dornoch Sandstone	4	0.43	2140
Ekofisk, Tor, Hod	32	0.32	2550
Rødby	10	0.38	2440
Humber, Heron	20	0.3	2300

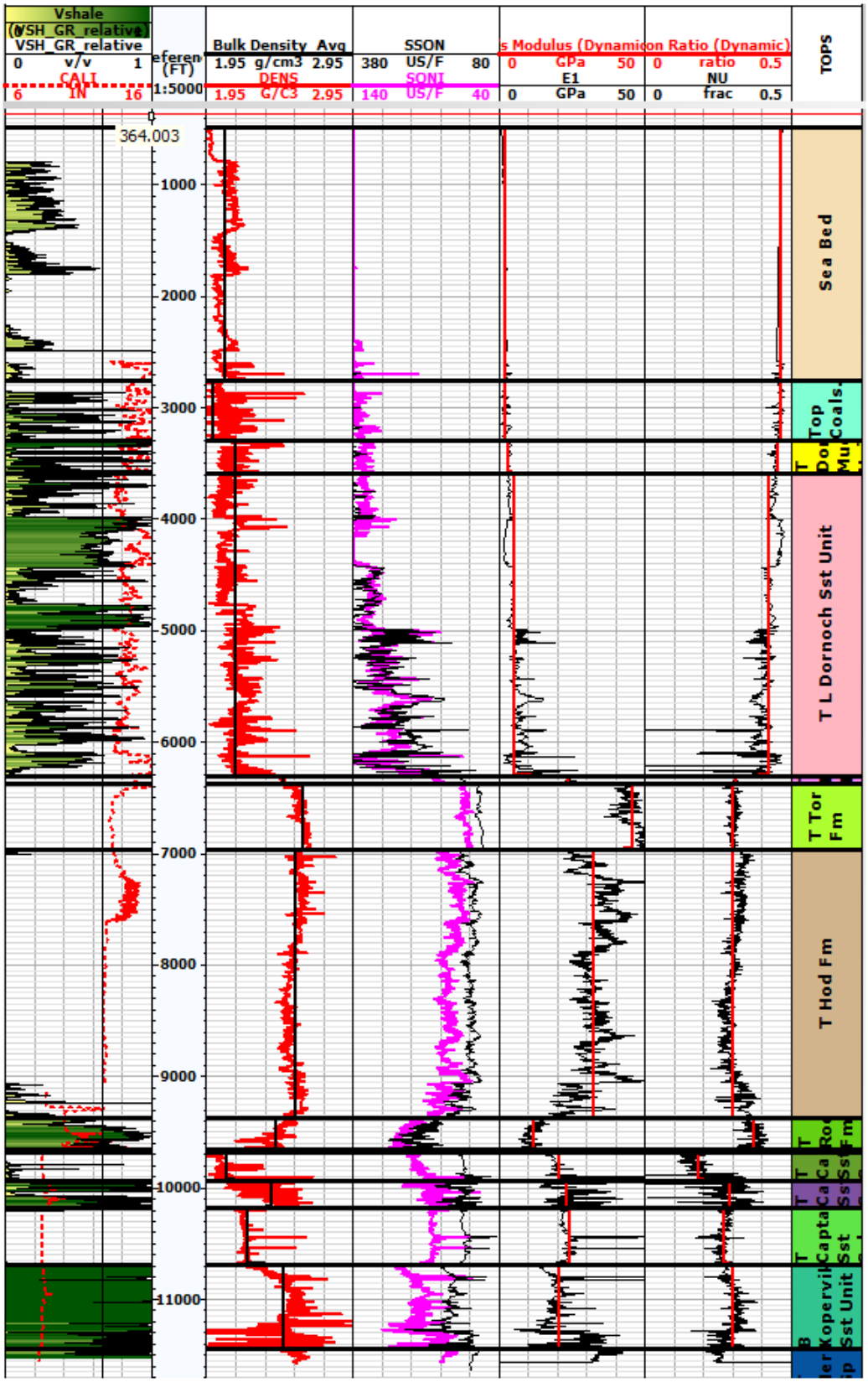

Fig. 3-11—Log of Well 14_29a-3 with DTP, DTS, RHOB and derived E_d and ν_d. Depth is given as measured depth MD.

Note that the well is deviated.

3.3.2. Failure parameters of the Rødby shale caprock

Owing to core degradation, no direct laboratory measurements could be performed on core samples from the unpreserved caprock. However, bulk physical properties, such as sonic log data, were used to predict the key mechanical parameters need, using published pre-determined correlations (48; 49) for shales - see Table 3-4. In addition to sonic log data, surface area measurements were carried out on shale cuttings taken from the Goldeneye appraisal Well 14/29a-3. These measurements can be correlated to the friction angle using a standard correlation (50), and yielded values for the friction angle of 13° to 22° for the Rødby Formation. From friction angle data, cohesion (C) can be calculated from the linear Mohr-Coulomb failure criterion via

$$C = \frac{UCS\,(1 - \sin\varphi)}{2\cos\varphi}, \tag{6}$$

Where:

UCS is the unconfined compressive strength [MPa],

φ is the friction angle [°].

As sonic log data is also available for the caprock, it is possible to correlate this data to cohesion using Shell proprietary correlations, as well as other correlations available in the literature (48; 49). Different values for the cohesion and friction angle, as displayed in Table 3-4, are due to differences between the empirical correlations used to derive them. Note that these correlations are generally derived for a specific set of samples, and hence might not be as accurate when used outside of this data set. However, such correlations can still be used to provide an estimated value for in-situ rock strength, when experimental data is lacking. As can be seen, the predicted values are in close accord with each other.

Table 3-4—Key findings from literature for failure parameters of the caprock.

Reference	Comment	UCS [MPa]	Cohesion [MPa]	Friction Angle [Deg]
Shell in-house correlations	Based on surface area measurements on shale cuttings and sonic log data (DTC = 105 µs/ft)		6.2-8.2	13-22
From Lal et al. (48)	High porosity North Sea, Tertiary shales			29
From Horsrud et al. (49)	North Sea and Norwegian Continental Shelf shales; C_{clay} > 30% and high porosity	17.4		22
Mohr-Coulomb failure criterion Eq. (6)	Based on UCS value by Horsrud (17.4 MPa) (49) and the friction angle averaged from Lal and Horsrud (26°)		5.5	

A base case using the lowest estimated values, i.e. a cohesion of 6 MPa [870 psia] and a friction angle of 13° was defined. However as check, an extremely conservative low case, defined by zero cohesion and a low friction angle of 13° was also defined.

3.3.3. Rock mechanical properties of the Captain Sandstone reservoir

Mechanical rock strength and failure parameters are in general not uniformly distributed throughout a reservoir, but have different values at different locations due to lateral variations in the sedimentological signature of the formation. As the change in reservoir pore pressure is the driving force behind changes in the overall stress distribution, accuracy of the geomechanical modelling is increased when non-uniform mechanical parameters are used in the modelling. Rock properties of the reservoir were taken from lab measurements, or estimated using empirical relations employing porosity and net to gross. As the latter two come from upscaled values of the reservoir simulator, overall consistency of flow and strength modelling is ensured. It also needs to be kept in mind that the elastic rock properties during production and injection are not necessarily equal.

Rock properties are directly measured or predicted using a pre-defined empirical correlation. Obviously measurements and correlations have uncertainties of which a reasonable range needs to be investigated. Measurements on a number of core plugs have shown that failure parameters are constant in the reservoir, both in the absence and presence of CO_2.

It should be noted that from a CO_2 storage capacity point of view, it is important to investigate a possible change of available storage volume due to gas depletion. Compaction experiments, aimed at determining the compressibility of the reservoir rock, showed that the compaction of the Captain Sandstone is partly elastic (i.e. reversible) and partly plastic (i.e. irreversible). When loaded from 17 to 34 MPa [2500 to 5000 psia], the material showed minimal compaction and the porosity change was about 0.3%. As a result this effect can be considered to have negligible impact on the difference in available pore volume between the gas depletion and CO_2 injection phases.

3.3.3.1. Elastic rock properties for the reservoir during depletion and injection

A number of laboratory experiments were performed on the available reservoir material, to determine the key input parameters for the geomechanical model. These measurements included triaxial compression experiments, with coupled flow, to determine the change in elastic and failure parameters for the Captain Sandstone in response to chemical CO_2/brine/rock interactions and uniaxial compressibility tests to determine the compressibility of the reservoir rock.

A total of six triaxial compression experiments were performed. Two types of triaxial deformation experiments were carried out:

- Mechanical tests with brine. This set aimed to determine the key mechanical properties of brine-saturated sandstone, under (near) in-situ conditions.
- Mechanical tests with brine, with or without injection of CO_2. These experiments were carried out in the presence of brine, with and without injection of CO_2 at high pressure, to assess the effect of calcite dissolution on the rock mechanical properties and failure strength.

All experiments were conducted at 20°C (samples 4 and 6) or 60°C (samples 1-3 and 5). The mechanical tests consisted of up to three stages, with key mechanical properties determined during each stage: 1) a set of two cycles simulating reservoir depletion and injection for brine-saturated samples (all samples), 2) continuous flow-through of synthetic reservoir brine, and 3) continuous flow-through of CO_2-saturated brine (samples 1-3). The depletion/injection cycles were carried out at a constant axial stress and confining pressure, and a varying pore pressure, simulating depletion and injection. The flow-through experiments were performed at constant axial stress, confining pressure and maximum pore pressures. It should be noted that the stress conditions employed during the different test stages yielded the same effective stresses as the in-situ stress-path of the Goldeneye

field, during the fluid depletion and injection phases (more details, see (51)). The results from these experiments are summarised in **Table 3-5** and **Table 3-6**. Note that the data from the first depletion/injection cycle was omitted, as these yielded unrealistically low results, most likely caused by settling of the sample and closing of cracks formed by core damage.

Under static conditions, i.e. no pore pressure changes, Young's Modulus was ~6 GPa [0.87 kpsi], while Poisson's Ratio was < 0.1. Under more representative conditions (i.e. poro-elastic response to pore pressure changes), Young's Modulus varied from ~12.6 GPa [1.8 kpsi] during depletion (P_p down – gas production) to ~16.2 GPa [2.3 kpsi] during injection (P_p up – CO_2 injection). Similarly, Poisson's Ratio varied from ~0.20 to ~0.26 (Table 3-5).

Table 3-5—Results from triaxial tests on Goldeneye reservoir core samples of the Captain D Sandstone. Sample 1 broke during the second cycle.

		Load test (production)		Unload test (injection)	
		Young's mod. [GPa]	Poisson's ratio [-]	Young's mod. [GPa]	Poisson's ratio [-]
Sample 1 (PS6)	Cycle 1	6.9	0.16	14	0.27
	Cycle 2	-	-	-	-
Sample 2 (PS9)	Cycle 1	12.3	0.14	19.8	0.21
	Cycle 2	17.6	0.21	19.0	0.21
Sample 3 (PS17)	Cycle 1	9.6	0.19	13.7	0.28
	Cycle 2	12.0	0.26	12.6	0.27
Sample 4 (GE01)	Cycle 1	8.4	0.17	16.2	0.25
	Cycle 2	15.2	0.23	15.8	0.27
Sample 5 (GE02)	Cycle 1	10.0	0.16	15.5	0.24
	Cycle 2	14.6	0.20	15.1	0.22
Sample 6 (GE03)	Cycle 1	9.6	0.16	17.3	0.29
	Cycle 2	16.7	0.26	17.2	0.32
Averages Samples 2-6					
	Both cycles	12.6	0.20	16.2	0.26

It should also be noted that the injection of CO_2, and concomitant dissolution of carbonate cement (cf. Section 2.1.1), did not significantly affect the Young's Modulus (E = ~18.4 GPa [2.7 kpsi]) nor the Poisson's Ratio (ν = ~0.22) – cf. Table 3-5 and Table 3-6).

Table 3-6—Results from triaxial tests on Goldeneye reservoir core samples of the Captain D Sandstone, employing fluid flow with brine and subsequently with CO_2-saturated brine.

		Brine flow		CO_2-saturated flow	
		Young's mod. [GPa]	Poisson's ratio [-]	Young's mod. [GPa]	Poisson's ratio [-]
Sample 2 (PS9)	160 ml flow	21.7	0.24		
	260 ml flow			21.5	0.25
	540 ml flow			21.4	0.27
	1230 ml flow			21.3	0.24
	1780 ml flow			21.9	0.25
Sample 3 (PS17)	300 ml flow	14.2	0.18		
	550 ml flow	15.4	0.20		
	840 ml flow			16.0	0.19
	1010 ml flow			16.2	0.19
	1130 ml flow			16.5	0.19
	1220 ml flow			16.2	0.21

In addition to the triaxial experiments, uniaxial compressibility testing was carried out on a single plug taken from the Captain D reservoir rock in the Goldeneye field, which yielded a vertical bulk compressibility of 5.4×10^{-7} [1/psia] under uniaxial strain conditions for a 25% porosity sample. Assuming that the grain compressibility is much smaller than the bulk compressibility, uniaxial compressibility C_m is allowed to be zero at zero porosity. This also implies that the Biot-Willis coefficient α is equal to one. Using these two constraints, a uniaxial compressibility-porosity function can be established, given as

$$C_m = 0.3132\ \Phi\ , \tag{7}$$

Where, C_m is the uniaxial bulk compressibility ($\times 10^{-5}$/MPa) at constant pore pressure, and Φ is the porosity (%).

$$E = \frac{1}{C_m} * \frac{(1-2\upsilon)(1+\upsilon)}{(1-\upsilon)}, \tag{8}$$

Given the variation in porosity throughout the reservoir (see Fig. 3-12), it is evident that the uniaxial compressibility (Eq. (8)) will also show some variation throughout the reservoir. In addition, the Poisson's ratio is also dependent on porosity, as suggested by a Shell in-house correlation fit to North Sea Φ-ν field data. Since Young's modulus E is related to the compressibility C_m and Poisson's ratio

ν as it becomes clear how the distribution of Young's modulus and Poisson's ratio within the reservoir can be calculated. In the process of upscaling the key reservoir parameters, one should also keep in mind the fraction of shale in the sandstone, as the three reservoir sections have different net to gross ratios. Note that the high values for Young's modulus and Poisson's Ratio obtained during the lab measurements, i.e. for rock with net to gross = 1, are well represented by the scaled elastic rock properties for the Captain E&D (Table 3-7). Furthermore, the difference in behaviour during loading and unloading of the sample is clearly a hysteresis effect (see Table 3-5 and Section 2.1.3). These variations in elastic properties have been accounted for in the geomechanical simulator GeoMec, by use of a bi-linear model, to represent the slightly different geomechanical parameters during the depletion and injection phases (Table 3-7).

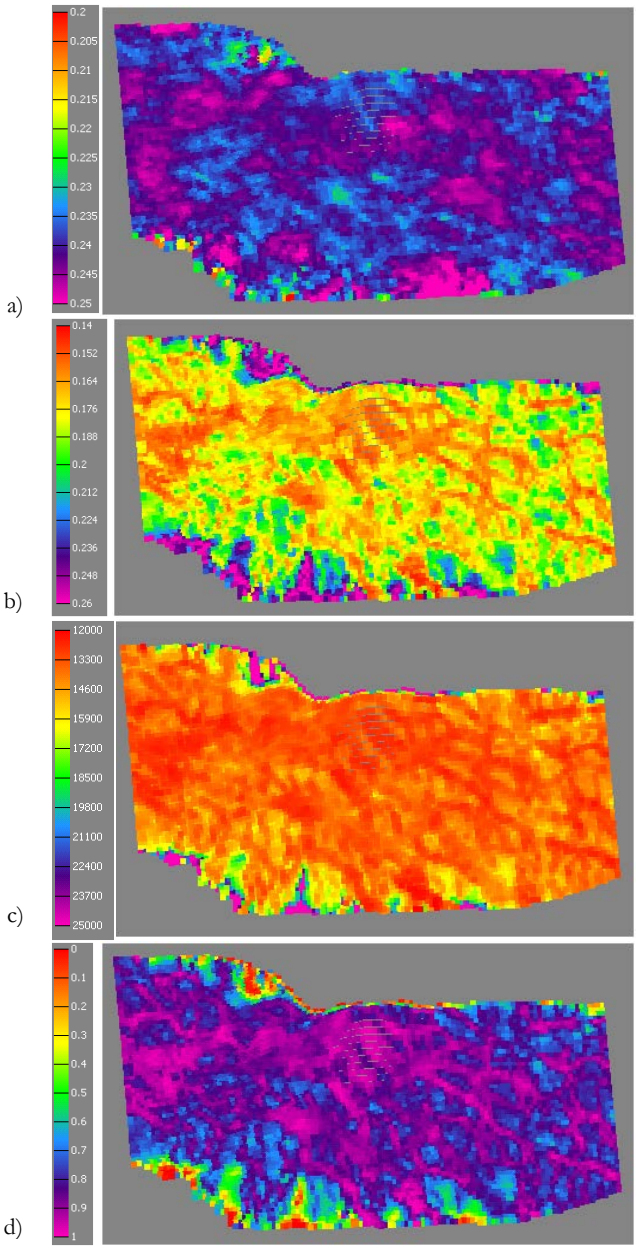

Fig. 3-12—Rock properties of the Captain E&D reservoir package during the production phase

Note: (a) porosity ranging from 0.2 to 0.25, (b) Poisson's ratio ranging from 0.14 to 0.26, (c) Young's modulus that ranges from 12 to 25 GPa [1.7 to 3.6 kpsi], and (d) Net to gross ranging from 0 to 1.

For the depletion phase, the values for Young's modulus and Poisson's Ratio were taken to vary with porosity throughout the reservoir (cf. Fig. 3-12). This leads to distributed values (point sets) for the Young's modulus and Poisson's ratio for a gross rock, as presented in Fig. 3-12 and Table 3-7. It can be observed from Fig. 3-12 that the overall distributions of porosity, Poisson's ratio, Young's modulus and net to gross follow an east-west trend throughout the reservoir. In contrast, for the injection phase it is assumed that the compressibility C_m is reduced by 50% compared to the C_m value during the production phase, as was also roughly indicated by lab measurements (51). In addition, since it is not known if, and if so how, porosity will vary across the field after CO_2 injection, values of E and ν for the injection phase have been taken as uniform across the reservoir and equal to the lab measurements as presented in Table 3-6.

Table 3-7—Base case values for the mechanical properties of the Captain Sandstone.

Formation	Phase	Young's modulus E [GPa]	Poisson's ratio ν	E and ν derived from	Average net to gross
Captain E&D	Production	12-25	0.15-0.26	upscaled using (45), see Table 3-5	1 (lab test on pure sand)
	Injection	20	0.26	upscaled using (45), consistent with lab tests, see Table 3-6	
Captain C	Production	28-30	0.24-0.26	upscaled using (45)	0.186 (from res. sim.)
	Injection	56	0.26	upscaled using (45)	
Captain A, Valhall, Scapa	Production	14-30	0.21-0.26	upscaled using (45)	0.445 (from res. sim.)
	Injection	37	0.26	upscaled using (45)	

A bi-linear model was used to describe differences in elastic rock properties during production and injection, for all three reservoir formations. Note that the mechanical properties for the production phase are distributed throughout the reservoir, in accordance with the porosity distribution. For the injection phase, the parameters are taken uniform across the reservoir.

3.3.3.2. Failure parameters of the Captain Sandstone reservoir

A total of nine triaxial tests were performed on samples from core taken from the Goldeneye field (51), aimed at determining the failure properties of the reservoir rock. Seven of these tests were performed employing brine, aimed at determining the failure strength of the reservoir rock. Furthermore, two samples were flushed with CO_2-saturated brine to study the effect of carbonate dissolution on rock strength (cf. Section 3.3.3.1), followed by measuring the failure strength. No weakening, induced by the dissolution of carbonate cement, was observed (cf. Section 2.1.1). In addition, a number of empirical correlations are also analysed in order to arrive at the key reservoir rock strength parameters required, i.e. cohesion and friction angle or angle of internal friction. Table 4-8 summarises the key findings.

Note that cohesion (C) is calculated from the linear Mohr Coulomb failure criterion as given by Eq. (6). From Table 3-8, it is clear that there is some scatter between the measured values and the values predicted by the empirical correlations. Since the correlations were not derived from Goldeneye field data, it was decided to be best to use the measured failure parameters for the base case, i.e. a cohesion of 3 MPa [435 psia] and a friction angle of 34.4°. However, note that the values predicted using the correlations by Sarda et al. (52) and Eq (6) (cf.) are not far off from the lab data. To investigate the full uncertainty range of the failure parameters, worst case values are defined as a formation with zero cohesion and a friction angle of 20°.

Table 3-8—Results from literature and experiments of failure parameters of reservoir rock

Reference	Comment	USC [MPa]	Cohesion [MPa]	Friction Angle [deg]
Goldeneye triaxial tests	Seven failure tests on brine-wet samples + two tests on CO_2-brine wet samples		3 ± 1.2	34.4 ± 1.6
From Mc Nally et al. (53)	Bowen Basin (Australia); fine-grained, consolidated and unconsolidated sandstones; all porosities	49.2		
From Sarda et al. (52)	Globally; Φ < 30%	27.2		
From Vernik et al. (54)	Sedimentary basins, worldwide; clean, well-consolidated arenites; Φ < 37%	26.8	3.7	
From Weingarten et al. (55)	Gulf of Mexico; sandstones with 20 < Φ < 37%			31.6
From Moos et al. (56)	Cook Inlet (Alaska); coarse-grained sandstones and conglomerates	24.3		
From Chang et al. (57)	Eq 3: Gulf Coast; weak and unconsolidated sandstones	20.2		
	Eq 11: globally; sandstones with 2 < UCS < 360 MPa and 0.2 < Φ < 33%	22.7		
Mohr-Coulomb failure criterion Eq. (6)	UCS averaged from above references (39.4 MPa) and friction angle averaged from measured and Vernik value (33°)		10.7	

4. Model case A: results, observations & interpretations

To assess the potential for shear and tensile failure of the reservoir and overlying caprock (cf. Table 2-1), a geomechanical model of the storage site using Shell proprietary geomechanical modelling software GeoMec was developed. This chapter is involved with the base case A scenario of our model. The mechanical parameters used in this base case are shown in Table 3-7. The mechanical state of the reservoir, before and after gas production (Section 4.3), and after CO_2 injection (Section 4.4), as well as the stress state of the caprock (Sections 4.5 and 0) are discussed in this chapter.

4.1. Stress changes in the reservoir and definition of failure criteria

Reservoir depletion or injection results in stress changes inside and outside the reservoir. The magnitude of these changes is dependent on the degree of pore pressure changes, on the rock properties and on the structure of the depleting volume. Stress changes can potentially lead to tensile or shear failure of the formations (see Fig. 4-1), reactivation of existing faults, or slip along very weak overburden layers. Stress changes are often described in terms of stress arching, i.e. non-uniform stresses over a plane due to local out of plane loading, by so called gamma factors or depletion constants (cf. Section 2.1.3).

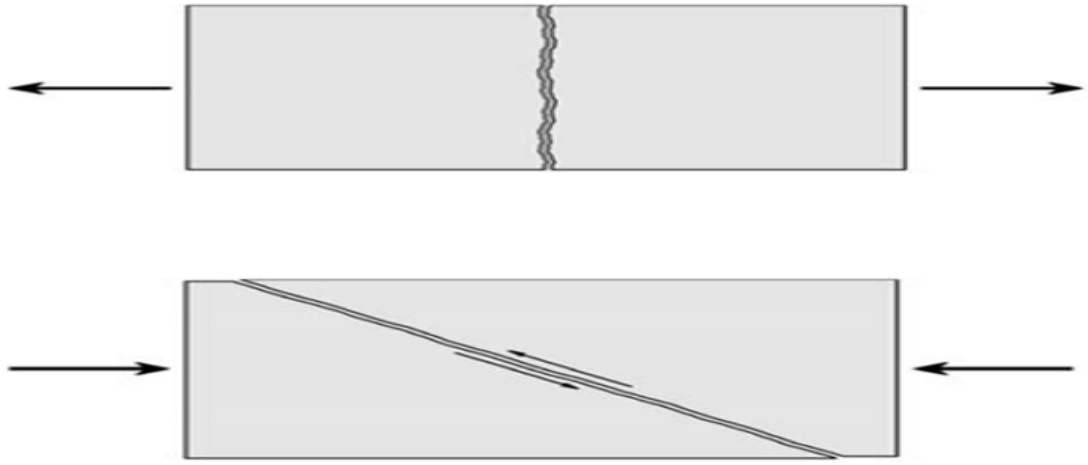

Fig. 4-1—Schematic failure modes, showing tensile failure (top) and shear failure (bottom).

Whether a certain (new) stress state will lead to shear failure of a formation can be assessed using the rock failure properties, such as represented by the Mohr-Coulomb criterion. The Mohr-Coulomb failure criterion is defined by the cohesion C and the friction angle φ, as shown in Fig. 4-2. Above the failure line, the material is mechanically unstable, while below the failure line the material is mechanically stable (intact). The stress condition of a material point is represented by a Mohr circle, such as shown for the effective principal stresses σ_1 and σ_3 in Fig. 4-2. A material point under consideration is perceived in an elastic state of deformation if the Mohr circle remains below the failure line, whereas the material is in shear failure if the circle touches the failure line. Stress conditions that cause the Mohr circle to intersect the failure line are not feasible.

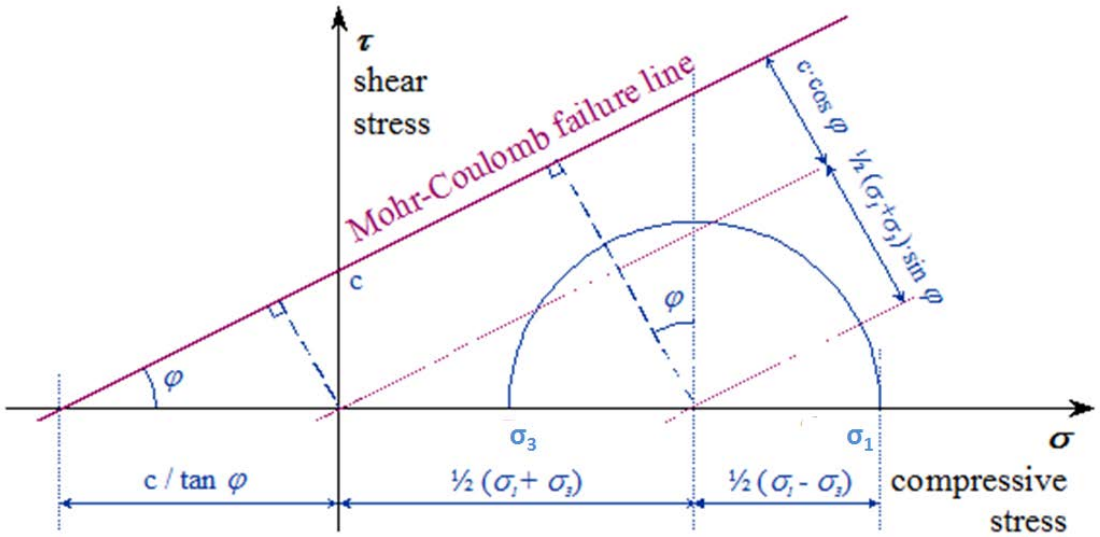

Fig. 4-2—Mohr-circle diagram relating the principal stress state and the Mohr-Coulomb failure condition

Note: The maximum shear stress τmax is represented by the blue dashed line through the centre of the circle, whereas the actual shear stress is equal to the radius of the Mohr circle.

The failure condition of a material point, or the proximity of the local stress state to failure, can be expressed by the shear capacity, or Shear Capacity Utilisation (SCU), which relates the actual level of shear stress to the maximum shear strength of that point. This is expressed as the τ/τ_{max} ratio, alternatively called the Mohr-Coulomb failure ratio.

The actual shear stress τ at a material point is equal to the radius of the Mohr circle, given as

$$\tau = \tfrac{1}{2}(\sigma_1' - \sigma_3'). \quad (9)$$

Where,

σ_1' is the maximum effective principal stress, given as $\sigma_1 - P_p$, and

σ_3' is the minimum effective principal stress, given as $\sigma_3 - P_p$.

At the same time, the value for the maximum shear stress τ_{max} at that point can be calculated from the cohesion C and the friction angle φ (Fig. 4-2) using

$$\tau_{max} = C\cos\varphi + \tfrac{1}{2}(\sigma_1' + \sigma_3')\sin\varphi, \quad (10)$$

As such, the shear capacity can be expressed as,

$$SCU = \frac{\tau}{\tau_{max}} = \frac{\tfrac{1}{2}(\sigma_1' - \sigma_3')}{C\cos\varphi + \tfrac{1}{2}(\sigma_1' + \sigma_3')\sin\varphi}. \quad (11)$$

By definition, the τ/τ_{max} ratio cannot become larger than one, as that would require the Mohr circle to exceed the failure line. However, any value beyond one can be calculated, in the absence of appropriate redistribution of stress due to failure, by employing linear elasticity theory only.

Throughout the report, shear capacity plots will be shown as a tool to represent the failure condition of the reservoir or caprock, for different scenarios of pore pressure changes and rock properties. Further, Mohr circles and failure lines are presented for a few selected points where the shear

capacity has relatively high values. These points lay within a selected "area of interest" (Fig. 4-3), defined as the area in the reservoir where the pressure changes are largest. At these locations the total maximum and minimum principal stresses along with the absolute pore pressure are taken from the GeoMec model. For clarification, approximate field outlines are represented by dotted lines in the map view plots in this chapter.

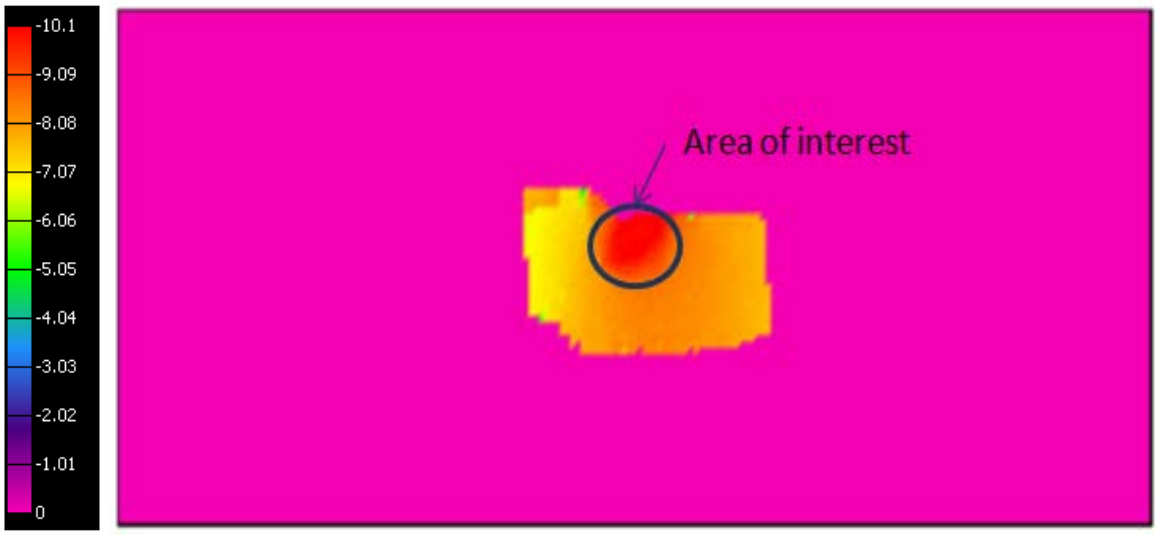

Fig. 4-3—Map view of the pore pressure change within the Captain E&D formations, from the initial phase to the end of the production phase.

Note: The area of interest is defined as the locations where the absolute pore pressure changes are largest. Colour scale is in MPa. Note the similarity to Fig. 3-10.

4.2. Initialisation of the simulation

Prior to starting the simulations, GeoMec was set to compute the initial total maximum principal stress and initial total minimum principal stress, as displayed in Fig. 4-4. These values are in close agreement with the vertical stress computed from the density logs in the wells (cf. Section 3.2.1) and the total minimum principal stress inferred from the depth trend from LOT data (cf. Section 3.2.2). This close agreement between the different methods to predict stress can be seen as a calibration of the model in the initial state.

If possible, field data should be used to calibrate the model. This is often done by comparing calculated and measured subsidence values but this is not possible in the case of the Goldeneye field, as no subsidence (or compaction) data are available.

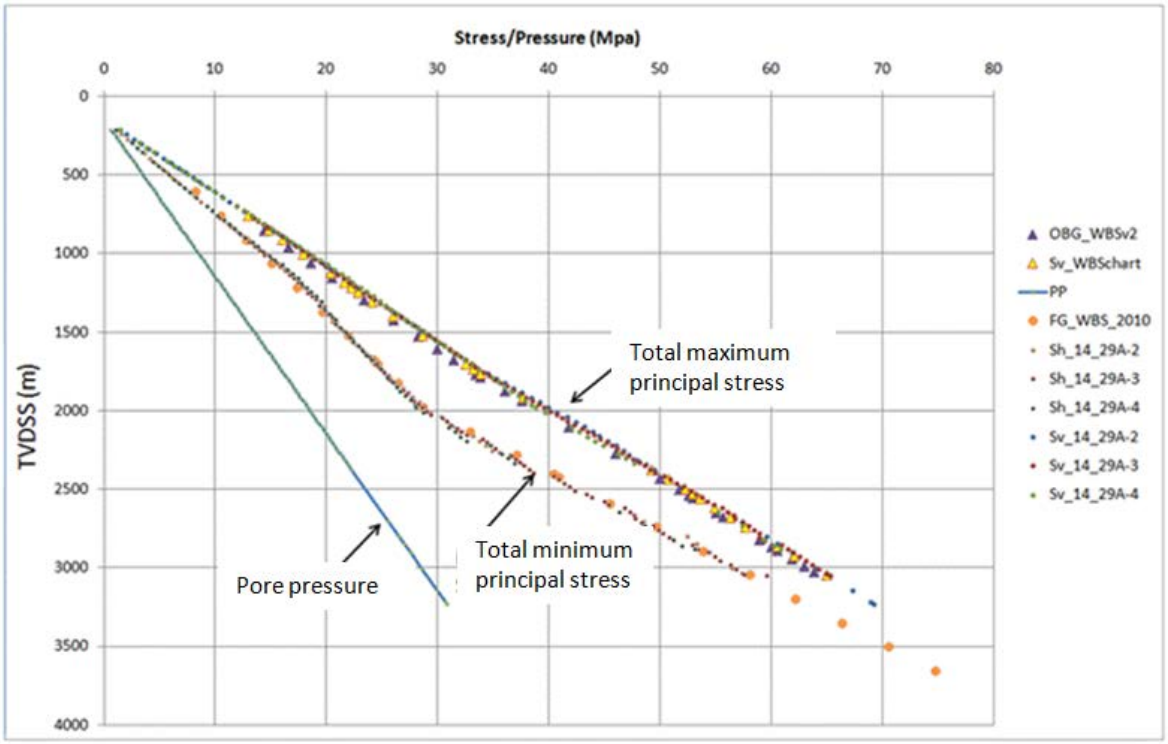

Fig. 4-4—Initial in-situ stresses and pore pressure profile compared to GeoMec computed initial total maximum principal stress and initial total minimum principal stress.

4.3. Production phase

This section describes the stress changes related to gas production, and the subsequent decrease in pore pressure, within the reservoir. It should be noted that the stress path of the reservoir during depletion can be described by the depletion coefficient, $\gamma = \Delta\sigma/\Delta P_p$, as described in Section 2.1.3 and Eqs. (1) and (2).

4.3.1. Stress changes during gas production

At the end of gas production, the pressure in the Captain E&D reservoir has dropped by approximately 10.1 MPa [1465 psia] (cf. Section 3.2.4). Overall, significant changes in the total minimum principal stress of the three Captain reservoirs are predicted, as shown in Fig. 4-5b, while outside the reservoir total minimum principal stress changes are negligible. Negligibly small changes in total maximum principal stress are predicted both in the reservoir and outside. Note that the observed high values at the boundary and outside of the defined "area of interest" (blue spots in Fig. 4-5c) are an effect of unrealistic jumps in the material properties within the reservoir model. These are an artefact resulting from missing data combined with the GeoMec extrapolation algorithm, and should therefore be ignored.

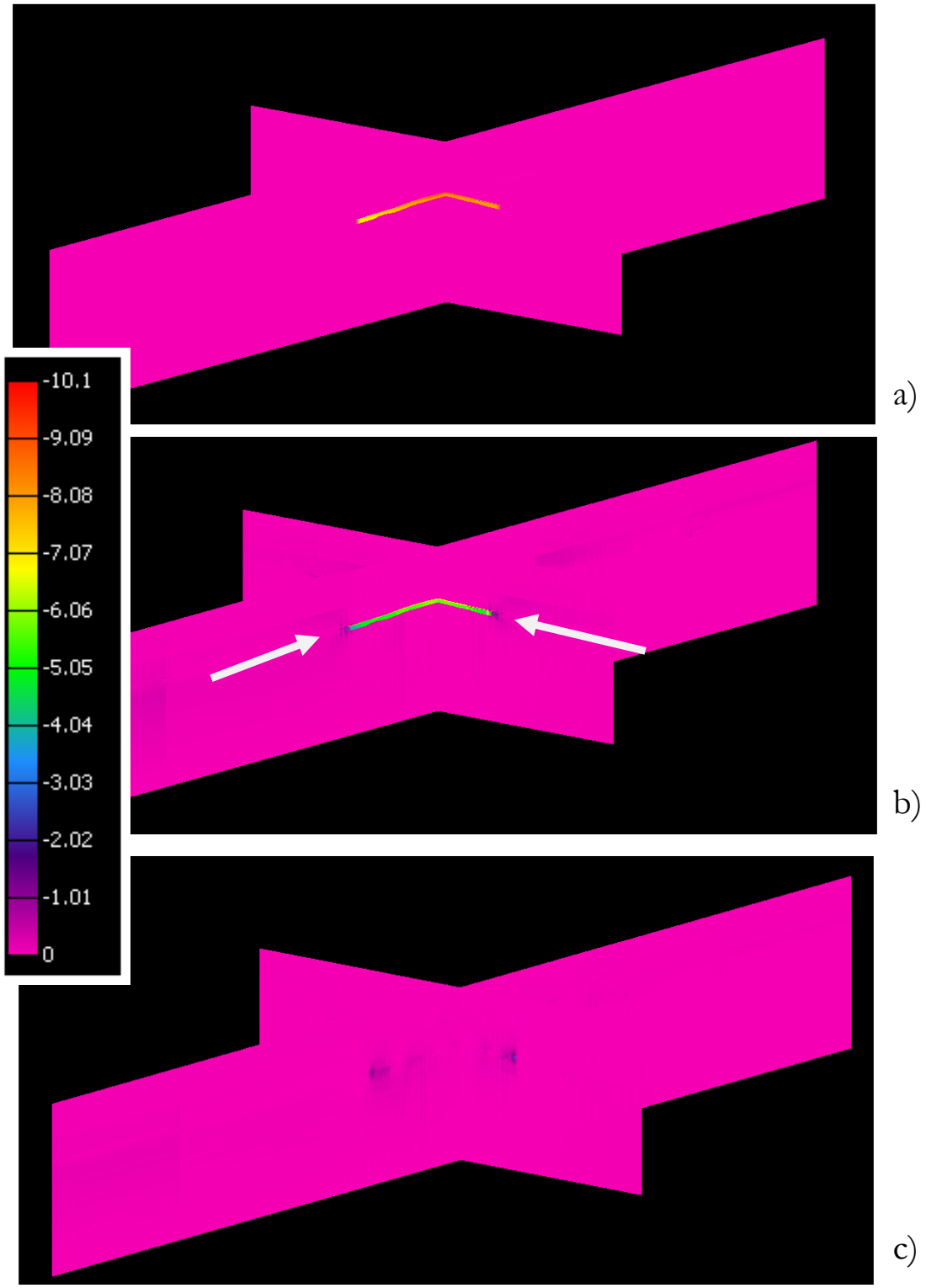

Fig. 4-5—3D bird's-eye view of two cross sections through all the formations

Note: reservoirs indicated by white arrows, showing (a) reduction in pore pressure from the initial phase to the end of production, (b) reduction in total minimum principal stress, and (c) reduction in total maximum principal stress. Colour scale is in MPa.

For a reduction in pore pressure of 10.1 MPa [1465 psia] in the Captain E&D Sandstones, from the initial phase to the end of production, the reduction in total minimum horizontal stress is predicted

to be 8.2 MPa [1189 psia] (Fig. 4-5 - cross sections; Fig. 4-6 - map view). The horizontal depletion factor γ_h is thus 0.81. The calculated reduction in total maximum vertical stress is low and on the order of 0.5 MPa, leading to a vertical depletion factor γ_v of 0.05.

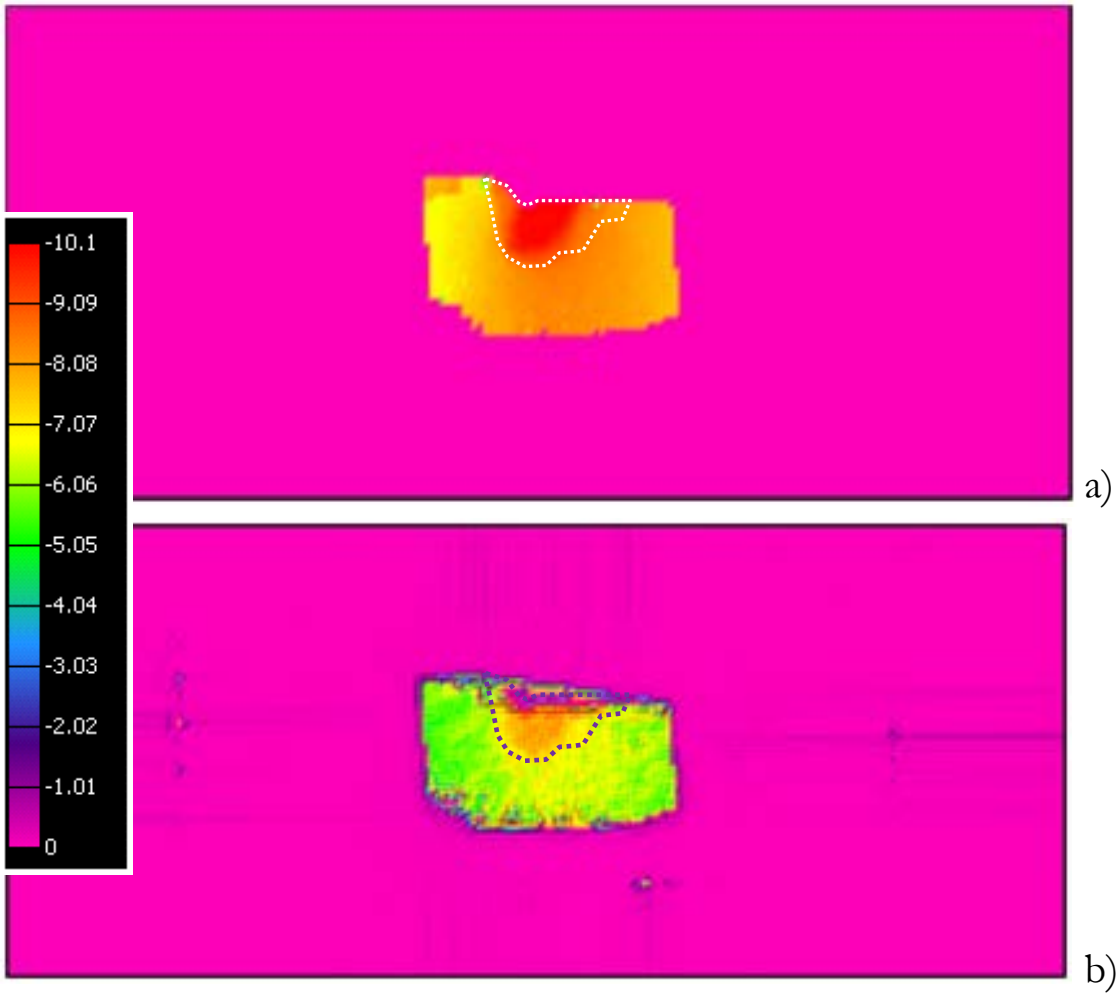

Fig. 4-6—Map view of Captain E&D reservoir

Note: showing (a) reduction in pore pressure of 10.1 MPa [1465 psia] from the initial phase to the end of production, and (b) reduction in total minimum principal stress of 8.3 MPa [1204 psia]. Colour scale ranges between 0 and 10.1 MPa [0-1465 psia]1.

The location where the pore pressure depletion is largest is N6429667, E478600, roughly at the heart of the area of interest (Fig. 4-3). This location coincides with that of the maximum stress change (see Fig. 4-6b for σ_3) and the maximum shear capacity. A Mohr circle analysis for the Captain E&D reservoir, for the maximum stress change location at the end of production, is shown in Fig. 4-7. As can be seen, even at the point of maximum change in principal stresses no shear failure of the reservoir is expected.

[1] Note that the approximate field outline is shown by dotted lines in all map view plots in this chapter.

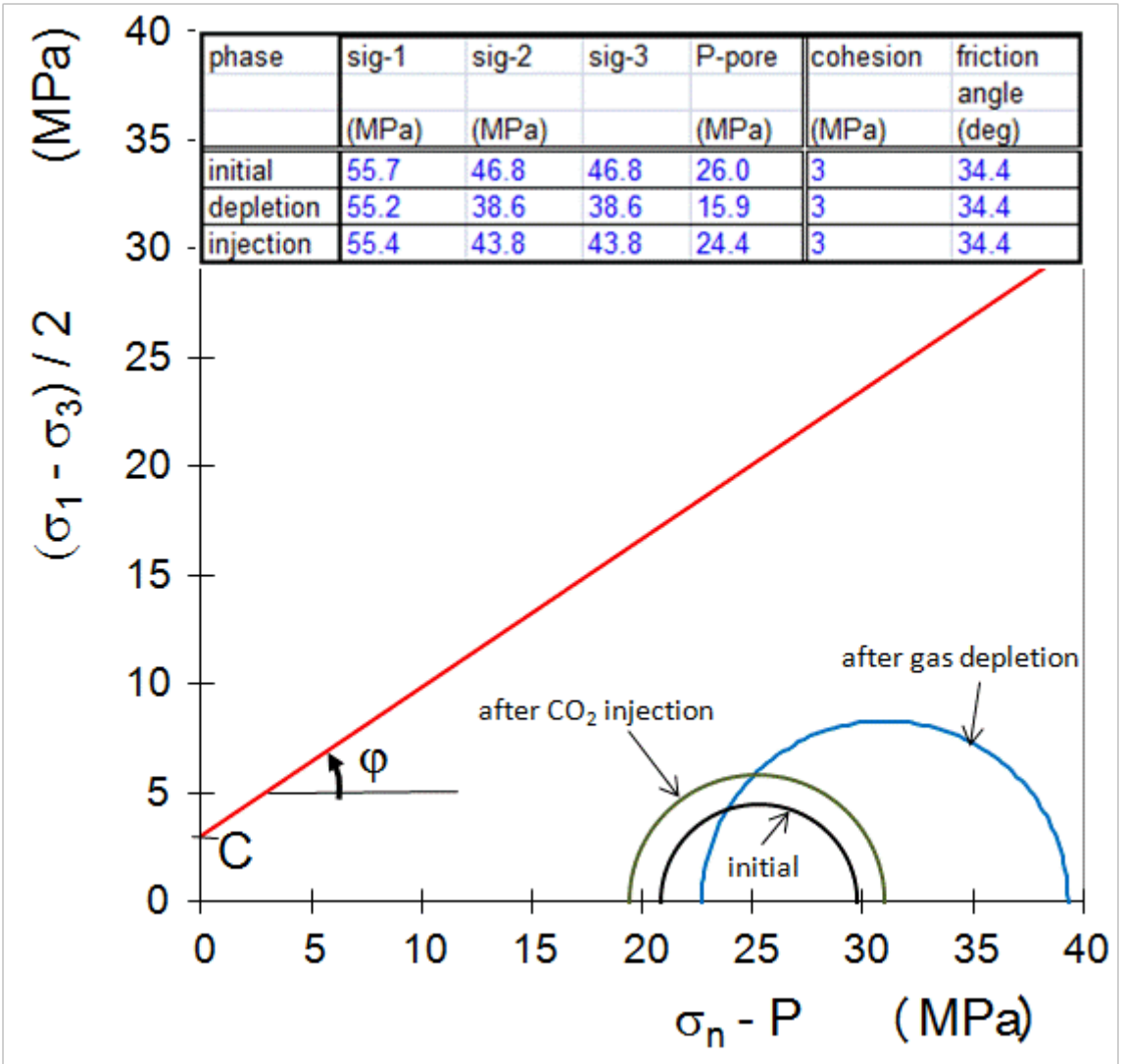

Fig. 4-7—Mohr circles and Mohr-Coulomb failure line for the Captain E&D reservoir formation

Note: Displayed at the point of maximum pore pressure change in the area of interest (see Fig. 4-3). At this point, the shear capacity is largest at the end of gas production and after CO_2 injection.

In addition, the SCU has been calculated for the reservoir as a whole. Its distribution, prior to production, at the end of production, and at the end of CO_2 injection, is shown in Fig. 4-8. Again note the observed high values at the boundary and outside the defined area of interest, which are an effect of unrealistic jumps in the material properties within the reservoir model. These are an artefact resulting from missing data combined with the GeoMec extrapolation algorithm, and should therefore be ignored. Overall, the shear capacity increases when going from the initial state of stress to the depleted state but is still well below one.

Therefore, no shear failure of the Captain E&D reservoir is expected to have occurred by the end of production. This is in line with current field observations, as production data do not indicate shear failure. Similar results were obtained for the Captain A and C formations (not shown).

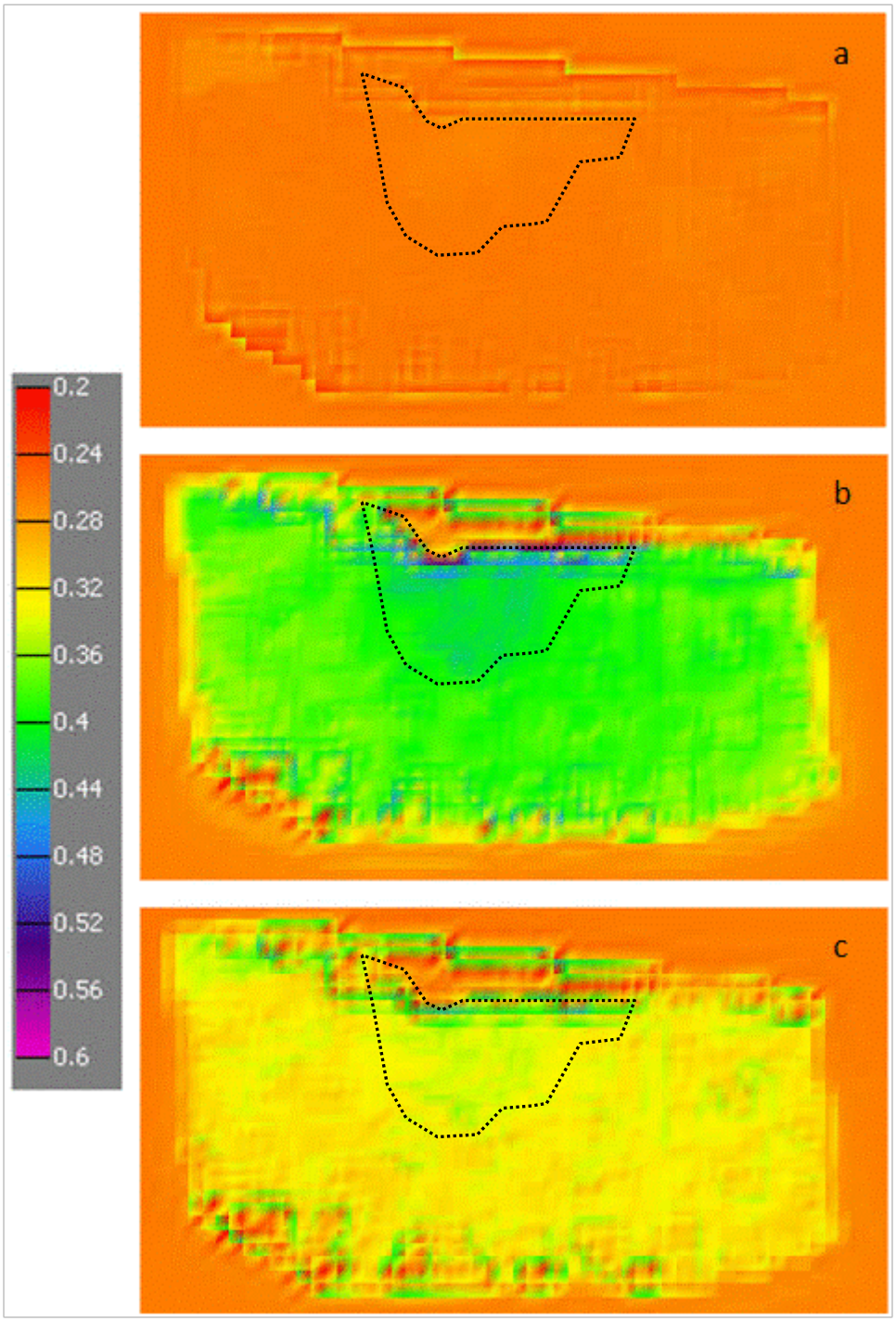

Fig. 4-8—Map of the shear capacity distribution for the Captain E&D reservoir

Note: at (a) initial state, and (b) after production, and (c) after injection. Colour scale of the shear capacity is dimensionless and ranges between 0.2 and 0.6.

4.3.2. Production-related reservoir compaction and sea-floor subsidence

As a consequence of the pore pressure drop due to gas production (dP_p = ~10.1 MPa [1465 psia]), compaction of the reservoir is expected to have occurred. The maximum subsidence of the sea-floor and vertical displacement at the top of the Captain E&D reservoir is 4.6 cm [1.8 in] and 8.9 cm [3.5 in], respectively. The subsidence bowl, as shown in **Fig. 4-9**, is expected to have an extent of about 14 km in the east-west direction and 9 km in the north-south direction. Note that no field data is available to validate this prediction. Results indicate no vertical stress arching (non-uniform stresses over a plane due to local out of plane loading) has occurred over the reservoir during depletion. The predicted amount of subsidence is commensurate with observations from other fields producing from similar stratigraphies in the North Sea (58).

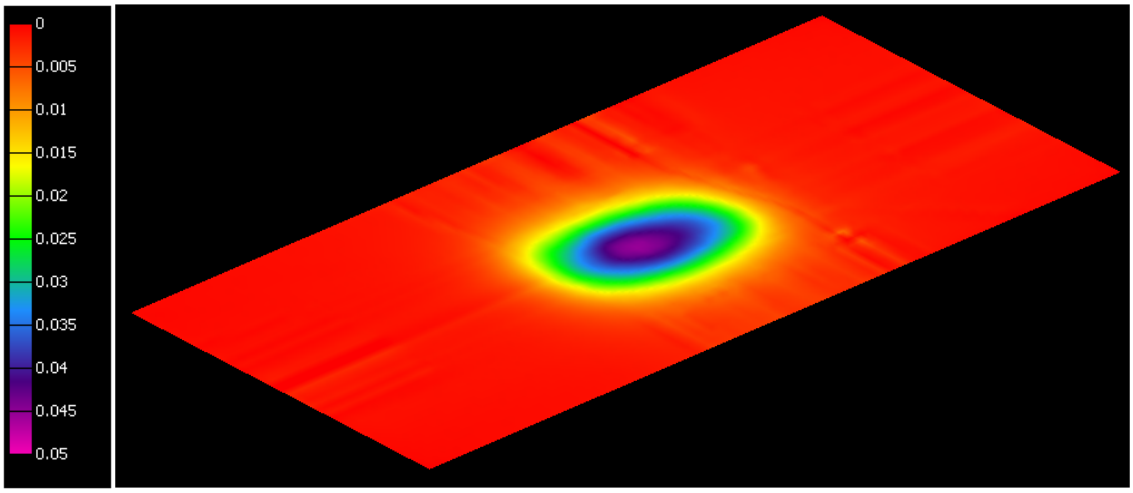

Fig. 4-9—Bird's-eye view of the sea-floor with subsidence (max 4.6 cm [1.8 in]) after production.

Note: colour scale ranges between 0 and 0.05 m [0-2 in].

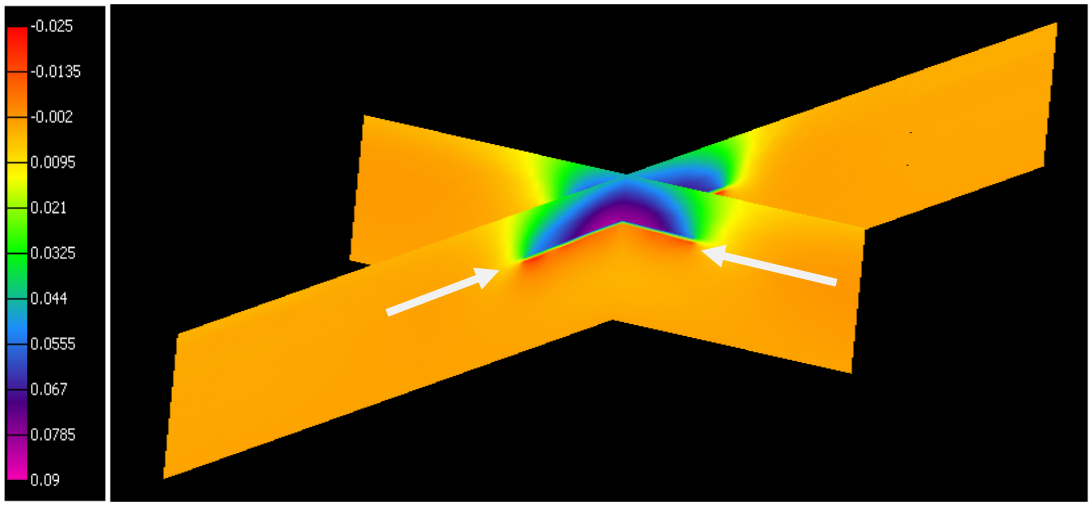

Fig. 4-10—Cross section of overburden, reservoirs (indicated by white arrows), and underburden with vertical displacement (8.9 cm [3 in] at the top of the Captain E&D reservoir) after production.

Note: Colour scale ranges from -0.025 to 0.09 m [-1 -3.5 in].

4.4. Injection phase

Following the same approach as for the depletion phase, the stress changes related to CO_2 injection, and the subsequent increase in pore pressure, within the reservoir are now described. Similarly, the stress path of the reservoir during depletion can be described by the inflation coefficient, $\gamma = \Delta\sigma/\Delta P_p$, as described in Section 2.1.3 and Eqs. (1) and (2).

4.4.1. Stress changes during CO_2 injection

After CO_2 injection of 20 Mt, the pressure in the Captain E&D reservoir is expected to increase by approximately 8.5 MPa [1233 psia] (see Section 3.2.4). Significant changes in the total minimum principal stress of the Captain E&D reservoir due to this pore pressure increase is predicted and displayed in Fig. 4-11, while total minimum principal stress changes are negligible outside the reservoir. Negligibly small changes in total maximum principal stress are predicted inside and outside the reservoir. Overall, predictions suggest a stress change pattern similar to that at the end of the production phase, but slightly smaller in magnitude and opposite in direction.

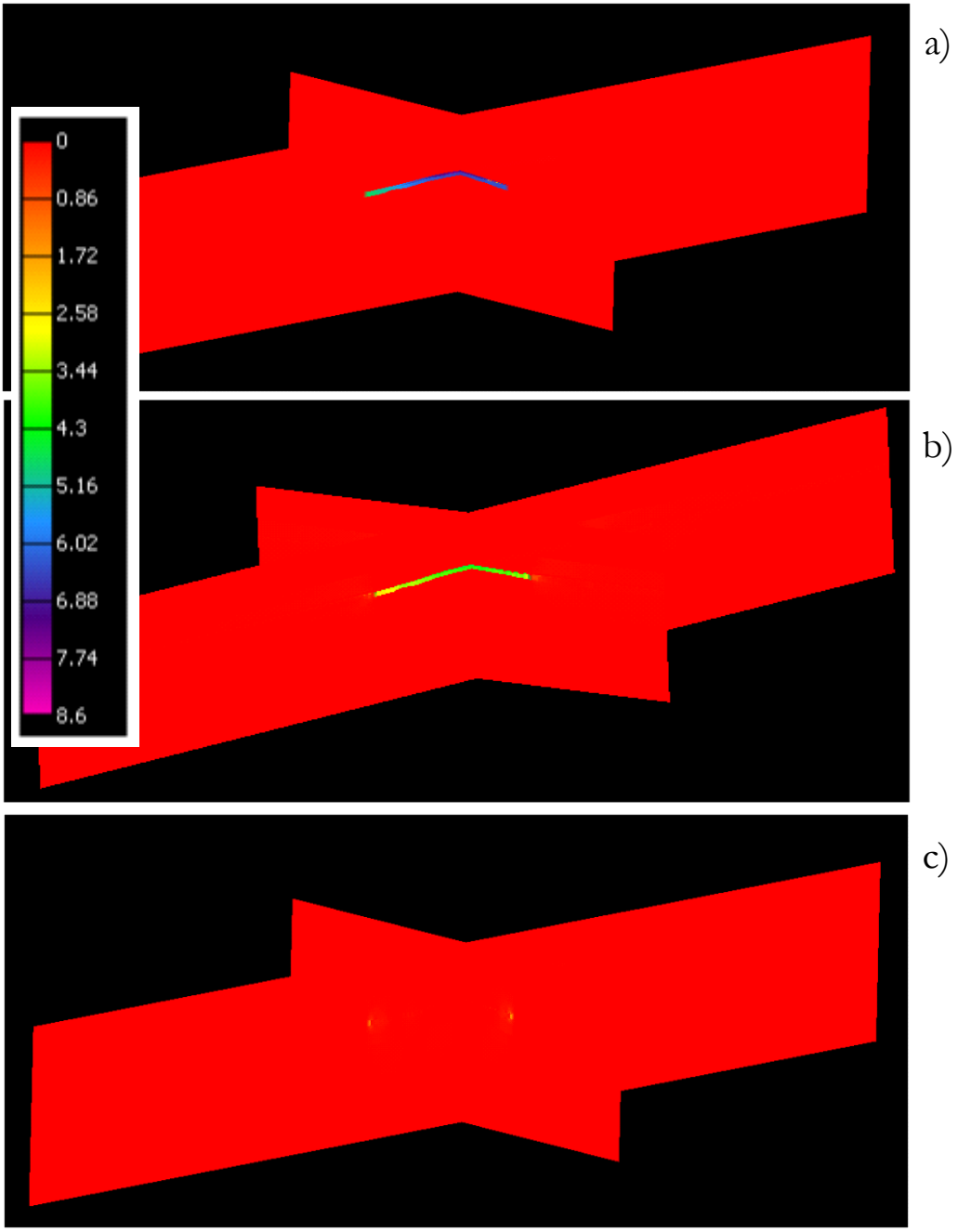

Fig. 4-11—3D bird's-eye view of two cross sections through all the formations

Note: showing (a) an increase in pore pressure from production to injection phase, (b) a reduction in total minimum principal stress, and (c) a reduction in total maximum principal stress. Colour scale ranges from 0 to 8.6 MPa [0 to 1247 psia].

For a typical increase in pore pressure of 8.5 MPa [1233 psia] in the Captain E&D reservoir, going from after the end of production to the end of injection, the increase in total minimum horizontal stress is 5.2 MPa [754 psia] (**Fig. 4-11** - cross sections; **Fig. 4-12** - map view). This leads to a γ_h of 0.61. The total maximum vertical stress is increased by 0.2 MPa [29 psia] leading to a γ_v of 0.02. Both the depletion factors calculated for the production and the injection phases will be used to represent the base case to verify the effect of uncertainties in rock properties in relation to hysteresis (see Section 2.1.3).

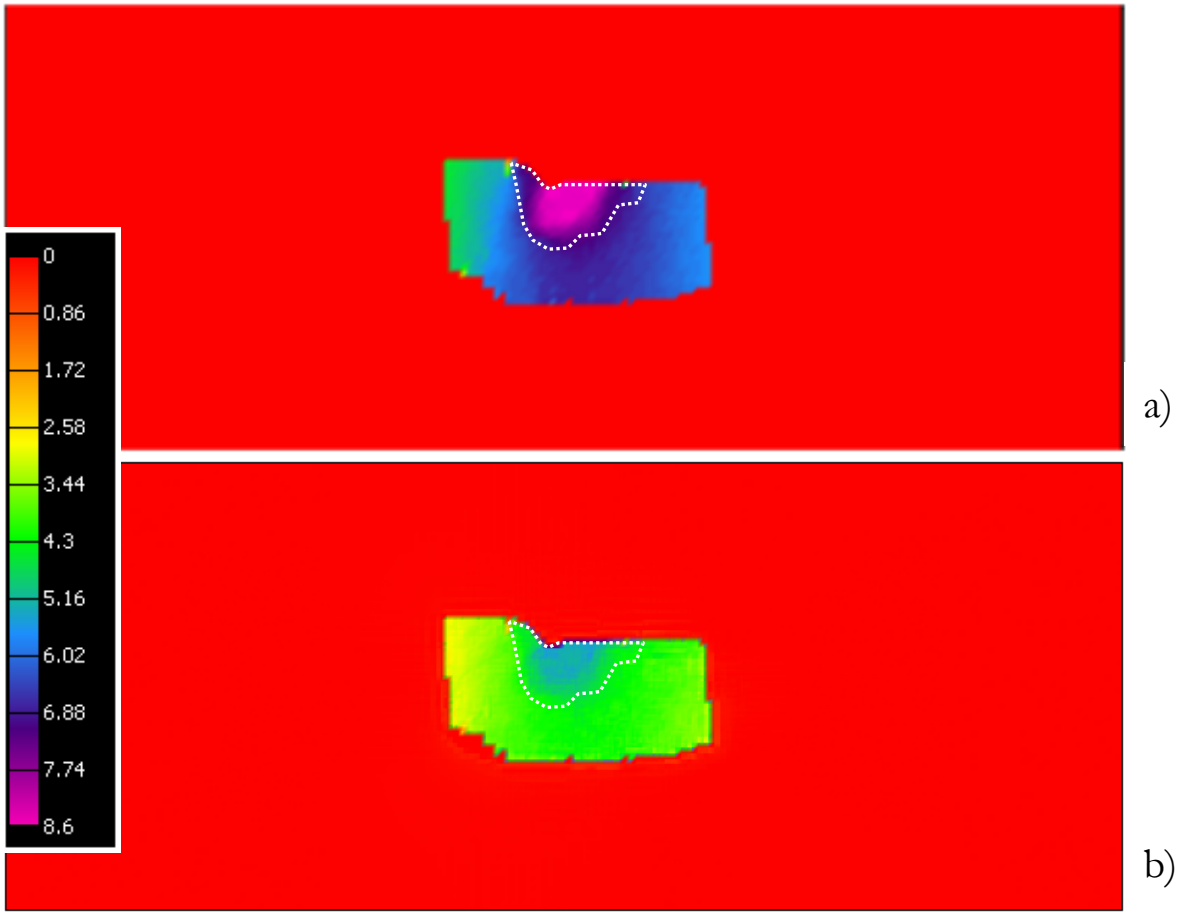

Fig. 4-12—Map view of Captain E&D reservoir

Note: showing (a) an increase in pore pressure of 8.5 MPa [1233 psia] during the injection phase, and (b) an increase in total minimum principal stress of 5.6 MPa [812 psia]. Colour scale ranges from 0 to 8.6 MPa [0 to 1247 psia].

Again, a shear capacity analysis was performed at the point of the largest stress perturbation (cf. Section 4.3.1), at the end of CO_2 injection. As can be seen in Fig. 4-7, no shear failure of the reservoir is expected, as the Mohr circle is well below the failure line. Failure parameters are described in Section 4.4.1.

It should be noted that during injection, the minimum effective principal stress increases to a larger extent than the maximum principal stress, leading to a decrease in the radius of the Mohr circle. As a result, SCU is expected to decrease throughout the reservoir during the injection period, as can also be seen when comparing Fig. 4-8b to c. The shear capacity decreases during injection and therefore stays well below one; so no shear failure is predicted for the Captain E&D reservoir after CO_2 injection. Similar predictions have been made for the Captain A and C Sandstones, which also indicated no expected shear failure of these formations.

4.4.2. Injection-related inflation and sea-floor uplift

After having the gas depleted, CO_2 is injected to a level of 8.5 MPa [1233 psia] above the maximum depletion value (see section 3.2.4). Then a maximum sea-floor subsidence of 3.6 cm [1.4 in] is predicted by GeoMec, see **Fig. 4-13**. A maximum subsidence of 5.6 cm [2.2 in] is predicted at the top of the Captain E&D sands, see **Fig. 4-14**. Comparing sea-floor subsidence after the gas production phase (4.6 cm [1.8 in]) and injection phase (3.6 cm [1.4 in]) leads to an uplift (heave) of

only 1 cm [0.4 in], due to injection and therefore not leading to subsidence problems that need to be mitigated.

These numbers could not be calibrated as no subsidence information is available.

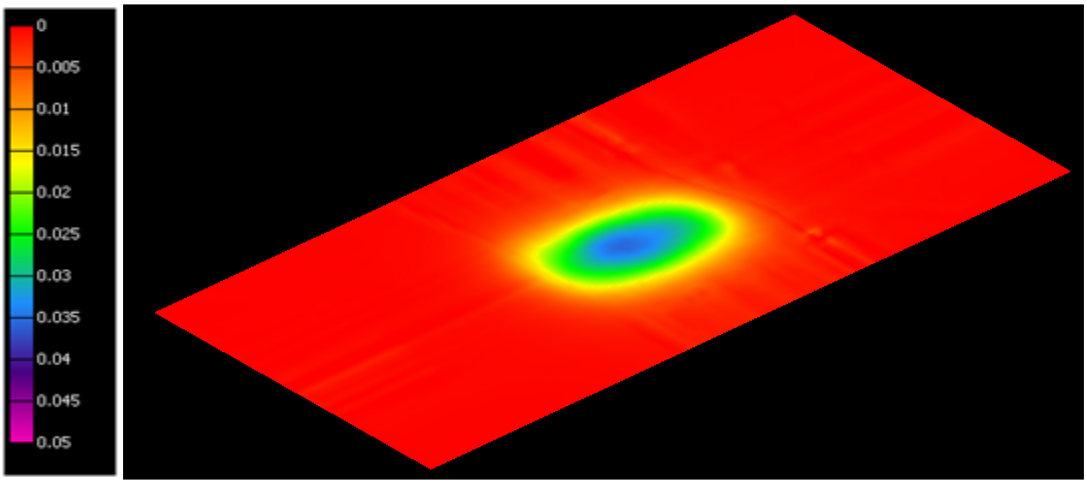

Fig. 4-13—Bird's-eye view of seafloor subsidence (max 3.6 cm [3.4 in]) after injection.

Note: colour scale ranges from 0 to 0.05 m [0 to 2 in].

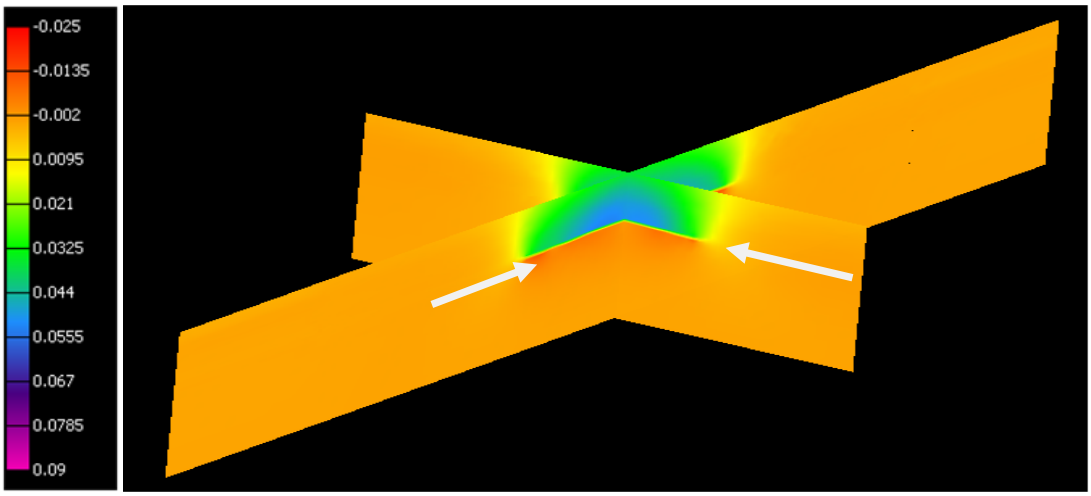

Fig. 4-14—Cross section of overburden, reservoirs (indicated by white arrows), and underburden with vertical displacement (5.6 cm [2.2 in] at the top of the Captain E&D reservoir) after injection.

Note: colour scale ranges from -0.025 to 0.09 m [-1 to 3.5 in].

4.5. Stress changes in the caprock during production and injection

As the top of the Captain reservoir is mechanically coupled to the bottom of the Rødby Shale, any stress changes in the reservoir, as a result of production or injection, are transferred to the caprock. To study the effect of stress changes in the reservoir on the change in stress state in the caprock, 3D geomechanical modelling is needed. As can be seen in **Fig. 4-15**, if the pore pressure in the Captain E&D reservoir is reduced by 10.1 MPa [1465 psia] due to gas production, the change of the total

minimum and maximum principal stresses in the Rødby Shale caprock varies by up to 0.5 MPa [73 psia], compared to stress changes in the Captain E&D reservoir.

Given these small stress changes in the caprock, going from the initial stress state to the end of the production phase, there is almost no change in the Mohr circle and the shear capacity value, as can be seen in Fig. 4-16 for the point of the largest stress perturbations. Overall, no shear failure of the caprock is predicted as the Mohr circle remains well below the failure line during depletion (see also Fig. 4-17b).

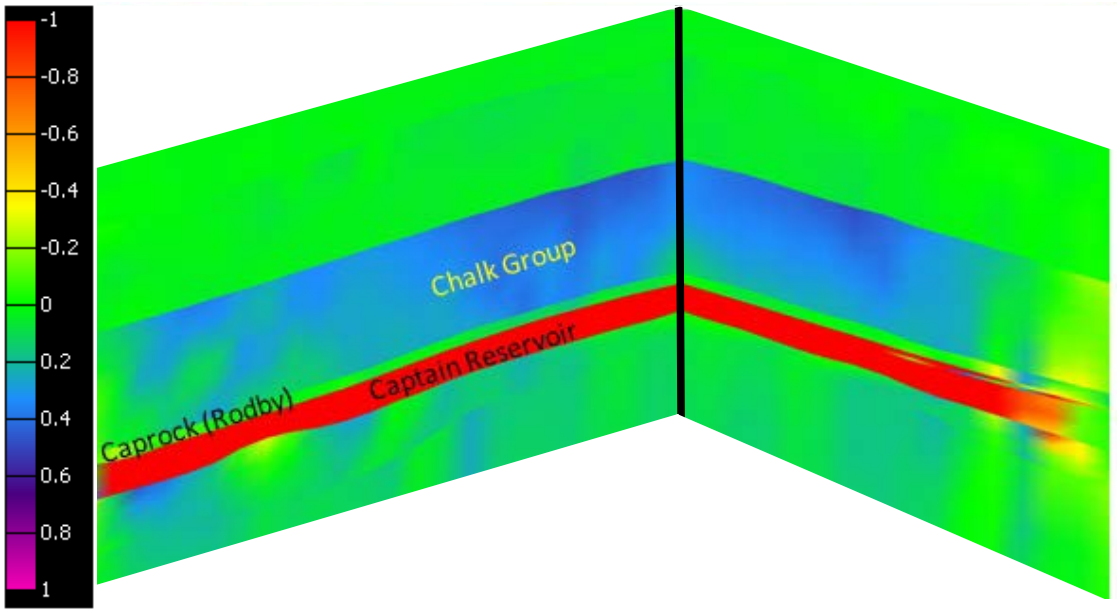

Fig. 4-15—3D zoomed-in bird's-eye view of two cross-sections (west-east and north-south, intersecting at black line) through parts of the reservoir, caprock, under- and overburden.

Note: colours display stress changes of the minimum total principal stress resulting from gas depletion at the end of production. Scale is in MPa, values are restricted to within -1 and +1 MPa [-145 to +145 psia].

If the pore pressure in the Captain E&D reservoir is increased by 8.5 MPa [1233 psia] due to CO_2 injection, the reduction of the total minimum and maximum principal stresses in the caprock are again very small compared to the stress changes in the Captain E&D reservoir (see Fig. 4-11). This suggests that at the point of maximum stress perturbation, no caprock failure as a result of CO_2 injection is to be expected either. The Shear capacity results for the entire caprock formation are presented in Fig. 4-17. As can be seen, no shear failure is expected for the whole of the caprock as the shear capacity remains well below one, going from the initial stress state, to the end of the gas production phase, and the end of the CO_2 injection phase.

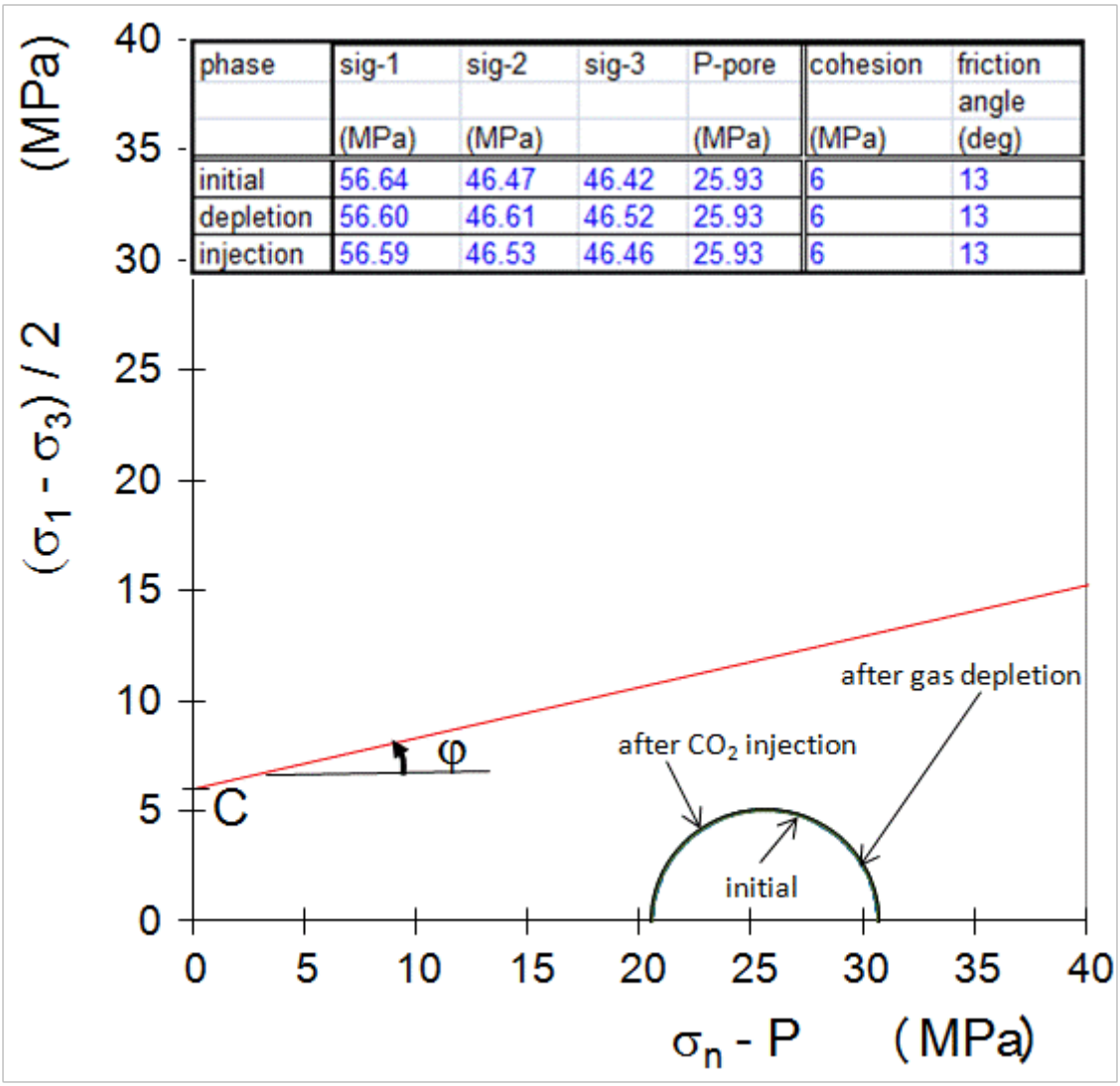

Fig. 4-16—Mohr circles and Mohr-Coulomb failure line for the Rødby Shale caprock formation, before production, after production, and after injection

Note that all three Mohr circles are on top of each other, due to the small stress changes between the three phases.

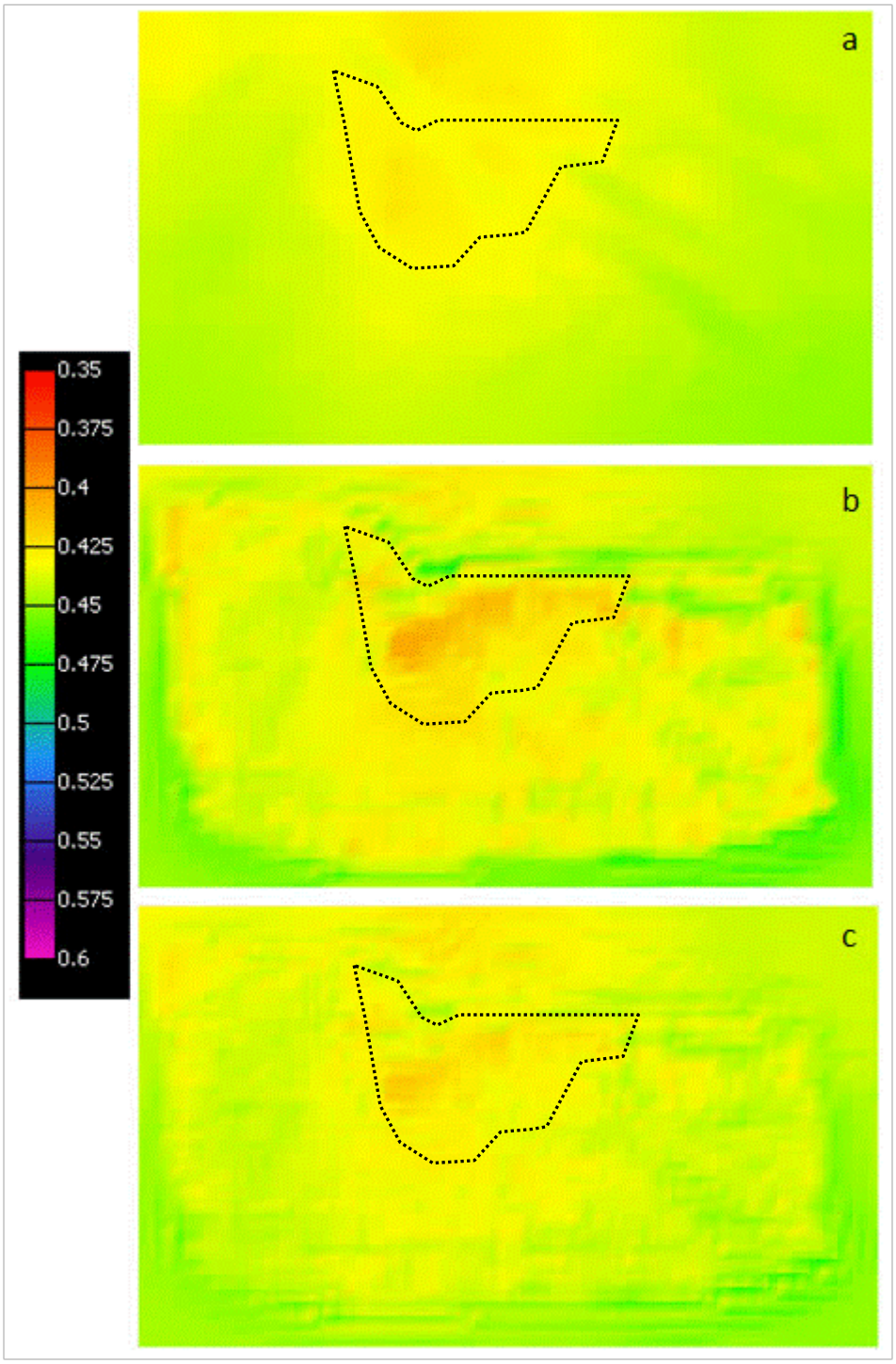

Fig. 4-17—Map of the shear capacity distribution for the Rødby Shale caprock formation

Note: (a) the onset of production, (b) the end of production, and (c) at the end of injection. Colour scale is dimensionless and ranges from 0.35 to 0.6.

4.6. Tensile failure potential of the reservoir during production and injection

The Mohr circles, as presented in the previous sections, show there is no tensile failure at the point of maximum stress perturbation locations as the minimum effective principal stress is always positive. **Fig. 4-18** shows a map of the whole of the Captain E&D reservoir, displaying the distribution of the minimum effective principal stress. The extreme low and high values, which are an effect of unrealistic jumps in the material properties within the reservoir model, are an artefact resulting from missing data combined with the GeoMec extrapolation algorithm, and should therefore be ignored.

It can be concluded that throughout the entire reservoir the minimum principal stress remains positive. Therefore, no tensile failure of the Captain E&D reservoir is to be expected, either after all the gas has been depleted, or after CO_2 has been injected.

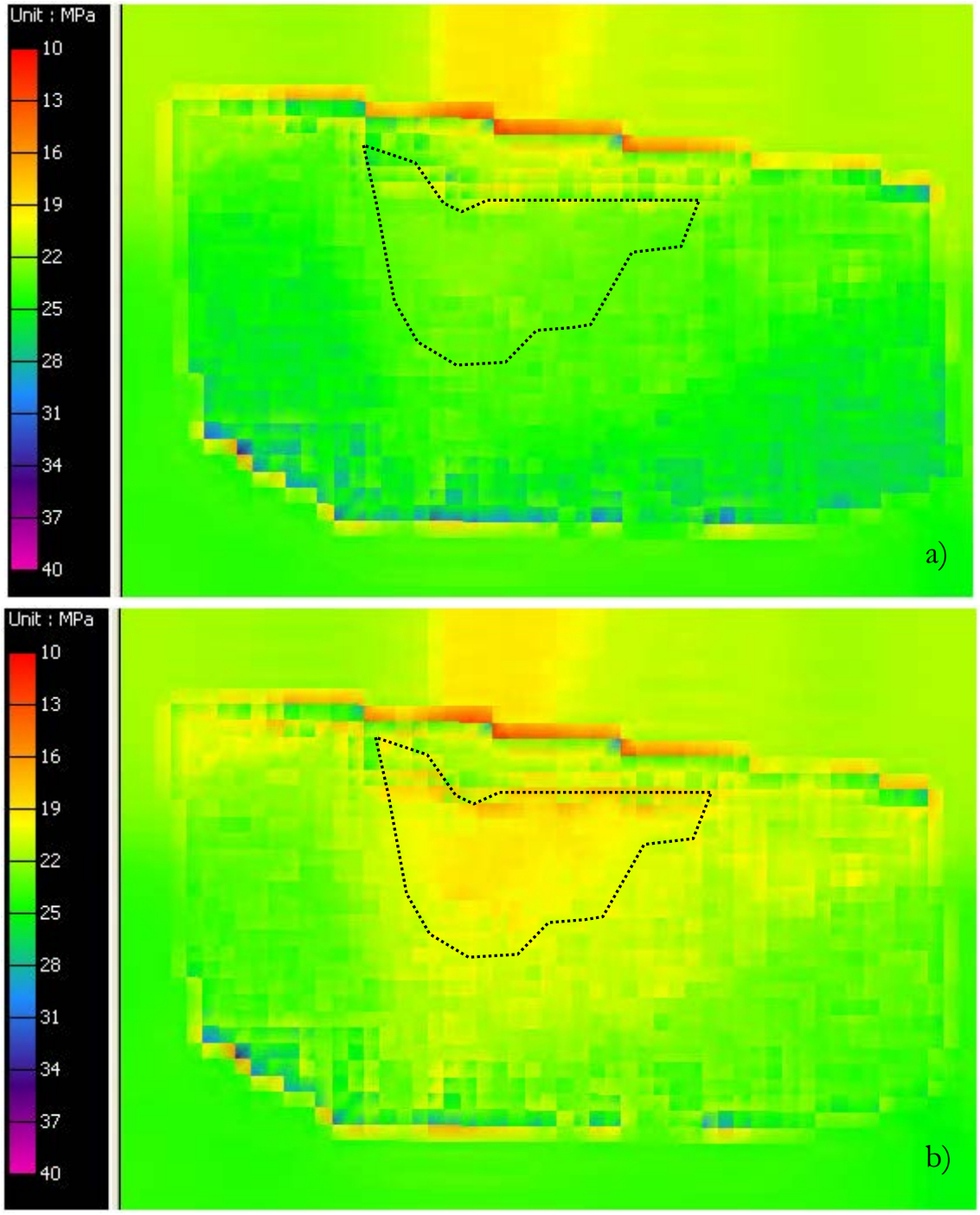

Fig. 4-18—Minimum effective principal stress

Note: (a) at the end of gas depletion, and (b) at the end of CO_2 injection. Colour scale ranges from 10 to 40 MPa [1450 to 5801 psia].

4.7. Summary of findings

The GeoMec model predictions suggest significant stress changes in minimum principal stress within the Captain Sandstone reservoir during the gas production phase, while negligible changes in σ_h are predicted outside of the reservoir. In contrast, negligible stress changes are expected for the maximum horizontal stress, both within and outside of the reservoir. Though the change in reservoir pore pressure during depletion is expected to have resulted in several centimeters of subsidence, no shear failure of the reservoir is expected to have occurred by the end of production.

Similar behaviour in stress changes and vertical displacement is predicted for the injection phase, though they are smaller in magnitude and opposite in direction. Since during injection the minimum effective principal stress is predicted to increase more than the maximum principal stress, no shear failure of the reservoir is expected during the injection period.

Geomechanical modelling predictions suggest that shear failure of the caprock did not occur during gas depletion. Similarly, no caprock failure as a result of CO_2 injection is to be expected either.

Predictions of the changes in minimum horizontal stress suggest that no tensile failure of the Captain E&D reservoir is to be expected, either after all the gas has been depleted, or after CO_2 has been injected.

5. Model input sensitivity analyses: modelling results

As all input parameters of the underlying geomechanical study have uncertainties, the modelling was extended by investigating the sensitivity of the model to this range of parameter values, especially those that affect the integrity of the reservoir and caprock most. **Table 5-1** gives an overview of the key reservoir and caprock parameters, and their magnitudes, which were varied, such as the elastic parameters (Young's modulus and Poisson's ratio), rock failure parameters (cohesion and friction angle) and pore pressure. Note that the base case values for mechanical rock strength and failure parameters are not uniformly distributed throughout the reservoir, but have different values at different locations due to lateral variations in the sedimentological signature of the formation (cf. Table 3-7 and Fig. 3-12).

In the following sections, the sensitivity analyses results will be presented for the Captain E&D reservoir and the Rødby Shale caprock. Overall, the results focus on the shear capacity or SCU values and their distributions for the two formations. Tensile failure is not expected for the different geomechanical scenarios described in Table 5-1, as the effective minimum horizontal stress will not become less than the pore pressure, and will therefore not be discussed.

For reference, the key results for the base case that were presented in Chapter 4 are summarised in Table 5-2. Note that these values represent the location in the area of interest (as defined in Fig. 4-3) where the stress perturbations were at its maximum, i.e. where SCU is largest. This holds for all tables in the remainder of this chapter. Furthermore, in some sections, pressure and stress state values are also shown on all Mohr circle diagrams. For clarification, approximate field outlines, delineated by the dotted lines, were added to the map view plots in this chapter.

Table 5-1—Cases that were modelled to investigate the effect of different rock properties and pressures in the integrity of the reservoir and caprock

Case	Described in	Description of Modelled Cases
A	Chapters 3 and 4 and Table 5-2	Base case (cf. Table 3-7 and Fig. 3-12 for distributions of rock properties)
B	Table 5-3	Same as base case, except that the Poisson's ratio is increased by 0.05 for the three Captain reservoir formations for both the production and the injection phase
C	Table 5-4	Same as base case, except that the Poisson's ratio is decreased by 0.05 for the three Captain reservoir formations for both the production and the injection phase
D	Table 5-5	Same as base case, except that the Young's modulus values for the over- and underburden are reduced by half, compared to the Base case
E	Table **5-6**	Same as base case, except that the failure parameters represent a worst case scenario, i.e. for the reservoir cohesion is assumed to be zero and friction angle = 20°, and for the caprock cohesion is also zero and friction angle = 13°
F	Table 5-7	Same as Case E, but Young's modulus and Poisson's ratio are changed for all three reservoir formations during the injection phase, such that the stress path differs from the Base case A to represent a worst case scenario
G	Table 5-8	Same as base case, but now with pressure support from the aquifer and the worst case scenario rock failure parameters for the reservoir and caprock
H	Table 5-9	Maximum injection pressure is increased to a value that is higher than the hydrostatic pressure by adding 2.2 MPa [319 psia] to the base case injection pressure, combined with worst case scenario rock failure parameters for the reservoir and caprock
I	Table 5-10	Base case pressures after gas depletion are lowered by 2 MPa [290 psia] to a level where the absolute minimum pore pressure is 13.8 MPa [2000 psia]. Again, worst case scenario rock failure parameters for the reservoir and caprock are used

Table 5-2—Base case results

Case A		Change of pore pressure ΔP [MPa]	Change of minimum principal stress $\Delta\sigma_3$ [MPa]	Change of maximum principal stress $\Delta\sigma_1$ [MPa]	Max SCU (approx)
Reservoir Captain E&D	Initial to production	-10.1	- 8.2	- 1.0	0.40
	Production to injection	+8.5	+ 5.2	+ 0.5	0.33
Rødby Caprock	Initial to production	0.0	0.1	0.0	0.43
	Production to injection	0.0	0.0	0.0	0.43

5.1. Case B: Poisson's ratio + 0.05

For sensitivity Case B, the Poisson's ratio used in the base case A was increased by 0.05 for the three Captain reservoir formations for both the production and the injection stages. This increase represents the high-end value of the uncertainty range for Poisson's Ratio, as seen on the well logs (cf. Fig. 3-11). Changes in total minimum and maximum principal stresses are summarised in Table 5-3. Stress changes in the Captain E&D reservoir are small compared to the base case, while stress changes in the caprock are essentially equal to the base case.

Table 5-3—Key results for Case B

Case B		Change of pore pressure ΔP [MPa]	Change of minimum principal stress $\Delta\sigma_3$ [MPa]	Change of maximum principal stress $\Delta\sigma_1$ [MPa]	Maximum SCU (approx)
Reservoir Captain E&D	Initial to production	-10.1	-10.1	-1.0	0.41
	Production to injection	+8.5	+5.5	+0.5	0.36
Rødby Caprock	Initial to production	0.0	0.1	0.0	0.45
	Production to injection	0.0	0.0	0.0	0.45

Shear capacity results for Case B for the Captain E&D reservoir prior to depletion, i.e. the initial stress state, are the same as presented in Fig. 4-8a. The shear capacity distribution throughout the reservoir, after production and after injection, is displayed in Fig. 5-1. No shear failure is predicted throughout the reservoir as the shear capacity remains less than one. Overall, the shear capacity only marginally decreases compared to the base case (cf. Fig. 4-8b and c).

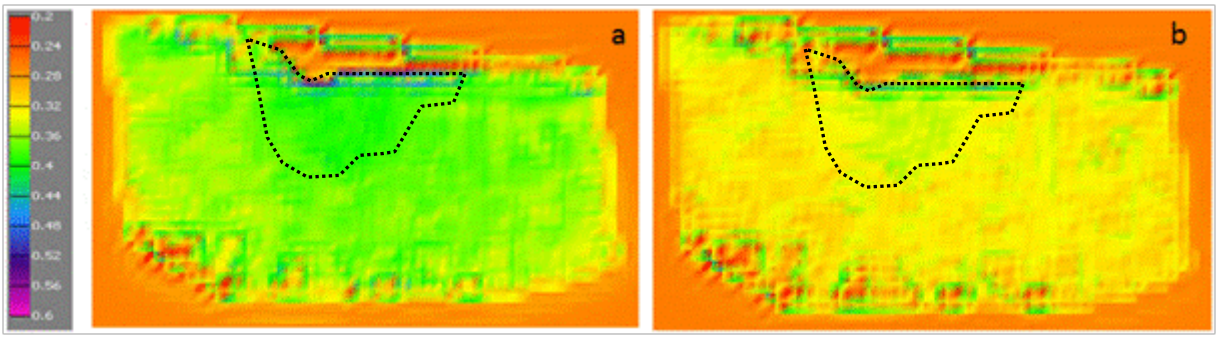

Fig. 5-1—Case B: Map of the shear capacity distribution throughout the Captain E&D formation (a) at the end of production and (b) at the end of injection

Note: colour scale is dimensionless and ranges between 0.2 and 0.62.

5.2. Case C: Poisson's ratio - 0.05

In contrast to Case B, the Poisson's ratio values used in the base case was decreased by 0.05, for each of the three Captain reservoir units, during both gas production and CO_2 injection. This value represented the low-end value of the uncertainty range as seen in the well logs (cf. Fig. 3-11). Changes in total minimum and maximum principal stresses at the point of maximum stress perturbation are summarised in Table 5-4. As for Case B, the predicted stress changes in the Captain E&D reservoir are small compared to the base case, while stress changes in the caprock are equal to the base case.

Table 5-4—Key results for Case C

Case C		Change of pore pressure ΔP [MPa]	Change of minimum principal stress $\Delta\sigma_3$ [MPa]	Change of maximum principal stress $\Delta\sigma_1$ [MPa]	Maximum SCU (approx)
Reservoir Captain E&D	Initial to production	-10.1	-9.0	-1.2	0.45
	Production to injection	+8.5	+6.2	+0.60	0.38
Rødby Caprock	Initial to production	0.0	-0.48	-0.80	0.45
	Production to injection	0.0	+0.13	+0.42	0.45

For Case C, the distribution of the SCU values throughout the Captain E&D reservoir prior to production (initial state) is the same as that presented in Fig. 4-8a. The shear capacity distributions at the end of gas production and at the end of injection are displayed in Fig. 5-2. As can be seen, the distributions are very similar to those predicted for Case B, with shear capacity values having only marginally increased compared to the base case - see Fig. 4-8b and c. No shear failure of the reservoir is expected, as throughout the entire formation shear capacity < 1.

[2] Note that for clarification, we added approximate field outlines, delineated by the dotted lines, to all map view plots in this chapter.

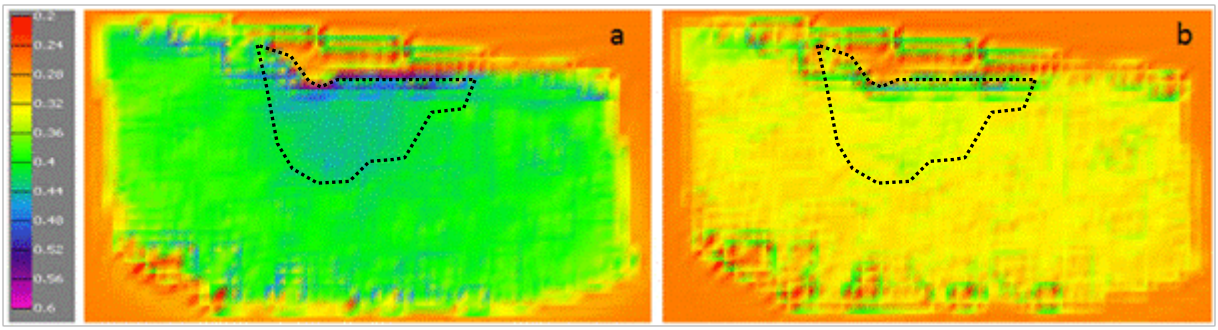

Fig. 5-2—Case C: Map of the shear capacity distribution throughout the Captain E&D formation (a) at the end of production and (b) at the end of injection.

Note: colour scale is dimensionless and ranges between 0.2 and 0.6.

5.3. Case D: Young's Modulus value divided by half for the over- and underburden formations

For Case D, the effect of decreasing the Young's modulus values for the over- and underburden formations, as used in the base case, by 50%, during both the production and the injection phases is explored. These Young's Modulus values represent the low-end value in the uncertainty range, as seen on the well logs (Fig. 3-11). For the point of maximum stress perturbation, the changes in total minimum and maximum principal stresses are summarised in Table 5-5. As can be seen, the maximum stress changes in the Captain E&D reservoir and the Rødby Shale caprock are small compared to the base case.

Table 5-5—Key results for Case D

Case D		Change of pore pressure ΔP [MPa]	Change of minimum principal stress $\Delta\sigma_3$ [MPa]	Change of maximum principal stress $\Delta\sigma_1$ [MPa]	Maximum SCU (approx)
Reservoir Captain E&D	Initial to production	-10.1	-8.2	-0.62	0.43
	Production to injection	+8.5	+5.3	+0.35	0.36
Rødby Caprock	Initial to production	0	±0.25	-0.6	0.44
	Production to injection	0	0	+0.23	0.44

For the stress state prior to production, the SCU values and their distribution for Case D are the same as for base case A (Fig. 4-8a). For the stress states after production and injection, the distributions are displayed in Fig. 5-3a and b, respectively. The shear capacity values within the reservoir are marginally changed as a result of the change in Young's Modulus in the over- and underburden, compared to the base case (cf. Fig. 4-8b and c).

Additionally, the shear capacity values and distribution for the Rødby Shale caprock are analysed. Similar to the Captain E&D reservoir, the initial state of stress shows the same distribution as that presented in Fig. 4-17 for base case A. The shear capacity distributions at the end of production and

at the end of injection are displayed in Fig. 5-4. As can be seen, shear capacity is only marginally decreased compared to the base case (Fig. 4-17b and c), and hence no shear failure is expected as shear capacity remains well below one.

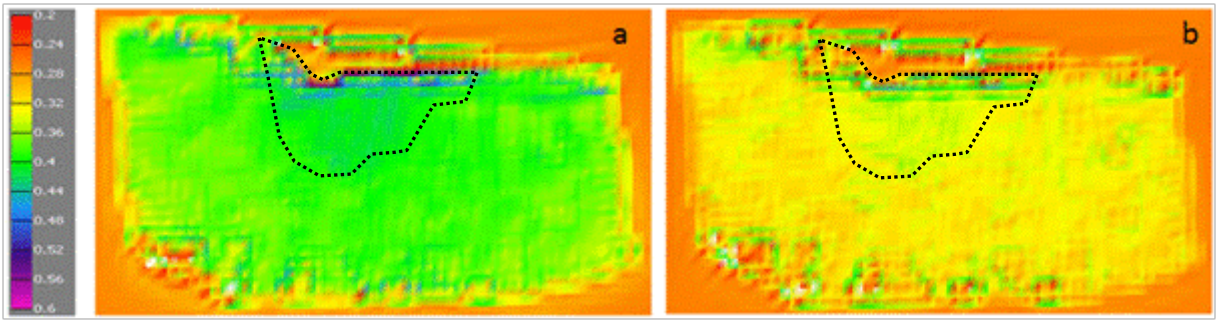

Fig. 5-3—Case D: Map of shear capacity distribution within the Captain E&D formation (a) at the end of production and (b) at the end of injection.

Note: colour scale is dimensionless and ranges between 0.2 and 0.6.

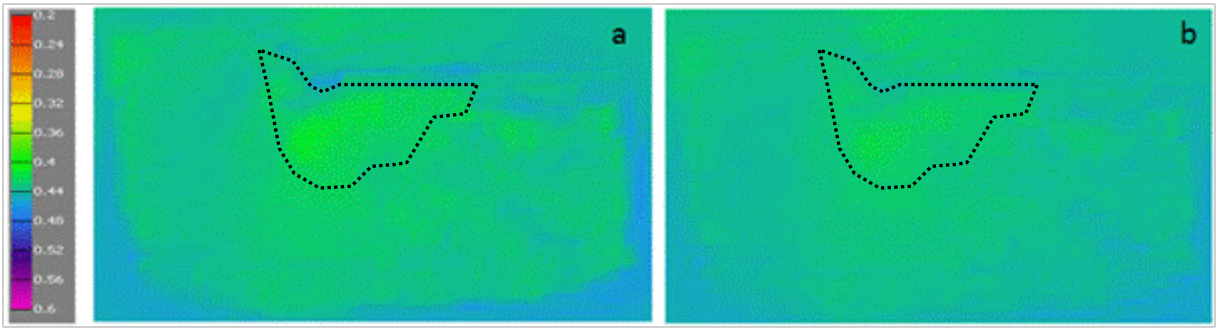

Fig. 5-4—Case D: Map of the shear capacity distribution within the caprock formation (Rødby Shale) (a) at the end of production and (b) at the end of injection.

Note: colour scale is dimensionless and ranges between 0.2 and 0.6.

5.4. Case E: worst case scenario rock failure parameters for reservoir and caprock

For sensitivity analysis Case E, the pressure and stress changes as predicted for the base case are employed, but the rock failure properties are varied. Cohesion and friction angle are changed to the worst case scenario values for both the Captain E&D reservoirs and the caprock. The key results and the main observations for both formations are summarised in

Table **5-6** and described in the following two sections. As the elastic parameters are still the same as those for Case A, no change in stress response is predicted. However, the lowering of the input values for the failure parameters, i.e. implicitly representing a weaker rock, means a change in the maximum shear capacity τ_{max}, and hence the shear capacity SCU = τ/τ_{max}, as the failure line moves down in the Mohr-Coulomb stress space.

Table 5-6—Key results for Case E

Case E	Change of pore pressure	Change of minimum principal	Change of maximum principal	Maximum SCU

		ΔP [MPa]	stress $\Delta\sigma_3$ [MPa]	stress $\Delta\sigma_1$ [MPa]	(approx)
Reservoir Captain E&D	Initial to production	-10.1	-8.2	-0.5	0.81
	Production to injection	+8.5	+5.2	+0.2	0.71
Rødby Caprock	Initial to production	0.0	+0.1	0.0	0.90
	Production to injection	0.0	-0.1	0.0	0.90

5.4.1. Reservoir formation (Captain E&D)

For this scenario case, the reservoir formation is assumed to be *unconsolidated*, i.e. have a cohesion of zero and a friction angle of 20°. The reservoir cores show that the Captain E&D are **not** unconsolidated so this must be viewed as test scenario: these low values are considered to represent the worst case failure scenario for the Captain reservoir. The effect of the change in failure parameters on SCU can be seen when comparing Case E (Fig. 5-5) to Case A (Fig. 4-7).

An overview of the shear capacity distribution throughout the Captain E&D reservoir is displayed in Fig. 5-6. Note that the observed high values at the boundary and outside of the defined area of interest are an effect of unrealistic jumps in the material properties within the reservoir model. These are an artefact resulting from missing data combined with the GeoMec extrapolation algorithm, and should therefore be ignored. As expected, the shear capacity increases when going from the initial, equilibrium state of stress to the stress state at the end of production, and decreases again going to the stress state at the end of injection. Shear capacity values for the location with the largest stress perturbations in the area of interest are on the order of 0.71 to 0.81 (Table 5-6). As these values are well below one, no shear failure of the reservoir is expected during the depletion and injection phases.

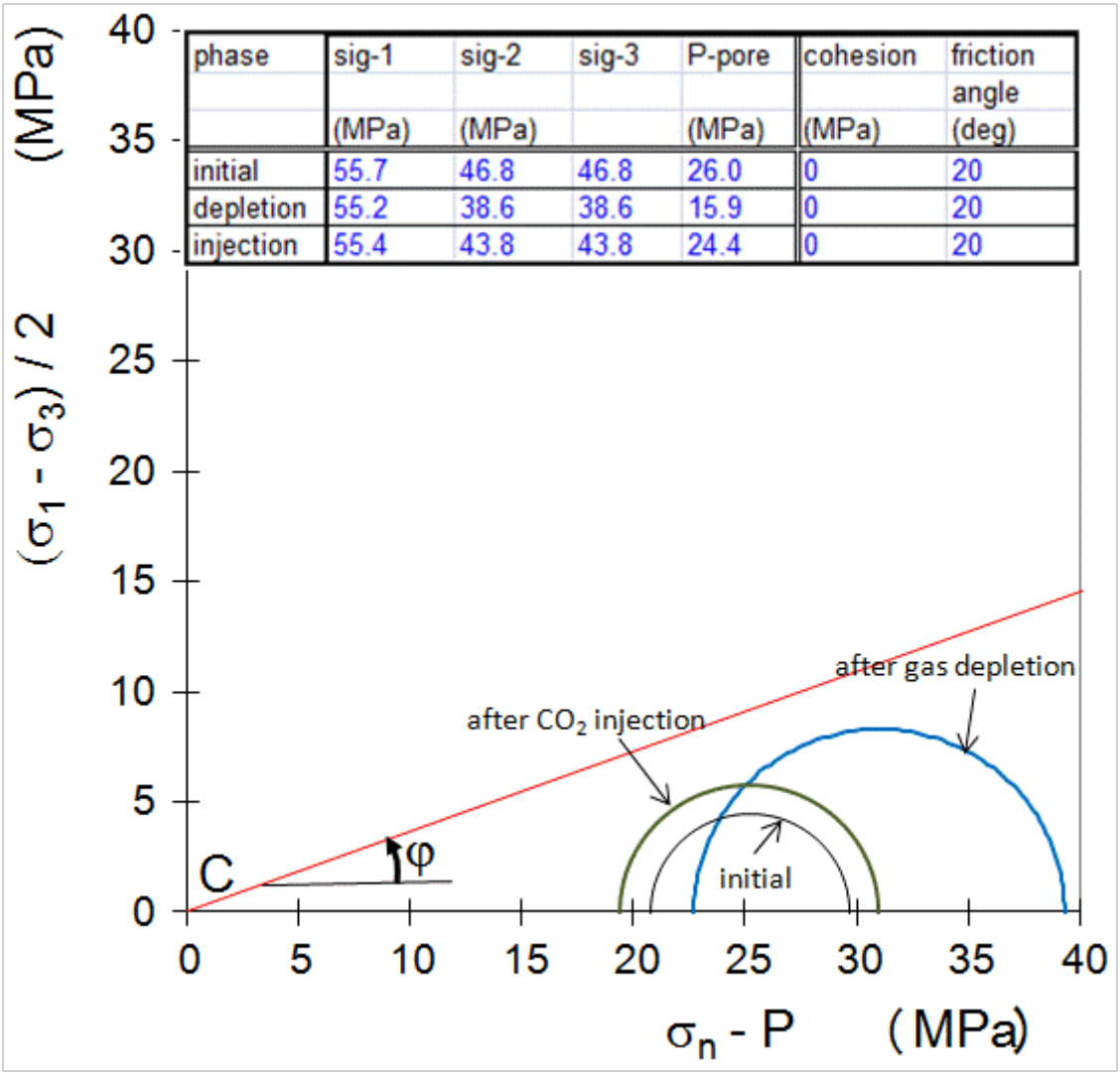

Fig. 5-5—Case E: Mohr-Coulomb failure line for the Captain E&D formation

Note: assuming a worst case failure scenario, and Mohr circles representing the initial state of stress, the state of stress after gas production, and the state of stress after CO_2 injection.

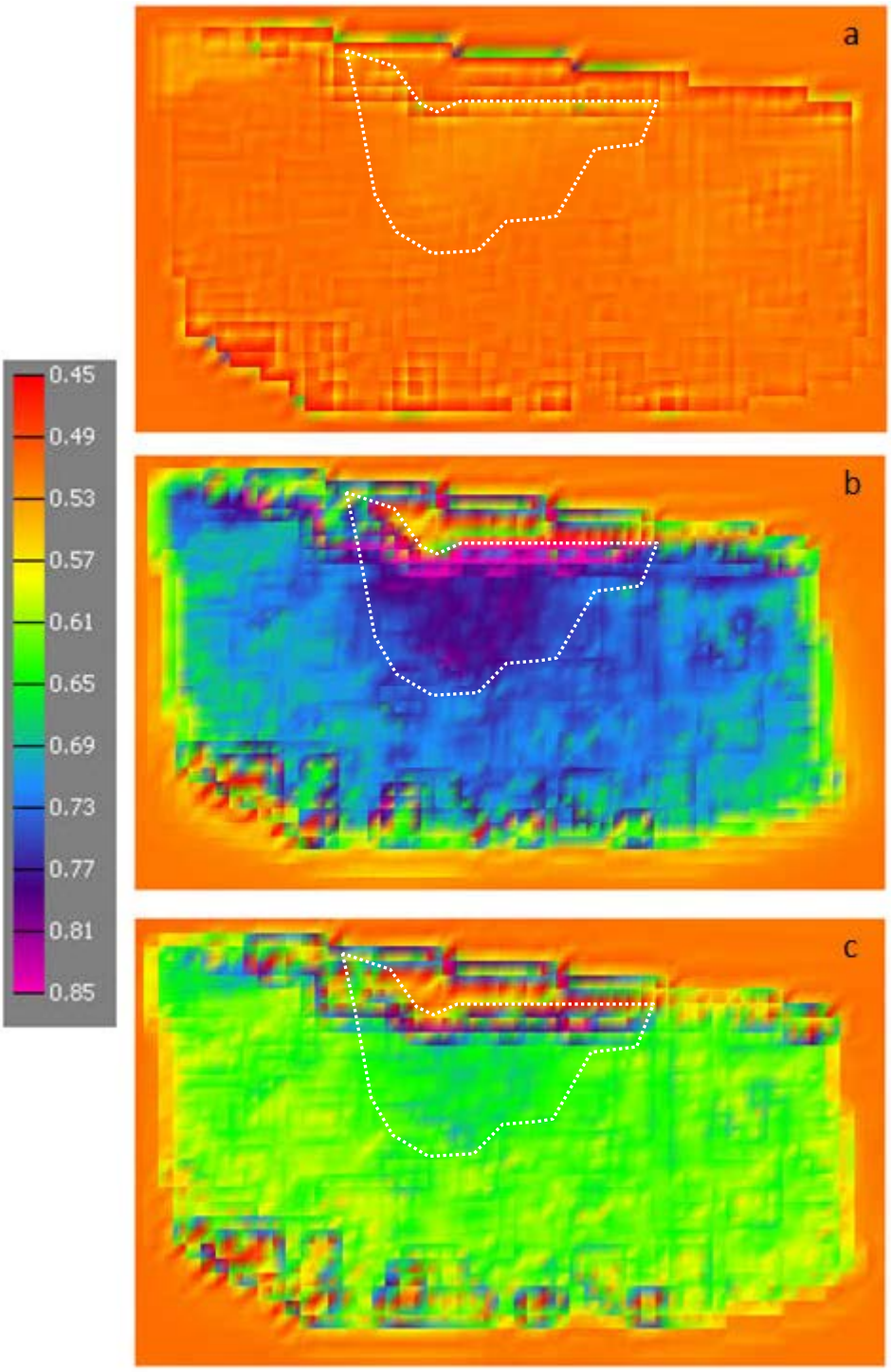

Fig. 5-6—Case E: Distribution map of the shear capacity values within the Captain E&D, assuming extreme worst case scenario failure parameters, i.e. a very weak, unconsolidated sandstone reservoir

Note: (a) prior to production, (b) at the end of production, and (c) at the end of injection. Colour scale is dimensionless and ranges between 0.45 and 0.85.

5.4.2. Caprock (Rødby Shale)

Similar to the reservoir, the values of the failure parameters of the caprock were reduced to consider an extreme worst case failure scenario, i.e. an unconsolidated shale caprock with a cohesion of zero and a friction angle of 13°. Again it must be stressed that the cores of the caprock do not show unconsolidated shale. The effect of this imposed material weakening on the maximum shear capacity and SCU value is shown in Fig. 5-7 (cf. Fig. 4-16 for comparison). The Mohr circle for the initial state of stress is just below the failure envelope, and does not move significantly by the end of the production phase, or at the end of the injection phase.

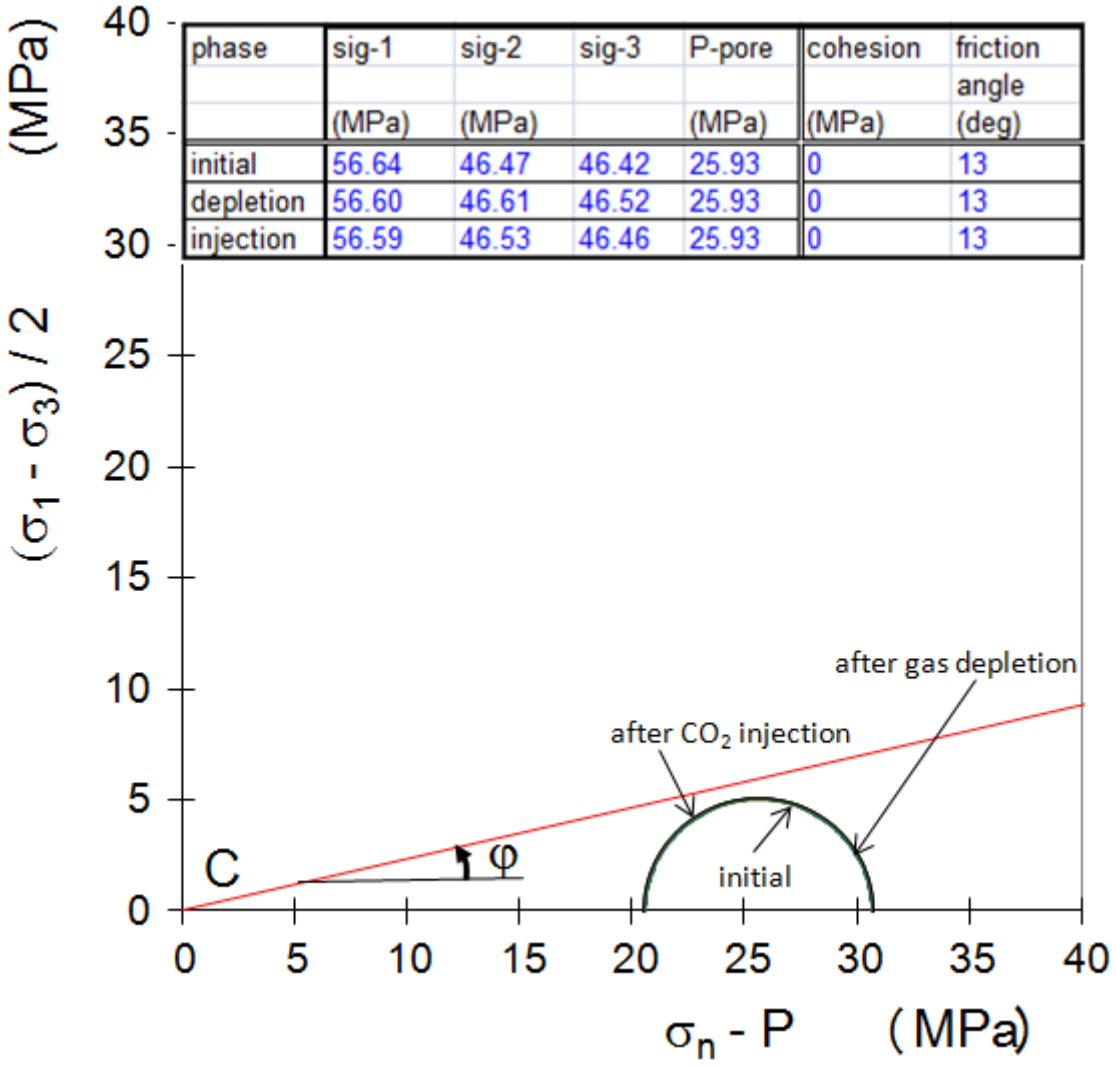

Fig. 5-7—Case E: Mohr-Coulomb failure line for caprock, modelled using worst case scenario failure parameters. In addition, Mohr circles are shown for the initial state of stress, the state of stress after production, and the state of stress after injection.

Note that all three circles are on top of each other, as the individual stress differences are small.

The distribution of shear capacity within the caprock is displayed in **Fig. 5-8**, assuming the above stated worst case scenario failure rock properties, i.e. representing a weak, unconsolidated shake, going from the initial state of stress, to the end of production and the end of the injection phase. The

maximum shear capacity value predicted within the area of interest is approximately 0.9, which means no shear failure of the caprock is predicted in the extreme worst case scenario.

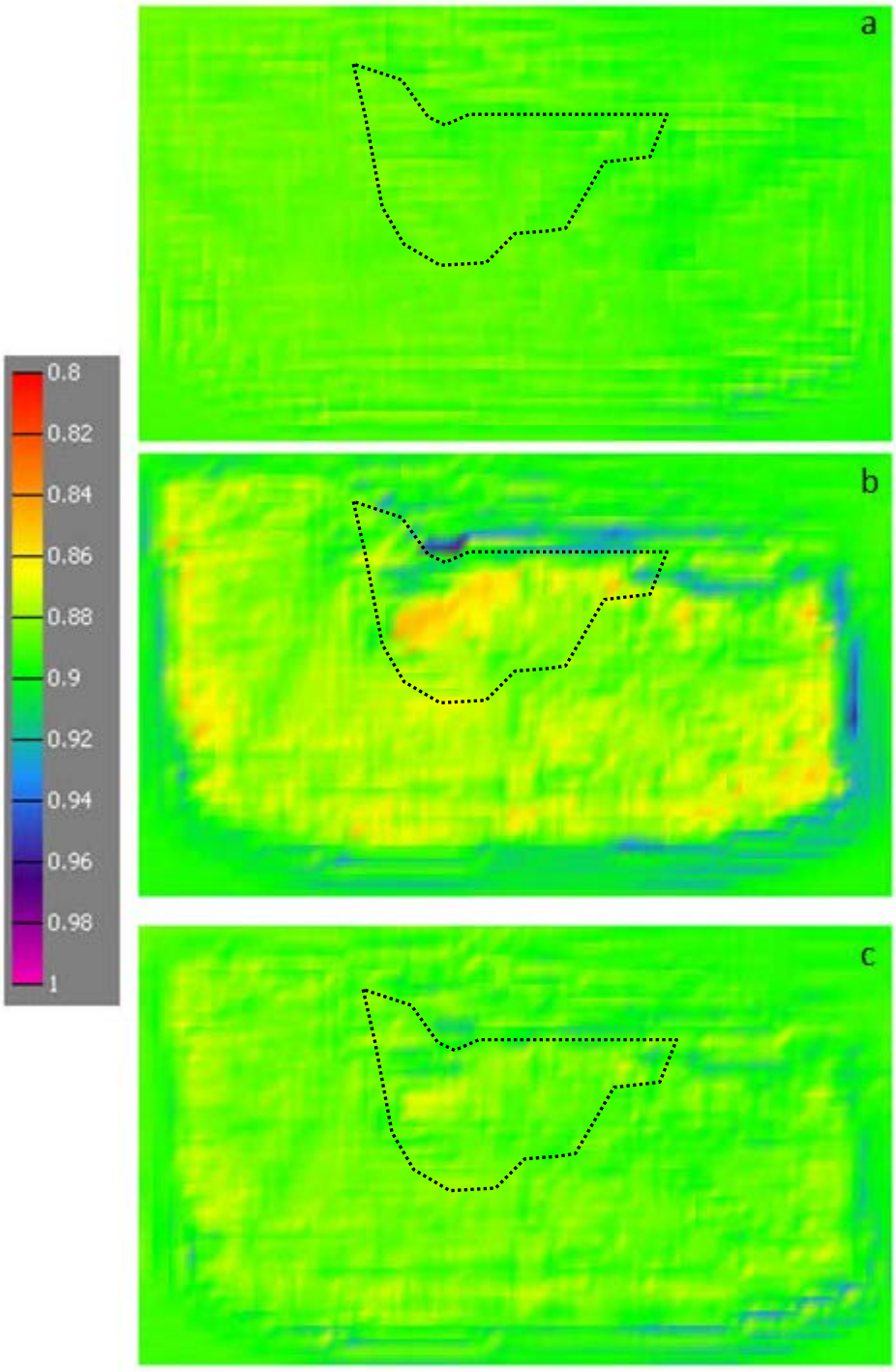

Fig. 5-8—Case E: Map of the shear capacity distribution throughout the caprock formation, assuming extreme worst case scenario failure parameters for essentially unconsolidated shale.

Note: shear capacity values are predicted for (a) the initial stress state, (b) the state of stress after production, and (c) the state of stress after injection. Colour scale is dimensionless and ranges between 0.8 and 1.

5.5. Case F: worst case scenario failure parameters (case e) plus different stress path during the injection phase

The effect of changing the stress path during injection was investigated, compared to the base case A, on stress changes in the reservoirs and caprock. This change in stress path was achieved by changing the Young's modulus and Poisson's ratio for all three Captain reservoirs during the injection phase. Therefore, the Young's modulus values were set to 6.5, 35, and 14.5 GPa for the Captain E&D, C, and A reservoirs respectively, while the Poisson's ratio is made equal to 0.45 for all three reservoirs. Changing the elastic response of the reservoir to a change in stress essentially reduced the γ_h, mimicking the effect of stress hysteresis. The predicted effects on principal stress changes and SCU are presented in Table 5-7, for both Captain E&D and the caprock.

For an increase in pore pressure of 8.5 MPa during the injection phase the minimum total principal stress is increased by 1.6 MPa; so, gamma horizontal becomes 0.19 (1.6/8.5). Gamma vertical becomes 0.01 (0.1/8.5) since the maximum total principal stress for this injection case is increased by 0.1 MPa. Comparing this with the values for the gamma of the base case during injection (see section 4.4 it is seen that gamma horizontal has decreased a lot (from 0.61 to 0.19) and the gamma vertical has a small decrease (from 0.02 to 0.01). Therefore it can be concluded that the geomechanical model of Goldeneye is handling hysteresis as described in Section 2.1.3.

Table 5-7—Key results for Case F

Case F		Change of pore pressure ΔP [MPa]	Change of minimum principal stress $\Delta\sigma_3$ [MPa]	Change of maximum principal stress $\Delta\sigma_1$ [MPa]	Maximum SCU (approx)
Reservoir Captain E&D	Initial to production	-10.1	-8.2	-0.5	0.81
	Production to injection	+8.5	+1.6	+0.1	0.97
Rødby Caprock	Initial to production	0	+0.1	0	0.90
	Production to injection	0	+0.12	+0.29	0.92

The failure parameters of the reservoir are taken as the extreme worst case situation, i.e. zero cohesion and a friction angle of 20°. As the initial state of stress and the stress state after production have not changed the Mohr-Coulomb failure analysis plot (Mohr circle and failure line) is equal to the plot in Fig. 5-5. The stress changes during injection are represented by the Mohr circle in Fig. 5-9. As the Mohr circles are below the failure line no shear failure is observed for this scenario.

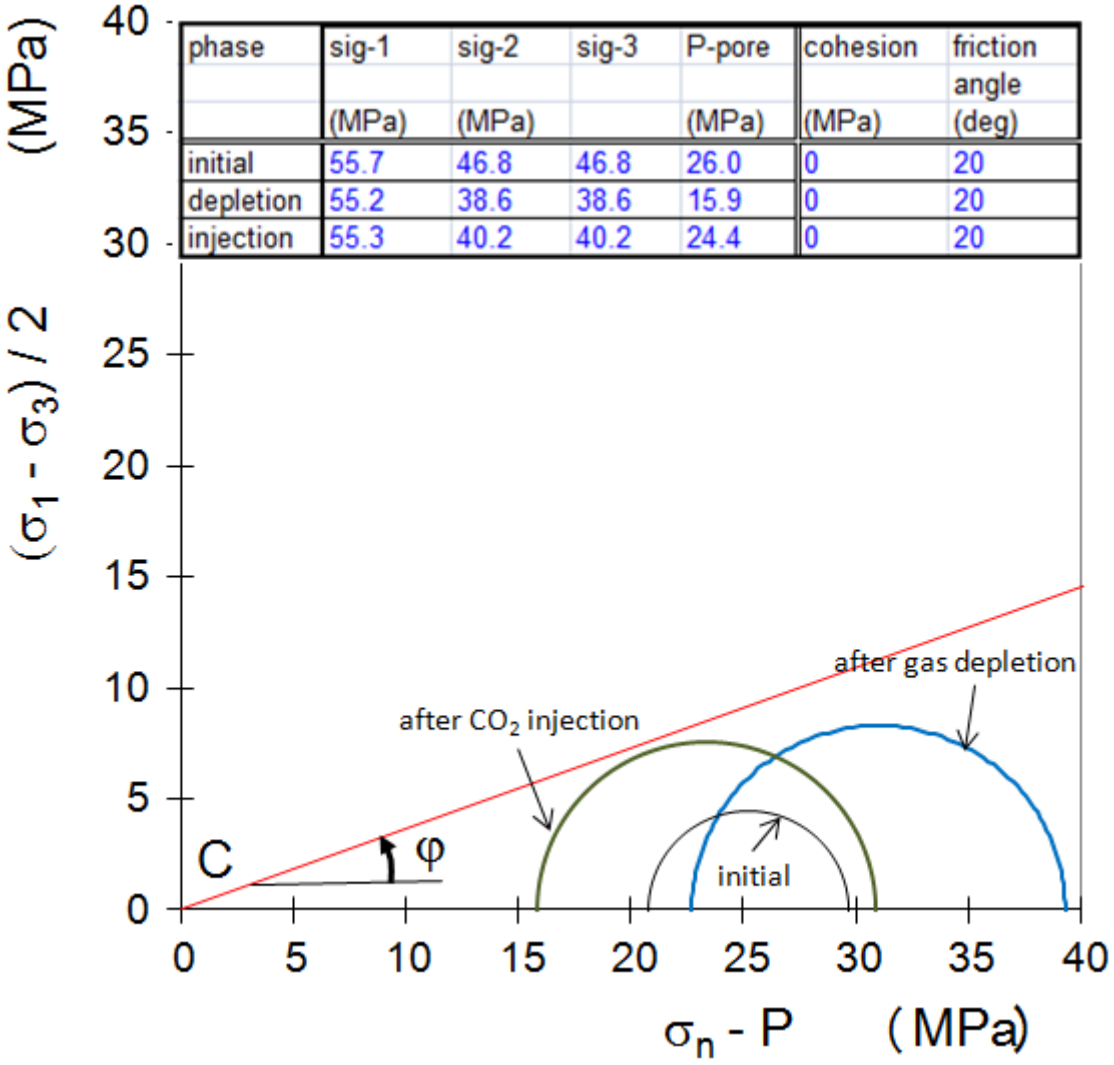

Fig. 5-9—Case F: Mohr-Coulomb failure line for Captain E&D reservoir for a worst case scenario represented by rock failure parameters representing an unconsolidated sandstone reservoir. Mohr circles represent the different stress states prior to depletion, at the end of production and at the end of injection.

Note that the stress path during the injection phase differs from the stress path of the base case (Case A).

As for this case no changes have been made to the initial stress state and the state of stress at the end of production, the distribution of the shear capacity values throughout the reservoir formation are the same as those for Case E, as seen in Fig. 5-6a and b. In contrast, the SCU values at the end of the injection phase have changed and are displayed in Fig. 5-10. At the point of maximum stress perturbation, a maximum shear capacity of 0.97 is predicted. These results demonstrate that the effect of stress hysteresis does not lead to shear failure issues within the reservoir formation, even in an extreme worst case scenario.

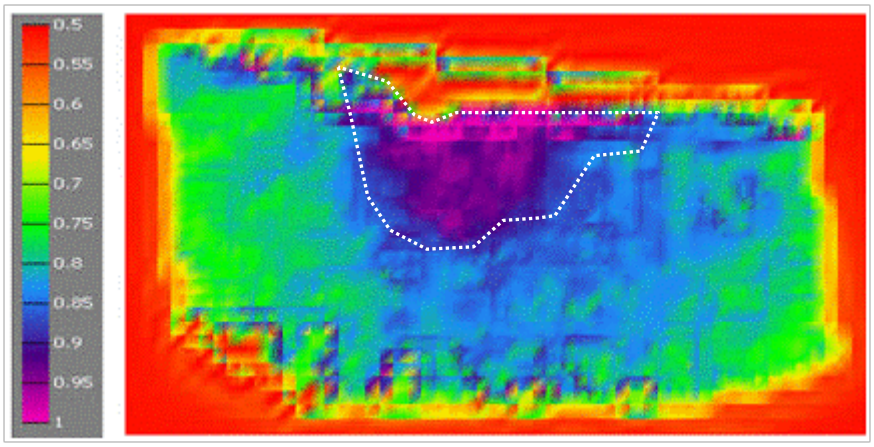

Fig. 5-10—Case F: Map of shear capacity values throughout the Captain E&D formation at the end of the injection phase, assuming extreme worst case scenario rock failure parameters for the reservoir rock.

Note that the stress path during the injection phase differs from the stress path of the base case (Case A). Colour scale is dimensionless and ranges between 0.5 and 1.

Furthermore, it can be concluded that significantly decreasing the values for Young's Modulus and nearly doubling Poisson's Ratio for the three reservoirs, for the CO_2 injection stage, did not lead to noticeable stress changes in the caprock. Therefore, results for the caprock are equal to the scenario that was discussed in Case E (Section 0) and was displayed in Fig. 5-8.

5.6. Case G: pressure support from the aquifer, plus worst case scenario rock failure parameters for reservoir and caprock

The reservoir pressures provided to GeoMec, as described in the previous cases, are supplied by the FFM. In this model, the pressure support from the aquifer was modelled analytically as a boundary pressure source at the edge of the FFM. The current section, employs an alternative approach by using an explicit and more accurate aquifer support that was available in the Fairway Aquifer Model (FAM)[3] (59). The FAM has more detail in the modelling of neighbouring field effects, by including the varying levels of pressure support resulting from production in those fields and the invasion of the aquifer into the depleting reservoir. The pressure data from the FAM model extends beyond the perimeter of the Goldeneye reservoir, and even beyond the boundaries of the GeoMec model. So, only a subset of the available data was incorporated into GeoMec model, in order to get aquifer-adjusted pore pressures for all Captain reservoir elements.

Fig. 5-11 illustrates the pressure changes in the Captain E&D reservoir (inside the marked area) and the surrounding aquifer due to gas production, when aquifer support is accounted for. Note that the maximum drawdown pressure of 10.9 MPa [1580 psia] is only slightly higher than without explicit aquifer support (10.1 MPa, cf. Fig. 4-3). In addition, Fig. 5-12 illustrates the pressure changes in the Captain E&D reservoir (marked area) and the aquifer due to CO_2 injection. The maximum injection

[3] Note that this is version 1 of the FAM. A history match update to this model was made in 2014 after receipt of new data on neighbouring fields from DECC and the collection of two years of additional data from the Goldeneye field. The effect of this update was to slightly weaken the aquifer recharge over long time periods. The effect of these changes on the geomechanical analysis would be expected to be negligible.

pressure increase of 9.6 MPa [1400 psia] is slightly higher than without explicit aquifer support (8.5 MPa [1233 psia], cf. Fig. 4-12).

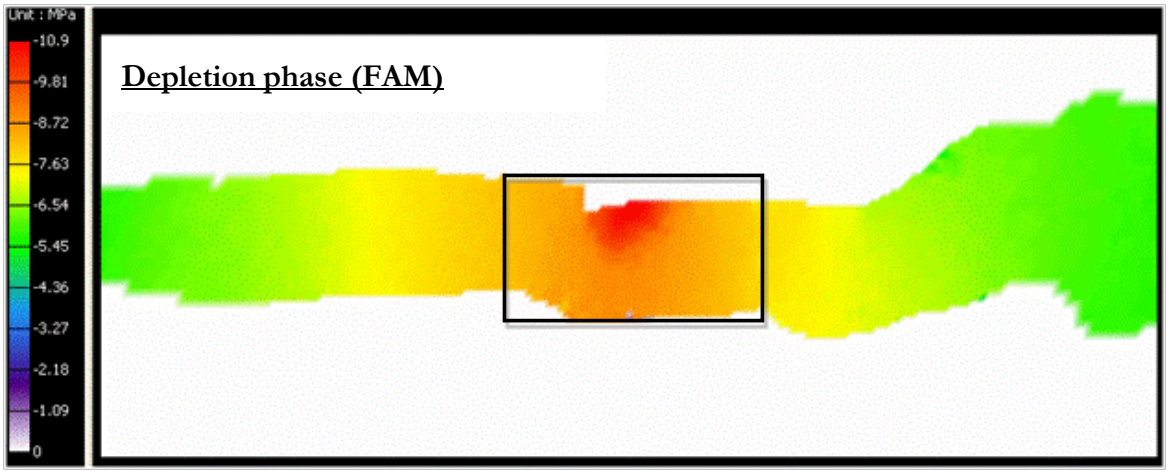

Fig. 5-11—Case G: Top view map of pressure changes in the Captain E&D reservoir (marked area) and the surrounding aquifer due to gas production, accounting for aquifer support.

Note: scale is between -10.9 and 0 MPa [-1581 and 0 psia].

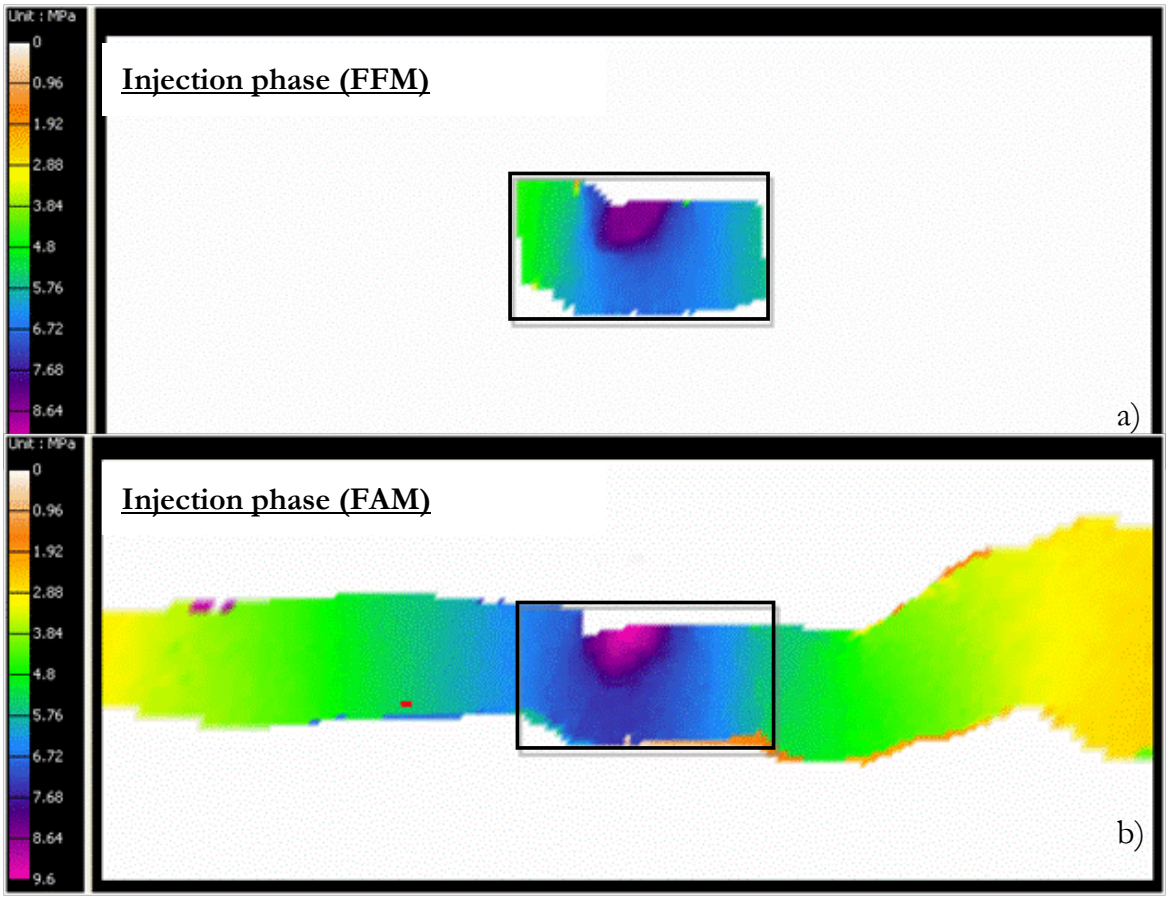

Fig. 5-12—Case G: Top view map of pressure changes in (a) solely the Captain E&D reservoir (marked area), assuming no aquifer support, and (b) the Captain E&D reservoir plus surrounding aquifer, accounting for aquifer support.

Note: scale is between 0 and 9.6 MPa [0 and 1392 psia]. In Case A, the maximum injection pressure is 8.5 MPa [1233 psia], while for Case G the reservoir pressure increases to 9.6 MPa [1392 psia], as a result of aquifer support.

The predicted principal stress changes and shear capacity values, assuming the worst case scenario failure parameters, for Case G are presented in Table 5-8.

Table 5-8—Key results for Case G

Case G		Change of pore pressure ΔP [MPa]	Change of minimum principal stress $\Delta\sigma_3$ [MPa]	Change of maximum principal stress $\Delta\sigma_1$ [MPa]	Max SCU (approx)
Reservoir Captain E&D	Initial to production	-10.4	- 8.8	- 0.34	0.82
	Production to injection	+9.0	+ 5.6	+ 0.09	0.71
Rødby Caprock	Initial to production	0	- 0.12	+ 0.10	0.91
	Production to injection	0	- 0.06	- 0.04	0.90

The distribution of the shear capacity values throughout the Captain E&D reservoir and the Rødby Shale caprock are shown in Fig. 5-13 and Fig. 5-14, respectively. As above, the observed high values at the boundary and outside of the defined area of interest are an effect of unrealistic jumps in the material properties within the reservoir model. These results should be ignored as they are merely an artefact resulting from missing data combined with the GeoMec extrapolation algorithm.

Comparing these results (Fig. 5-13 and Fig. 5-14) to Case E (Fig. 5-6 and Fig. 5-8) suggests that there are no significant differences for the shear capacity distribution between the model where the aquifer pressure support was modelled analytically (Case E) and that where it was modelled numerically (Case G). As such, shear capacity values based on pressure data from the FAM are consistent with those based on pressure data of the FFM.

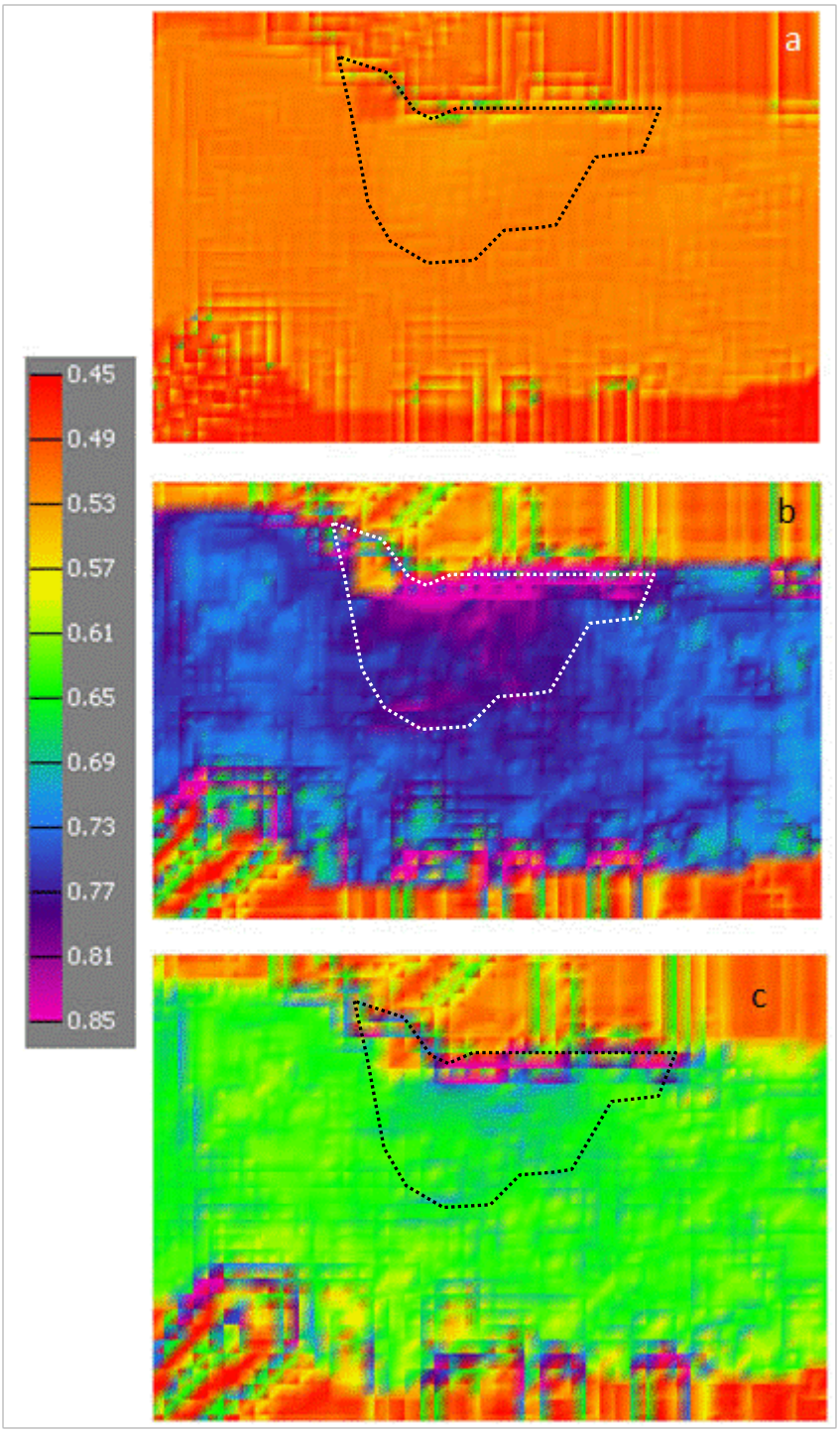

Fig. 5-13—Case G: Distribution map of the shear capacity values for Captain E&D formation (a) for the initial stress state, (b) for the stress state after production, and (c) for the stress state after injection.

Note: support from the aquifer pressure is accounted for and worst case scenario failure parameters were used. Colour scale is dimensionless and ranges between 0.45 and 0.85.

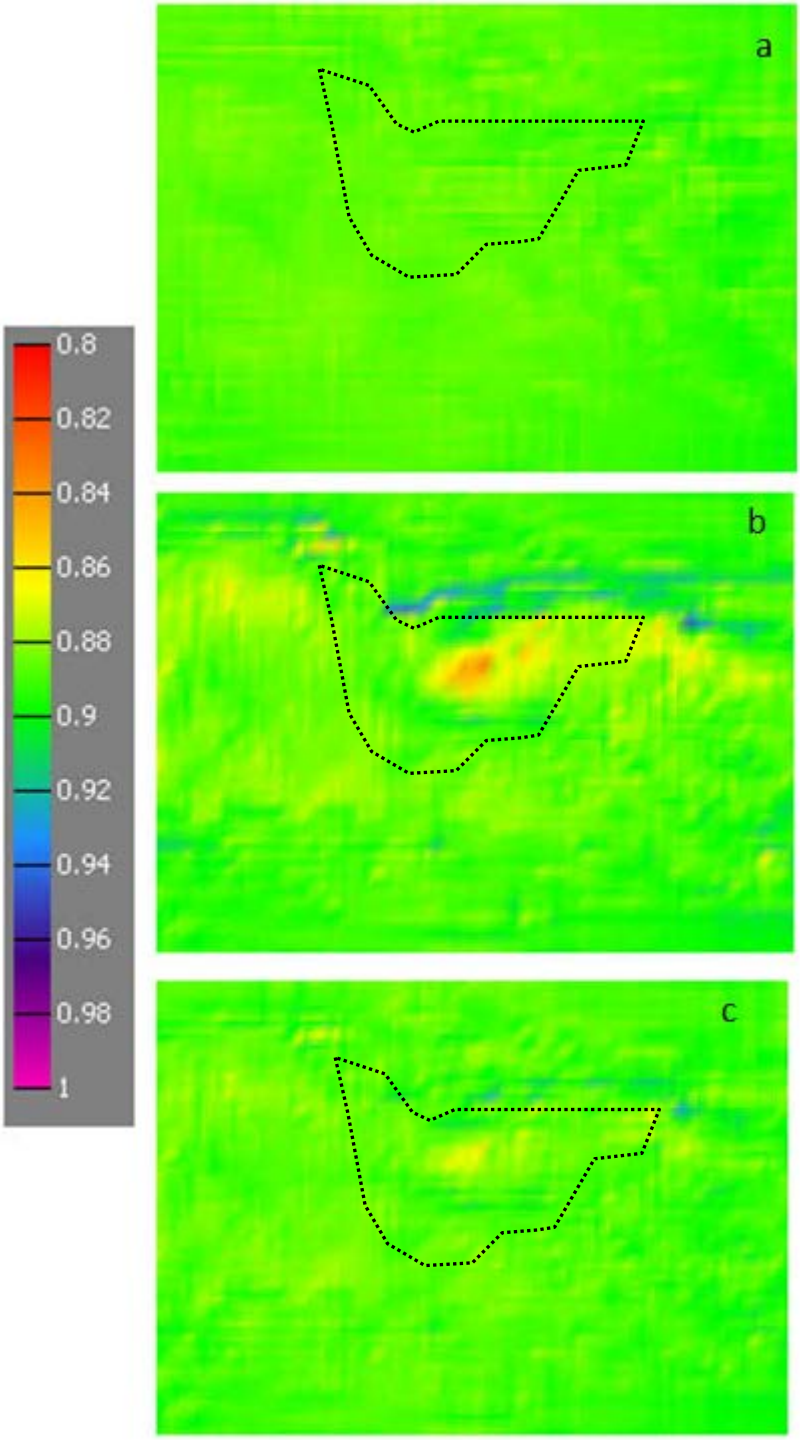

Fig. 5-14—Case G: Map of shear capacity values throughout the caprock formation (a) prior to depletion, (b) at the end of production, and (c) at the end of the injection phase.

Note: corrections were made for aquifer support, while worst case scenario failure parameters were assumed. Colour scale is dimensionless and ranges here between 0.8 and 1.

5.7. Case H: injection pressure > hydrostatic pressure, plus worst case scenario rock failure parameters for reservoir and caprock

This case investigates the risk of rock failure of the reservoir and/or caprock, for the case where the maximum downhole injection pressure is above the original pressure (see section 3.2.4 and Fig. 3-9). This section discusses the hypothetical case where this difference is assumed to be by an amount of 1.5 MPa [220 psia]. As the aquifer slowly re-pressurises the field, this case is also representative for the long term, after the field has been abandoned, although as CO_2 is denser than hydrocarbon gas the pressure at the crest of the field would, in the long term, always be expected to be lower than the pressure when it held hydrocarbons.

The pressure distribution throughout the reservoir for this increased injection pressure is displayed in Fig. 5-15. Note that this figure is essentially the same as Fig. 4-12, but with pressure values elevated by 2.2 MPa [319 psia], such that the average pressure is increased by 1.5 MPa [218 psia] to 26.6 MPa [3857 psia].

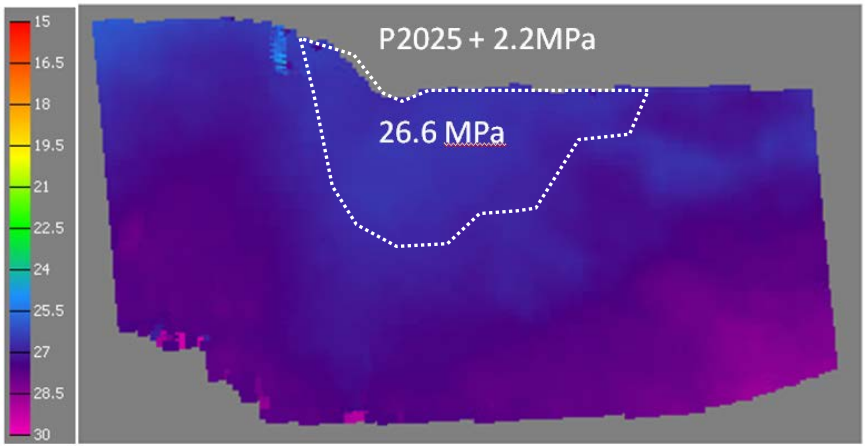

Fig. 5-15—Case H: Distribution map of the injection pressure in the Captain E&D reservoir in 2025.

Note: to the base case scenario, 2.2 MPa [319 psia] is added thereby reaching a level above the original pressure (25.5 MPa [3698 psia] at 2549 m [8363 ft]). Colour scale is in MPa between 15 and 30 MPa [2175 and 4351 psia].

Fig. 5-16 shows the distribution of the difference between the injection pressure and the original pressure.

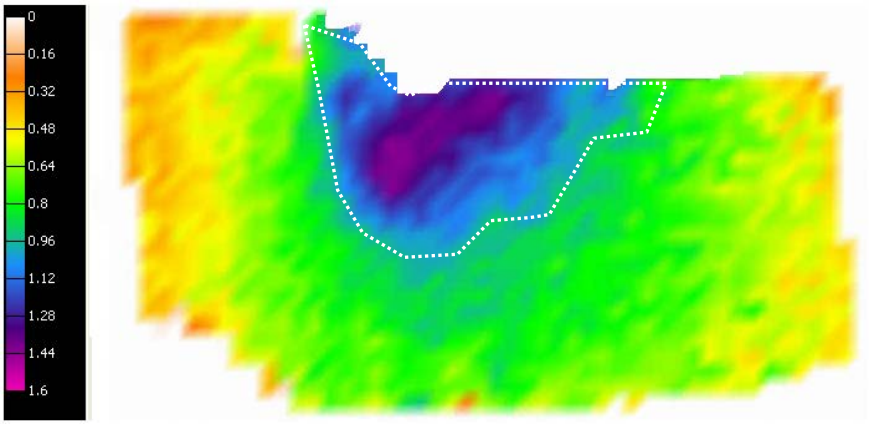

Fig. 5-16—Case H: Map of the pressure difference between the final injection pressure in the Captain E&D reservoir in 2025 and the hydrostatic pressure.

Note: colour scale is in MPa between 0 and 1.6 MPa [0 and 232 psia].

Table 5-9—Key results for Case H

Case H		Change of pore pressure ΔP [MPa]	Change of minimum principal stress $\Delta\sigma_3$ [MPa]	Change of maximum principal stress $\Delta\sigma_1$ [MPa]	Maximum SCU (approx)
Reservoir Captain E&D	Initial to production	-9.4	- 7.8	0.2	0.81
	Production to injection	+10.1	+ 6.4	0.0	0.66
Rødby Caprock	Initial to production	0.0	+ 0.1	0.0	0.90
	Production to injection	0.0	0.0	0.0	0.90

The distribution for the SCU values throughout the Captain E&D reservoir are displayed in Fig. 5-17, assuming a worst case scenario for the failure rock properties input. The observed high values at the boundary and outside of the defined area of interest should be ignored as they are an artefact resulting from unrealistic jumps in the material properties within the reservoir model, caused by missing data combined with the GeoMec extrapolation algorithm. Since the injection pressure in this case is slightly higher than for the base case, the in-situ state of stress is further away from the failure line (cf. Case E in Fig. 5-6c to Fig. 5-17). Shear capacity numbers at a location in the area of interest where these have a maximum value are presented in Table 5-9. The shear capacity values, based on the worst case scenario failure parameters plus an increased maximum injection pressure, at the point of maximum shear capacity changes, for both Captain E&D reservoir and the Rødby Shale caprock are presented in Table 5-9. Note that at this location the pressure changes do not necessarily have to reach a maximum, and that this location is slightly different from the one used for Case E (Table **5-6**). In addition, the shear capacity results predicted throughout the caprock are displayed in Fig. 5-18, again using the worst case scenario failure rock properties. As can be seen, the results are similar to the results presented in Fig. 5-8c. Overall, throughout the reservoir and the caprock, no

shear failure is predicted by an increase in injection pressure, as the shear capacity is below one throughout the entire field.

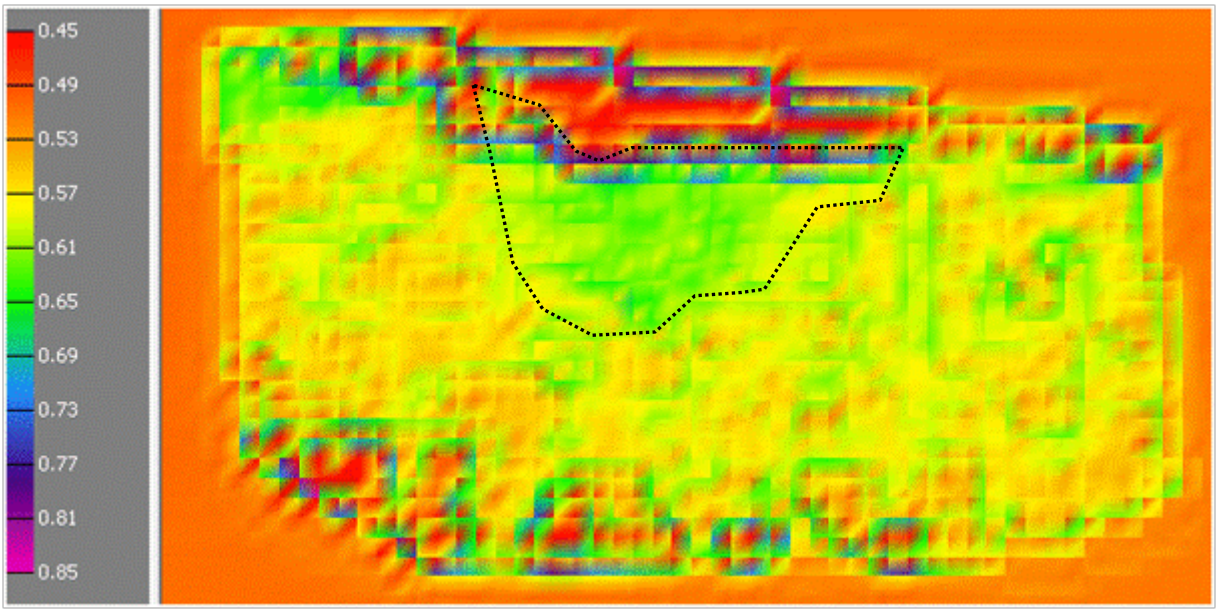

Fig. 5-17—Case H: Map of shear capacity results for Captain E&D reservoir, using the worst case scenario failure parameters, after the injection pressure was increased by 2.2 MPa [319 psia].

Note: colour scale is dimensionless and ranges between 0.45 and 0.85.

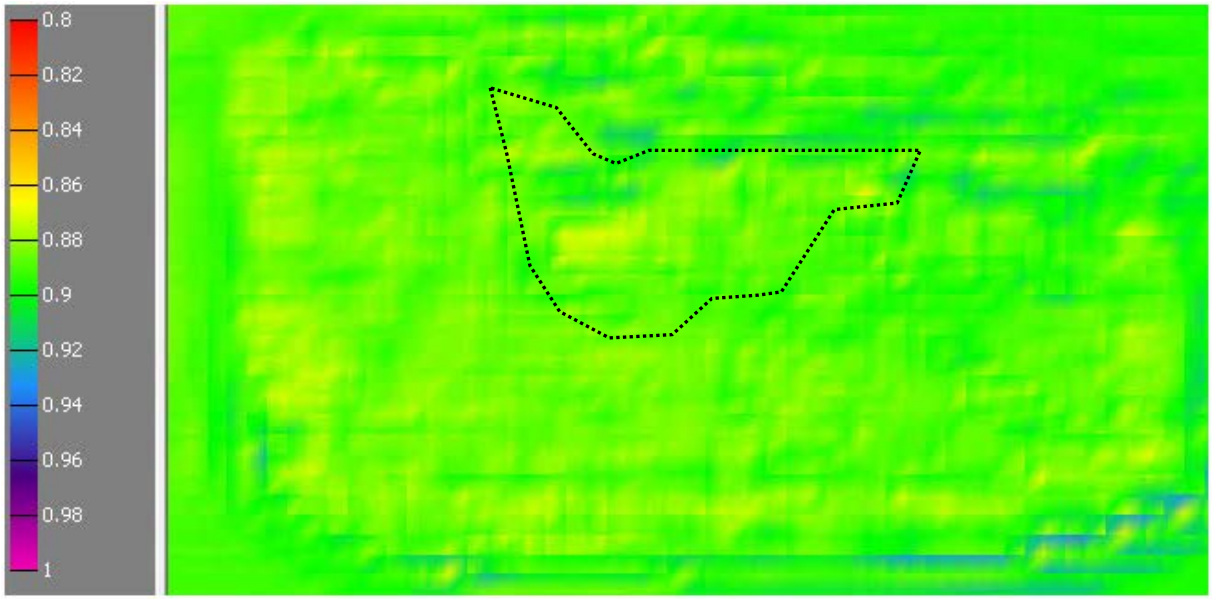

Fig. 5-18—Case H: Map of shear capacity distribution throughout the caprock formation after having injected the reservoir with a pressure that is 1.5 MPa [218 psia] higher than the hydrostatic pressure.

Note that worst case scenario failure parameters were used. Colour scale is dimensionless and ranges between 0.8 and 1.

5.8. Case I: pressure at the end of depletion is assumed to be 13.8 MPa [2000 psia], plus worst case scenario rock failure parameters for reservoir and caprock

The final case study is based on the assumption that the pore pressure at the end of depletion is actually lower than that of the Base case. As a lower pore pressure results in a higher shear stress τ, the value for shear capacity increases. Therefore, the pore pressures in the reservoir as used in the base case (see section 3.2.4) were lowered by 2 MPa [290 psia] to a level where the absolute minimum pressure within the field was 13.8 MPa [2000 psia]. For the shear capacity investigation, the worst case scenario rock failure parameters for the reservoir and caprock are taken.

The pore pressure changes, principal stress changes and SCU values predicted for this scenario are presented in **Table 5-10**, for both Captain E&D reservoir and the Rødby (caprock) Formation. Note that the location where the shear capacity is maximal is not necessarily the point where the absolute pressure is minimal. Predictions were only made for changes within the field when going from the initial stress state to the stress state at the end of production.

Table 5-10—Key results for Case I

Case I		Change of pore pressure ΔP [MPa]	Change of minimum principal stress $\Delta\sigma_3$ [MPa]	Change of maximum principal stress $\Delta\sigma_1$ [MPa]	Maximum SCU (approx)
Reservoir Captain E&D	Initial to production	-11.4	- 9.4	+0.22	0.85
Rødby Caprock	Initial to production	0.0	+0.1	0.0	0.90

Shear capacity predictions, assuming worst case scenario failure parameters for an essentially unconsolidated Captain E&D reservoir and overlying Rødby Shale caprock, are displayed in **Fig. 5-19** and **Fig. 5-20**, respectively. The high values at the border of the reservoir are due to unrealistic jumps in the material properties due to missing data and the GeoMec extrapolation algorithm, and are best to be ignored. It is observed that, for a lower pore pressure of 13.8 MPa [2000 psia] at the end of depletion, the predicted shear capacity values are higher than those for Case E (P_p = 15.8 MPa [2292 psia], worst case scenario failure parameters) as can be seen when comparing to Fig. 5-6b and Fig. 5-8b. In conclusion, no shear failure of either the reservoir or the caprock is predicted as shear capacity remains below one.

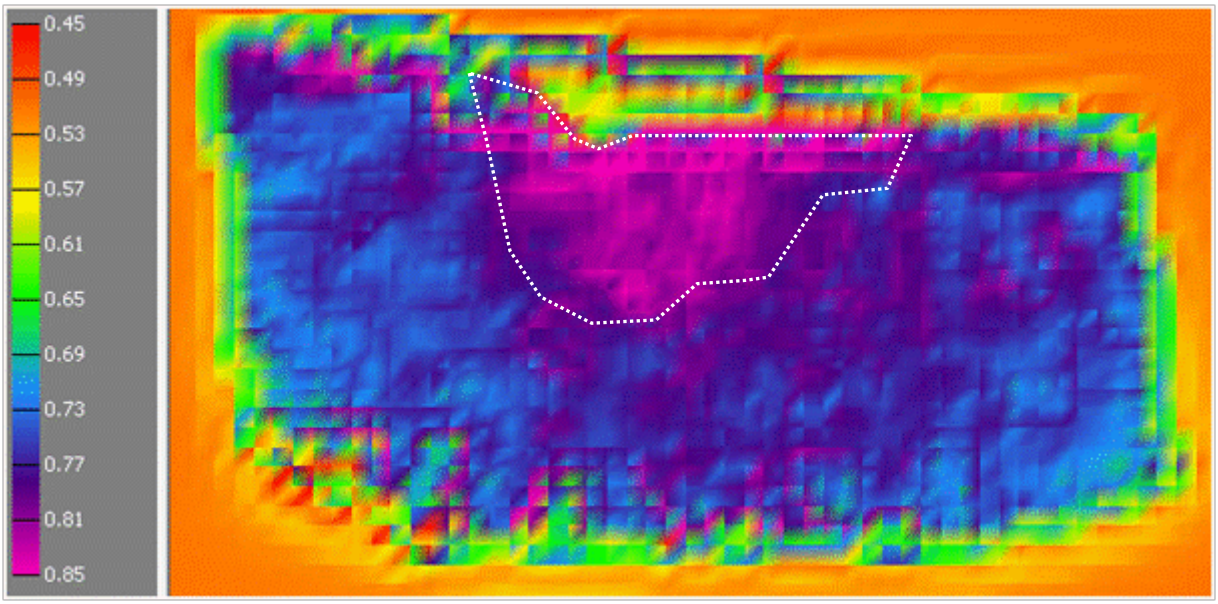

Fig. 5-19—Case I: Distribution map of shear capacity values for Captain E&D reservoir, assuming it consist of unconsolidated sandstone (worst case scenario failure parameters), at the end of the depletion stage, when the minimum pore pressure was 13.8 MPa [2000 psia].

Note: colour scale is dimensionless and ranges between 0.45 and 0.85.

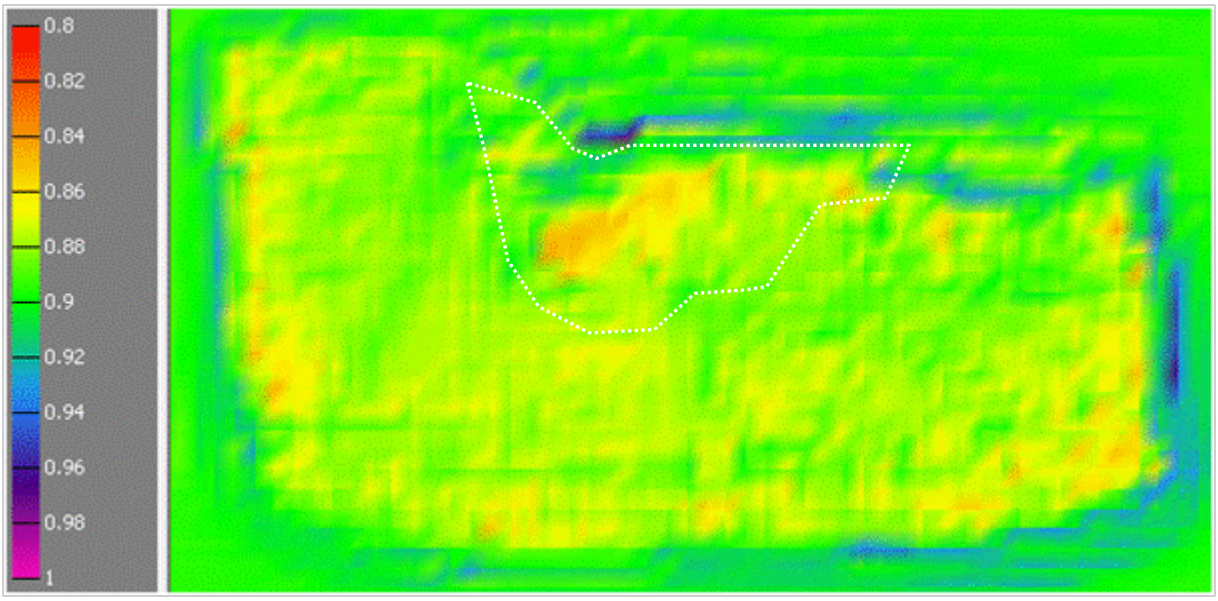

Fig. 5-20—Case I: Distribution map of shear capacity results for the Rødby Shale caprock, assuming worst case scenario failure parameters, after depletion has ended, resulting in a minimum pore pressure of 13.8 MPa [2000 psia] (b).

Note: colour scale is dimensionless and ranges between 0.8 and 1.

6. Impact of cooling on wellbore and caprock integrity

6.1. Introduction

During production, the near wellbore temperature in the reservoir and overburden will be little affected as the fluid temperature is equal to or very close to the formation temperature. This will not be true during CO_2 injection, as the predicted bottom hole temperature of the supercritical CO_2 is 20-25°C, depending on the well configuration, whilst the original reservoir temperature was measured at 83°C (60). At an injection rate of 2 million tonnes of CO_2 per year, the models predict cooling around the injection wells, which then spreads into the reservoir as CO_2 saturation increases and the plume develops. This cooling, resulting from the injection of a colder fluid, will induce stress and strain changes in the reservoir and the overburden. It must be checked to see if these changes have the potential to result in near wellbore or caprock failure. As the density of the supercritical CO_2 is low and the upper injection point is adjacent to the Rødby caprock, the CO_2 plume will most likely reside directly under the Rødby shale caprock; which is to be expected for large-scale structural trapping.

This Chapter investigates the effect of thermal cooling, by the injection of cold CO_2, on stress and strain changes for the vertical wells within the Goldeneye field. In addition to the work presented here, an additional, similar study was performed for the deviated wells (61). In both cases there appears to be a beneficial effect of decreasing temperature, though failure depends on the cohesion of the caprock (cf. Section 3.3.2). For the case of vertical wells, Fig. 6-1 shows the reservoir model prediction of the temperature in the grid block adjacent to the injection well where the cooling to the CO_2 injection temperature for the reservoir volume takes approximately one year.

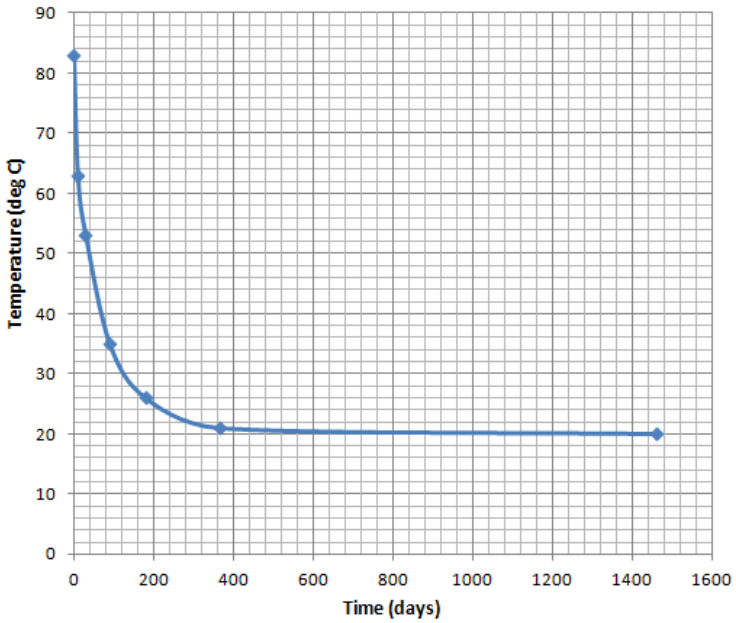

Fig. 6-1:--Reservoir simulation of cooling in the grid block adjacent to injection well.

Note: supercritical CO2 injection temperature = 20°C; reservoir temperature = 83°C.

Firstly, any assessment of thermal fracturing of the caprock in the near wellbore area of the vertical wells needs to take account of the fact that the injection wells have a casing shoe in the caprock (Rødby Formation) and an open annulus in communication with the reservoir below the shoe.

Above the shoe, a separate analysis (35) asserts that the cement provides an adequate seal and the reservoir can be considered isolated from the reservoir. Below this point, this is no longer the case. The shoe is located approximately 10 m [33 ft] above the base of the Rødby Formation, except for Well GYA02S1, and the thickness of the Rødby is approximately 60 m [197 ft] at the injector well locations. The stress changes related to potential near wellbore failure above the shoe are addressed first (Section 6.2.1.1), followed by an analysis of the situation below the shoe (Section 0). In addition the effect of cooling in the farther field reservoir and at the base of the caprock (Section 6.2.2) is investigated.

Secondly, it should be noted that the temperature of the caprock will change, from the base upward, over the 10 year injection period. The modelled temperature diffusion into the Rødby caprock over time is shown in Fig. 6-2. As can be seen, the thermal effect extends tens of metres into the Rødby Formation.

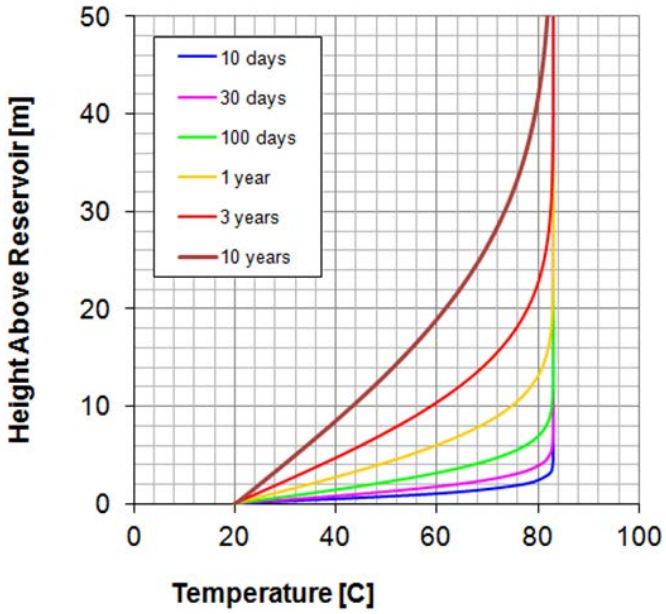

Fig. 6-2—Prediction of cooling by diffusion, over a 10 year period, in the Rødby caprock adjacent to the Captain reservoir

Note: the cooled reservoir temperature is 20°C.

The cooling of the rock by up to 60°C has the potential to generate considerable thermal stresses in the reservoir and caprock, either near the well bore, directly after injection, or with time in the farther field. To demonstrate this, we can make a simple calculation for the thermo-elastic stresses affecting the rock mass under uniaxial strain conditions as:

$$\sigma_t = E.\alpha_t.\Delta T/(1-\nu) \quad (12)$$

Where σ_t is the thermal stress in the lateral direction, E is the Young's modulus, α_t is the linear thermal expansion coefficient, ΔT is temperature change, ν is Poisson's ratio. Table 6-1 gives the calculated thermo-elastic stresses for the Captain Sandstone and the Rødby Shale caprock. These calculations are highly sensitive to the input parameters, as Table 6-1 demonstrates for the Rødby Shale. The first sensitivity (#1) employs a linear thermal expansion coefficient (LTEC) measured on shale of similar age and physical properties to that of the Rødby Formation (62). The second

sensitivity (#2) uses a Young's modulus based on the Shell algorithm for shale properties (static) using the compressional sonic data and surface area data measured on cuttings.

Table 6-1—Thermal stresses due to 60°C cooling of the Goldeneye reservoir and caprock.

Parameter	Captain Sandstone	Rødby Shale Base Case	Rødby Sens #1: α_t	Rødby Sens #2: E
E (GPa)	17	7	7	2
α_t (10^{-5} °C $^{-1}$)	1.0	3.5	1.7	3.5
ν	0.26	0.38	0.38	0.38
Calculated σ_t (MPa)	-13.8	-21.0	-10.2	-6.0

The impact that these thermal stresses have on the in-situ stress and the possibility of failure in the Rødby caprock is shown in **Fig. 6-3**. The minimum principal stress at the base of the Rødby is calculated to be 44.5 MPa [6454 psia] and the temperature is estimated to be 83°C. Using Eq. (13) and the range of input parameters as discussed above, the minimum principal stress (i.e. the approximate fracture pressure) at 23°C to range from 23.5 to 38.5 MPa [3408 to 5584 psia] is calculated. The calculated bottomhole injection pressures for the 10 year injection period are 21.7 to 26.9 MPa [3147 to 3900 psia]. The red region in Fig. 6-3 highlights the area where the injection pressures could be greater than the predicted fracture pressure in the cooled rock and tensile failure could occur. This could result in a hydraulic fracture propagating into the Rødby caprock.

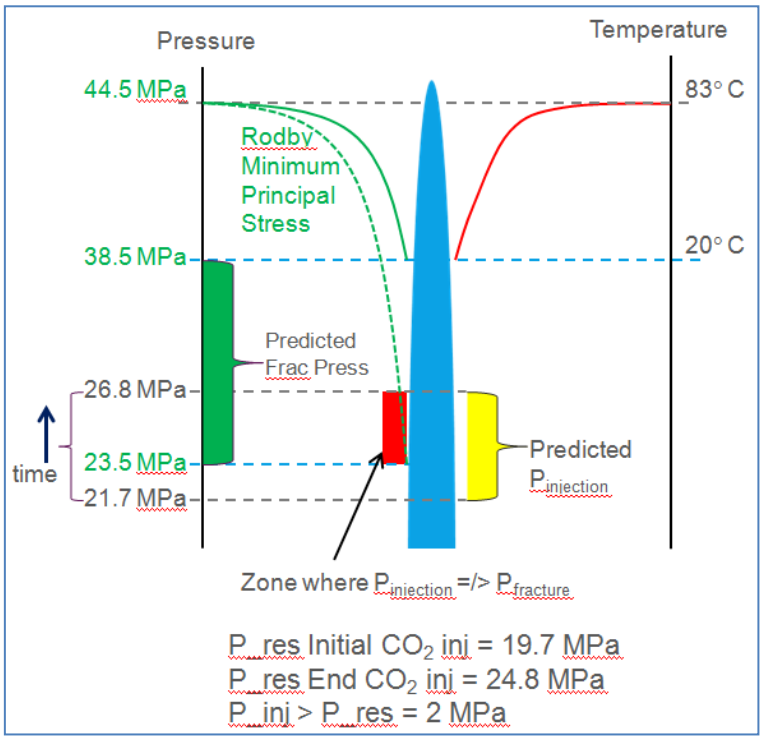

Fig. 6-3—Schematic diagram illustrating the impact of the temperature change on the in-situ stresses and the range of predicted injection pressures

Note: the red zone indicates the pressure range where the predicted fracture pressure and injection pressures coincide.

As is clear from the simple calculations above, the effect of thermal changes on the state of stress, and hence the potential for tensile fracturing, can be significant. However, in order for thermally-induced fracturing to cause leakage of CO_2 out of the reservoir, there are four key conditions that need to be fulfilled:

1) The effect of thermal changes on the state of stress needs to be significant, so that tensile fracturing of the surrounding rock is possible.
2) In order for an initiated fracture to continue propagating, cold CO_2 needs to be continuously replenished at the crack tip, ensuring that the tensile stress state remains.
3) For a propagating fracture to cross an interface, such as the reservoir-caprock interface or bedding planes within the caprock, the stiffness contrast between the two layers cannot be too high; otherwise the fracture will be arrested.
4) Once a fracture of significant extent is formed, it should be sufficiently permeable to serve as a leakage pathway.

Only when all four criteria are met will thermal changes pose an issue for containment and lead to the creation of migration pathways. This Chapter deals with the precise analysis of thermally-driven fracturing in two different cases: 1) in the near wellbore area of the vertical wells, and 2) at the base of the caprock away from the wellbore. All four criteria to assess the likelihood of leakage in each case will be evaluated, as can be seen in Table 6-2.

Table 6-2—Overview of the four key conditions for the different cooling area: 1) near wellbore area, within the cemented region of the caprock ; 2) near wellbore area, within the open hole section of the caprock; and 3) in the farther field of the reservoir and at the base of the caprock. References indicate the sections where each condition will be discussed.

Location	Condition #1: Thermal stress	Condition #2: Replenishment	Condition #3: Interface propagation	Condition #4: Permeability
Near wellbore, cemented region	Section 6.2.1	Section 6.3	Section 6.4	Section 6.5
Near wellbore, open hole	Section 0			
Farther field base of caprock	Section 6.2.2			

6.2. Condition #1: effect of thermal changes on the state of stress

6.2.1. The near wellbore area

As stated earlier, the injection wells have a casing shoe located within the Rødby Shale, while there is an open hole below it. Above the casing shoe, the temperature in the reservoir and caprock formations prior to injection is assumed to be 83°C. Expected temperature profiles as a function of time in the near wellbore region above the casing shoe after injection of 20°C CO_2 are shown in Fig.

6-4. The temperature profiles as a function of time have been derived by a numerical solution to the thermal diffusion equation in cylindrical coordinates which is:

$$\frac{\partial T}{\partial t} = \frac{\kappa_T}{r}\frac{\partial}{\partial r}\left(r\frac{\partial T}{\partial r}\right) \tag{13}$$

Where T is the temperature,

t is the time, and

r is the radius from the axial origin.

The critical input parameter in this equation is the thermal diffusivity, κ_T, and is given by the relation:

$$\kappa_T = \frac{k_T}{\rho\, c} \tag{14}$$

Where k_T is the thermal conductivity,

ρ is the density, and

c is the specific heat.

Typical values have been used for these parameters and are k=1.5 W/(mK), ρ=2100 kg/m^3 and c=900 J/(kgK). Comparison of these calculations to an analytical approximation of the diffusive temperature profile (63) is favourable (see Fig. 6-4). As one can see, the most significant temperature changes happen within 5m of the well even after four years of injection.

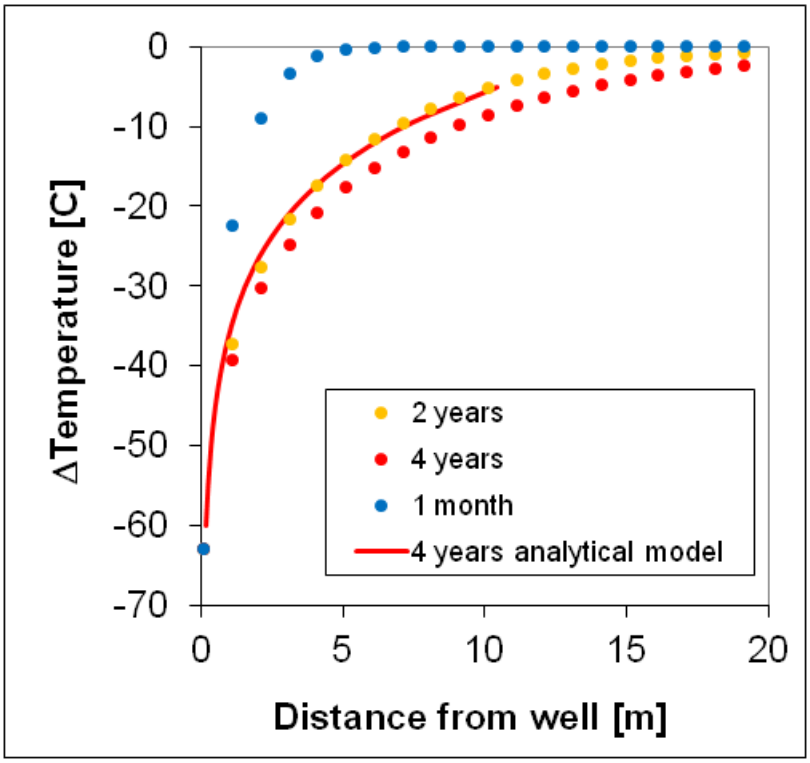

Fig. 6-4—Near wellbore temperature profiles as a function of time

Note: dotted lines represent numerical solutions to the diffusion equation. Solid line is an approximate analytical solution to the diffusion problem for comparison.

For materials in the subsurface, the temperature distribution is independent of the pore pressure distribution. The pore pressure distribution can be derived assuming diffusive flow and a coupling with the temperature distribution (64), *i.e.*,

$$\frac{\partial p}{\partial t} = \frac{\kappa_p}{r}\frac{\partial}{\partial r}\left(r\frac{\partial p}{\partial r}\right) + c'\frac{\partial T}{\partial t} \tag{15}$$

Where κ_p is the hydraulic diffusivity that can be expressed as

$$\kappa_p = \frac{k}{\eta}\left(\frac{\varphi}{K_f} + \frac{b-\varphi}{K_s} + \frac{b^2}{K_{fr} + \frac{4}{3}G_{fr}}\right)^{-1} \tag{16}$$

where k is the permeability,

η is the viscosity,

K_f is the fluid bulk modulus,

K_{fr} is the frame bulk modulus,

K_s is the grain bulk modulus,

b is the Biot constant,

G_{fr} is the frame shear modulus, and

φ is the porosity.

Typical values used here are k=1-10 nD, η= 1cp, K_f =2.6 GPa, K_{fr} =1.6 GPa, K_s =37 GPa, b=1, G_{fr} =0.96 GPa, and φ= 0.12. The parameter c' is the thermoporoelastic coupling coefficient and can be derived from laboratory experiments. The coupling coefficient can be expanded as:

$$\begin{aligned} c' &= \left.\frac{dp_p}{dT}\right|_{p_c} + \frac{\partial p_p}{\partial p_c}\frac{\partial p_c}{\partial T} \\ &= \left.\frac{dp_p}{dT}\right|_{p_c} + B\left[\frac{2E_u\alpha_{s,u}}{9(1-\nu_u)}\right] \end{aligned} \tag{17}$$

The first term is the change in pore pressure, p_p, with temperature at constant confining pressure, p_c, and can easily be measured in the laboratory, B is the Skempton coefficient, E_u is undrained Young's modulus, $\alpha_{s,u}$ is the undrained solid volumetric thermal expansion coefficient and ν_u is the undrained Poisson's ratio. Here a representative value of 0.4 MPa/°K for c' is chosen. Pore pressure profiles using these parameters are shown in Fig. 6-5. Here it is assumed that there is a zero fluid flux boundary condition at the wellbore wall and a constant hydrostatic pore pressure in the far field. The zero flux boundary condition is justified as no micro-annulus or radial cracking is expected between the casing, cement and formation.

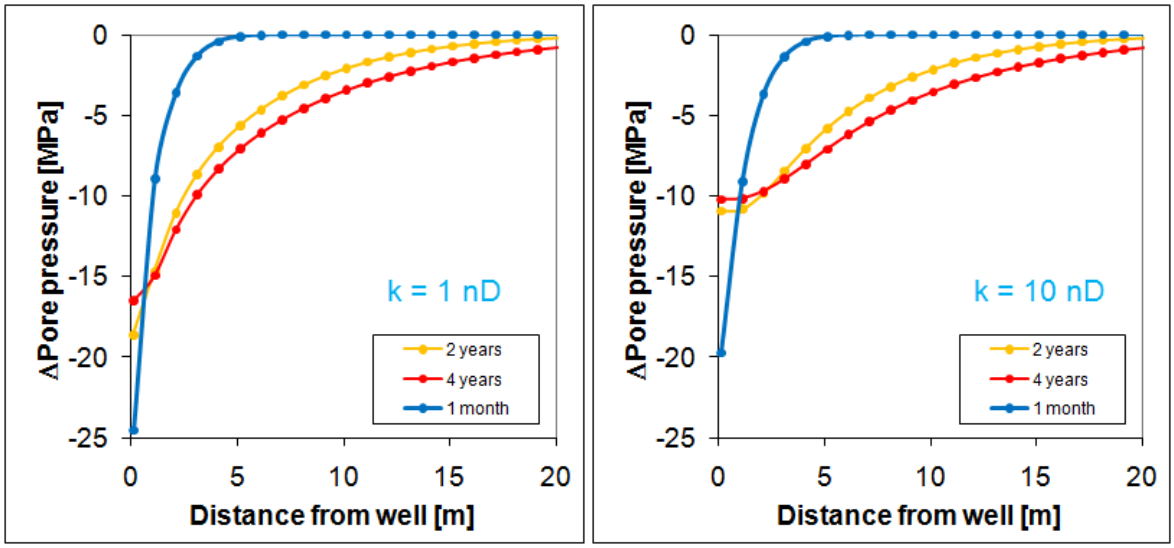

Fig. 6-5—Pore pressure profiles as a function of radial distance from the wellbore and time for permeability in the range of 1 (left) to 10 (right) nanoDarcy.

On short time scales, the pore pressure response is undrained and slowly changes to drained behaviour at longer time scales, as evidenced by the reduction in the pore pressure gradient from the well bore face as a function of time. Similar to the temperature predictions, the biggest perturbations are in the near wellbore region. The next two sections evaluate the effect of temperature changes on the cemented region in the wellbore, above the casing shoe, as well as the open hole, directly in contact with the caprock.

6.2.1.1. Near wellbore stress state in cemented region within the caprock

The impact of the near wellbore pressure and temperature variations in the caprock is assessed using an analytical solution (65) for the stress changes in a heated region around an infinitely extending well. No thermal diffusion or pore pressure diffusion from the far field is present in this model. Instead a step function change is assumed from low to background temperature in the near wellbore region. This model has been shown to produce the same or greater maximum stress perturbations in the near wellbore region compared to more realistic models where the temperature and pore pressure profiles are similar to those shown in Fig. 6-4 and Fig. 6-5. Using this model, the expansion of the thermoporoelastic coupling coefficient given in Eq. (18) and the input parameters given in Table 6-3, the resulting near wellbore stress state is determined for the undrained (short time scale) state as shown in Fig. 6-6. The undrained elastic parameters in Table 6-3 have been determined from sonic logs and the thermal expansion parameters represent the range of values seen in a variety of measurements on shales.

The drained parameters are also listed in Table 6-3. They are present because in some cases the thermal expansivity of the fluid/solid system is so high that the pore pressure would take on negative values for the temperature change considered. As this is unphysical, undrained conditions over a range of temperature change are assumed where the pore pressure is predicted to be greater than or equal to 0 (ΔT_1 in Fig. 6-4). The remaining amount of temperature change (ΔT_2 in Fig. 6-5) is applied under drained conditions where the pore pressure is held at a constant value of zero.

Table 6-3—Undrained material parameters for the Rødby Shale used in the near wellbore stress analysis

Case	E_{undr}	ν_{undr}	E_{dr}	ν_{dr}	$\alpha_{V,dr}$	$\alpha_{V,undr}$	ΔT	ΔT_1	ΔT_2	$\left(\frac{\Delta P_p}{\Delta T}\right)_{p=const}$	B	$P_{p,0}$	σ_1'	σ_3'
	[GPa]		[GPa]		[10^{-6} K^{-1}]	[10^{-6} K^{-1}]	[K]	[K]	[K]	[MPa/K]		[MPa]	[MPa]	[MPa]
Low	10	0.38	-	-	-	60	-60	-60	0	0.1	0.8	25	26.9	18.1
Base	10	0.38	-	-	-	105	-60	-60	0	0.1	0.8	25	26.9	18.1
High	10	0.38	8	0.11	120	150	-60	-47.2	-12.8	0.1	0.8	25	26.9	18.1

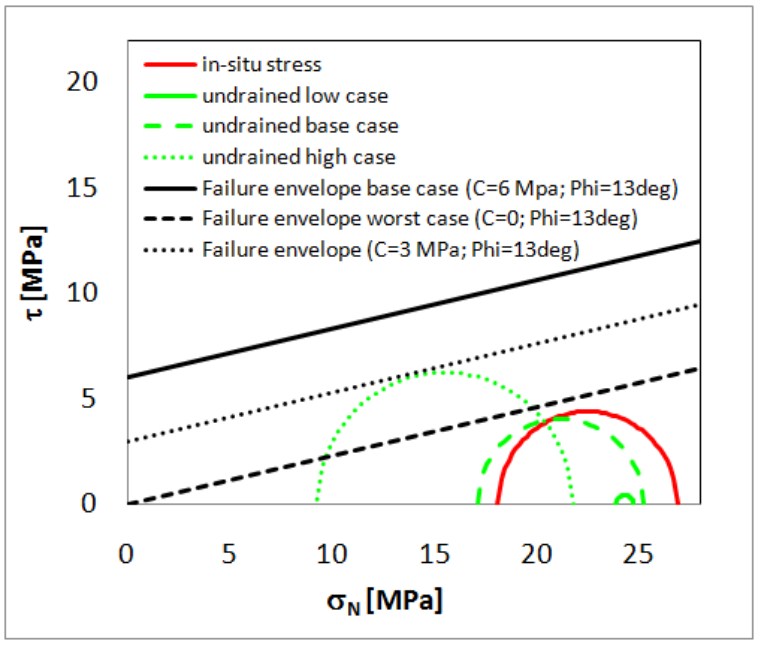

Fig. 6-6—Effective stress state of the near wellbore environment after cooling under undrained conditions.

Note: the stress state is displayed in Mohr's space relative to the base case (solid), intermediate (dotted), and worst case (dashed), Mohr-Coulomb failure line for the Rødby Shale before (red circle) and after cooling (green circles) for three different scenarios (see Table 6-3).

It can be seen from these results that shear failure of the caprock assuming a Mohr-Coulomb criterion is not expected over the range of uncertainty considered except in the undrained high case with the worst case failure envelope for the Rødby Shale. This combination is considered to be extremely unlikely especially as the high undrained thermal expansion values come from experiments on shallowly buried, relatively unconsolidated shales, which are not an appropriate analogue for the Rødby Shale. However, the desire was to include this value for completeness in the analysis. Note that tensile failure is not expected in any of the cases considered as evidenced by the fact that the predicted minimum principal stress remains well above zero.

A similar exercise has been carried out assuming drained conditions, which would be realised in the long time scale limit. The model parameters are given in Table 6-4 and the results shown in Fig. 6-7.

Table 6-4—Drained material parameters for the Rødby Shale used in the near wellbore stress analysis.

Case	$E_{drained}$	$\nu_{drained}$	α_V	ΔT	$P_{p,0}$	σ_1'	σ_3'
	[GPa]		[10^{-6} K^{-1}]	K	[MPa]	[MPa]	[MPa]
Low	1.62	0.37	60	-60	25	26.9	18.1
Base	2.4	0.25	60	-60	25	26.9	18.1
High	8.0	0.11	60	-60	25	26.9	18.1

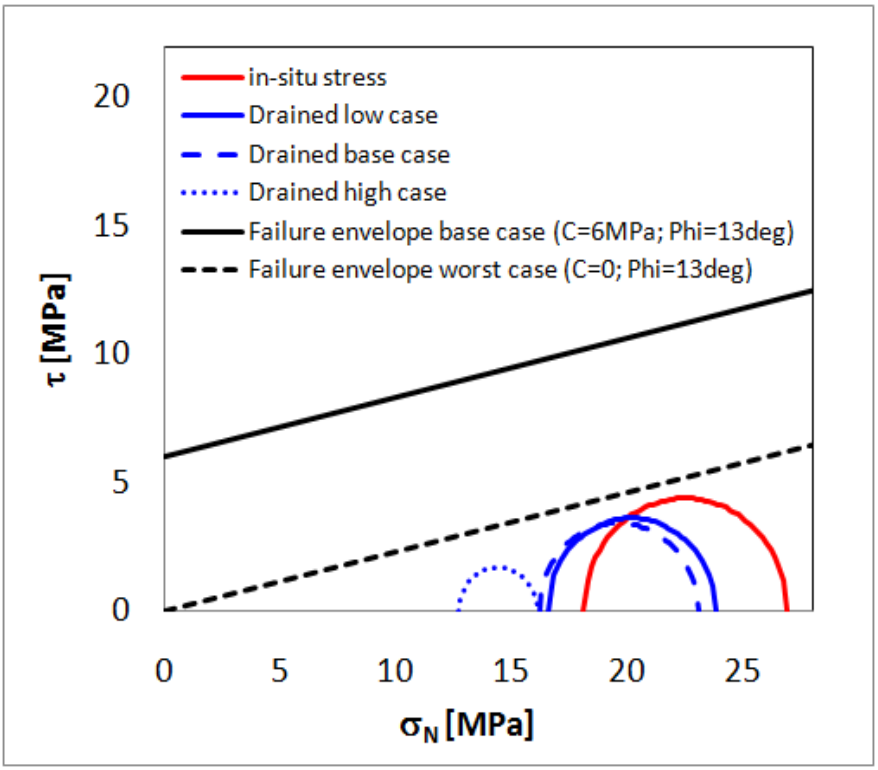

Fig. 6-7—Effective stress state of the near wellbore environment after cooling under drained conditions.

Note: the stress state is displayed in Mohr's space relative to the base case (solid) and worst case (dashed) Mohr-Coulomb failure line for the Rødby Shale before (red circle) and after cooling (blue circles) for three different scenarios (see Table 6-3).

Here, the major source of uncertainty is in the drained elastic parameters and thus the drained thermal expansion values are kept fixed at the base case values for simplicity. The elastic parameters were derived by Gassmann fluid substitution with a range of grain moduli expected for a shale. As Fig. 6-7 clearly displays, shear failure assuming a Mohr-Coulmb criterion or tensile failure of the Rødby is not expected within this uncertainty range.

Thus, thermal cooling of the caprock formation does not appear to be an issue for the section of the caprock sealed from pressure variations.

6.2.1.2. Near wellbore stress state for the caprock exposed to reservoir pressure variations

In the wellbore below the casing shoe, a zero flux boundary condition no longer holds. In this case, pore pressure diffusion from the wellbore face into the formation will occur. This will alter the effective stress state in the near wellbore region significantly from that shown above. In order to evaluate this, the wellbore simulator PBore (66) was employed, which makes it possible to investigate the coupled effects of pore pressure and temperature variations at the wellbore face.

In the PBore analysis, two cases will be considered; a base case and low case. The low case uses the highest values of κ_T, $E_{drained,}$ and $\alpha_{s,drained}$ to explore the largest expected variations in temperature and pore pressure. The parameters that are input into the PBore model are given in Table 6-5 and the initial stress state, viscosity, permeability, etc. are as above. In Table 6-5 the failure parameters are cohesion (C) and friction angle (θ). For both cases, the pore pressure at the wellbore face and in the far field is set to hydrostatic. This is appropriate for the situation during the initial drilling of the wells (near hydrostatic mudweight used) and at the end of the injection period.

Table 6-5—Base and low case parameters used in the PBore model

Case	$E_{drained}$	$\nu_{drained}$	ν_u	$\alpha_{s,drained}$	α_f	$\varkappa_T$	C	θ
	[GPa]			[10^{-6} K^{-1}]	[10^{-6} K^{-1}]	[10^{-7} m^2s^{-1}]	[MPa]	[deg]
Base	2.4	0.25	0.38	10	500	3	6	13
Low	8.0	0.11	0.38	60	500	6	0	13

Temperature and pressure perturbations for the base case model assuming a 100 nanoDarcy permeability as is shown in Fig. 6-8. The permeability value of 100 nanoDarcy was chosen to ensure the calculations would be conservative. The temperature distribution is very similar to that given in Fig. 6-4 as expected. However, the pore pressure distribution now shows a peak near the wellbore due to pore pressure diffusion from the wellbore face in contrast to the distribution shown in Fig. 6-5.

In Fig. 6-9, the failed zone predicted around the well is compared in two scenarios assuming a permeability of 100 nanoDarcy and the base case rock properties. In the first scenario, the temperature change is accounted for and in the second one it is not. No difference between the two scenarios is found. With this important observation the statement can be made that the failure zone is due to the initial drilling of the well and subsequently exposing the wellbore face to the hydrostatic reservoir pressure. At this time, the total radial stress has to equal the pore pressure in the open annulus due to force balance. This greatly increases the shear stress and causes some failure. As the failure is fairly limited, it should pose no problem in completing the well. Indeed the well summary reports mention some hole instability in the caprock near the top of the reservoir section, but nothing that stopped the running of the completion. The same behaviour is seen when the permeability is reduced to 1 nanoDarcy.

Because the failure zone does not grow when cooling takes place, it means that the temperature has no effect on the size of the failure. This has important implications for the GYA02S1 well as it was completed near the top of the Rødby. These results show that a failed zone is not expected to propagate from the openhole section below the shoe to the top of the Rødby, as the shoe is approximately 10m below the top of the Rødby Formation and the failed zone is on the order of centimetres.

Under low case conditions, the hole is completely unstable. Thus, this case is unrealistic as no such problems were experienced during drilling and completion of the well. Still, something very useful can be learned from this example. In the no temperature change scenario, the hole is immediately unstable. However, with a temperature reduction, the hole is not immediately unstable. In **Fig. 6-10**, a progression of increasing instability as a function of time is seen. This is not surprising as the effect of temperature is to decrease the pore pressure more than the total stress, leading to an increase in effective stress and driving the system away from shear failure as long as the shear stress does not increase significantly in the process. Pore pressure diffusion then leads to a pore pressure increase that the total stresses cannot match in the near wellbore invironment as the radial stress must equal the pore pressure at the wellbore face. Thus the effective stress goes down, driving the system towards failure.

The important aspect to note here is that temperature should lead to a stabilisation and not a destabilisation. Thus, if the cohesion of the Rødby is raised, which is the most uncertain failure parameter, such that the hole becomes stable under isothermal conditions, then the addition of cooling will not make the hole unstable and the conclusion about restricted failure around the wellbore under the base case remains valid under low case conditions.

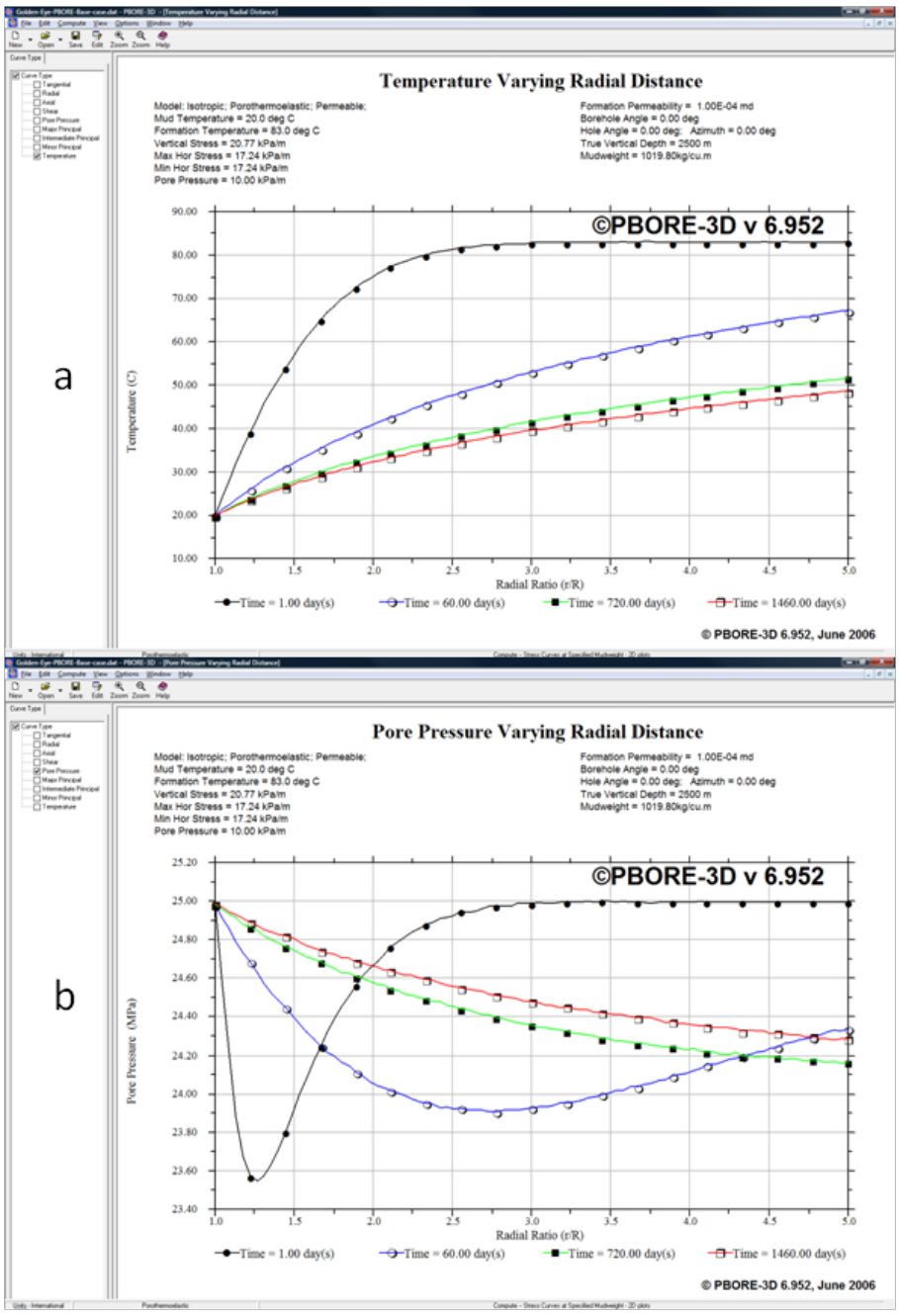

Fig. 6-8—(a) Temperature and (b) pore pressure distributions as a function of time for the base case PBore model assuming a 100 nD permeability.

Note: pore pressure or temperature after 1 day is shown in black, 60 days in blue, 2 years in green and 4 years in red.

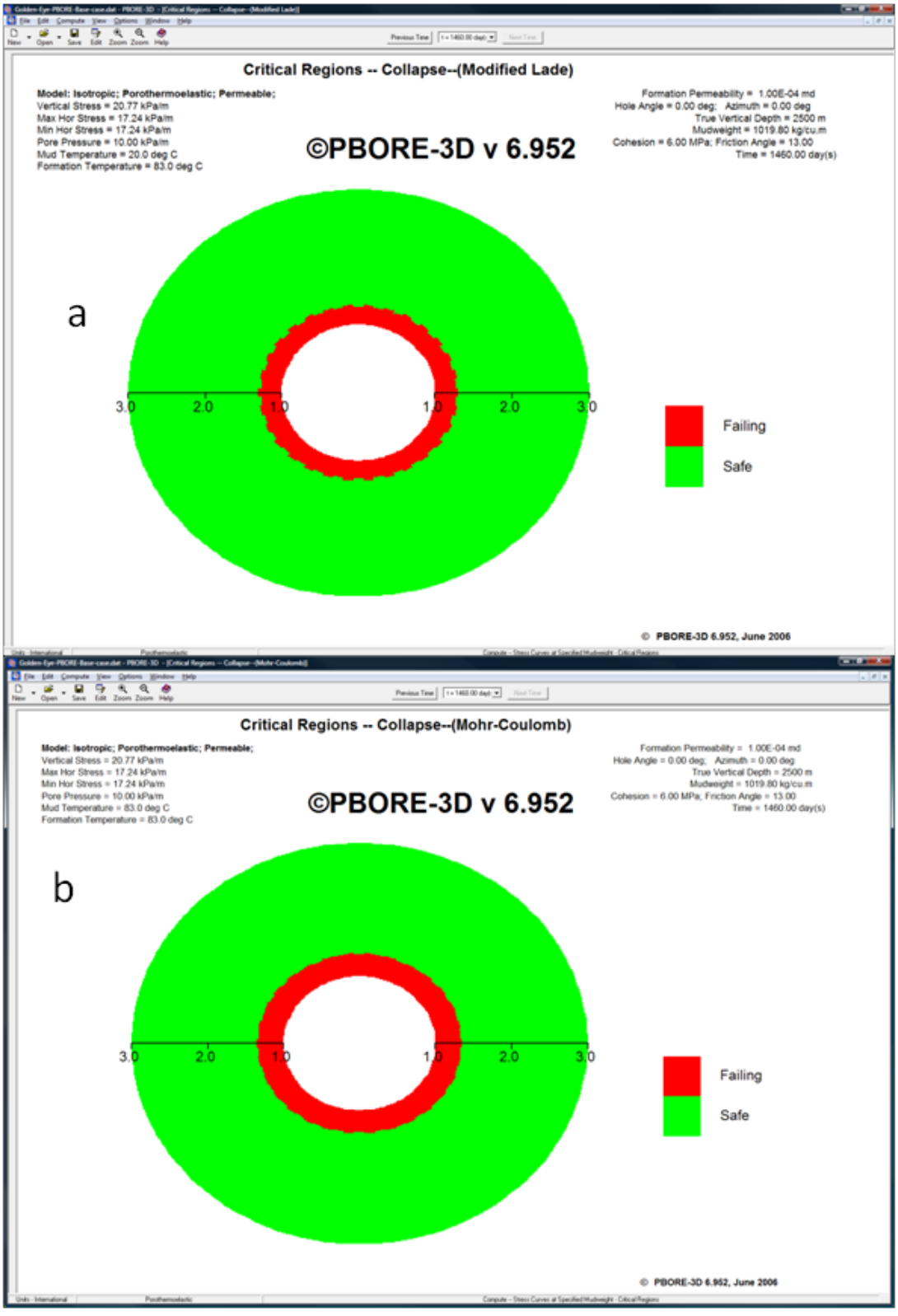

Fig. 6-9—Comparison of the failed zone (red area) around well from the base case PBore simulation with (a) cooling of the formation for 4 years, and (b) no temperature change in the formation.

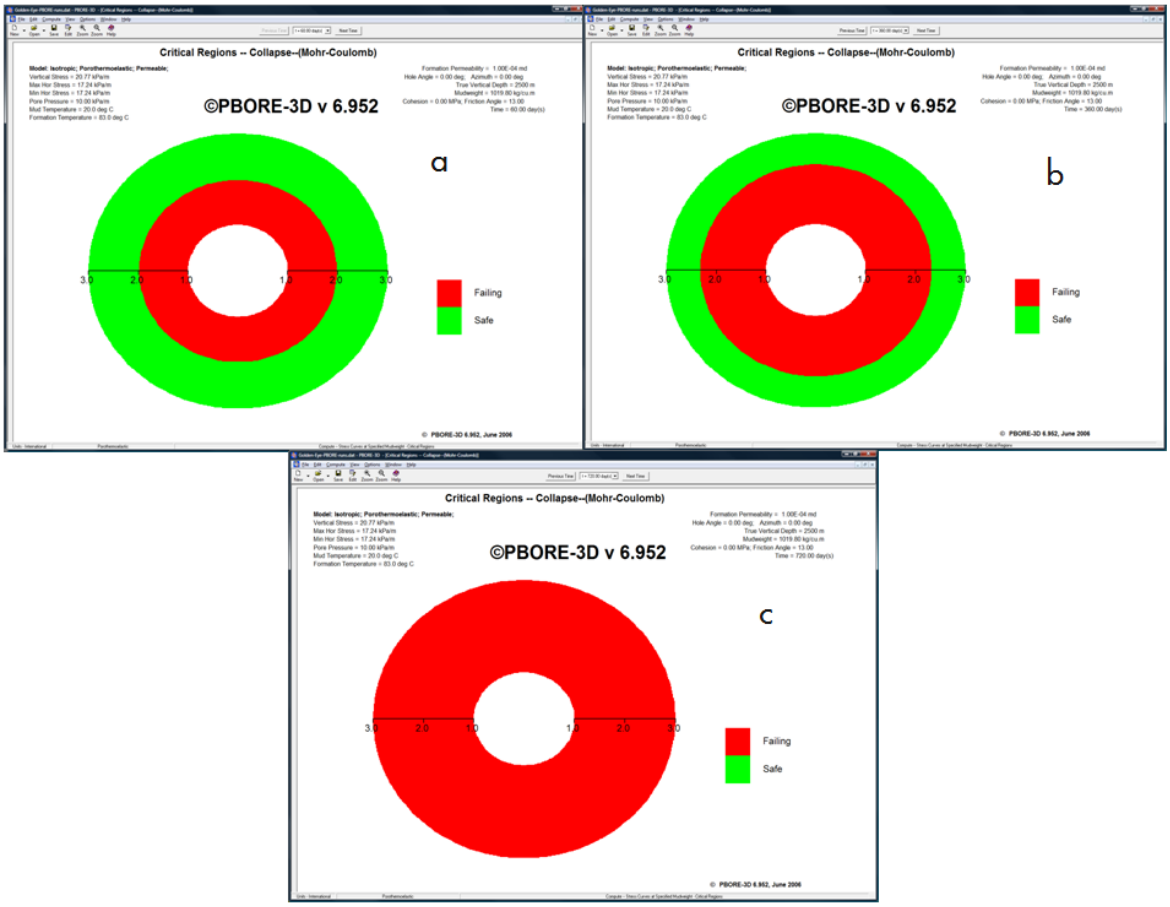

Fig. 6-10—Evolution of wellbore shear failure (red areas) from the low case PBore simulation as a function of time under cooling conditions.

Note: the amount of failure is shown after (a) 60 days, (b) 1 year, and (c) 2 years.

6.2.2. The farther field reservoir and base of the caprock

6.2.2.1. Simple, uniaxial hydraulic fracture simulations

6.2.2.1.1. PWRI simulations

In addition to near wellbore failure due to the injection of cold CO_2, the potential of reservoir and caprock failure in the farther field was also investigated. To this end, simulations of hydraulic fracturing in the Goldeneye reservoir were completed using Shell's internal software application PWRI-Frac. The model was constructed using the same suite of inputs as the 3-D numerical model in terms of the in-situ stresses and rock properties (Chapter 3). The physical properties of the supercritical CO_2 were entered, as were the well configurations and injection schedule in terms of rates, volumes and time.

The predicted dimension of the hydraulic fracture for the base case realisation is shown in Fig. 6-11. For the 10 year injection period of 2 million tonnes per year, the predicted fracture length is 130 ft [40 m].

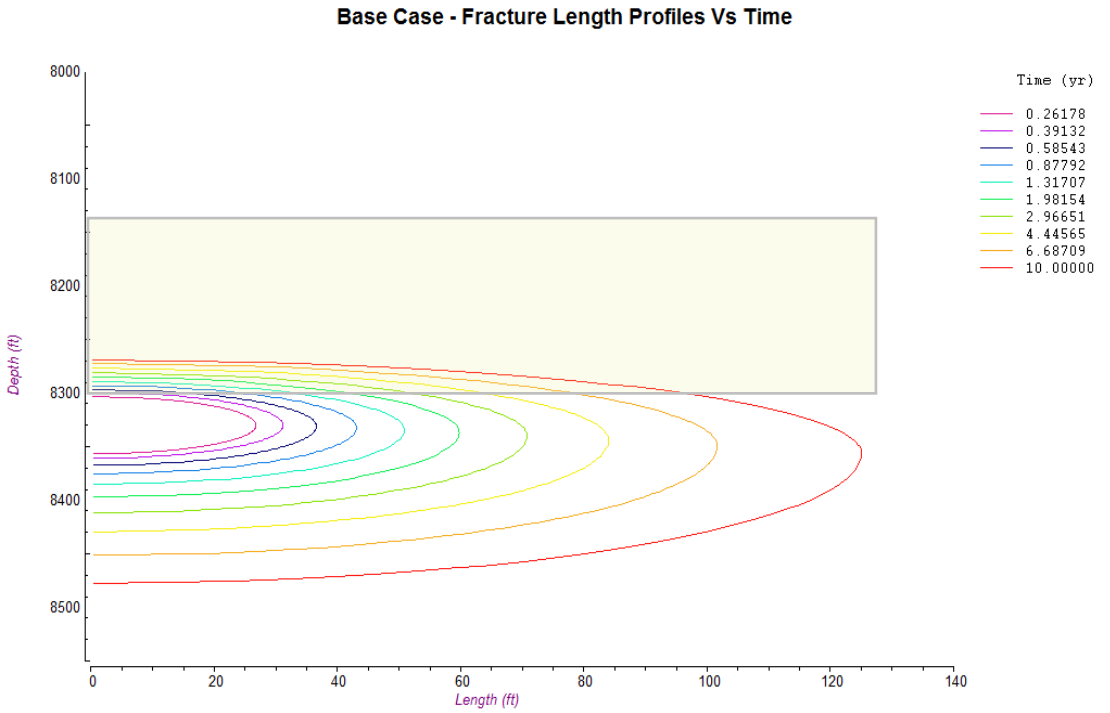

Fig. 6-11—PWRI-Frac simulation for Goldeneye reservoir

Note: the results show the predicted fracture growth for 20 million tonnes injected over a 10 year period. The majority of the fracture is contained in the Captain, with only limited growth into the caprock.

Containment in the reservoir sandstone is predicted primarily due to the high minimum principal stress in the reservoir (owing to the low reservoir pressure after depletion), the relatively high Young's modulus and the high porosity and permeability (good leak-off and storage potential). Based on the simulations, only limited growth into the Rødby caprock is predicted, in the order of 25 ft [7.5 m].

The issue which then arises, based on these results, is what impact the thermo-elastic stresses have on the fracture behaviour in the Rødby shale when extremely low leak-off occurs. As Fig. 6-12 shows, the thermo- and poro-elastic response of the rock in the PWRI simulations is controlled by the fluid invasion and whilst this doesn't occur in the Rødby Formation, diffusive cooling will (Fig. 6-13).

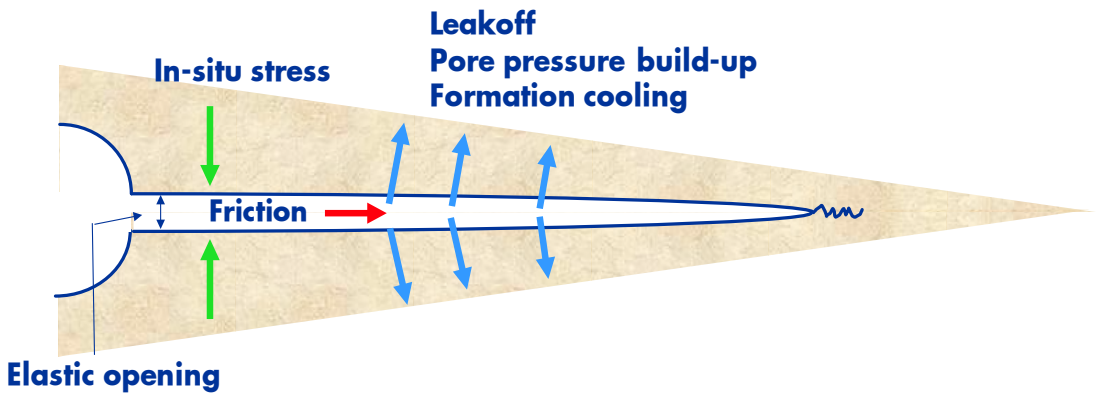

Fig. 6-12—PWRI-Frac calculates the thermo-poro-elastic effects where fluid leak-off occurs in the permeable units.

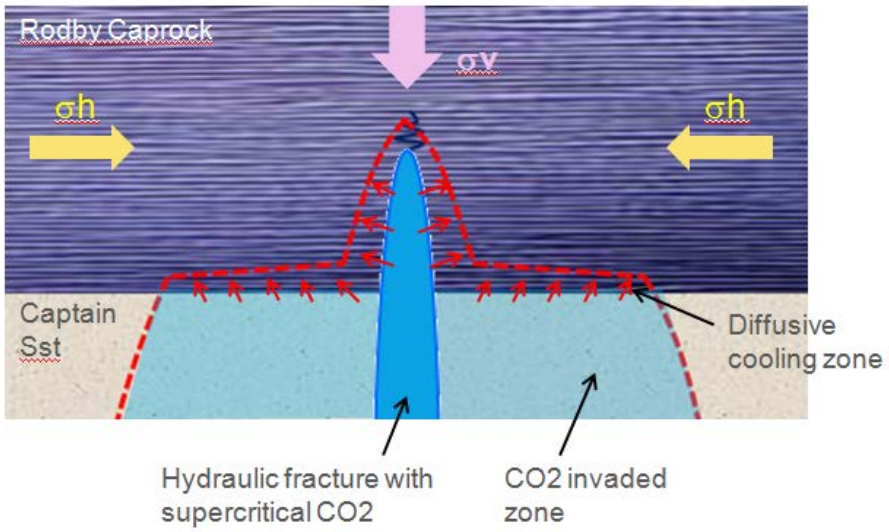

Fig. 6-13—Schematic diagram to illustrate the problem with diffusive cooling of the caprock adjacent to a fracture and plume of CO_2

Note: thermo-elastic stresses are accounted for in the invaded zone, however, the low permeability of the caprock means that almost no leak-off occurs in the time-scale of injection and hence diffusion-based cooling is required in the modelling.

To further evaluate this behaviour, a number of PWRI-Frac simulations were run which attempted to account for this cooling of the caprock by reducing the Rødby minimum principal stress according to the calculated thermo-elastic stresses for various input parameters. These evaluations are discussed in the next section.

6.2.2.1.2. PWRI-Frac results

The details of the general set up of the PWRI simulations are given in reference (35). The work reported here attempts to take the same model setup but evaluate the impact of cooling on the caprock by initialising the model with the reduced minimum principal stress at the start of the injection.

Another simulation issue is the initial reservoir pressure and the impact the aquifer has on the pressure with time. The reservoir model simulations indicate that at the start of the injection the pressure will be approximately 19.3 MPa [2799 psia] which then increases during the 10 year injection period to approximately 25.5 MPa [3698 psia]. It is difficult to replicate these boundary conditions in the PWRI model set-up, therefore, the simulations evaluated injection of the 20 million tonnes over 10 years with reservoir pressures ranging from the initial pressure through to the final predicted pressure.

The model versions evaluated are summarised in Table 6-6. Note, this modelling was completed relatively early in the thermal impact evaluations and hence some of the input parameters were varied as more data came to light. This is especially the case for the Rødby LTEC input, where the initial low case in Table 6-6 (V4) was further lowered owing to a higher Young's Modulus being determined for the Rødby (V9-11). An important relationship used in the determination of the minimum principal stress as a function of the reservoir pressure change is the stress path γ_h, which is defined as

$$\gamma_h = \frac{\Delta\sigma_h}{\Delta P_f} \quad (18)$$

Where σ_h is the minimum total principal stress and P_f is the formation pressure. Different γ_h values were tested in the PWRI-Frac simulations, as detailed in Table 6-6.

Table 6-6—Details of the model versions for the PWRI-Frac simulations.

Model Version	Details
V1	Base case set up, initial reservoir pressure is 19.3 MPa [2800 psia]
V2	As V1 except initial reservoir pressure is 25.5 MPa [3700 psia]
V3	As V2 except used γ_h of 0.3, i.e. higher σ_3 in Captain D reservoir
V4	As V2 except low case α_T for Rødby
V5	As V3 except initial reservoir pressure 19.3 MPa [2800 psia]
V6	As V5 except γ_h of 0.6, i.e. higher σ_3 in Captain D reservoir
V7	As V6 except low case α_T for Rødby
V8	As V4 except only last 12 months of injection
V9	As V1 except SIEP α_T for Rødby (very low case)
V10	As V9 except initial reservoir pressure 22.4 MPa [3250 psia]
V11	As V10 except initial reservoir pressure 25.5 MPa [3700 psia]

The results of the simulations are given in

Table 6-7. This table summarises some of the input variables and the impact these variations have in terms of the fracture size and the BHP at the end of the simulation. The key output from these simulations is the prediction for upward growth of the hydraulic fracture from the point of injection. Fig. 6-14 shows the predicted upward growth of the fracture for each model version. The range in upward growth is 18-51m [59-167 ft], with the highest growth upwards being associated with the cases where the Rødby has a very low minimum principal stress; in the versions V4 and V7-11 the model initialisation starts with the minimum principal stress in the Rødby being *lower* than the Captain D sand. It is interesting to note that even in these cases where the full thermal cooling effect is applied to the whole of the Rødby the fracture in the Rødby is still retained. As Fig. 6-15 shows, for the height growth upwards for V9-V11 (increasing reservoir pressure in the Captain D) the simulations show that the fracture is still confined to the Rødby Formation. Each of these versions simulated the injection of 20 million tonnes over a 10 year period.

Taking the caprock package as the Rødby and Hidra Formations, then the results suggest even in the most pessimistic cases the caprock integrity is not compromised.

Table 6-7—Results of the different model versions for the PWRI-Frac simulations.

Model Version	P_res	Sh_CapD	CapD Gamma_h	Sh_Rod (Thermal)	Length	Ht_Up	Ht_dwn	Width	BHP end
	MPa	MPa	-	MPa	m	M	m	mm	MPa
V1	19.3	33.2	0.1	36.0	40.5	20.0	45.8	33.5	36.5
V2	25.5	33.8	0.1	36.0	33.6	23.1	39.1	45.3	38.1
V3	25.5	36.0	0.3	36.0	32.1	35.9	28.2	45.8	39.4
V4	25.5	33.8	0.1	30.8	58.3	49.2	9.0	6.3	33.5
V5	19.3	34.2	0.3	36.0	32.9	23.8	35.7	49.1	38.8
V6	19.3	35.6	0.6	36.0	30.7	38.2	27.0	47.6	39.3
V7	19.3	35.6	0.6	30.8	83.5	44.9	-5.9	0.1	33.0
V8	25.5	33.8	0.1	30.8	15.7	18.5	9.0	18.2	37.3
V9	19.3	33.2	0.1	29.5	57.1	45.9	9.2	6.4	32.7
V10	22.4	33.5	0.1	29.5	75.6	48.3	-3.8	0.1	31.4
V11	25.5	33.8	0.1	29.5	66.3	51.4	-4.2	0.1	31.6

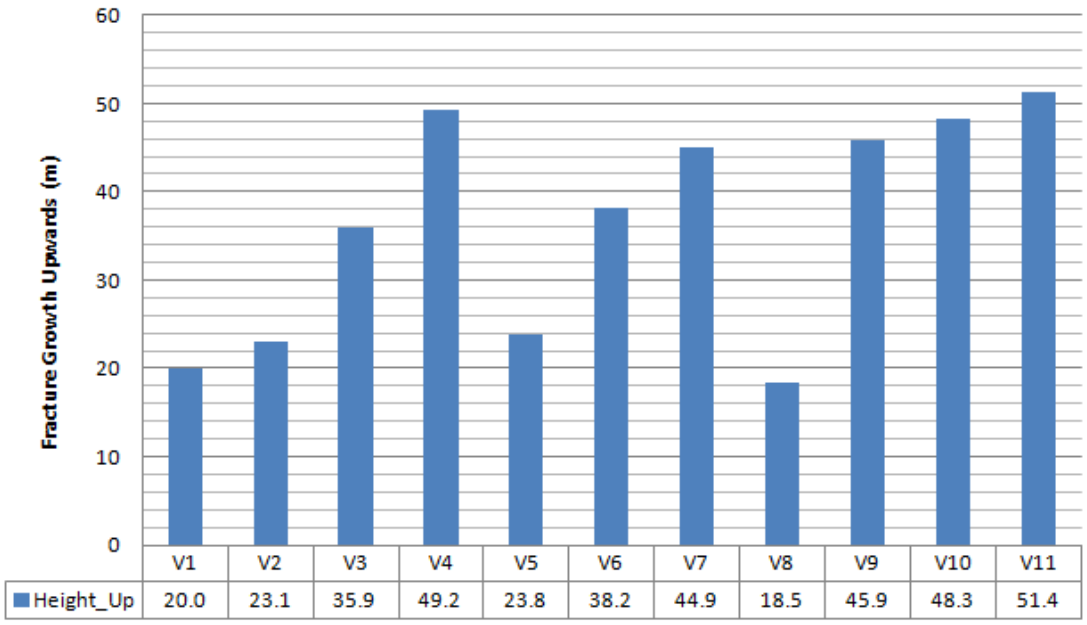

Fig. 6-14—lot of the predicted vertical fracture growth for the different model versions of the PWRI-Frac simulations.

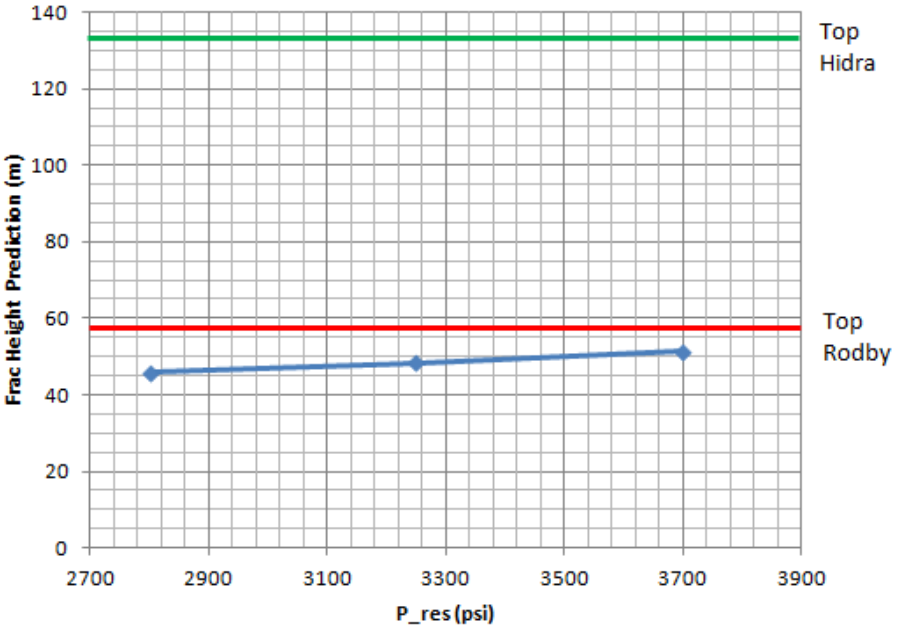

Fig. 6-15—Plot of the predicted vertical height growth for model versions V9-V11, where the minimum principal stress in the Rødby was reduced by the high case thermo-elastic stress across the whole unit

Note: For each version the initial reservoir pressure was varied from 19.3 to 25.5 MPa [2799 to 36895 psia], representing the range in the reservoir pressure from the start to the end of the injection period.

Table 6-7 indicates that, even in the cases where the minimum principal stress in the Rødby caprock is lower than the Captain D reservoir, significant fracture growth still occurs in the latter owing to the Young's Modulus of the sandstone, the low density of the CO_2 as well as the high storage capacity of this formation. Given the BHP pressure and volumes of CO_2 injected, the fracture created provides enough leak-off capacity and hence overall containment even in the worst case scenarios.

6.2.2.2. 2D simulations of thermo-elastic stresses

To this point calculations have been based on a simple uniaxial thermo-elastic behaviour using the linear thermal expansion coefficient, according to Eq (13). As Fig. 6-3 shows, depending on the input parameters used, it might be possible to cool the shale caprock sufficiently for tensile failure and fracture propagation to occur.

To extend these calculations to 2D stress field around a cooled fracture, studies by Perkins and Gonzalez (65) provided the analytical solution for determining the impact of the temperature change on the two principal stresses. This work was extended by Ghassemi (67) who evaluated the pore pressure and stress changes around a cooled fracture in a low permeability rock ($4.0 \cdot 10^{-7}$ Darcy). The study used a 2D poro-thermo-elastic displacement discontinuity boundary element model to calculate the thermally-induced stresses and pore pressures around a fracture, however, it didn't consider fracture propagation mechanics. The study showed that the difference in major and minor principal stress was greatly reduced in the cooled region around the fracture owing to the large reduction in the major principal stress parallel to the fracture. Both studies (65; 67) demonstrated that in sufficiently cooled region, the stress parallel to the fracture can become less than the stress perpendicular to the

fracture. Given that the fracture long-axis is perpendicular to the minor principal stress, this suggests that the main fracture would cease propagating parallel to the initial major principal stress direction and start to open perpendicular to this direction once the cooling is sufficient **(Fig. 6-16)**.

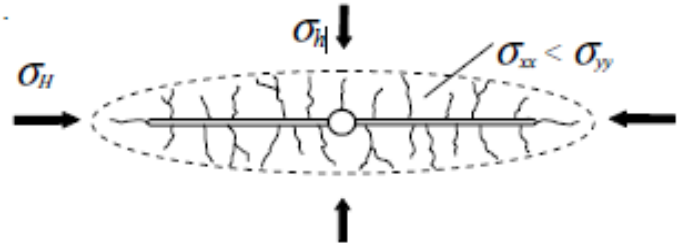

Fig. 6-16—Illustration of the formation of secondary fractures due to the change in the ratio of the in-situ stresses in an elliptical cooled zone (65).

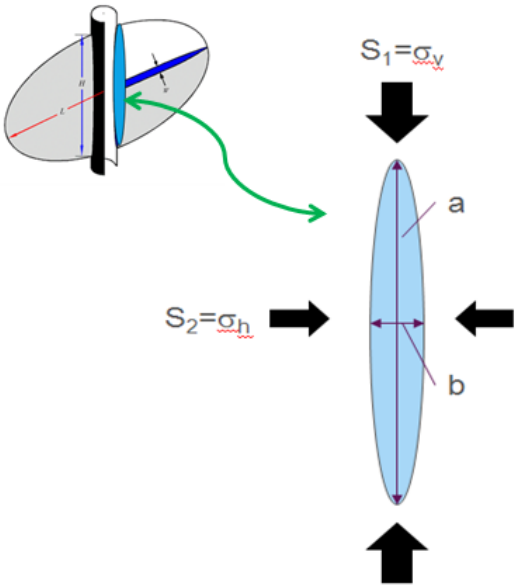

Fig. 6-17—2D in-situ stresses for an elliptical zone; (a) the long-axis is parallel to the major principal stress and (b) the short-axis is parallel to the minor principal stress.

This analysis can be applied to the thermal cooling of the Rødby caprock in the Goldeneye Field. Consider a hydraulic fracture where the long axis *a* is in the direction of the major principal stress (S1 or σ_v) and the short axis *b* is in the direction of the minor principal stress (S2 or σ_h); see **Fig. 6-17**. The expressions for $\Delta\sigma_v$ and $\Delta\sigma_h$ in the uniformly cooled region are given by (65):

$$\Delta\sigma_v = \frac{1}{(1+b/a)} \cdot \frac{E\beta_s \Delta T}{3(1-v)} \tag{19}$$

$$\Delta\sigma_h = \frac{b/a}{(1+b/a)} \cdot \frac{E\beta_s \Delta T}{3(1-v)} \tag{20}$$

The notation and values used in the above equations are given in **Table 6-8**.

Table 6-8—Notation and values for the calculation of the change of in-situ stress for an elliptical cooled zone.

Parameter	Notation	Value
Ellipse long axis [m]	a	10
Ellipse short axis [m]	b	1
Young's modulus [GPa]	E	7
Poisson's ratio [-]	ν	0.30
Volumetric Thermal Expansion Coeff.[10^{-5}/°C]	β_s	10.5
Linear Thermal Expansion Coeff. [10^{-5}/°C]	α_t	3.5
Major principal stress [MPa]	σ_H	52.6
Minor principal stress [MPa]	σ_h	44.5

Based on the input values in Table 6-8, the change in S1 and S2 as a function of cooling by 60°C is shown in **Fig. 6-18**. Also plotted in Fig. 6-18 is the reduction in S2 based on the linear thermal expansion coefficient. The results confirm the previous studies which showed that the change in the minimum principal stress as a function of the temperature change is much less the major principal stress. Once cooling occurs by 30°C in the zone around the fracture, then there is a change in the major principal stress from vertical to horizontal plane. If the injection pressures were sufficiently high, then this suggests that the fracture would propagate horizontally. However, as Fig. 6-18 illustrates, given the expected injection pressures in the Goldeneye field over the 10 year time period, there is a significant pressure buffer between the hydraulic fracture pressure and the minor principal stress in the Rødby. What Fig. 6-18 also shows quite clearly is using the simple linear elastic calculation that the injection pressure would be greater than the minimum stress in the cooled zone once the temperature was reduced by about 50°C.

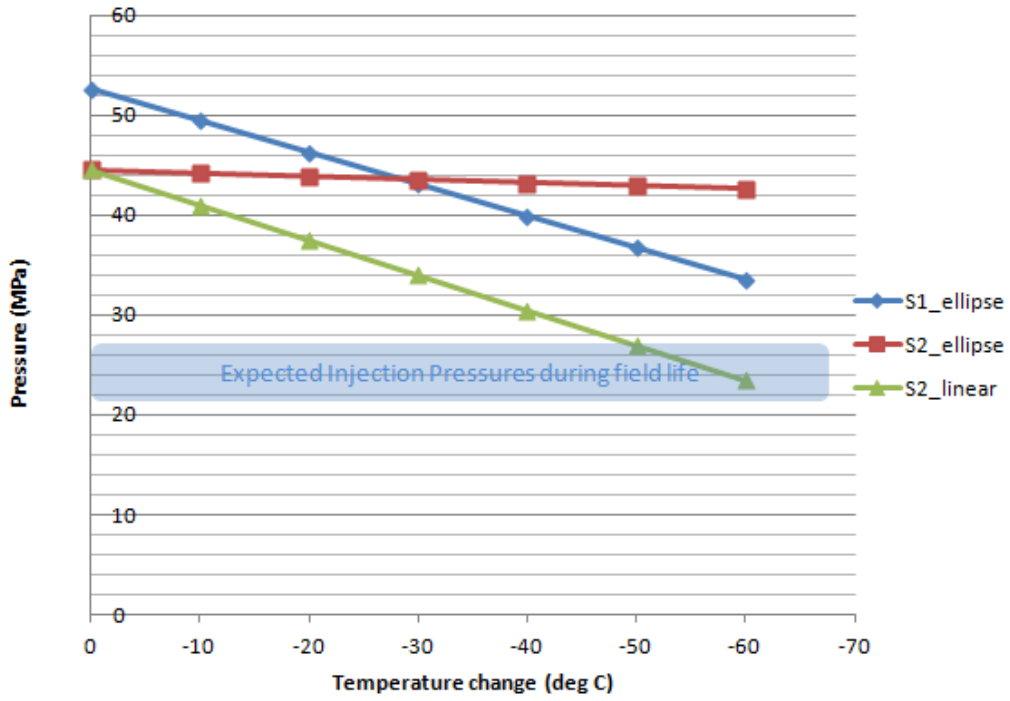

Fig. 6-18—Calculated change in the major (S1) and minor (S2) principal stress for the elliptically cooled zone in the Rødby caprock.

Note: As the temperature decreases the difference between the stresses reduces to the point where S1 will change from the vertical to the horizontal plane. At no point are the expected injection pressures greater than the minor principal stress. However, using the simple linear calculation for the thermo-elastic stress shows that cooling is required of ~ 50°C before the minor principal stress coincides with the expected injection pressures.

A number of sensitivity analyses have been run using the 2D analytical solutions and in all cases the minimum principal stress reduces very little compared to the major principal stress. At no point does the minimum principal stress come close to the predicted injection pressures. This analysis suggests that using the simple 1D approach is too pessimistic compared to the 2D analytical approach.

6.3. Condition #2: continuous replenishing of cold CO_2 at the fracture tip

As is shown in the above section, thermally-induced stress changes can result in tensile failure of the caprock, and in a specific situation also in the cemented region of the wellbore. However, it is thermal diffusion processes that will involve the required heat exchange and if the constant replenishment of cool CO_2 at the fracture face isn't achieved, then fracture arrest would be highly likely. In order to ensure growth of the created fracture by the changes in stress state, it is important that the fracture tip remains cooled, i.e. that cold CO_2 is continuously being transported to the fracture tip. The likelihood of this depends on the geometry of the fracture.

Overall, the hydraulic fracture simulators assume a pseudo 3D shape. They predict the fracture morphology in 2D then use model approximations for the 3rd dimension; for example using PKN and GDK models as discussed by Meyer (68), the height and length can be calculated, and then the width is calculated based on the net pressure in the fracture. Using these models produces typical fracture morphologies as shown in **Fig. 6-19**.

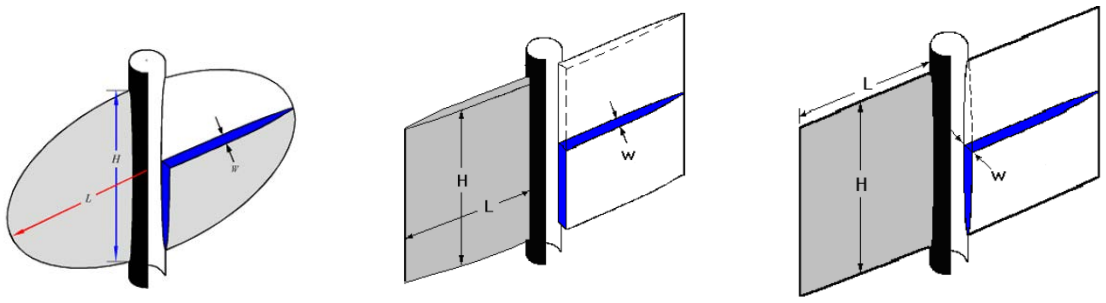

Fig. 6-19—Example of 3 models used to calculate the morphology of hydraulic fractures in simulation software. From left to right: elliptical, PKN and GDK (68).

It is important to remember that for the Goldeneye CCS scenarios, the actual injection pressure is less than the minimum principal stress in the Rødby. Therefore, only for those locations where significant cooling occurs will the pressure in the fracture be enough to drive propagation. If the newly injected CO_2 doesn't permeate to the fracture tip, then propagation will cease.

In order to assess this problem, a scenario can be invoked, where the cooling occurs at the top of the fracture if the "perforations" are close to the top of the injection interval and adjacent to the shale caprock, as is the case for at least one of the injection wells in the Goldeneye Field. In the worst case

scenario, the predicted lowest injection temperature can be used and apply it to the calculations of thermo-elastic stress reduction. However, the reality in terms of the fracture morphology will be very different to the idealised penny-shaped hydraulic fracture discussed above.

A number of papers have reviewed field observations about fracture morphology and the implications in terms of practical application of hydraulic fracturing for stimulation purposes [see (69; 70)). As **Fig. 6-20** shows, evidence from mine-back experiments, log data and lab tests all show that although the full 'process zone' may well be represented by a disc-shaped zone, there are numerous physical heterogeneities, such as bedding planes and natural fractures, which impact the detailed fracture morphology. In these cases, the fluid dynamics in the fracture, especially where there are strong temperature impacts on the fluid density, will imply a much more complex system than a simple penny-shaped fracture would produce.

Given the complexity of the created fractures, it is therefore unlikely that CO_2 will be transported at a sufficient rate to the fracture tip to promote fracture growth. Once the onset of the fracture is created it will most likely propagate for a limited distance, much less than the numerically predicted 18 to 51 m [59 to 167 ft] into the caprock.

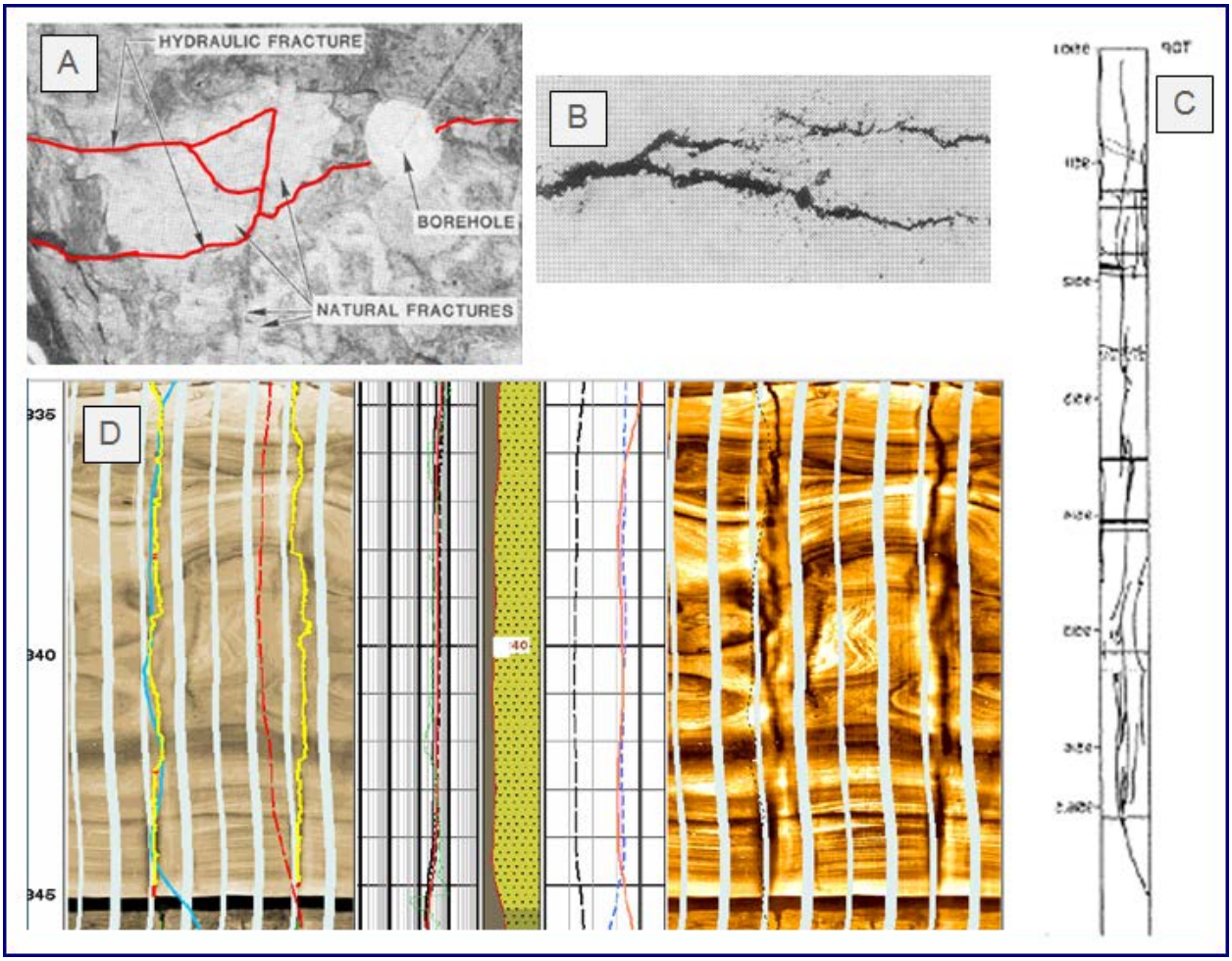

Fig. 6-20—Examples of hydraulic fracture morphology reported in the literature.

Note: A – photo of hydraulic fracture in mine-back tests **(71)**. B – Photo of laboratory generated hydraulic fracture experiments in homogenous sandstone **(72)**. C – sketch of core taken from a well where hydraulic fracture was induced **(73)**. D – UBI log of tensile fractures in sandstone [Source: Kovacs, Schlumberger UBI Tool Review).

6.4. Condition #3: propagation of the fracture across an interface

In addition to cold CO_2 replenishment, fracture propagation is also hindered by formation heterogeneities, as already mentioned in Section 6.3. The behaviour of hydraulic fractures at interfaces, such as bedding planes or joints in the rock, have been studied and reported in the literature (74; 71; 75; 76). These studies have employed laboratory and field studies, as well as numerical modelling to explain the branched and non-planar fracture growth such as the examples shown in Fig. 6-20.

In this section, the predicted behaviour of a hydraulic fracture growing towards a bedding interface, such as a fracture in reservoir sand approaching an interface with an overlying shale formation, will be investigated. A numerical study by Zhang et al (74) demonstrated in the case of a fracture growing in a stiff material which intersects a softer material, such as a sandstone and shale interface, that opening at the interface produces a T-shaped fracture, where fracture termination occurs rather than reinitiating in the soft rock.

The suspension of propagation was also studied where modest loading was applied perpendicular to the interface. Slip and opening along the interface occurred as the fracture tip approached and reduced the stress concentration thereby arresting fracture growth [see (77) and (78)]. However, it appears that if the cohesion and/or compressive force is sufficient then opening and interface slip is inhibited and what was termed 'compressional crossing' occurs (76). The study by Renshaw & Pollard (76) developed a compressional crossing criterion [CCC) which was validated by their own lab tests as well as previously published data.

The CCC is described in **Fig. 6-21**. It considers, in 2D, the stress induced on an interface by an approaching fracture tip where no stress singularity exists at the fracture tip in contact with frictional interface if the driving force is tensile. This suggests that reinitiation on the opposite side of the interface may occur prior to contact with the fracture tip when a stress singularity still exists.

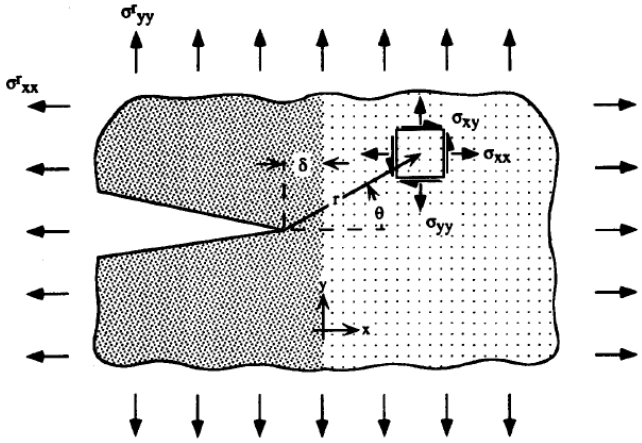

Fig. 6-21—Interface geometry and coordinate system to describe the 2D stresses near a fracture tip approaching a frictional interface (76).

Using linear elastic fracture mechanics theory and the material elastic moduli on both sides of the interface the maximum magnitudes of the components of stress that act along the frictional interface are calculated. The assumption being that for fracture propagation on the other side of the interface, the tensile stress induced by the approaching fracture must be equal to the tensile strength of the material on the opposite side of the interface. The CCC is described by the following relation:

$$\frac{-\sigma'_{xx}}{T_0 - \sigma'_{yy}} > \frac{0.35 + \frac{0.35}{\mu}}{1.06} \quad (21)$$

Where σ'_{xx} is major effective principal stress (S1), σ'_{yy} is the minor principal stress (S2), μ is the coefficient of friction, T_o is the tensile strength of the rock. **Fig. 6-22** shows the CCC as a function of the coefficient of friction of the interface. The CCC was validated by numerous lab tests and previously reported data in the literature.

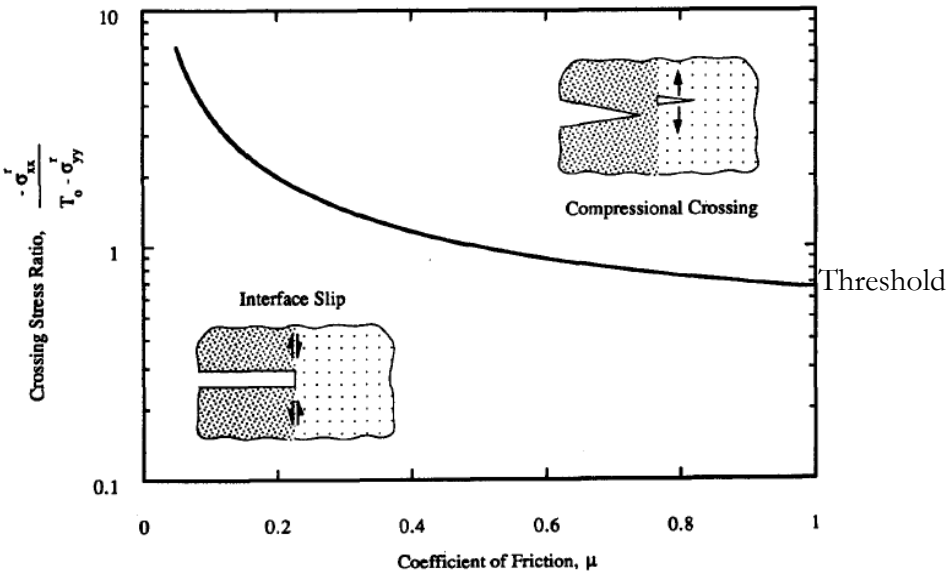

Fig. 6-22—Plot of the crossing stress ratio criterion from Renshaw & Pollard (76)

Note: At stress ratios above this threshold compressional crossing occurs due to the stresses ahead of the fracture tip reinitiating a new fracture on the other side of the interface. For stress ratios below this threshold, interface slip occurs and propagation terminates.

The CCC developed by Renshaw and Pollard (76) was applied to the Goldeneye case. The inputs used to determine whether compressional crossing on the interface between the Captain Sandstone and the Rødby shale caprock are given in **Table 6-9**. The tensile strength of rock can be variable and difficult to determine without laboratory test data, so a range of strengths for the Rødby were used from 1 to 10 MPa [145 to 1450 psia]. **Fig. 6-23** shows that the calculated CCC for the range of tensile strengths predicts that compressional crossing would occur with an offset in the hydraulic fracture at the bedding interface.

Table 6-9—Input parameters for the calculation of the CCC (76)

Parameter	Value
S1 [MPa]	52.7
S2 [MPa]	43.5
Pore Pressure [MPa]	25.5
μ	0.5
T_o [MPa]	1, 3.5, 5, 10

This CCC can be built on for Goldeneye by incorporating the thermo-elastic response for the in-situ stresses around an ellipse, as discussed in Section 6.2.2.2, where the stress difference between the major and minor principal stresses is significantly reduced in the cooled region. **Fig. 6-24** shows the change in the crossing stress ratio due to cooling for a tensile strength of 3.5 MPa [508 psia]. As the cooling occurs then the calculated crossing stress ratio reduces to the point where compressional crossing would not occur and interface slip would take its place.

Based on this analysis, it appears that the cooling of the fractured zone would reduce the likelihood for the fracture to cross the interface between lithological units, such as from the Captain Sandstone into the Rødby Shale, and instead interface slip would be more likely. This behaviour was also suggested by the study of Zhang et al (74) where frictional slip at the interface between a stiff and soft rock would arrest the fracture growth across the interface.

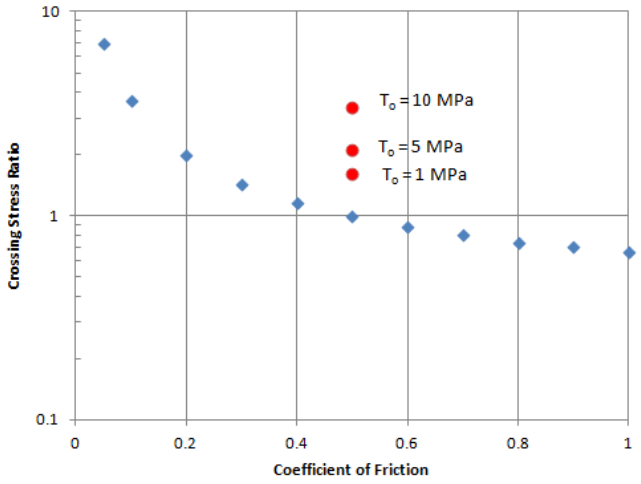

Fig. 6-23—Calculation of the compressional crossing ratio for an interface such as between the Captain and Rødby Formations

Note: Compressional crossing is predicted for a range of tensile strengths from 1 to 10 MPa [145 to 1450 psia]. In these cases, the fracture would reinitiate across the interface with an offset, creating a discontinuous fracture.

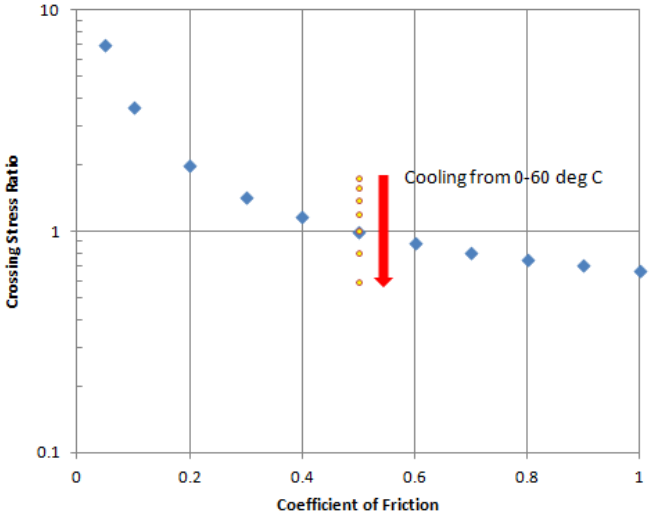

Fig. 6-24—Calculation of the compressional crossing ratio for an interface such as between the Captain and Rødby Formation

Note: The effects of cooling on the major and minor principal stresses have been calculated according to the analytical solution by Perkins and Gonzalez **(65)**. As cooling reduces the stress difference, the results suggest that initially compressional crossing would occur, however, if cooling was sufficient, then the stress difference moves below the threshold indicating interface slip would occur.

6.5. Condition #4: sufficient permeability increase within the created fracture

In the above analysis, the focus has been on whether tensile or shear failure of the Rødby Shale is expected. Implicit in this is the assumption that failure will lead to a significant leakage of CO_2 through the Rødby Shale. In order for this to occur, failure should result in significant dilation, and subsequently permeability increase. Generally speaking, brittle behaviour leads to dilation and permeability increase while ductile behaviour leads to compaction and permeability reduction. Industry experience of leakage from injection projects is predominantly concerned with tensile failure, where high injection pressure exceeds the caprock minimum principal stress and hydraulic fracture is formed. However, shear failure and permeability increase is more equivocal in nature.

Whether shale shows brittle or ductile behaviour depends on the stress history, clay content, degree of cementation and other parameters (79). Normally consolidated shales tend to deform in a ductile way, while overconsolidated, i.e. shales that were exposed in the past to higher stresses than present day stresses, or well-cemented shales exhibit brittle behaviour. The reduction of total mean stress by cooling of the shale would bring it into an overconsolidated state, more prone to brittle failure.

It is also known, from X-ray diffraction data and dielectric constant measurements, that the Rødby Shale should have a high smectite constant. Smectite-rich rocks generally have a low friction angle, a low pre-consolidation pressure and a low to zero dilation angle (80). This means that they are expected to behave in a ductile rather than in a brittle fashion. Smectite rich rocks also hydrate easily and disperse in water, thus a water pill applied prior to injection could be a mitigation measure. In any case, at this point, brittle deformation of the Rødby Shale cannot be excluded in the unlikely event of cooling induced rock failure.

Permeability measurements on shales are limited, especially coupled to the degree of deformation, due to the technical challenges associated with fluid flow through such low permeability rocks. The Swiss National Cooperative for the Disposal of Radioactive Waste (NAGRA) project performed a number of deformation experiments on Opalinus Shale, and coupled those measurements to permeability (81). The Opalinus Shale is immature shale, which contains some smectite, similar to the Rødby Shale. Shear deformation of samples taken perpendicular to the foliation, as is representative for the in-situ geometry of the shale, showed a reduction in initial permeability (10^{-18}-10^{-19} m^2/s) upon an increase in stress. In addition, these experiments were repeated for samples taken parallel to the foliation (initial permeability 10^{-15}-10^{-16} m^2/s), which showed similar behaviour. At low confining pressure, some increase in permeability was observed upon failure, though the final permeability value would not exceed the initial permeability. At higher confining pressure (> 5 MPa [725 psia]), no increase in permeability was observed upon failure of the rock.

These measurements suggest that the ductile nature of the Rødby Shale will most likely not lead to significant permeability changes upon failure.

6.6. Conclusions

As mentioned at the start of this Chapter, in order for thermal cooling induced failure to become a containment issue, four key conditions need to be met. The findings for each of these conditions, for our three different cases, are summarised in **Table 6-10**. Detailed summaries of our findings for the near well bore and farther field scenarios are given below.

Table 6-10—Overview of the four key conditions for the different cooling area: 1) near wellbore area, within the cemented region of the caprock ; 2) near wellbore area, within the open hole section of the caprock; and 3) in the farther field of the reservoir and at the base of the caprock.

Location	Condition #1: Thermal stress	Condition #2: Replenishment	Condition #3: Interface propagation	Condition #4: Permeability
Near wellbore, cemented region	Potential issue under worst case conditions	Unlikely due to complex shape of fractures	n.a.	Not significantly increased due to ductile nature of shale
Near wellbore, open hole	Temperature decrease leads to stabilisation		n.a.	
Farther field base of caprock	Potential for fracturing of the reservoir and/or caprock		Propagation from reservoir to caprock unlikely	

6.6.1. Near wellbore, within the cemented region and within the open hole

In the cemented section above the casing shoe, the results of the analysis presented here show a very low probability of failure of the caprock. Analysis of the caprock below the casing shoe also shows a very low probability of failure due to thermal loading. Failure could lead to a permeability decrease (ductile behaviour) or permeability increase (brittle behaviour). As mentioned in Section 2.1.6, the CO_2 flux from the permeability increase is likely to be negligible. Regardless, it is recommended to apply a water pill prior to injection to increase the likelihood of ductile behaviour.

6.6.2. Farther field reservoir and at the base of the caprock

As the simple uniaxial thermo-elastic calculations have demonstrated, only where cooling of 50-60°C is coupled with the higher injection pressures predicted in the latter part of the injection period is there a possibility of hydraulic fracturing in the Rødby Shale.

For more sophisticated PWRI-Frac analyses, taking into account diffusive cooling of the caprock, results showed that even in the worst case scenario, where the Rødby fracture gradient was significantly lower than the Captain reservoir fracture gradient, that the hydraulic fracture was still predicted to be contained in the Rødby Formation.

The PWRI simulations applied the full thermo-elastic stress reduction to the Rødby fracture gradient, thus simulating the case where the full 60°C cooling occurred throughout the fracture with time. In reality the fluid dynamics within the fracture will be complex and warm-back from the formation would occur. A review was conducted of fracture morphology which confirms that the detailed morphology of fractures is complex, with numerous branching and rock heterogeneities which impact the hydraulic fracture propagation. These complex morphologies would make the replenishment of the supercritical CO_2 at the fracture face unlikely and hence the temperature reduction at the fracture face will be significantly less than the 60°C for the majority of the propagating fracture.

Thermo-elastic stress and the impact on hydraulic fracturing has been studied in the past, most often in the context of stimulation treatments, water flooding or disposal scenarios. Using the analytical solution of Perkins and Gonzalez (65) for a 2D stress field and a elliptical cooled zone around a hydraulic fracture, it was found that the minor principal stress, the minimum horizontal stress acting perpendicular to the fracture, was reduced much less than the major principal stress, the vertical stress acting parallel to the hydraulic fracture. Using the input parameters for the Rødby Formation, the stresses in the elliptical cooled zone were significantly greater than the calculated injection pressures over the full ten year time period. This analytical solution predicts hydraulic fracturing would not occur in the Rødby Formation.

The importance of bedding interfaces on hydraulic fracture growth has been demonstrated in many studies of field data, laboratory experiments and numerical modelling. Using the CCC developed by Renshaw and Pollard (76) it is shown that with the in-situ stresses and rock properties pertaining to the interface of the Rødby and Captain Formations, the calculations support compressional crossing of this interface where no thermo-elastic stresses are incorporated, i.e. discontinuous fracture propagation would occur in the Rødby, with an offset at the interface. However, by integrating the thermo-elastic response for the 2D stress field around a cooled ellipse (65), then the cooling promotes interface slip without fracture propagation in the Rødby Formation. The numerical study by Zhang et al. (74) supports interface slip where a fracture propagates from a stiff material to a less stiff material, such as from the Captain Sandstone to the Rødby Shale.

7. Onset of fault slip

Pressure changes in the reservoir due to gas depletion or CO_2 injection can potentially open fractures and cause slip on faults that exist in the reservoir and overburden formations. In Section 2.1.7, fault reactivation was discussed in general terms. In this section an attempt is made to quantify assess the fault stability in the Goldeneye field at the end of the injection period. The idea is to focus on the stress injection response within the reservoir and to map these computed stresses on the faults. A methodology to quantify and investigate the onset of fault slip is by using the Coulomb friction law, which uses these mapped stresses. This is a frequently employed, commonly accepted, and simple way to take into account the resistance to fault slip. It should be noted that this is a simplified representation of reality, as in nature, faults reactivation and movement will depends on the weakest element on the fault plane (82), whereas in this analysis the fault plane is assumed to have constant failure properties (friction and cohesion). When applying this criterion the following assumptions need to be made:

- The initial stress state of the faults, before depletion or injection, is the same as the initial stress state of the surrounding rock.
- The onset of fault instability is caused by the perturbation of the initial stress state.
-

The results for the faults that are investigated in this section have to be interpreted as the outcome of possible scenarios applied to potential faults. Section 7.3 reports more details on the uncertainty of this prediction. In the following, first a deterministic approach will be presented followed by an uncertainty assessment.

7.1. Principle of fault stability

Increased formation pressures due to CO_2 injection can potentially open fractures and cause slip on faults that exist in the reservoir and overburden formations. Increasing the pore fluid pressures (P_p) on faults leads to lower effective stresses, defined as $\sigma' = \sigma - P_f$. Positive effective normal stresses $\sigma_n' = \sigma_n - P_p$ press opposing fault blocks together and resist the sliding motion along the fault surface, which can be induced by shear stresses (τ) acting parallel to the fault as shown in **Fig. 7-1.** Thus, an increasing pore fluid pressure decreases the effective normal stress and therefore increases the risk of sliding.

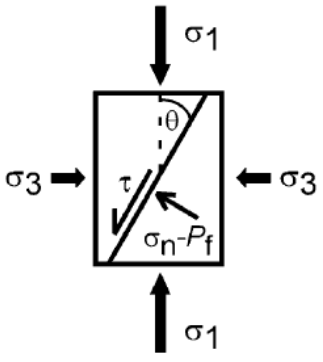

Fig. 7-1—Schematic diagram showing the stresses acting on a fault

The shear and effective normal stresses that act on a fault segment are a function of the fault orientation and in 2D are given as (see also Chapter 2 of Fjaer et al (36))

$$\tau = \tfrac{1}{2}(\sigma_1' - \sigma_3')\sin 2\theta,, \tag{22}$$

$$\sigma_n' = \frac{1}{2}(\sigma_1' + \sigma_3') + \frac{1}{2}(\sigma_1' - \sigma_3')\cos 2\theta, \tag{23}$$

where,

τ is the shear stress, acting on the fault plane, potentially causing sliding,

σ_n' is the effective normal stress that resists sliding,

$\sigma_1' = \sigma_1\text{-}P_p$ is the effective maximum principal stress,

$\sigma_3' = \sigma_3\text{-}P_p$ is the effective minimum principal stress, and

θ is the angle between the normal to the fault and σ_1 as shown in Fig. 7-1.

As θ is of direct importance for fault slip analysis, knowledge of the orientation of the stresses with respect to the orientation of the pre-existing faults is needed for analysing the slip tendency of these faults. From a straight forward Mohr-Coulomb analysis, the shear capacity or SCU parameter can be defined that is a direct indicator for slip tendency (see also Section 4.4.1):

$$\text{shear capacity (SCU)} = \frac{\tau}{C + \sigma_n' \tan\varphi} \tag{24}$$

where, C is the cohesion, and

φ is the friction angle of a fault.

A fault does not slip if the shear capacity is less than one.

7.2. Fault interpretation for the Goldeneye field

Seismic re-interpretation for the Goldeneye field was carried out in July 2010. On (vertically) noisy seismic approximately 40 different potential faults were tentatively identified in the reservoir, caprock and chalk formations. **Fig. 7-2-Fig. 7-5** show the possible faults from different views, and viewpoints in 2D and 3D. The locations are displayed in **Fig. 7-3**. These potential faults, of which the size and vertical positioning might be questionable, are near vertical, have a dominant north-west to south-east trend, and are consistently developed in the eastern flank.

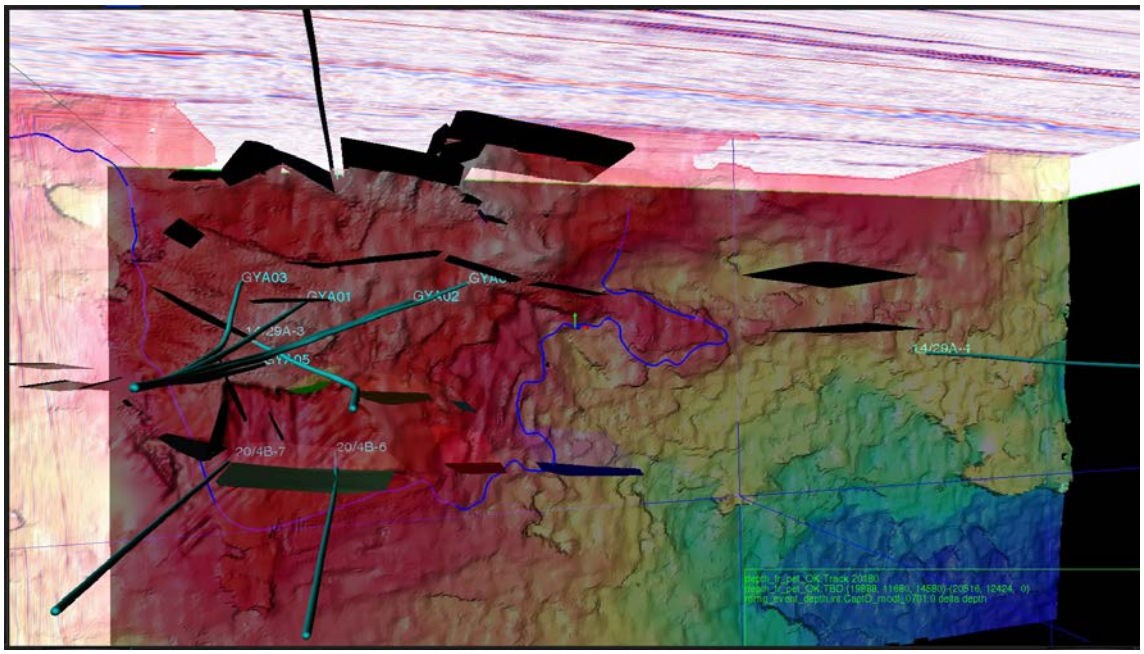

Fig. 7-2—3D top view of the Captain D with potential faults, gas water contact (blue line), wells and seismic sections.

The faults have been interpreted, as sticks, in Shell's proprietary seismic interpretation system, 123DI, exported to gOcad® – where surfaces were generated. Subsequently, the faults were imported into SVS (Simplified Visualisation Software, Shell proprietary), a structural geology and geomechanics tool. In addition, the stress states predicted by GeoMec, for the initial, production and injection phases for different scenarios, were also imported into SVS. SVS then calculated the 3D effective normal stress and maximum shear stress for every single fault plane. Next, the slip tendency as defined in Eq. (25) was calculated by SVS for the three stress stages: before production (initial), after production of the gas, and after having injected the CO_2.

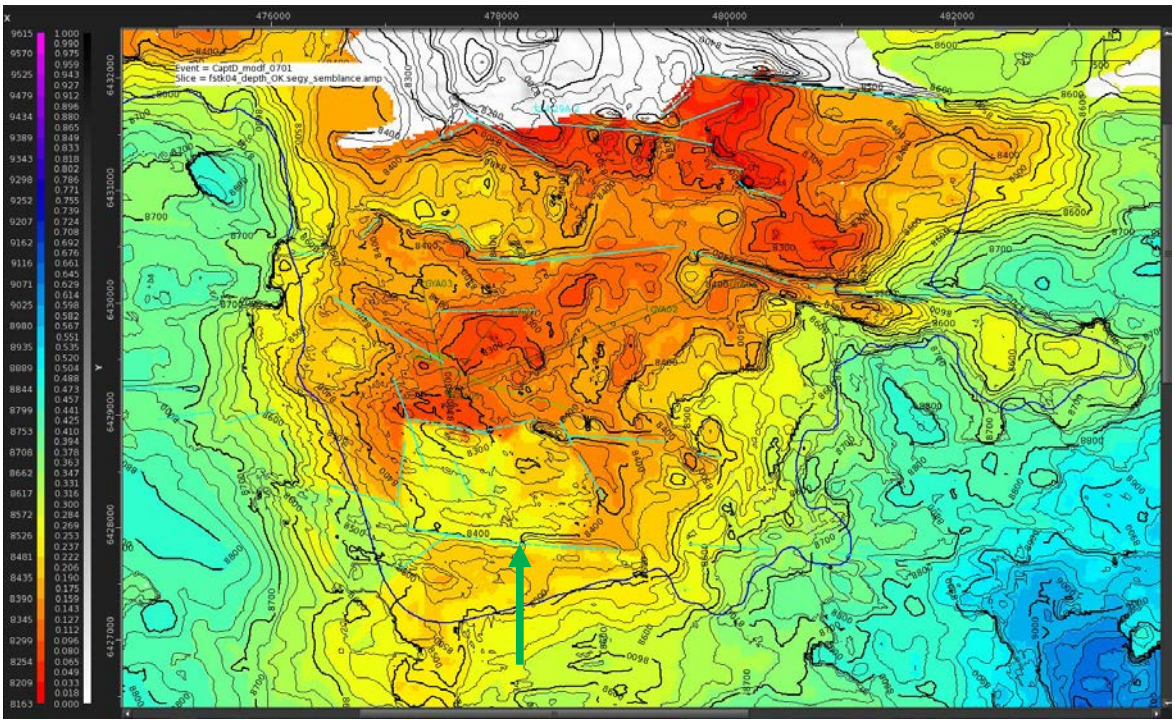

Fig. 7-3—Top view of many potential faults (indicated by green lines) crossing the Captain D reservoir

Note: Axes show northing (vertical) and easting (horizontal) coordinates. The blue curve is the gas water contact. Green arrow points to a fault for reference.

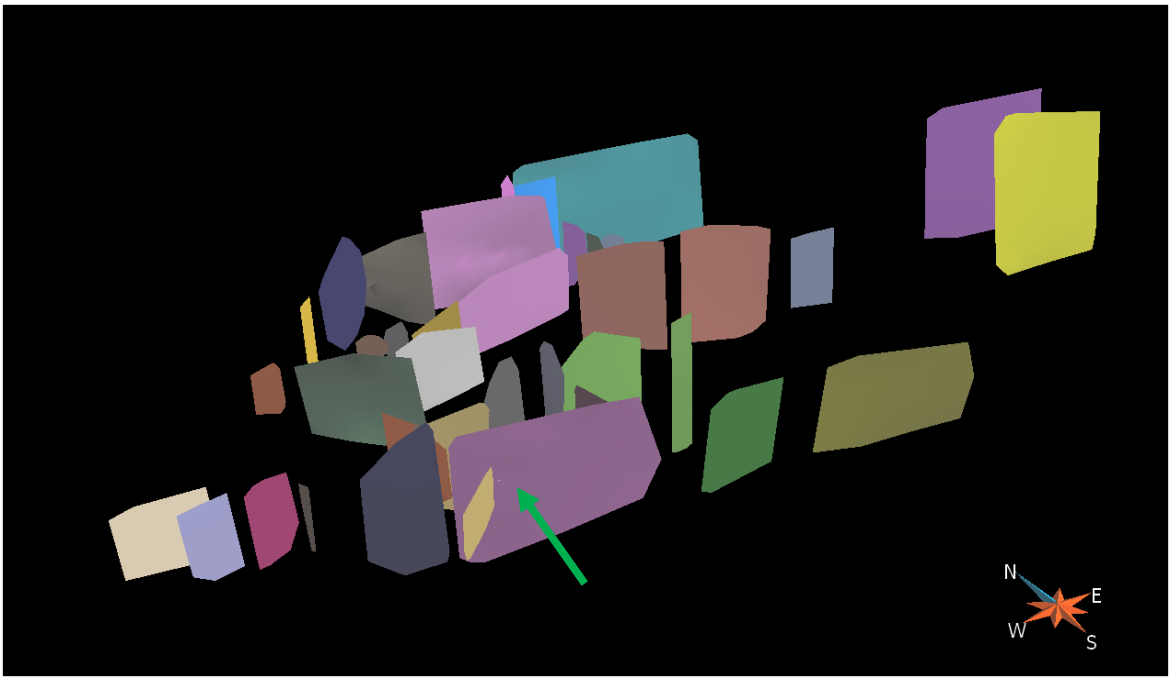

Fig 7-4—3D bird's-eye view (south-west to north-east direction) of many potential faults through the reservoir formations

Note: The green arrow points to a fault that is also indicated in Fig. 7-3 by a green arrow.

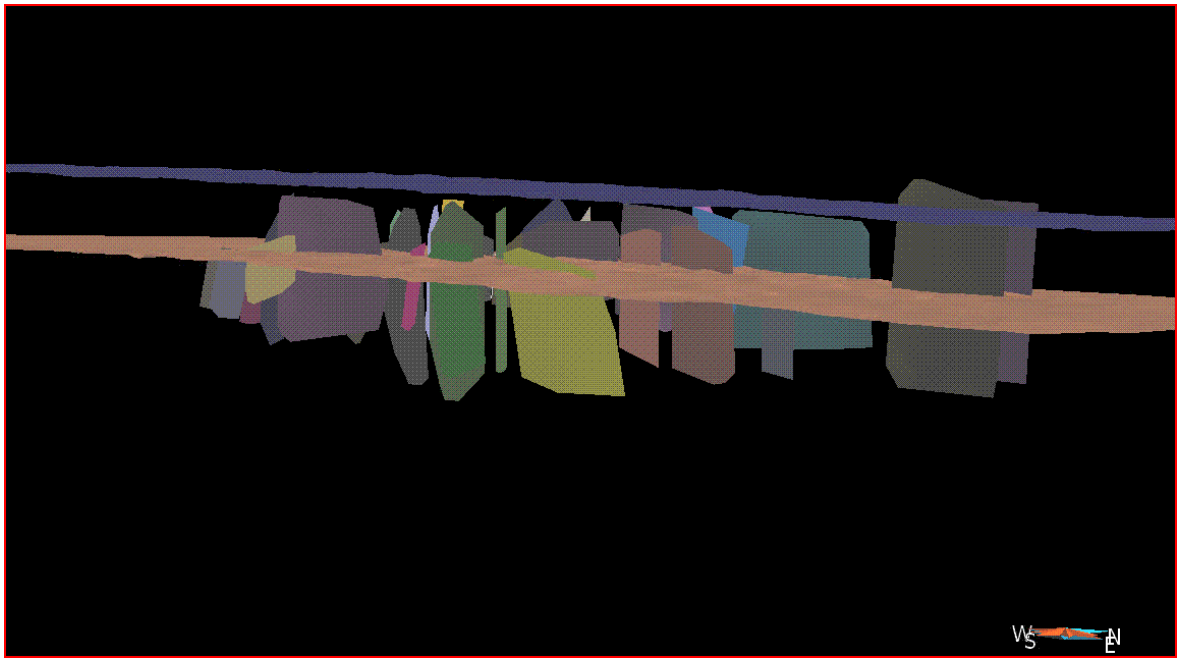

Fig. 7-5—3D bird's-eye view (south-east to north-west direction) of many potential faults through the reservoir formations

Note: Most faults are crossing the Top Rødby (light brown surface) and a few cross the Top Ekofisk (dark blue surface).

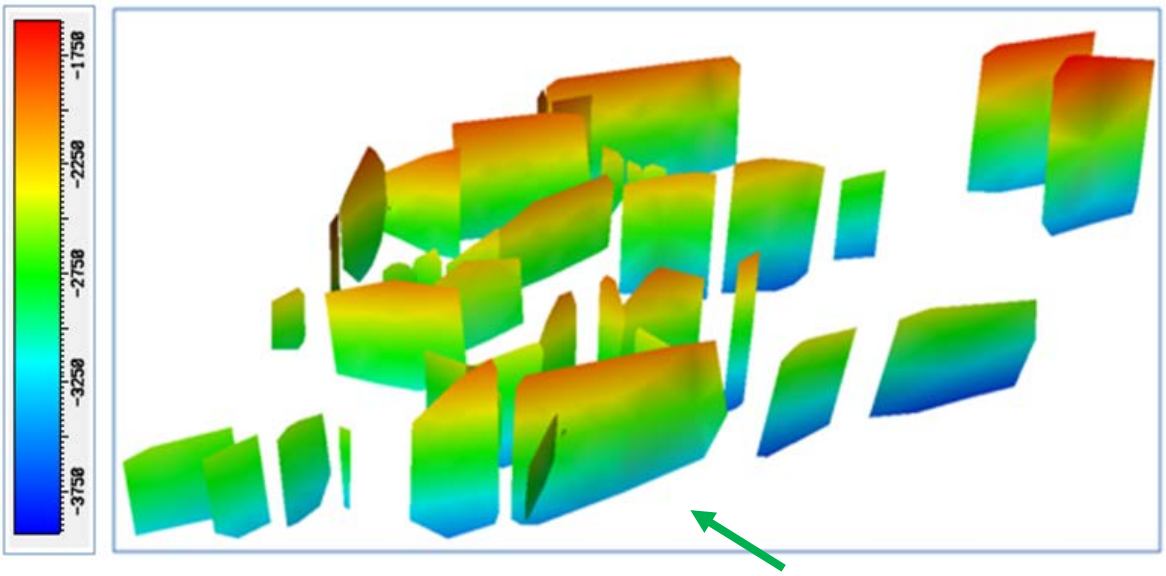

Fig. 7-6—3D bird's-eye view (south-west to north-east direction) of many potential faults

Note: Colours indicate depth in metres and range from 1600 to 3900 m [5249 to 12795 ft]. The green arrow points to a fault that is also marked in Fig. 7-3.

7.3. Deterministic assessment: results and uncertainty

The fault reactivation study is restricted to three scenarios that have been selected from all the different cases as discussed in Chapter 5. First the results from the base case as discussed in Chapter 4 and summarised in Table 5-2 will be used together with fault slip properties that are equal to the

failure parameters (cohesion and friction angle) of the caprock (Rødby Formation). The second case uses the base case data but now the fault slip properties are chosen to be equal to the failure parameters of the Captain E&D reservoir. The third case is investigating the consequences for the worst case scenario parameters, i.e. Case F of Chapter 5 (Poisson's ratio for all the three Captain reservoirs during the injection phase is taken to be 0.45), and fault slip properties are chosen to be equal to the worst case scenario failure parameters. In all three cases the assumption is made that the fault slip properties are close to the failure properties of the formations around the faults. **Table 7-1** summarises these three cases.

Table 7-1—Parameter sensitivity study

SVS Case	Parameter variations as defined in Table 5-1 for stress modelling	Fault rock properties
I	Case A (base case)	C=6 MPa, φ=13° (equal to Rødby caprock)
II	Case A (base case)	C=3 MPa, φ=34.4° (equal to Captain reservoir)
III	Case F (worst case)	C=0, φ=13^0 (equal to worst case for Rødby Shale caprock)

For these cases SVS is used to calculate shear stress and effective normal stress in 3D for every fault plane. Then, shear capacity numbers are plotted on the faults such that fault reactivation can easily be visually inspected. The results of Case I, Case II, and Case III are discussed in the following subsections.

7.3.1. SVS case I: typical failure parameters for Rødby Shale

This section discusses the results for the parameters as defined in Table 7-1 for the SVS case I scenario. Effective normal stress and maximum shear stress after the injection phase are displayed in **Fig. 7-7**. It is observed that the effective normal stress increases with depth from 8 to 41 MPa [1160 to 5946 psia]. As most of the faults are near vertical and this is also the dominant orientation of the maximum principal stress, the magnitude of the maximum shear stress is expected to be low. A variation between 0 and 2.8 MPa [0 to 406 psia] is observed.

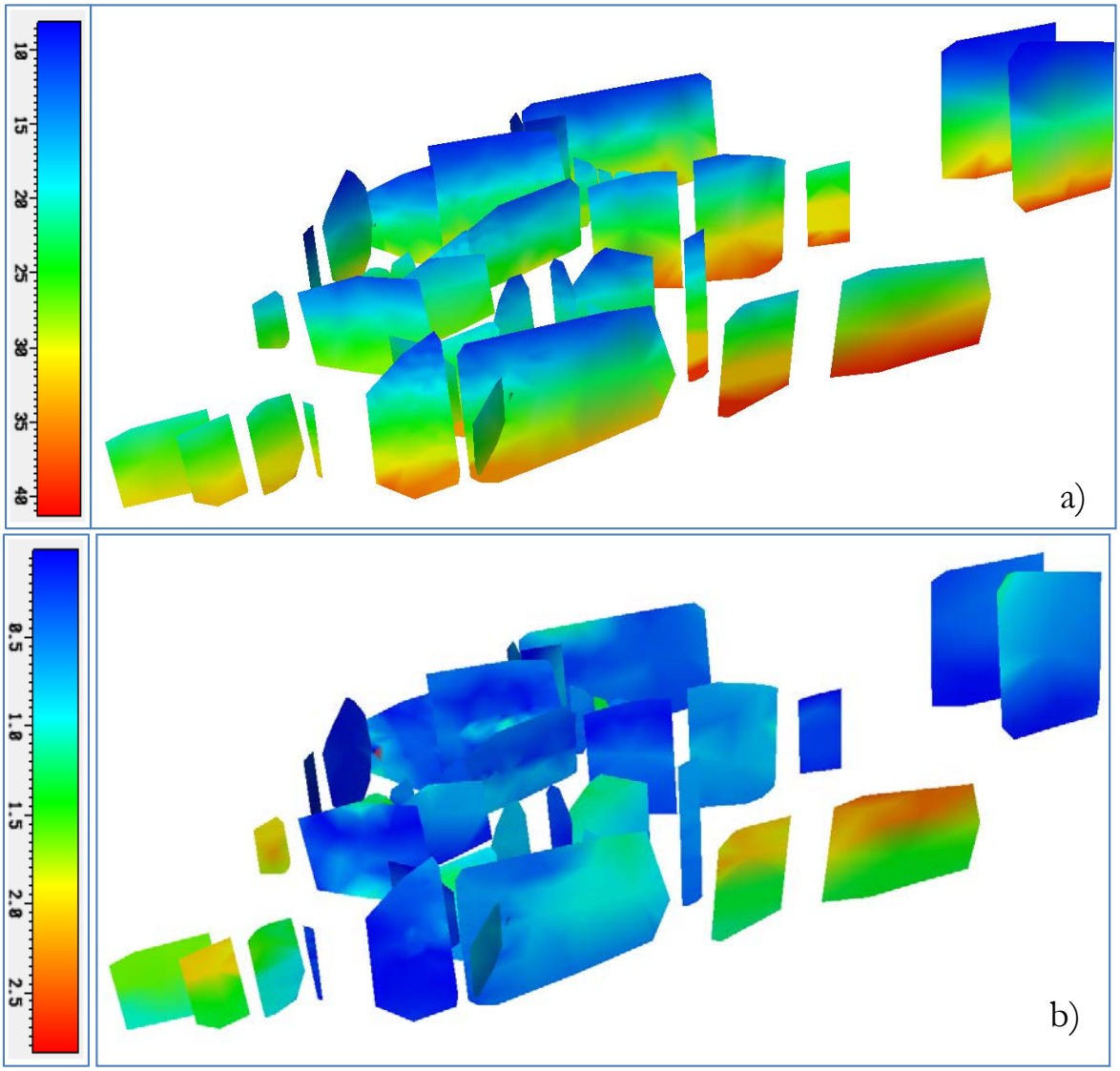

Fig. 7-7—SVS case I scenario after injection: 3D bird's-eye view

Note: (south-west to north-east direction; location and viewing direction are equal to Fig. 7-6) showing (a) the effective normal stress, and (b) the maximum shear stress on all the potential faults. Colours indicate stress in MPa.

As stated above, the fault failure properties are taken to be equal to the failure properties of the caprock, i.e. to the Rødby Formation that has a cohesion of 6 MPa [870 psia] and a friction angle of 13°. **Fig. 7-8** shows the shear capacity results as defined in Eq. (24) at the end of CO_2 injection. The maximum values are around 0.3, no fault-slip is expected to occur on any of the faults. For the stress states before and after production (not shown here) results are approximately equal to those found after injection and thus the same conclusion holds: no fault-slip is expected to occur.

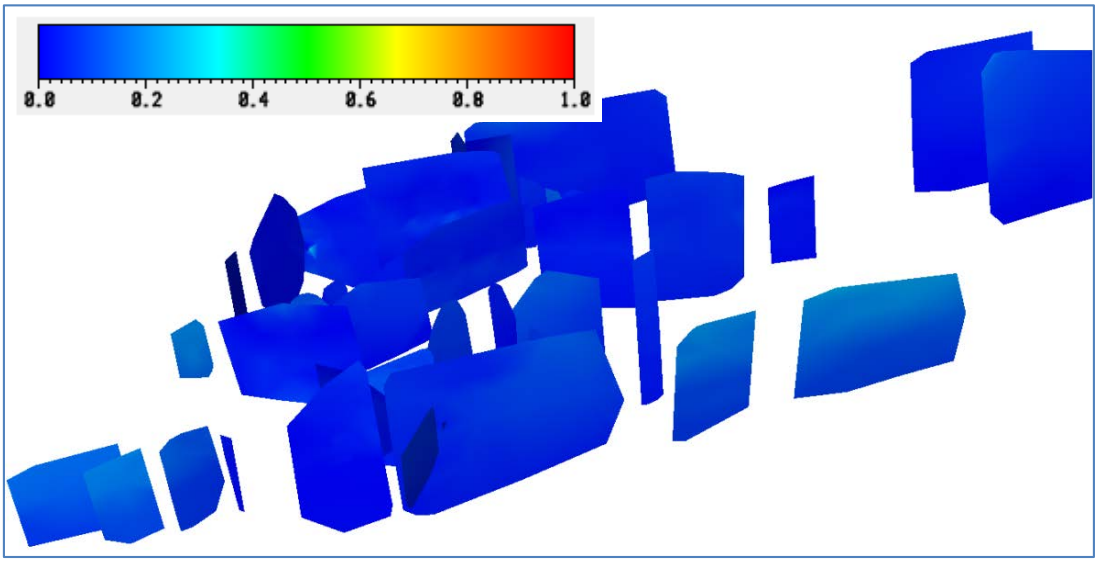

Fig. 7-8—SVS case I scenario: 3D bird's-eye view

Note: (south-west to north-east direction; location and viewing direction are equal to Fig. 7-6) showing, shear capacity results of all the faults after injection. Colours indicate shear capacity (fault slip tendency) in dimensionless units.

7.3.2. SVS case II: typical failure parameters for Captain E&D reservoir

This section discusses the results for the parameters as defined in Table 7-1 for the SVS Case II scenario. Fault failure properties are taken to be equal to the failure properties of the Captain E&D reservoir, which has a cohesion of 3 MPa [435 psia] and a friction angle of 34.4°. **Fig. 7-9** shows the shear capacity results as defined in Eq. (24) after injection. The maximum values are around 0.18 and no fault-slip is expected to occur. For the stress states before and after production, results are approximately equal to those found after injection and thus the same conclusion holds: no fault-slip is expected to occur.

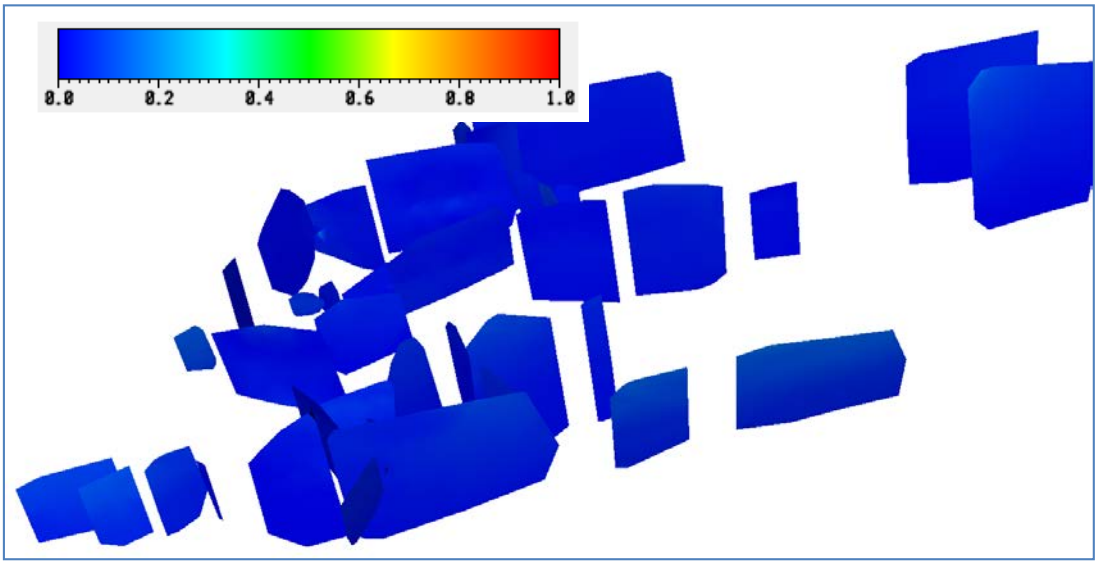

Fig. 7-9—SVS case II scenario: 3D bird's-eye view

Note: (south-west to north-east direction; location and viewing direction are equal to Fig. 7-6) showing shear capacity results of all the faults after injection. Colours indicate shear capacity (fault slip tendency) in dimensionless units.

7.3.3. SVS case III: worst case scenario failure parameters for Rødby Shale

This section discusses the results for the parameters as defined in Table 7-1 for the SVS case III scenario. Fault failure properties are taken to be the worst case scenario failure properties for the caprock, i.e. zero cohesion and a friction angle of 13°. **Fig. 7-10** shows the shear capacity results as defined in Eq. (15) after injection. As the values are at most 0.6, no fault-slip is expected to occur. For the stress states before and after production, results are approximately equal to those found after injection and thus the same conclusion holds: no fault-slip is expected to occur.

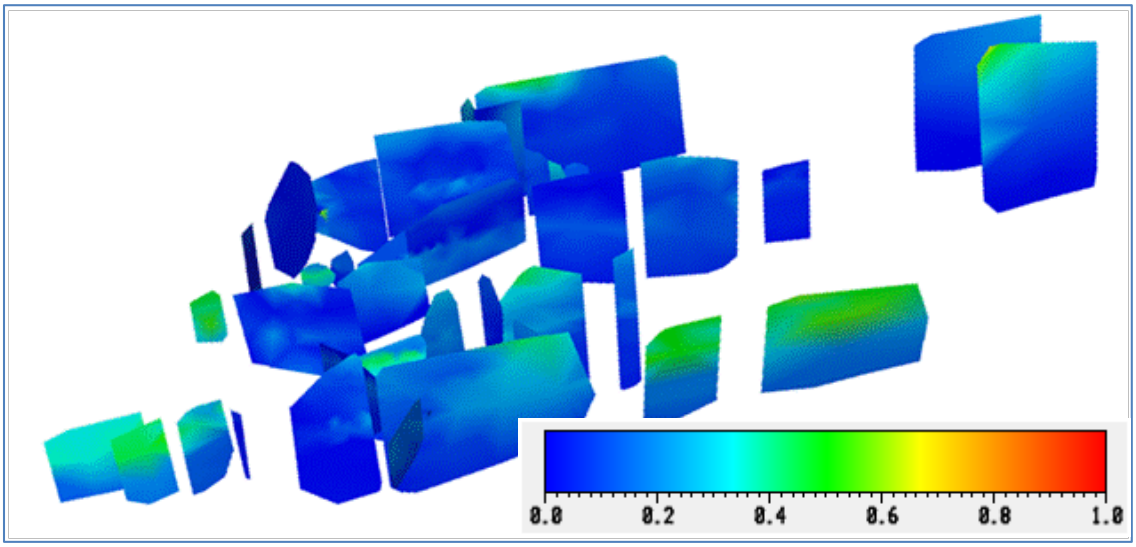

Fig. 7-10—3D bird's-eye view

Note: (south-west to north-east direction; location and viewing direction are equal to Fig. 7-6) showing, for the SVS case III scenario, shear capacity results of all the faults after injection. Colours indicate shear capacity (fault slip tendency) in dimensionless units.

7.4. Uncertainty analysis: distribution of elastic fault properties

To assess the likelihood of fault slippage, a full probabilistic approach is followed taking into account the uncertainty in all main formations and fault properties. This means that instead of distinct values, (normal) probability distribution functions are assumed as the input parameters of the model and that hence the predicted results are distributed over a range of values. Normal distributions with P10, P50, and P90 values were assumed to hold for the Young's modulus and Poisson's ratio of the Ekofisk, Rødby, Captain, Humber and Heron Formations, as well as the cohesion and friction angle of the faults **(Table 7-2).** This resulted into the geomechanical modelling of 18 different scenarios, determined by an experimental design method. GeoMec has been used to calculate the total and effective stress on the fault plane after depletion and after subsequent CO_2 injection. SVS has been used to investigate the sensitivity of shear capacity on these parameters

Table 7-2—Normal distribution functions for Young's modulus and Poisson's ratio of the main formations, as well as fault cohesion and friction angle for the faults, specified by their P10, P50 and P90 values.

Formation	Dynamic Young's modulus [GPa] P10 – P50 – P90	Poisson's ratio [-] P10 – P50 – P90
Ekofisk (chalk)	25 – 32 – 39	0.28 – 0.32 – 0.36
Rødby (shale)	5 – 10– 15	0.34 – 0.38 – 0.42
Captain E&D, C, A (sandstone)	8.5 – 13.5 – 18.5	0.14 – 0.17 – 0.20
Humber, Heron	14 – 20– 26	0.26 – 0.30 – 0.34
Fault	**Cohesion [MPa] P10 – P50 – P90**	**Friction angle [degree] P10 – P50 – P90**
All faults	4 – 8 – 12	12 – 18 – 24

Shell proprietary software CORA was used to evaluate the results that came from GeoMec and SVS. The analysis is displayed in a tornado chart in **Fig. 7-11**, which shows that fault cohesion and friction angle have by far the biggest impact on the maximum SCU value for the most critical fault, in this case the fault that has the highest SCU values of all the mapped faults. The expectation value is 0.18, which is the symmetry line in the Tornado plot, and represents the outcome for the P50 values of all uncertain parameters. This P50 value can be considered to be the base case result. The upper and lower bound values for each uncertain parameter are obtained by substituting their P10 and P90. The length of an uncertainty bara is a reflection of the sensitivity and the uncertainty of the corresponding input parameter. The fault cohesion and friction angle are by far the most important parameters. The key learning is that the Young's modulus and Poisson's ratio of the Ekofisk, Rødby, Captain, Heron and Humber Formation layers are not that relevant for fault slip evaluation. Furthermore, it should be pointed out that even in a worst-case scenario, in which all parameters yield the highest SCU, the SCU value remains well below one. In view of the low SCU even in a worst-case scenario, it is not strictly necessary to acquire additional fault data to reduce uncertainties.

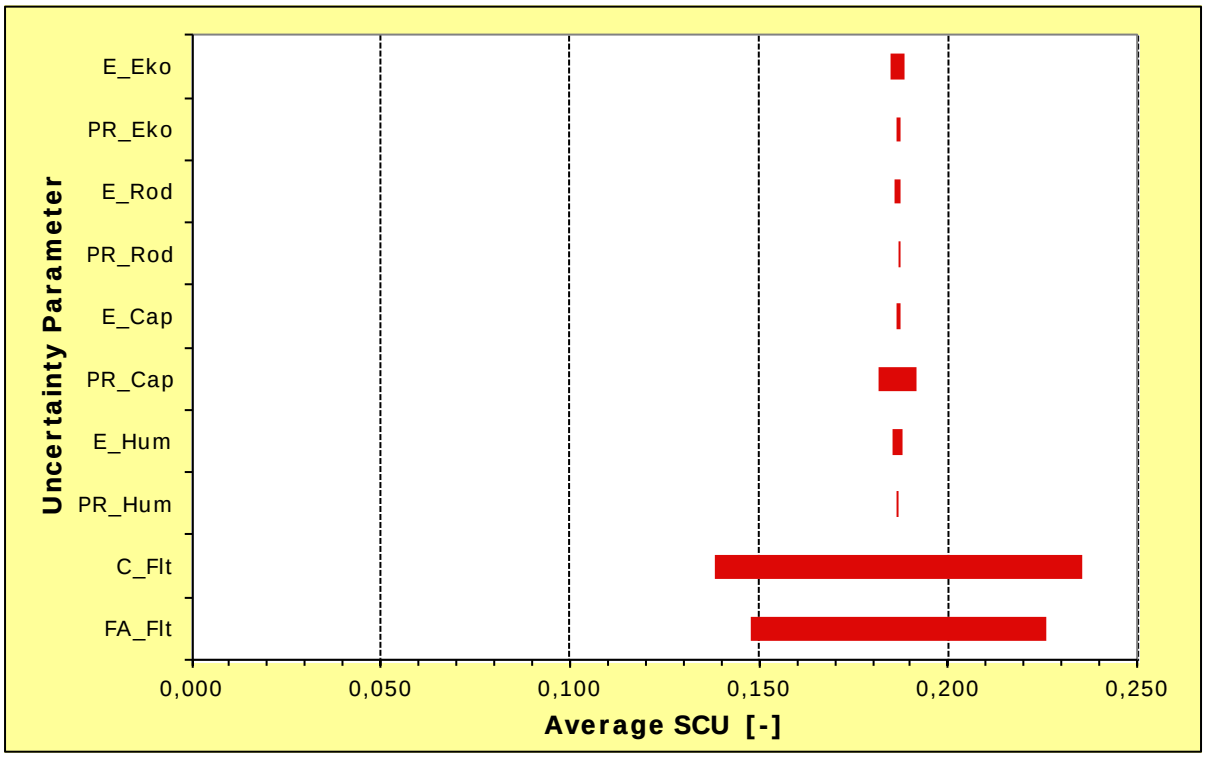

Fig. 7-11—Tornado chart showing the impact of the uncertainties in Young's modulus and Poisson's ratio of the formations, and in fault cohesion and friction angle of the faults, on the maximum SCU of the most critical fault.

The results of the uncertainty analysis confirm the findings of the deterministic (comprehensive) geomechanics evaluation described in the beginning of this section. The likelihood of fault slippage is virtually non-existent.

7.5. Conclusions

For every potential fault the slip-tendency was investigated: in a deterministic expectation case and the impact of uncertainties, by calculating the shear capacity for all the three stress stages (before and after production of the gas, and after injection of the CO_2). No fault-slip is expected to occur. Even the worst case scenario was not significantly close to onset of slip. This conclusion is based on the assumption that the initial stress state of the faults, before depletion or injection, is the same as the initial stress state of the surrounding rock. Further, it was assumed that the faults are not critically stressed. This result implies that if faults are currently not leaking, which they are unlikely to be, given that a gas field is present, then they are extremely unlikely to start leaking as a result of CO_2 injection.

It should be noted that formation offset has a strong impact on the onset of fault slip. In the approach followed here, it is implicitly assumed that no peak shear and normal (effective) stresses occur along the fault plane that could lead to the onset of fault slip at a lower injection level (83; 84).

In case onset of fault slip does occur, for example because the state of stress on the fault is different from that of the surrounding field, or because there are weaker elements in the fault that have not been accounted for, then the creation of a leakage path depends on the permeability of the fault, similar to described in Section 6.5. If fault permeability remains sufficiently low than no significant CO_2 migration would be expected.

Furthermore, it should also be noted that the potential for induced seismicity not only depends on fault reactivation, but also on the frictional stability of the fault. When a fault zone begins to fail, a second order effect takes place in which the coefficient of friction of the fault zone either increases or decreases. The fault has the potential, depending on other factors, to fail seismically (85; 86). Studies on natural (87; 88; 89) and simulated fault gouges (88; 90; 91; 89), composed of quartz, carbonates and/or clays/shale, showed that quartz- and clay/shale-rich generally behave aseismic. In contrast, carbonate-rich fault gouge has the potential to behave seismically at elevated temperatures (T > 120°C) (89).

Given that for the Goldeneye field no onset of fault slip is expected, no induced seismicity is expected either.

8. Risk mitigation of CO_2 migration: barriers in place

The key threats to loss of containment were highlighted in the bow tie diagram shown in Fig. 2-2. Barriers aimed at reducing the risk of containment loss can be divided in a number of categories:

1. Geological barriers: inherent to the geometry, lithology and structure of the field of choice.
2. Operational barriers: put in place by optimising the operational conditions and applying the appropriate technological tools.
3. Geomechanical barriers: linked to the geomechanical properties of the different elements within the storage complex.

This section describes these natural and operational barriers. Some of these barrier act prior to loss of containment (Sections 8.1-8.3), while others serve to limit the extent of migration (Sections 8.4-8.6).

8.1. Geological barrier: geology of the field

The Goldeneye field has a thick caprock, in the form of the Rødby Shale (~60 m [197 ft] thick), which, when intact, will act as a sufficient barrier to upward migration of the CO_2 by buoyancy forces. Numerical modeling efforts have shown that failure of the caprock is not to be expected considering its thickness (see Sections 4.5 and 6.2.2).

8.2. Geological barrier: structural trapping

Trapping within the Goldeneye field will occur via a three-way dip closure and a pinch out in the north. No major faults were identified within the Captain Sandstone reservoir and the Rødby Shale caprock, or bounding the field – see Section 7.2. However, a total number of 43 smaller faults, located within the reservoir, were inferred from seismic data.

It should be kept in mind that the occurrence of a gas reservoir at the Goldeneye field proves that the caprock, and any faults within the field, provide sufficient sealing at the virgin gas pressure, i.e. at 26 MPa [3770 psia]. For the injection of 20 million tonnes the maximum CO_2 pressure will be maintained well below this virgin pressure. No reactivation of faults is to be expected (cf. Chapter 7). Furthermore, given the mineralogical composition of the main formations within the storage complex (sandstone and clay-rich shale), induced seismicity is not expected.

8.3. Operational barrier: bottom hole pressure

The integrity of the storage complex could potentially be affected by the initiation and growth of fractures within the storage reservoir. Generally speaking, fracturing of the Captain E&D reservoir is undesirable, as it affects CO_2 plume migration and can potentially result in CO_2 fingering, leading to loss of conformance. However, it is not considered to affect containment of the system unless the induced fractures propagate upwards into the seal(s), and remain conductive.

In order to prevent reservoir fracturing, it should be ensured that the maximum bottom-hole injection pressure remains below the minimum fracture extension pressure within the Captain E&D Sandstone. If pressures in the reservoir and around the wellbore remain below this value, new fractures are not likely to be induced, and any existing open natural fractures are not likely to propagate.

8.4. Operational barrier: tracking wellbore leakage

The emplacement of downhole temperature and pressure systems can be used to monitor any changes within the wellbore. Such temperature changes can be caused by CO_2 migrating up along the well bore casing. By timely identification of such migration appropriate actions can be taken to limit the extent of leakage, and mitigate loss of containment.

8.5. Geomechanical barrier: fracturing of the caprock by thermal effects

In the case of the *Barendrecht* CCS project, two barriers were defined that were expected to mitigate the thermal effects of CO_2 injection on the stress state. The first barrier was concerned with the implementation of a heater at the injector well, effectively reducing the temperature difference between the injected CO_2 and the formations. The second barrier relates to the state of stress and pore pressure in the caprock. Similar to the reservoir, the minimum horizontal stress within the caprock remains higher than the CO_2 injection pressure (cf. Fig. 3-8). This means that inducing tensile fracturing in the caprock is unlikely, even when worst case scenario thermal cooling effects are taken into account (Section 6.2.2). Furthermore, the pore pressure in the caprock will most likely be higher than in the reservoir, as the low permeability of the caprock leads to a delayed response of caprock pore pressure decrease to depletion. Therefore, in the unlikely case of tensile fracturing at the base of the caprock, the higher pore pressure in the caprock will prevent CO_2 from entering the fracture, as the pressure gradient is pointing form the caprock into the reservoir.

It should be noted that any thermally-induced fracturing only persists if cold CO_2 keeps being provided to the tip of the fracture – as discussed in Section 6.3. Similarly, when the injection well is shut-in, re-heating of the cooled sections of the reservoir and caprock will occur again. As a result, pore pressure will increase, which affects the effective stresses within the system. The magnitude of this re-heating on pressure can be quantified using well shut-in pressure data. However, as the injection pressure of the CO_2 is well below the minimum horizontal stress within the reservoir and the caprock, it is unlikely that re-heating of the reservoir, e.g. upon abandonment, will result in fracturing. In essence, this scenario is similar to those that do not take into account any thermal effects, such as presented in Chapters 4 and 5.

8.6. Geomechanical barrier: fracture propagation across interface

As pointed out above (cf. Section 8.1), fracturing of the Captain E&D reservoir is undesirable, but does not threaten containment unless the induced fractures propagate upwards, into the overlying seal formation, and remain open. It is known that opening-mode fractures propagate perpendicular to the direction of minimal stress, which is often orientated vertically within homogeneous formations. However, there are several mechanisms able to arrest this vertical fracture extension within the formations in the Goldeneye storage complex. As was discussed in Section 6.4, under the initial temperature conditions within the reservoir compressional crossing across the interface is possible. However, as cold CO_2 is injected into the Captain Sandstone reservoir, any new fractures created in the reservoir will no longer propagate across the reservoir-caprock interface. Instead, due to the drop in compressional crossing ratio interface slip would occur instead.

9. Conclusions

9.1. General conclusions from the geomechanical modelling efforts

The geomechanical integrity of the Captain E&D reservoir and the Rødby Shale caprock was investigated using a geomechanical simulator. The geomechanical model was composed of the following:

- The structural geometry of the reservoir, overburden and underburden formations,
- In-situ stress and pore pressure profile,
- Mechanical rock properties of all formations, and
- Pressure changes in the reservoir due to depletion and injection.

Apart from the structural geometry, for each of these components a range of values were identified with varying likelihood. The values with the highest likelihood were used to define a so-called "base case" model. Those values with a negative effect on integrity, with respect to the base case, were used to define a so-called "worst case" models. With these models, the sensitivity of the geomechanical model to the different parameters, and combinations of them, was studied. General criteria for tensile failure and Mohr-Coulomb shear failure were used to define norms, and to quantify the risk of failure.

Overall, the geomechanical simulations, for both the base case and worst case scenarios, showed no risk of tensile failure or shear failure within either the reservoir or the overlying caprock, for the intended injection pressure [20 Mt CO_2 at 2 Mtpa], which is well below the minimum total principal stress in the reservoir.

In addition to the overall integrity of the reservoir-caprock system, the potential for fault slip reactivation was also rigorously investigated. The results obtained for these faults, interpreted from seismic, are to be interpreted as the outcome of a possible scenario. For every fault, the slip-tendency was investigated by calculating the shear capacity for all three stress stages, i.e. before and after production of the gas, and after injection of CO_2. Overall, no fault-slip was expected to occur, for any of the faults. Even for the worst case scenario, none of the faults was significantly close to slip. This conclusion was based on the assumption that the initial stress state of the faults, before depletion or injection, is the same as the initial stress state of the surrounding rock. Further, it was assumed that the faults are not critically stressed. These results implied that if faults are currently not leaking, which they are unlikely to be, given that a gas field was present, then they are extremely unlikely to start leaking as a result of CO_2 injection.

There are a number of geomechanical threats that can potentially affect the integrity of the storage complex. One of these threats is the difference in temperature between the lower temperature, near wellbore area in the top of the reservoir and the bottom of the overburden compared to the higher temperature, formation temperature. This cooling will induce significant stress and strain changes in the reservoir and the overburden near the wellbore. Therefore, the possibility of failure of the caprock in the near wellbore region due to temperature changes and the possibility of migration resulting from failure required investigation. In the cemented section above the casing shoe, the results of the analysis presented showed a very low probability of failure of the caprock. Analysis of the caprock below the casing shoe also showed a very low probability of failure due to thermal loading. Should failure occur, it is not clear if it would lead to significant migration, as failure could

lead to a permeability decrease (ductile behaviour) or permeability increase (brittle behaviour). However, in this case, the CO_2 flux from the permeability increase is expected to be negligible. The introduction of a water pill before injection has the potential to enhance ductile behaviour of the caprock however it could also lead to damage of the gravel pack. It is therefore recommended that this possible mitigation strategy be explored as part of the well workover design.

For the farther field, the behaviour of the Rødby Formation caprock directly adjacent to the cold plume of CO_2 in the Captain reservoir was also investigated. The simple uniaxial thermo-elastic response of the Rødby to 60° C cooling showed that, for the high case Young's modulus and linear thermal expansion coefficient, it is possible that with time the injection pressure in the field becomes high enough to induce tensile failure (under this simplified model). To understand this risk, fracture growth into the Rødby Shale formation was studied using a hydraulic fracture modelling tool (PWRI-Frac), and taking into account fracture morphology considerations. It was shown that significant fracture growth within the caprock was highly unlikely. This conclusion was underpinned by a 2D analytical study of the in-situ stresses undergoing thermal alteration in an elliptical zone, which confirmed that the minimum principal stress remained significantly greater than the predicted injection pressures for the 10 year injection period. On the basis of the rock properties, in-situ stresses and pore pressures, it was concluded that hydraulic fracture from the Captain reservoir into the Rødby caprock will not occur, but instead that slip along the reservoir-caprock interface is most likely.

10. Glossary of Terms

Term	Definition
123DI	Shell proprietary software used for seismic interpretation
1D, 2D, 3D	One, two, three Dimensional
ALARP	As Low As Reasonably Practicable, and is a term often used in the environment of safety-critical and high-integrity systems. The ALARP principle is that *the residual risk shall be as low as reasonably practicable*
Barrier	Barriers prevent or mitigate the probability of each threat or prevent, limit the extent of, or provide immediate recovery from the Consequences
Bg	Formation Volume Factor (Gas)
BHP	Bottom Hole Pressure
Bo	Formation Volume Factor (Oil)
Bow-Tie	The bow-tie is a model that represents how a Hazard can be released, escalate, and how it is controlled. Bow-ties can also be used to support risk management of non-HSSE processes, Hazardous Activities, and HSSE critical processes
CBIL	Circumferential Borehole Imaging Log
CCS	Carbon Capture & Storage
CO_2	Carbon Dioxide
CoP	Cessation of Production
DIANA	Software package from TNO that solves, with the aid of FEM, problems relating to design and assessment activities in concrete, steel, soil, rock and soil-structure.
DP	Differential Pressure
EOR	Enhanced Oil Recovery
Escalation Factor	Factors that defeat, or reduce the effectiveness/reliability of a Barrier
ESG	Microseismic monitoring company, Canada. www.esg.ca
FAM	Fairway Aquifer Model
FEED	Front End Engineering Design
FEM	Finite Element Modelling
FFM	Full Field Model
FFSM	Full Field Simulation Model
FMI	Full bore formation Micro-Imager
GBV	Gross Bulk Volume
GeoMec	Shell proprietary software used for modelling stress changes due to reservoir depletion or injection
GIIP	Gas Initially In-Place
gOcad®	3rd Party software to build and update 3D subsurface models
GRV	Gross Rock Volume
Hazard	The potential to cause harm, including ill health and injury, damage to property, products or the environment; production losses or increased liabilities. In this report: buoyant CO_2
HCPV	Hydrocarbon Pore Volume
HSSE	Health, Safety, Security, and Environment
IIP	Initially In-Place (volumes)
Injection phase	The injection phase includes the period of site preparation for injection, the injection period itself and the period of well abandonment
InSAR	Interferometric Synthetic Aperture Radar

IPCC	International Panel on Climate Change
kgW	Kilogram of water (pure H_2O)
KNMI	The Royal Netherlands Meteorological Institute
Leakage	Migrated CO_2 out of the containment that leaks into the biosphere (shallow subsurface and atmosphere). In contrast to seepage, leakage involves medium fluxes and medium concentrations
Leakage scenario	Group of threats that form cause-consequence relations leading to a certain route of migration and eventually leakage into the biosphere
LOP	Leak-off pressure
LOT	Leak-off Test
LT	Limit Test
LTEC	Linear thermal expansion coefficient
Mcf	Thousand cubic feet at reservoir conditions
Migration	Escaped CO_2 out of the containment into the subsurface where it moves or trapped in other layers
MoRes	Shell proprietary software used for simulating fluid flow in a reservoir
Mscf	Thousand cubic feet at standard conditions
NAGRA	Swiss National Cooperative for the Disposal of Radioactive Waste
NAM	Nederlandse Aardolie Maatschappij BV (Joint venture Shell/XOM 50/50)
NPV	Net Pore Volume
NRV	Net Rock Volume
NtG	Net-to-Gross
PBore	3rd Party software to model bore hole stability
PDG	Permanent downhole gauge
Petrel	3rd Party software "seismic to simulation"
pH	measure of the acidity or basicity of an aqueous solution
PVT	Pressure, Volume, Temperature
PWRI-frac	Shell proprietary software used for modelling the effect of fluid injection on fracture development and growth
RFT	Repeat formation tester
Risk management	Risk management is the human activity, which integrates recognition of risk, risk assessment, developing strategies to manage it, and mitigation of risk using managerial resources
SCU	Shear Capacity Utilisation
SEC	Securities and Exchange Commission
SEM	Scanning Electron Microscope
Seepage	Migrated CO_2 out of the containment that seeps into the biosphere (shallow subsurface and atmosphere). In contrast to leakage, seepage involves low fluxes and low concentrations
SRM	Static Reservoir Model
SVS	Simplified Visualization Software, Shell proprietary
TDS	Total Dissolved Solids
Threat	Means by which a hazard can be released and thus cause the top event
TNO	Netherlands organization for applied scientific research
Top Event	Incident that occurs when a hazard is realized, or the release of the hazard. The Top Event is typically some type of loss of control or release of energy. If this event can be prevented there can be no effect or consequence from the hazard
TWT	Two-way time
UBI	Ultra-sonic Borehole Imager
UCS	Unconfined Compressive Strength

UGS	Underground Gas Storage
XLOT	Extended Leak Off Test
XRD	X-ray diffraction

11. Glossary of Unit Conversions

For the provision of the SI metric conversion factor as applicable to all imperial units in the Key Knowledge Deliverable.

Table 11-1: Unit Conversion Table

Function	Unit - Imperial to SI Metric conversion Factor
Length	1 Foot = 0.3048m Metres 1 Inch = 2.54cm Centimetres 1 Inch = 25.4mm millimetres
Pressure	1 Psia = 0.0690 Bara
Temperature	1°F Fahrenheit = -17.22°C Centigrade
Weight	1lb Pound = 0.45kg Kilogram

In the text well names have been abbreviated to their operational form. The full well names are given in **Table 11-2**. Furthermore, volumes quoted at 'standard conditions' assume temperature of 60°F and pressure of 14.7 psia [101.35 MPa]. A conversion of 1 m : 3.28048 ft has been assumed

Table 11-2: Well name abbreviations

Full well name	Abbreviated well name
DTI 14/29a-A3	GYA01
DTI 14/29a-A4Z	GYA02S1
DTI 14/29a-A4	GYA02
DTI 14/29a-A5	GYA03
DTI 14/29a-A1	GYA04
DTI 14/29a-A2	GYA05

12. Bibliography

1. *Aquifer disposal of CO2-rich gases: Reaction design for added capacity.* **Gunter, W.D., E.H. Perkins, and T.J. McCann.** 9-11, 1993, Energy Conversion and Management, Vol. 34, pp. 941-948.

2. *Aquifer disposal of CO2: hydrodynamic and mineral trapping.* **Bachu, S., W.D. Gunter, and E.H. Perkins.** 4, 1994, Energy Conversion and Management, Vol. 35, pp. 269-279.

3. **Hitchon, B.** *Aquifer disposal of carbon dioxide: hydrodynamic and mineral trapping - proof of concept.* Sherwood Park, Alberta, Canada : Geoscience Publishing Ltd., 1996. p. 165.

4. **Hangx, S.J.T.** *Geological storage of CO2 - Mechanical and chemical effects on host and seal formations.* Utrecht : Utrecht University, 2009. p. 234.

5. **Baines, S.J., and R.H. Worden.** The long-term fate of CO2 in the subsurface: natural analogues for CO2 storage. *Geological storage of carbon dioxide.* London : Geological Society of London, 2004, pp. 59-85.

6. *Solubility trapping in formation water as dominant CO2 sink in natural gas fields.* **Gilfillan, S.M.V., B.S. Lollar, G. Holland, D. Blagburn, S. Stevens, M. Schoell, M. Cassidy, Z. Ding, Z. Zhou, G. Lacrampe-Couloume, and C.J. Ballentine.** 7238, 2009, Nature, Vol. 458, pp. 614-618.

7. *Geological CO2 disposal: understanding the long term fate of CO2 in naturally occurring accumulations.* **Baines, S.J. and R.H. Worden.** [ed.] et al. D.J. Williams. Cairns, Australia : s.n., 2000. Proceedings of 5th International Conference on Greenhouse Gas Control Technologies (GHGT-5). pp. 311-316.

8. *Numerical simulation of CO2 disposal by mineral trapping in deep aquifers.* **Xu, T., J.A. Apps, and K. Pruess.** 2004, Applied Geochemistry, Vol. 19, pp. 917-936.

9. *Computer simulation of CO2 trapped through mineral precipitation in the Rose Run Sandstone, Ohio.* **Zerai, B., B.Z. Saylor, and G. Matisoff.** 2006, Applied Geochemistry, Vol. 21, pp. 223-240.

10. *Geomechanical factors affecting geological storage of CO2 in depleted oil and gas reservoirs.* **Hawkes, C., P.J. McLellan, and S. Bachu.** 10, 2005, Journal of Canadian Petroleum Technology, Vol. 44, pp. 52-61.

11. **Johnson, J.W., J.J. Nitao, and J.P. Morris.** Reactive transport modeling of cap rock integrity during natural and engineered CO2 storage. [book auth.] D.C. Thomas and S.M. Benson. *Carbon Dioxide Capture for Storage in Deep Geologic Formations.* s.l. : Elsevier, 2004, pp. 787-813.

12. *Comparison of geomechanical deformation induced by megatonne-scale CO2 storage at Sleipner, Weyburn, and In Salah.* **Verdon, J.P., J.M. Kendall, A.L. Stork, R.A. Chadwick, D.J. White, and .C. Bissell.** 2013, PNAS Early Edition.

13. *Estimating maximum sustainable injection pressure during geological sequestration of CO2 using coupled fluid flow and geomechanical faultslip analysis.* **Rutqvist, J., J. Birkholzer, F. Cappa, and C. F. Tsang.** 6, 2007, Energy Conversion Management, Vol. 48, pp. 1798-1807.

14. *Coupled reservoir-geomechanical analysis of the potential for tensile and shear failure associated with CO2 injection in multilayered reservoir-caprock systems.* **Rutqvist, J., J. T. Birkholzer, and C.-F. Tsang.** 2008, International Journal of Rock Mechanics and Mining Sciences, Vol. 45, pp. 132-143.

15. *Semi-analytical models for stress change and fault reactivation induced by reservoir production and injection.* **Soltanzadeh, H., and C. Hawkes.** 2008, Journal of Petroleum Science and Engineering, Vol. 60, pp. 71-85.

16. *Estimating fault stability and sustainable fluid pressures for underground storage of CO2 in porous rock.* **Streit, J. E., and R. R. Hillis.** 2004, Energy, Vol. 29, pp. 1445-1456.

17. **Shell.** *Static Model (Field) for Goldeneye CCS Project.* Aberdeen : Shell, 2010. PCCS-05-PT-ZG-0580-00004, Key Knowledge Deliverable 11.108.

18. **Global CCS Institute.** Large-scale Integrated CCS Projects 2013. *http://www.globalccsinstitute.com/projects/browse.* [Online] 2013.

19. **Shell.** *Goldeneye CCS Storage Development Plan(SDP).* Aberdeen : Shell, 2011. Scottish Power Consortium UKCCS Demonstration Competition. GCCKT-03-PT-ZG-7753-00008..

20. **Shell.** *MER ondergrondse opslag van CO2 in Barendrecht.* Den Haag : Shell CO2 Storage B.V., 2008.

21. *Comparison of numerical codes for geochemical modelling of CO2 storage in target sandstone reservoirs.* **Gundogan, O, E. Mackay, and A. Todd.** 9, 2011, Chemical Engineering Research and Design, Vol. 89, pp. 1805–1816.

22. *Geochemical interactions between CO2 and minerals within the Utsira caprock: A long-term experimental study.* **Bateman, K., C. Rochelle, G. Purser, S. Kemp, D. Wagner, and A. Benham.** Vienna, Austria : EGU General Assembly, 2013. Geophysical Research Abstracts. Vol. 15.

23. *Feldspar dissolution kinetics and Gibbs free energy dependence in a CO2-enriched groundwater system, Green River, Utah.* **Kampman, N., M. Bickle, J. Becker, N. Assayag, and H. Chapman.** 2009, Earth and Planetary Science Letters, Vol. 284, pp. 473–488.

24. *Geochemistry of CO2 sequestration in the Jurassic Navajo Sandstone, Colorado Plateau, Utah.* **Parry, W.T., C.B. Forster, J.P. Evans, B. Beitler Bowen, and M.A. Chan.** 2, 2007, Environmental Geosciences, Vol. 14, pp. 91–109.

25. **Kampman, N.** *Fluid-rock interactions in a carbon storage site analogue, Green River, Utah.* Cambridge, UK : Cambridge University, 2010. p. 272.

26. *Onshore Otway Basin carbon dioxide accumulations: CO2-induced diagenesis in natural analogues for underground storage of greenhouse gas.* **Watson, M.N., N. Zwingmann, N.M. Lemon, and P.R. Tingate.** 2003, APPEA Journal, pp. 637-653.

27. *The Ladbroke Grove-Katnook carbon dioxide natural laboratory: a recent CO2 accumulation in a lithic sandstone reservoir.* **Watson, M. N., N. Zwingmann, and N. M. Lemon.** 2004, Energy, Vol. 29, pp. 1457-1466.

28. *Geochemical Reactivity Report.* **Shell.** Rijswijk : Shell, 2010. UKCCS-KT-S7.19-Shell-003..

29. *Experimental investigation of the CO2 sealing efficiency of caprock.* **Wollenweber, J., S. Alles, A. Busch, B.M. Krooss, H. Stanjek, and R. Littke.** 2, 2010, International Journal of Greenhouse Gas Control, Vol. 4, pp. 231-241.

30. *Carbon dioxide storage potential of shales.* **Busch, A., S. Alles, Y. Gensterblum, D. Prinz, D.N. Dewhurst, M.D. Raven, H. Stanjek, and B.M. Krooss.** 3, 2008, International Journal of Greenhouse Gas Control, Vol. 2, pp. 297–308.

31. *Experimental characterisation of the hydrocarbon sealing efficiency of cap rocks.* **Schlömer, S., and B.M. Krooss.** 1997, Marine and Petroleum Geology, Vol. 14, pp. 565-580.

32. *Molecular transport of methane, ethane and nitrogene and the influence of diffusion on the chemical and isotopic composition of natural gas accumulations.* **Schlömer, S., and B.M. Krooss.** 2004, Geofluids, Vol. 4, pp. 81-108.

33. *Site-specific geomechanical modeling for predicting stress changes around depleted gas reservoirs considered for CO2 storage in the Netherlands (ARMA 13-446).* **Orlic, B.** San Francisco, USA : American Rock Mechanics Association, 2013.

34. *Reservoir stress path: The depletion and the rebound.* **Santarelli, F.J., Tronvoll, J.T., Svennekjaer, M., Skeie, H., Henriksen, R. and Bratli, R.K.** Trondheim : SPE, 1998. SPE/ISRM Eurock '98. Norway, 8-10 July. SPE 47350.

35. **Shell.** *Goldeneye CCS Injection Fraccing Conditions.* Aberdeen : Shell, 2010. Scottish Power Consortium UKCCS Demonstration Competition. UKCCS-KT-S7.18-Shell-004.

36. **Fjaer, E., Holt, R.M., Horsrud, P., Raaen, A. M. and Risnes, R.** *Petroleum related rock mechanics.* s.l. : Elsevier Science Ltd., 2008.

37. *Experimental assessment of brine and/or CO2 leakage through well cements at reservoir conditions.* **Bachu, S., and D.B. Bennion.** 2009, International Journal of Greenhouse Gas Control, Vol. 3, pp. 494–501.

38. **Zoback, M.** *Reservoir Geomechanics.* Cambridge, UK : Cambridge University Press, 2007.

39. *Bergermeer seismicity study.* **Muntendam, A.G., Wassing, B.B.T., Geel, C.R., Louh, P. and van Thienen-Visser, K.** Utrecht : TNO, 2008. TNO report 2008-U-R1071/B.

40. *A Full Field Simulation of the In Salah Gas Production and CO2 Storage Project Using a Coupled Geo-mechanical and Thermal Fluid Flow Simulator.* **Bissell, R.C., D. W. Vasco, M. Atbi, M. Hamdani, M. Okwelegbe, and M.H. Goldwater.** 2011. Energy Procedia - GHGT-10. Vol. 4, pp. 3290–3297.

41. *Satellite-based measurements of surface deformation reveal fluid flow associated with the geological storage of carbon dioxide.* **Vasco, D.W., A. Rucci, A. Ferretti, F. Novali, R.C. Bissell, P.S. Ringrose, A.S. Mathieson, and I.W. Wright.** 2010, Geophysical Research Letters, Vol. 37, p. L03303.

42. *Microseismic monitoring and interpretation of injection data from the In Salah CO2 storage site (Krechba), Algeria.* **Oye, V., E. Aker, T.M. Daley, D. Kühn, B. Bohloli, V. Korneev.** 2013. Energy Procedia - GHGT-11. Vol. 37, pp. 4191-4198.

43. **Shell.** *FFM Dynamic Model Report for Goldeneye CCS Project.* Aberdeen : Shell, 2011. UKCCS-KT-S7.21-Shell-005.

44. **Shell**. *Goldeneye CCS Static model (Overburden).* Aberdeen : Shell, 2010. UKCCS-KT-s7.22-Shell-002.

45. *Upscaling mechanical rock properties and pore fluid pressure: An application to geomechanical modelling.* **Schutjens, P., and Snippe, J.** 2009. DEVEX 2009 (presentation 2B1335), Aberdeen, UK, 12-13 May. Oral presentation given at DEVEX 2009 (presentation 2B1335), Aberdeen, UK, 12-13 May. presentation 2B1335.

46. *Tectonic stress in the Earth's crust: advances in the World stress map project, .* **Sperner B., Müller, B., Heidbach, O., Delvaux, D., Reinecker, J. and Fuchs, K.** 2003, Geological Society of London Special Publication 212, pp. 101-116.

47. **WSM.** *World Stress Map Project.* [Online] 2011. http://www.world-stress-map.org .

48. *Shale Stability: Drilling Fluid Interaction and Shale Strength.* **Lal, M.** s.l. : SPE, 1999, Vol. SPE 54346.

49. *Estimating Mechanical Properties of Shale From Empirical Correlations .* **Horsrud, P.** s.l. : SPE Drilling and Completion, 2001, Vol. 16 (2).

50. *Dielectric Constant Measurements: A New, Rapid Method To Characterize Shale at the Wellsite. .* **Leung, P.K. and Steig, R.P.** New Orleans : s.n., 1992. SPE/IADC Drilling Conference. New Orleans, Louisiana, 18-21 February. Paper SPE 23887.

51. *The effect of CO2 on the mechanical properties of the Captain Sandstone: Geological storage of CO2 at the Goldeneye field (UK).* **Hangx, S., A. van der Linden, F. Marcelis, A. Bauer.** in press, International Journal of Greenhouse Gas Control.

52. *Use of porosity as a strength indicator for sand production evaluation.* **Sarda, J.-P., N. Kessler, E. Wicquart, K. Hannaford, and J.-P. Deflandre.** Houston, USA : s.n., 1992. SPE Annual Technical Conference and Exhibition.

53. *Estimation of coal measures rock strength using sonic and neutron logs.* **McNally, G.H.** 4-5, 1987, Geoexploration, Vol. 24, pp. 381-395.

54. *Empirical relations between compressive strength and porosity of siliciclastic rocks.* **Vernik, L., M. Bruno, and C. Bovberg.** 7, 1993, International Journal of Rock Mechanics, Mining Sciences and Geomechanics Abstracts, Vol. 30, pp. 677-680.

55. *Prediction of Sand Production in Gas Wells: Methods and Gulf of Mexico Case Studies.* **Weingarten, J.S and Perkins, T.K.** 7, s.l. : Society of Petroleum Engineers, July 1995, Journal of Petroleum Technology, Vol. 47, pp. 596-600.

56. *Feasibility study of the stability of openhole multilaterals, Cook Inlet, Alaska (SPE 73192).* **Moos, D.B., M.D. Zoback, and L. Bailey.** 3, 2001, SPE Drilling & Completion, Vol. 16, pp. 140-145.

57. *Empirical relations between rock strength and physical properties in sedimentary rocks.* **Chang, C., Zoback, M. and Khaskar, A.** (3-4), 2006, Journal of Petroleum Science and Engineering, Vol. 51, pp. 223-237.

58. *The Role of Geomechanics in the Development of an HPHT Field.* **De Gennaro, S., Schutjens, P., Frumau, M., Fuery, M., Ita. J. and Fokker, P.** Salt Lake City: Utah : ARMA, 2010. 44th US Rock Mechanics Symposium,. 27-30 June. ARMA 10-450 .

59. **Shell.** *Goldeneye CCS Static Model (Aquifer).* Aberdeen : Shell, 2010. Scottish Power Consortium UKCCS Demonstration Competition. UKCCS-KT-S7.22-Shell-001.

60. **Shell.** *Goldeneye CCS Injectivity Analysis Preparation.* Aberdeen : Shell, 2011. Scottish Power Consortium UKCCS Demonstration Competition. UKCCS-KT-S7.18-Shell-002.

61. **Wentinck, H.M.** *Modelling of thermo-poro-elastic effects in the caprock around a borehole following the injection of cold CO2.* s.l. : Shell Global Solutions International BV., Rijswijk, 2011. p. 52. SR.11.13395.

62. *Self-sealing of fractures in argillaceous formations in the context of geological disposal of radioactive waste.* **Bock, H., B. Dehandschutter, C.D. Martin, M. Mazurek, A de Haller, F. Skoczylas, C. Davy.** NEA Report No. 6184, s.l. : NEA, 2010. ISBN 978-92-64-99095-1.

63. **Butler, R.M.** *Thermal Recovery of Oil and Bitumen.* Englewood Cliffs, New Jersey : Prentice Hall, 1991.

64. *Thermoporoelastic effect on wellbore stability* . **Chen, C. and Ewy. R.T.** s.l. : SPE, 2005, SPE Journal, pp. 121-129. SPE 89039.

65. *Changes in Earth Stresses around a wellbore caused by radially symmetrical pressure and temperature gradients* . **Perkins, T.K. and Gonzalez, J.A.** s.l. : SPE, 2004, SPE Journal, pp. 129-140. Paper No. SPE 10080.

66. *Time-dependent coupled processes in wellbore design and stability: PBORE-3D.* **Abousleiman, Y.N., Ekbote, S., Cui, L., Mody, F., Roegiers, J.C. and Zaman, M.** Houston, Texas : SPE, 1999. 74th SPE Annual Technical Conference and Exhibition. 3rd - 6th October. Paper SPE 56759.

67. *Stress and pore pressure distribution around a pressurized, cooled crack in low permeability rock.* **Ghassemi, A.** SGP-TR-183, s.l. : Proceedings of the thirty second workshop on geothermal reservoir engineering, Stanford University, 2007.

68. *Meyer Fracturing Simulators, User's guide, 8th Edition.* **Meyer, B.** s.l. : Meyer & Associated Inc., 2008.

69. *Hydraulic fracture with multiple segments I. Observations and model formulation.* **Germanovich, L.N., D.K. Astakhov, M.J. Mayerhofer, J. Shlyapobersky, L.M. Ring.** 097, s.l. : International Journal Rock Mechanics & Mineral Science, 1997, Vols. 34:3-4.

70. *Far-field hydraulic fracture geometry: A changing paradigm.* **Mahrer, K.D., W.W. Aud, & J.T. Hansen.** Paper 36441, s.l. : SPE, 1996.

71. *Influence of geologic discontinuities on hydraulic fracture propagation.* **Warpinski, N.R, and L.W. Teufel.** s.l. : Journal Petroleum Technology, 1987, Vols. pp 209-220.

72. *Laboratory investigation of fracture processes in hydraulic fracturing, Annual Report* . **Dudley, J.W., J. Shlyapobersky, R.B. Stanbery, A. Chudnovsky, M. Gorelik, Z. Wen, S. Glaser, M.K. Hand, G. Weiss.** Chicago, Illinois : GRI, 1995.

73. **(GRI), Gas Research Institute.** *Staged Field Experiment No. 3.* s.l. : GRI, 1991. Report GRI-91\0048.

74. *Deflection and propagation of fluid-driven fractures at frictional interfaces: A numerical investigation.* **Zhang, X, R.G. Jeffrey, & M Thiercelin.** s.l. : Journal Structural Geology, 2007, Vols. 29, pp 396-410.

75. *Progress in understanding jointing over the past century.* **Pollard, D.D, A.A. Aydin.** s.l. : Geological Society of America Bulletin, 1988, Vols. 100, pp 1181-1204.

76. *An experimentally verified criterion for propagation across unbounded frictional interfaces in brittle, linear elastic materials.* **Renshaw, C.E., and D.D. Pollard.** s.l. : International Journal Rock Mechanics & Mineral Science, 1995, Vols. 32, pp 237-249.

77. *Slippage and re-initiation of hydraulic fractures at frictional interfaces.* **Lam, K.Y., M.P. Cleary.** s.l. : Internationl Journal od Numerical and Analytical Methods Engineering, 1984, Vols. 8, pp 589-604.

78. *The interaction of a pressurised crack with a joint.* **Keer, L.M, S.H. Chen.** s.l. : Journal of Geophysical Research, 1981, Vols. 86, pp 103-1038.

79. *Top-seal leakage through faults and fractures: the role of mudrock properties. In Muds and Mudstones: Physical and Fluid Flow Properties, l., 158,.* **Ingram, G.M. and Urai, J.L.** [ed.] A.C., Fleet, A.J. and MacQuaker, J.H Aplin. 1999, Geollogical Society London Special Publication, Vol. 158, pp. 125-135.

80. *The influence of swelling clays on the deformation of mudrocks.* **Olgaard, D.L., Urai, J., Dell'Angelo, L.N., Nuesch, R. and Ingram, G.M.** (3-4), 1997, International Journal of Rock Mech & Min. Sci., Vol. 34, p. 235.

81. **Bock, H.** *RA Experiment: Updated review of the rock mechanics properties of the Opalinus Clay of the Mont Terri URL based on laboratory and field testing.* s.l. : National Cooperative for the Disposal of Radioactive Waste (NAGRA), 2009. p. 68. 2008-04.

82. *Stable creeping fault segments can become destructive as a result of dynamic weakening.* **Noda, H. and N. Lapusta.** 2013, Nature - Research Letter, p. 6.

83. *Modelling stress development and fault slip in producing hydrocarbon reservoirs overlain by rock salt caprocks.* **Orlic, B, and B.B.T. Wassing.** 2012. 46th US Rock Mechanics Conference. pp. ARMA 12-145.

84. **Mulders, F.M.M.** *Modelling of stress development and fault slip in and around a producing gas reservoir.* s.l. : Technical University Delft, 2003.

85. *Laboratory derived friction laws and their application to seismic faulting.* **Marone, C.** 1998, Annual Review of Earth and Planetary Sciences, Vol. 26, pp. 643–696.

86. *Earthquakes and friction laws.* **Scholz, C.H.** 1998, Nature, Vol. 391, pp. 37–42.

87. *Fault friction and slip stability not affected by CO2 storage: Evidence from short-term laboratory experiments on North Sea reservoir sandstones and caprocks.* **Samuelson, J., and C.J. Spiers.** CATO: CCS Research in the Netherlands, 2012, International Journal of Greenhouse Gas Control, Vol. 11, pp. S78–S90.

88. *Frictional and hydrologic properties of clay-rich fault gouge.* **Ikari, M. J., D. M. Saffer, and C. Marone.** B5, 2009, Journal of Geophysical Research, Vol. 114, p. B05409.

89. *Frictional Properties of Sedimentary Rocks and Natural Fault Gouge from the Longmen Shan Fault Zone, Sichuan, China.* **Verberne, B. A., C. He, and C. J. Spiers.** 5B, 2010, Bulletin of the Seismological Society of America, Vol. 100, pp. 2767-2790.

90. *Effect of hydration state on the frictional properties of montmorillonite-based fault gouge.* **Ikari, M. J., D. M. Saffer, and C. Marone.** B6, 2007, Journal of Geophysical Research, Vol. 112.

91. *Comparison of smectite- and illite-rich gouge frictional properties: application to the updip limit of the seismogenic zone along subduction megathrusts.* **Saffer, D. M., and C. Marone.** 1-2, 2003, Earth and Planetary Science Letters, Vol. 215, pp. 219-235.

92. **Metz, B. et al.** *Special Report on Carbon Dioxide Capture and Storage Prepared by Working Group III of the Intergovernmental Panel on Climate Change* . [ed.] B., O. Davidson, H. C. de Coninck, M. Loos, and L. A. Meyer Metz. Cambridge and New York : Cambridge University Press, 2005. p. 442.

93. *Feasibility of CO2 Storage in Barendrecht/ Barendrecht-Ziedewij: Caprock and Fault Integrity Study* . **Orlic, B., Fokker, P., Geel, K.** s.l. : TNO, 2007. TNO report 2007-U-R0461/C.

94. **Shell.** *Goldeneye CCS Monitoring Technology Feasibility Report.* Aberdeen : Shell, 2010. Scottish Power Consortium UKCCS Demonstration Competition. UKCCS-KT-S7.20-Shell-003.

95. —. *Goldeneye CCS Pore Pressure Prediction.* Aberdeen : Shell, 2011. Scottish Power Consortium UKCCS Demonstration Competition.UKCCS-KT-S7.21-Shell-006.

96. —. *Goldeneye CCS Cement concept select.* Aberdeen : Shell, 2010. Scottish Power Consortium UKCCS Demonstration Competition. UKCCS-KT-S7.16-Shell-007.

97. *Laboratory testing of long term fracture permeability in shale* . **Cuisiat, F., Grande, L. and Høeg, K.** Irving, Texas : s.n., 2002. SPE/ISRM Rock Mechanics conference. 20-23 October. paper SPE 78215.

98. **Mulders, F.M.M., R. Gouwen, B. Orlic, and T. Benedictus.** *Well Integrity for CO2 storage in the fields Barendrecht and Barendrecht-Ziedewij,.* Utrecht : TNO, 2007. TNO report 2007-U-R0377/C.

99. *Gas breakthrough experiments on fine-grained sedimentary rocks.* **Hildenbrand, A, S. Schlomer, and B. M. Krooss.** 2002, Geofluids, Vol. 2, pp. 3–23.